Johann Wolfgang Goethe-Universität Frankfurt am Main
Department of Physics
Program of Study Astrophysics (Ph.D.)

S-Process Nucleosynthesis in and from Asymptotic Giant Branch Stars

Doctoral Thesis
for obtaining the academic degree
Doctor of Natural Sciences

submitted by
Alexander J. Dimoff (3007 08 211 640)
date of submission
29. August, 2025

Supervisor:	Prof. Dr. Camilla J. Hansen
First Referee:	Prof. Dr. Camilla J. Hansen
Second Referee:	Sen. Lec. Dr. Richard J. Stancliffe

Abstract

This thesis investigates the synthesis and transfer of s-process elements in low-mass binary stars by combining stellar spectroscopy, stellar evolution modeling, and nuclear physics experiments.

The first project follows a four-year high-resolution spectroscopic observation campaign. I observe intrinsic asymptotic giant branch and extrinsic binary companions across a broad range of metallicities, for which I derive orbits, stellar parameters, and chemical abundances. I determine abundances of carbon, α-elements, and s-process elements, expanding the census of heavy element abundance patterns. Comparisons with AGB yield models confirm s-process enrichment in binary systems and reveal correlations between enrichment levels and progenitor AGB masses, establishing observational benchmarks for nucleosynthesis and mass transfer.

For the second project, I compute a grid of 2691 binary stellar evolution models with the STARS code, spanning a range of metallicities, donor masses, and accreted masses. By comparing models with my observations of Ba, CH, and CEMP-s stars and the literature, I constrain accretion efficiencies and progenitor properties. I find consistent AGB donor masses across metallicities. Results show CH and CEMP-s stars form through small accretion events ($\sim$0.1 M$\odot$), weak Ba stars through moderate accretion ($<$0.5 M$\odot$), and that strong Ba stars require more substantial mass transfer ($>$0.5 M$\odot$). Metal-rich systems are found to accrete more material than metal-poor ones, linking abundance patterns and metallicity to accretion histories.

In the third project, I perform a nuclear physics experiment to probe neutron-capture reactions that shape the end of the s-process. Using the activation method and beta spectroscopy, I measure the cross section of the double-magic nucleus ^{208}Pb at 25 keV and establish an upper limit at 5 keV. These data provide useful inputs for stellar nucleosynthesis models, clarifying the role of Pb as an s-process termination point.

Together, these studies bridge observations, modeling, and experiments to advance our understanding of the synthesis, transfer, and surface imprint of s-process elements in low-mass binary stars.

Contents

1 Introduction

1.1 Motivation

Stellar nucleosynthesis is a cornerstone of modern nuclear astrophysics and is central for explaining the origin of the elements. Understanding the slow neutron-capture process (s-process), one of the main mechanisms responsible for producing elements heavier than iron (A>90), is essential for explaining the observed chemical abundances in stars and the chemical evolution of the Galaxy. This thesis presents insights into the three disciplines of nuclear astrophysics to build a comprehensive picture of s-process nucleosynthesis. To this end, I seek to better understand the asymptotic giant branch (AGB) stars where the s-process takes place.

To investigate the origin of heavy elements, we examine the fundamental nucleosynthesis processes responsible for shaping the cosmic abundances. Observations provide the empirical signatures of the s-process in stellar atmospheres, especially in binary systems affected by mass transfer. With observations, I aim to constrain the mass of the AGB star that has produced the observed abundance pattern. Theoretical models describe the evolution of stars and simulate the complex mixing and accretion histories of binary companions. Through simulations, I aim to determine how much mass is transferred from the AGB star to its companion to explain the observations. Experimental measurements of neutron-capture cross sections supply the key nuclear data needed to anchor and validate theoretical predictions. With experiments, I aim to measure the neutron interaction cross-section to provide further constraints on modeling the s-process in AGB stars. Combining these approaches provides a detailed investigation of heavy element synthesis in stars.

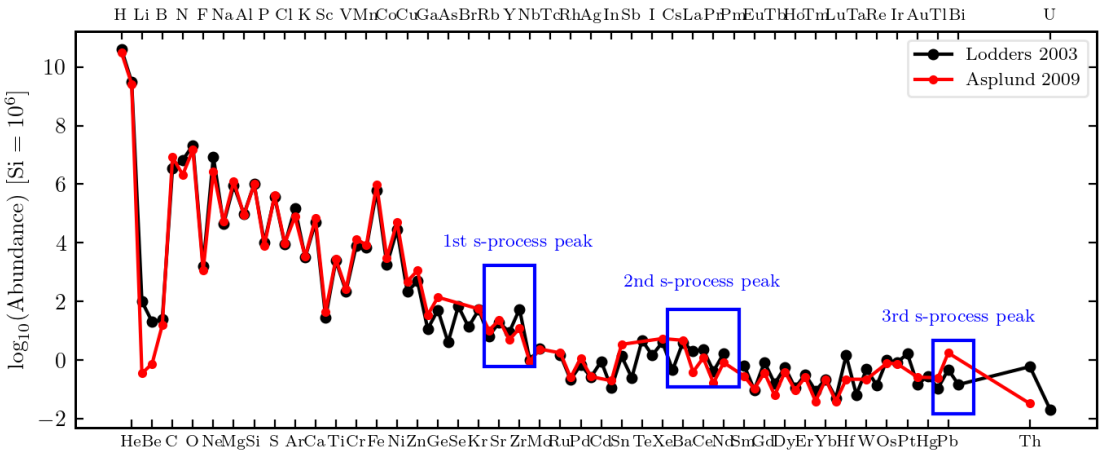

Figure 1.1: The solar system abundance pattern, using data from Lodders (2003) and Asplund et al. (2009). The first, second, and third s-process peaks are highlighted in blue boxes.

1.2 Nucleosynthesis

Nucleosynthesis theory works to explain the natural processes that produce differing chemical abundances and their isotopes. When plotting the abundances against the atomic number of an element as in Figure 1.1, it is clear to see that heavier elements are less abundant than light elements by factors up to 10 million, and there is a jagged structure with even-odd nuclei.

Nucleosynthesis is the creation of new elements, and stars produce heavy elements by combining lighter nuclei. Generations of star formation have increased the overall metal content of the universe and lowered the overall hydrogen mass fraction. The production of heavier elements ($Z \geq 6$; carbon and heavier) requires extreme temperatures and pressures that can only be found in stellar interiors and supernovae.

Eddington suggested that stars produce energy by fusing hydrogen into helium (Eddington, 1920, 1926), but the nuclear mechanism was not understood at the time. Hans Bethe was the first to identify the mechanisms by which hydrogen is fused into helium: the proton-proton (PP) chain and the carbon-nitrogen-oxygen (CNO) cycle (Bethe, 1939). Fred Hoyle explained the production of heavier elements starting from hydrogen, and how the abundances of the elements increases with time (Hoyle, 1946, 1954). The seminal paper from Burbidge et al. (1957) defined new

and accepted processes for the transformation of nuclei within stars, which could be observed and documented by astronomers.

Elemental abundances carry the nucleosynthetic fingerprint of their stellar origins. Beyond the iron peak, the solar system abundance curve presents a different trend compared to predictions from isolated stellar evolution. There are double-peaked structures in the solar system abundance pattern near mass numbers A = 80, 130-140, and 195-208, or neutron numbers N = 50, 82, or 126 corresponding to stable neutron shell configurations, indicating neutron-based nuclear processes; see Figure 1.1.

1.2.1 The s-process in AGB Stars

The slow neutron-capture process (s-process) is the primary mechanism responsible for producing roughly half of the elements heavier than iron. Upon capturing a neutron, a seed nucleus becomes a heavier isotope of that element. If the newly formed nucleus is unstable, it can decay through the β^- conversion channel to a stable isotope of another element before another neutron is captured. In low- and intermediate-mass stars (1–6 $M_\odot$), this process occurs during the thermally-pulsing asymptotic giant branch (TAGB) phase, specifically within the He-intershell region outside of the He-burning layer (Busso et al., 1999; Käppeler et al., 2011).

A nucleus can capture a free neutron and increase its mass number by one, following

$$ {}^{A}_{Z}X + n \;\rightarrow\; {}^{A+1}_{Z}X + \gamma \;\rightarrow\; {}^{A}_{Z+1}Y + e^- + \bar{\nu}_e, \tag{1.1} $$

where A is the mass number of element X and Z is the atomic number, or number of protons. The newly produced nucleus ${}^{A+1}_{Z}X$ may be radioactive, and can decay through the β^- conversion, producing a new element Y with a higher atomic number as the neutron is converted to a proton, releasing an electron and an antineutrino.

Through a sequence of neutron captures and β-decays, seed nuclei (mainly iron-peak elements) are converted to heavier stable isotopes. This can be seen in Figure 1.2 in the black curve increasing with neutron and proton number. In the s-process, the progression of synthesizing heavy elements closely follows the valley of stability.

In AGB stars, thermal pulses (TPs) and third dredge-up (TDU) events drive periodic helium-shell flashes with the ingestion and partial mixing of protons into the

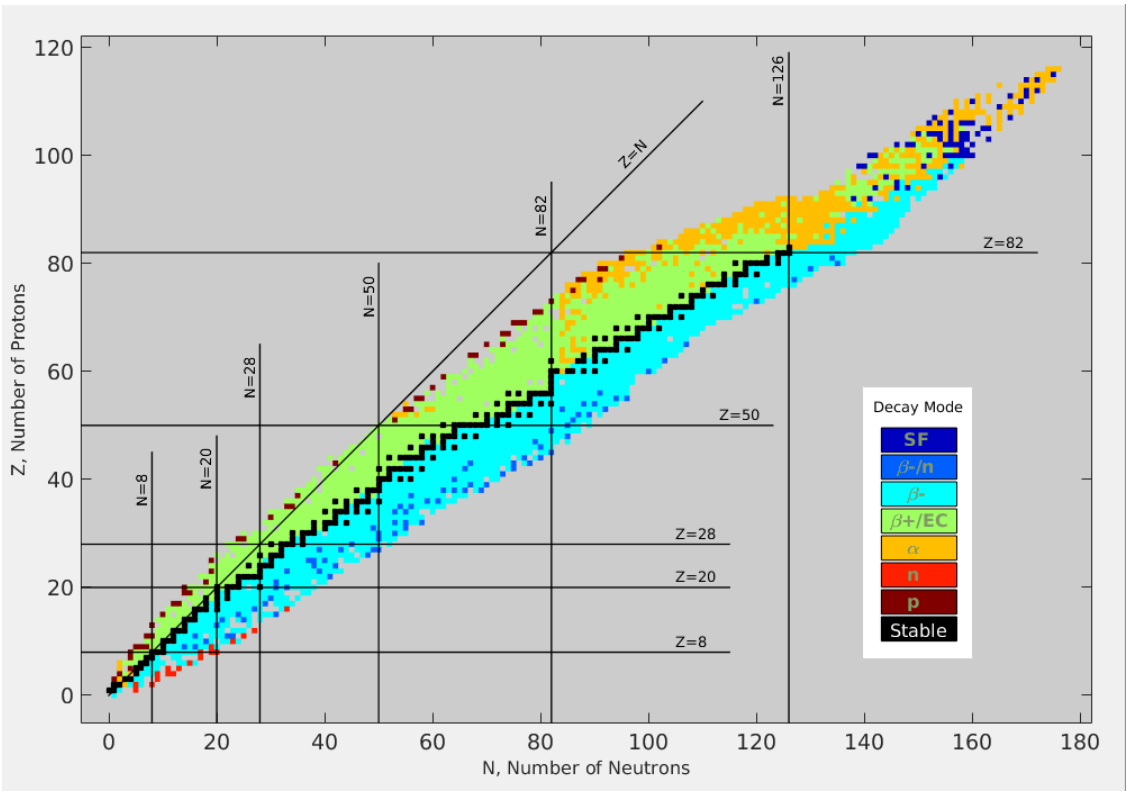

Figure 1.2: The nuclear valley of stability, indicating stability and decay processes. Vertical and horizontal lines indicate nuclear shell closures, highlighting more stable nuclei.

He-intershell region, seen in Figure 1.3, adopted from Kippenhahn et al. (2013). The region between the outer convection zone (OCZ) and the carbon-oxygen core is shown, with TPs and TDU events. At time t_1, the thermal pulse begins and instigates an intershell convection zone (ISCZ), which grows in mass and may reach the H-burning shell, which temporarily halts fusion as it expands. With the termination of the pulse, the OCZ extends into the intershell region, bringing protons into the hotter environment.

The H-shell reignites, and high temperatures allow the ^{12}C(p,γ)^{13}C reaction to occur, forming a ^{13}C pocket and initiating s-process nucleosynthesis. Ambient α particles interact with ^{13}C to release neutrons, producing moderate neutron densities (10^5–10^9 cm^{-3}) at high temperatures ($T \sim 3 \times 10^8$ K), conducive to neutron capture events Käppeler et al. (2011). The dominant neutron sources in this environment are the reactions ^{13}C(α,n)^{16}O at lower temperatures and ^{22}Ne(α,n)^{25}Mg at higher

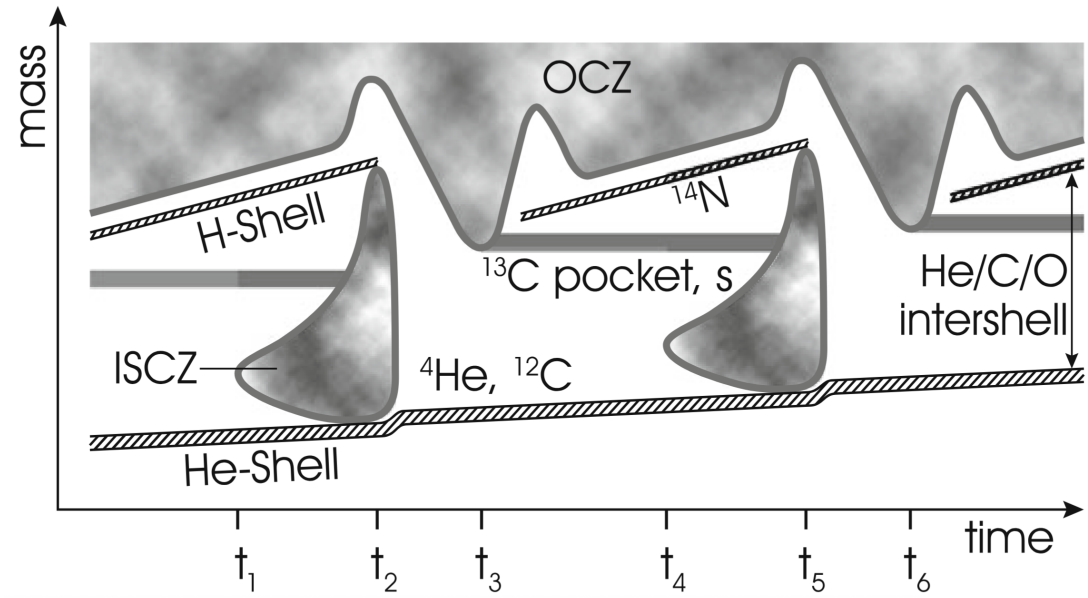

Figure 1.3: Schematic of mixing episodes and nucleosynthesis during AGB thermal pulses, from Kippenhahn et al. (2013).

temperatures within thermal pulses (Gallino et al., 1998). The ^{13}C(α,n)^{16}O reaction is the primary source of neutrons under typical AGB conditions. Heavy seed nuclei (e.g., Fe) capture the neutrons and, through the s-process, slowly build up heavier elements.

The s-process in AGB stars primarily synthesizes heavy elements up to Pb and Bi, with the overall abundance patterns being highly sensitive to the stellar mass and metallicity. These signatures are commonly characterized using elements at the first s-process peak ($N \approx 50$, including Sr, Y, and Zr) and the second peak ($N \approx 82$, including Ba, La, and Ce) by comparing average abundances or individual elements from each group (Busso et al., 2001; Cseh et al., 2018; Lugaro et al., 2020). The newly synthesized s-process elements are mixed to the stellar surface via convection and TDU events. This material is later expelled through mass loss in stellar winds and TPs, contributing to overall galactic chemical enrichment (Herwig, 2005; Straniero et al., 2006; Karakas and Lattanzio, 2014). At very low metallicities ([Fe/H] $<$ -2.5), there are insufficient seed nuclei for the s-process to operate, thus s-process enhancement from AGB stars is not expected at such metallicities (Hansen et al., 2014; Lombardo et al., 2025).

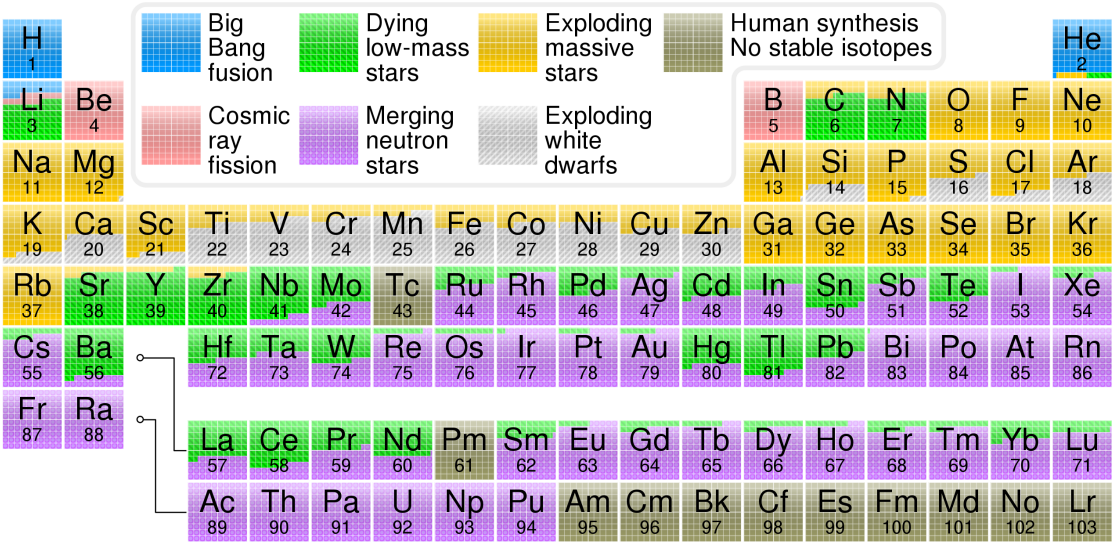

Figure 1.4: Periodic table highlighting the origin of the elements. Elements in green that are produced in 'dying low-mass stars' are of particular interest to this study. Based on the work from Kobayashi et al. (2020).

A striking observational signature of the s-process is the overabundance of heavy elements in AGB star atmospheres. For example, Ba enhancements of 20–50 times the solar value have been observed, even up to 100 times in extreme cases. The most compelling evidence for ongoing s-process nucleosynthesis came with the detection of technetium (Tc) in the spectra of red giants (Merrill, 1952). The radioactive element Tc has no stable isotopes and a maximum half-life of around 4.2×10^6 years, indicating that it must have been recently synthesized within the AGB star.

From a broader perspective, the study of s-process elements in AGB stars is critical for understanding stellar life cycles and galactic chemical evolution (Nomoto et al., 2013; Arcones and Thielemann, 2023). Different initial masses and metallicities of AGB stars lead to varied s-process signatures, allowing these stars to serve as cosmic laboratories for nucleosynthesis and chemical evolution modeling. Ultimately, low-mass AGB stars contribute to the chemical enrichment of galaxies by returning their processed material to the interstellar medium through repeated mass-loss episodes, representing a major source of heavy elements throughout cosmic history.

1.2.2 Big Bang Nucleosynthesis

The primordial nucleons formed out of the quark-gluon plasma minutes after the big bang as the universe rapidly expanded and cooled. With only protons and neutrons, the nuclear reactions that formed the first light nuclei are collectively called Big Bang Nucleosynthesis (BBN). As the universe cooled below about 10^9 K, energetic collisions between particles ceased, and only the fastest and simplest reactions occurred. This filled the early universe with hydrogen and helium, and trace amounts of deuterium and lithium. After approximately 20 minutes, the continued expansion reduced temperatures and densities, halting the initial burst of element formation. While BBN sets the primordial chemical foundation, the study of stellar nucleosynthesis is essential for understanding the full chemical evolution of the universe.

1.2.3 Nucleosynthesis in Stars

A defining feature of stars is that they perform nuclear fusion in and around their cores. As stars evolve, they progressively synthesize heavier elements. Nuclear fusion reactions in stars create many of the elements, up to and including iron and nickel in massive stars. In most cases, these nucleosynthesis products remain trapped in the stellar interior until they are released via stellar winds or explosive events. Low mass stars ($M < 8\mathrm{M}_\odot$) will eject their enriched atmospheres, and high mass stars will eject mass through catastrophic and explosive supernovae.

Fusion of hydrogen nuclei to form a ^{4}He nucleus is the dominant energy production process in the cores of main sequence stars. There are two main channels through which H-fusion (or H-burning) occurs: the proton-proton (PP) chain and the carbon-nitrogen-oxygen (CNO) cycle. The initial stellar mass, and therefore the interior conditions temperature and pressure, mediates which process is more efficient.

PP-Chain Low mass stars like the Sun fuse hydrogen through the PP-chain. In this channel, two protons (^{1}H) fuse to form deuterium with the emission of a positron and a neutrino, as one of the protons is converted to a neutron via the β^+ decay. The deuterium nucleus and a third proton quickly fuse to create ^{3}He. These two steps must happen twice, such that two ^{3}He nuclei are synthesized. There are different branches within the PP-chain through which ^{4}He can be generated once the ^{3}He

has been produced. The PP-I branch is most common in the Sun following ^{3}He + ^{3}He $\rightarrow$ ^{4}He + 2^{1}H, and delivering 26.73 MeV of energy. For stars with masses up to about 1.3 $M_\odot$, energy is transported from the core towards the stellar surface via radiative diffusion rather than convection Reiners and Basri (2009).

CNO Cycle In higher mass stars ($M \geq 1.3$ $M_\odot$), the process through which H is fused to form He is the CNO cycle (also called the Bethe-Weizäcker cycle). The CNO cycle uses nuclei of carbon, nitrogen, and oxygen as intermediates to produce the ^{4}He nucleus. The intermediate nuclei are each consumed at one step during the fusion cycle, but are regenerated at a later step. While the total number of nuclei in the cycle are conserved, the relative proportions of the nuclei are changed through the CNO cycle. In this regime, convective energy transport dominates in the core due to high energy generation rates. This mixes the hydrogen within the fusion zone, and can supply fresh H from the surrounding envelope.

Once the core hydrogen fuel is exhausted, the star will ignite hydrogen burning in a shell around the He core. This H-burning proceeds through the CNO cycle. The thermal energy release from shell burning drives the expansion of the outer hydrogen envelope and the star ascends the red giant branch (RGB). Hydrogen fusion on the main sequence and on the RGB creates an internal core of He that remains inert until the temperatures reach about 10^8 K, where He fusion is possible.

Helium Burning Helium burning produces ^{12}C via the triple-α process, a bottleneck in the entire nucleosynthesis process, where three helium nuclei are combined to create ^{12}C with a brief intermediary ^{8}Be. This marks a particular and important phase in the evolution of a star. In the electron-degenerate cores of red-giant stars, the entire core is the same temperature and pressure. When the core density reaches the critical point, He fusion ignites throughout the core, known as the helium flash. Although the luminosity of this event is extremely high ($\sim 10^{11}$ $L_\odot$), no effects are immediately observed because the energy is used to lift the degeneracy conditions of the star. With hydrostatic equilibrium restored, the star begins to fuse He in the core while continuing to burn H in a layer above the core, entering a steady-state He burning phase on the red clump. Initially, the star may move toward bluer colors along the horizontal branch, then loop back toward the Hayashi track and ascend the AGB. When the core helium fuel is exhausted, He fusion continues in a shell

around a core of carbon and oxygen.

Alpha Process and advanced Burning Stages At higher temperatures and pressures, heavier nuclei will capture ^{4}He and create new elements like oxygen, neon, and magnesium; the 'alpha' elements. This process produces elements with even-numbered nuclei, contributing to the sawtooth pattern seen in Figure 1.1.

In the cores of more massive stars (> 4 M$_\odot$), carbon fusion produces Ne, Na, and Mg. Stars with masses > 8 M$_\odot$, fuse carbon, neon, oxygen, and silicon in successive burning stages, each requiring higher and higher core temperatures and resulting in the production of elements up to iron and nickel. The chain of fusion reactions could theoretically continue to heavier and heavier elements. However, after the synthesis of Fe and Ni, the reactions become endothermic, and photodisintegration prevents further progress. Silicon burning is the final stage of fusion in the cores of massive stars, after which an iron-group core forms and collapses, triggering a supernova.

Explosive Nucleosynthesis Explosive nucleosynthesis is driven through the gravitational collapse and subsequent heating of the upper layers of massive star atmospheres, as they are shocked in the supernova explosion. The outward compressive shockwave raises the gas temperatures causing furious burning for a brief time (~ 1 second), and creates elements in the mass range A=28-56 (Si - Ni).

Such explosive events feature extreme temperatures and densities, causing the formation and destruction of nuclei. Spallation reactions from other particles can strip nucleons from nuclei reducing the mass number. Emitted neutrinos will interact with nuclei causing them to eject neutrons or protons via the ν-process. Electrons will also be captured, shifting nuclei towards unstable isotopes and triggering decay.

Ultimately, stellar nucleosynthesis creates stable elements with high binding energies per nucleon. Elements heavier than iron cannot be formed efficiently through fusion processes alone, due to the increasing Coulomb barrier and the fusion reactions becoming endothermic. Instead, they are primarily synthesized through the slow (s-), intermediate (i-), and rapid (r-) neutron capture processes. This is visualized in Figure 1.2, displaying the nuclear valley of stability. With proton number on the y axis and neutron number on the x axis, this plot displays isotopes of the elements and their decay channels. The black curve denotes the stable isotopes. The blue region indicates neutron-rich isotopes; with high neutron numbers, they have

lower binding energies and may be unstable or radioactive. Capturing a neutron increases the atomic mass, and the β^- decay process converts this neutron into a proton with the release of an electron and a neutrino. The increase in proton number then leads to the synthesis of the next heavier element. This chain of captures and decays will produce stable isotopes that can be measured and observed.

Other Neutron Capture Processes

i-Process The intermediate neutron capture process (i-process) is characterized by neutron densities $n_n \sim 10^{13}$ to 10^{15} cm^{-3}, between those typical of the s- and r- processes (Choplin et al., 2021). Isotopes produced are within the neutron-rich light blue region in Figure 1.2, and remain only a few isotopes away from stability. First proposed to explain peculiar abundance patterns in certain stars, the i-process operates with neutron capture rates faster than the s-process but slower than the r-process.

Astrophysical sites for the i-process include proton ingestion events (PIEs) in low-metallicity or low-mass AGB stars (Choplin et al., 2021), rapidly accreting white dwarfs (RAWDs) (Denissenkov et al., 2017), very late thermal pulses of post-AGB stars, or helium shell flashes in rapidly rotating massive stars. PIEs occur when convective helium-burning shells engulf hydrogen-rich material, leading to rapid neutron production via the ^{13}C(α,n)^{16}O reaction. The i-process provides a plausible explanation for the abundance patterns observed in carbon-enhanced metal-poor (CEMP)-r/s stars, which show mixed signatures of both s- and r-process enrichment.

r-Process The rapid neutron-capture process (r-process) is responsible for the creation of about half of the atomic nuclei heavier than iron. Occurring at extremely high neutron densities (on the order of 10^{24} neutrons per cm^3) where the neutron capture rate is significantly faster than the β-decay rate, neutron-rich nuclei are formed up to the limit of stability (also called the neutron drip line) Burbidge et al. (1957). In Figure 1.2, this is the edge of the light blue region to the right of the valley of stability. The r-process is responsible for the formation of the most neutron-rich stable isotopes, and typically the heaviest isotopes of every element. Abundance peaks for the r-process occur near mass numbers A=82 (Se, Br, Kr), 130 (Te, I,

Xe), and 196 (Os, Ir, Pt).

Astrophysical sites for the r-process include core-collapse supernovae, magneto-rotational supernovae, collapsars, neutron star mergers (e.g., GW170817) and, more recently proposed, magnetar flares. The relative contributions of each remain an active area of research. The resulting heavy elements are ejected during explosive events, and are incorporated into new generations of stars.

1.3 Astrophysical Observations: Spectroscopy

Stars are excellent astrophysical laboratories for studying nucleosynthesis. The photospheric abundances of stars reflect the signatures of internal nucleosynthetic and mixing processes, as well as external processes such as accretion. Binary systems in which one star has evolved through the AGB phase and transferred s-process enriched material onto a companion are particularly valuable, as they provide different methods to determine fundamental parameters and investigate the s-process. The enriched star (a main sequence or a giant star) is referred to as an "extrinsic" star, as it did not produce these heavy elements itself (as an "intrinsic" star would, e.g. an evolved AGB star), but instead obtained them from its evolved companion.

Nucleosynthesis theory predicts how elements form, and observational studies reveal these processes in action. By collecting and analyzing light from stars, we can learn about their chemical composition. High-resolution, high signal-to-noise (SNR) spectroscopy allows the derivation of detailed abundance patterns of elements produced by, e.g., the s-process. Comparing these abundances to nucleosynthesis model predictions constrains the physical conditions in the AGB stars that produced these elements, as well as the efficiencies of mixing and mass transfer processes. Additionally, precise radial velocity monitoring of such stars confirms their binarity, allows derivation of orbital parameters, and provides further insight into the mass transfer history.

By dispersing starlight into its component wavelengths, spectroscopy reveals information about the physical processes that emit or absorb light in different parts of the electromagnetic spectrum. The spectral resolution $R = \lambda/\Delta\lambda$ defines how finely the light is split. Instruments with resolutions $R \leq 2000$ are commonly referred to as low-resolution, $R \geq 20000$ as high resolution, and between as medium or moderate

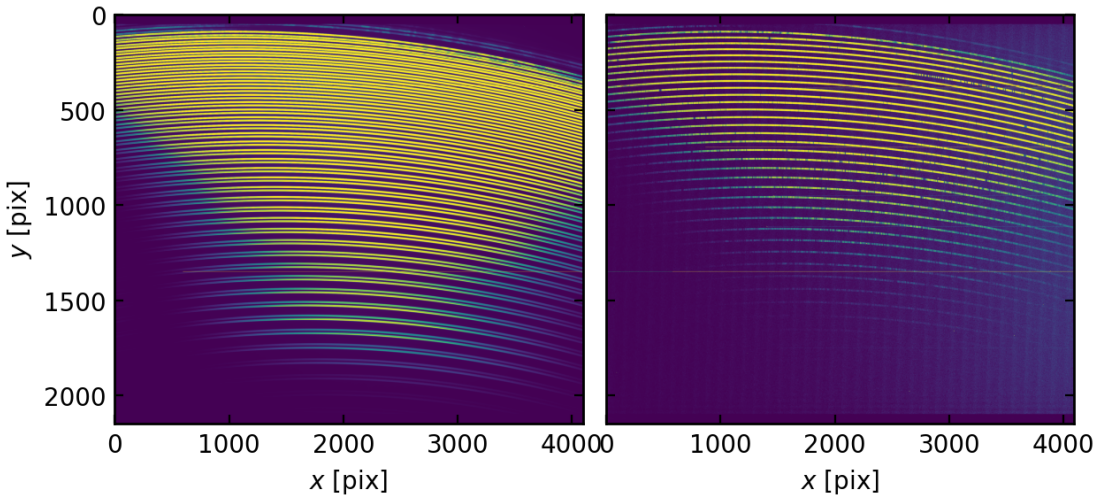

Figure 1.5: Left: A flat field 2D echelle spectrum from the FEROS instrument. Right: A raw echellogram of the barium star HD 102762.

resolution. Higher resolution means a finer sampling in wavelength, but this comes at a cost where more light is required to produce the same signal-to-noise ratio.

Optical spectra effectively scan the photosphere of the star, from 4000 Å to 7000 Å. One specific type of high-resolution spectroscopy is echelle spectroscopy, where the light across a broad range in wavelength is cross-dispersed in channels across the two-dimensional plane of the detector. Example echelle spectra from the FEROS instrument can be seen in Figure 1.5, where the flux is recorded along the bright spectral orders. Redder wavelengths are towards the top, and bluer wavelengths are towards the bottom. In the left frame is a flat field image, where two channels are seen in every spectral order. Here, the lower channel is used for wavelength calibration and the upper channel is for flat field calibration. In the right panel of Figure 1.5, a raw stellar spectrum of the barium star HD 102762 is shown. Absorption features in the stellar flux are seen as dark gaps along the bright channels.

Stellar spectra are incredibly data-rich, and a multitude of information can be extracted from a stellar spectrum. They reveal radial velocities (RVs) and stellar parameters such as effective temperature ($T_{\rm eff}$), surface gravity (log(g)), metallicity ([Fe/H]), and microturbulence (ξ). By studying individual spectral features, chemical abundances of elements in the stellar photosphere can be computed. To this

end, we must compute the transport of radiation through the stellar atmosphere.

1.3.1 Radiation in Stellar Atmospheres

The specific intensity I_ν quantifies how much radiant energy is emitted in a specific direction per unit frequency per unit solid angle:

$$I_\nu = \frac{dE}{\cos\theta \, dA \, dt \, d\nu \, d\Omega} \tag{1.2}$$

with dE being the transported energy, dA the patch of surface area, dt the time interval, $d\nu$ the frequency interval, $d\Omega$ the solid angle, and θ the angle between the direction of radiation and the surface normal direction. Flux is a measure of the energy flow across an area over time in a spectral range $d\nu$, and is related to the intensity through the expression

$$F = \oint I_\nu \cos\theta \, d\Omega, \tag{1.3}$$

which can be used to compute the theoretical spectrum of a star. When passing through a medium, the intensity of light diminishes an amount defined by the density of the material, ρ, the thickness of the material, dx, and the (continuous) absorption coefficient, κ_ν, following

$$dI_\nu = -\kappa_\nu \rho I_\nu \, dx. \tag{1.4}$$

The processes contributing to the absorption lead to scattering and thermalization. The optical depth of a material is defined as the integral of the absorption coefficient and the density over some path l with

$$\tau_\nu = \int_0^l \kappa_\nu \rho \, dx. \tag{1.5}$$

Using the optical depth, the expression for the absorption can be rewritten as

$$dI_\nu = -I_\nu d\tau_\nu, \tag{1.6}$$

with the solution being an exponential function with the negative optical depth: $I_\nu = I_\nu^0 \exp(-\tau_\nu)$.

The total continuum absorption is the combined result of many different electronic transition processes, namely bound-free and free-free transitions between atoms, molecules, and electrons in the stellar atmosphere. This happens through the atmosphere up to the deepest layers in the photosphere at the $\tau = 1$ surface of last scattering. Similar to absorption, the emission from a medium of thickness dl and a density of ρ is defined as

$$dI_\nu = j_\nu \rho dl. \tag{1.7}$$

The processes contributing to emission are creation and scattering of photons. Here, scattering is defined to be the absorption and immediate re-emission of a photon of equal energy. The ratio of emission to absorption is the specific intensity emitted at some point in a hot gas. This ratio is defined as the source function,

$$S_\nu = j_\nu / \kappa_\nu. \tag{1.8}$$

Emission from a gas in thermodynamic equilibrium is described by black-body radiation, using Planck's radiation law as the source function. The Planck function describes the intensity distribution across wavelengths

$$B_\nu(T) = \frac{2h\nu^3}{c^2} \frac{1}{e^{\frac{h\nu}{kT}} - 1}, \tag{1.9}$$

where $h = 6.626 \times 10^{-27}$ erg s is Planck's constant, ν is the frequency, $c = 2.99792 \times 10^{10}$ cm s^{-1} is the speed of light, $k = 1.380649 \times 10^{-16}$ erg K^{-1} is Boltzmann's constant, and T is the temperature in Kelvin.

The Transfer Equation

The change in specific intensity over a path length, dl, is the sum of the losses and gains expressed in the absorption and emission coefficients κ_ν and j_ν,

$$dI_\nu = -\kappa_\nu \rho I_\nu dl + j_\nu \rho dl. \tag{1.10}$$

Dividing by the increment optical depth $d\tau_\nu$, we find

$$\frac{dI_\nu}{d\tau_\nu} = -I_\nu + j_\nu / k_\nu,$$

and using the source function, we arrive at the equation of radiative transfer,

$$\frac{dI_\nu}{d\tau_\nu} = -I_\nu + S_\nu. \tag{1.11}$$

In the case of local thermodynamic equilibrium (LTE), using the Planck function as the source function and knowing the temperature distribution through the atmosphere provide a solution to the transfer equation.

Radiative Equilibrium

The nuclear energy generated in the core of a star flows outwards to the outer boundary. The conservation of energy must apply through the stellar photosphere. For the plane-parallel geometry, the total energy flux $F(l)$ is held constant. When this energy is being carried by radiation, the total energy flux is

$$F(l) = \int_0^\infty F_\nu(\tau_\nu) d\nu = F_0. \tag{1.12}$$

If convection plays a significant role in transporting energy, the convective flux, $\Phi(l)$, should be included such that

$$\Phi(l) + \int_0^\infty F_\nu(l) d\nu = F_0. \tag{1.13}$$

The flux constant, F_0, is often expressed in terms of effective temperature $F_0 = \sigma T_{\rm eff}$, where $\sigma = 5.670 \times 10^{-5}$ erg cm^{-2} s^{-1} K^{-4} is the Stefan-Boltzmann constant and $T_{\rm eff}$ is the effective temperature in Kelvin.

Excitation equilibrium refers to the balance of level populations in atoms or ions, within the same ionization state. The fraction of atoms or ions that have been excited to the nth level is proportional to the statistical weight $g_n = 2J + 1$, with J being the inner quantum number, and the Boltzmann factor $N_n = \text{const}\, g_n \exp(-\chi_n/kT)$. The ratio of populations in two levels m and n is then

$$\frac{N_n}{N_m} = \frac{g_n}{g_m} \exp(-(\chi_n - \chi_m)/kT). \tag{1.14}$$

We can also define the number of atoms in a level n as a fraction of all atoms of the same species N with

$$\frac{N_n}{N} = \frac{g_n \exp(-(\chi_n)/kT}{g_1 + g_2 \exp(-\chi_2)/kT) + g_3 \exp(-\chi_3/kT) + ...} \tag{1.15}$$

$$= \frac{g_n}{u(T)} \exp(-\chi_n/kT). \tag{1.16}$$

The function $u(T) = \sum g_i \exp(-\chi_i/kT)$ is called the partition function, and is typically precomputed and tabulated. Similarly, ionization equilibrium is the balance of different ionization states of a given element (e.g., Fe I and Fe II), and is governed by the Saha equation under the assumptions of LTE. For a collision-dominated gas, the ionization is computed using

$$\frac{N_1}{N_0} P_e = \frac{(2\pi m_e)^{3/2} (kT)^{5/2}}{h^3} \frac{2u_1(T)}{u_0(T)} \exp(-I/kT). \tag{1.17}$$

In this expression, N_1/N_0 is the ratio of ions to neutral atoms, $u_1(T)/u_0(T)$ is the ratio of the partition functions, I is the ionization energy, m_e is the mass of the electron, and h is Planck's constant. This equation is also written as

$$\frac{N_1}{N_0} = \frac{1.2020 \times 10^9 \frac{u_1}{u_0} \theta^{-5/2} 10^{\theta I}}{P_e}, \tag{1.18}$$

with $\theta = 5040/T$, with the temperature in units of K.

Formation and Behavior of Spectral Lines

Depending on the localized temperature and pressure, bound-bound and bound-free transitions give rise to spectral lines. The strength of the line depends on the number of absorbers along the line-of-sight through the visible atmosphere. Thus, the atomic level populations and the path length are important. Across a line profile, the line absorption coefficient, l_ν, will change, being larger towards the center of the line. For lines formed in LTE, the line source function is the same as the Planck function. In the non-equilibrium case, S_l and I_ν are interdependent because collisions and radiation affect the excitation.

Absorption lines may form at different depths within the atmosphere, where weak absorption lines form deeper within the photosphere. Since strong absorption lines are formed over a wide range of depths in the atmosphere, it is difficult to specify a

single depth of formation of the line.

Broadening Mechanisms The strength or width of a spectral line depends on the thermal and microturbulent velocities and the number of absorbers. The most important variables are temperature, pressure, and abundance. The interaction of light with atoms results in absorption or attenuation, whose damping profile is described as Lorentzian. Through quantum mechanics and the Heisenberg uncertainty principle, the oscillator strength, f, different for each atomic level, is indicative of the transition probability.

Temperature is the variable that most strongly controls the line strength. The ratio of the line opacity to the continuum opacity is considered when predicting how a line profile will change with temperature. This ratio depends on temperature and electron pressure P_e, which itself depends on temperature. Thermal broadening (or Doppler broadening) is caused by the random thermal motion of particles in the gas. This produces a Gaussian profile and is highly temperature dependent, where higher temperatures will result in broader lines. Thermal broadening strongly affects the Gaussian cores of spectral lines. An example of thermal broadening is shown in Figure 1.6. Panel (a) shows how changes in temperature affect the strength of the absorption features in the spectrum, with residuals in Panel (b).

Small-scale (smaller than the photon mean free path) motions in the atmosphere give rise to microturbulent broadening. This is not directly observable, but is inferred from line strengths adding to the Gaussian effect of Doppler broadening, and influences the equivalent width of strong lines. Doppler broadening is the dominant source of line broadening for cooler stars. In hotter stars, pressure broadening may overwhelm the contributions of Doppler broadening.

Pressure broadening (or collisional broadening) implies a collisional interaction between ions, electrons, atoms, or molecules. The pressure is controlled by the surface gravity through $P_g \approx \text{const}\, g^{2/3}$, and $P_e \approx \text{const}\, g^{1/3}$. Depending on the distribution of the separations of the collisions, the net effect may result in asymmetries and broadening of spectral lines. Pressure effects in shaping spectral lines are visible in three ways. The first follows ionization equilibrium, in the ratio of the number of absorbers to the continuous opacity. The second is the pressure sensitivity of damping for strong lines, and the third is the Stark broadening in hydrogen. Stark broadening arises from the interaction of the atom with charged particles, and

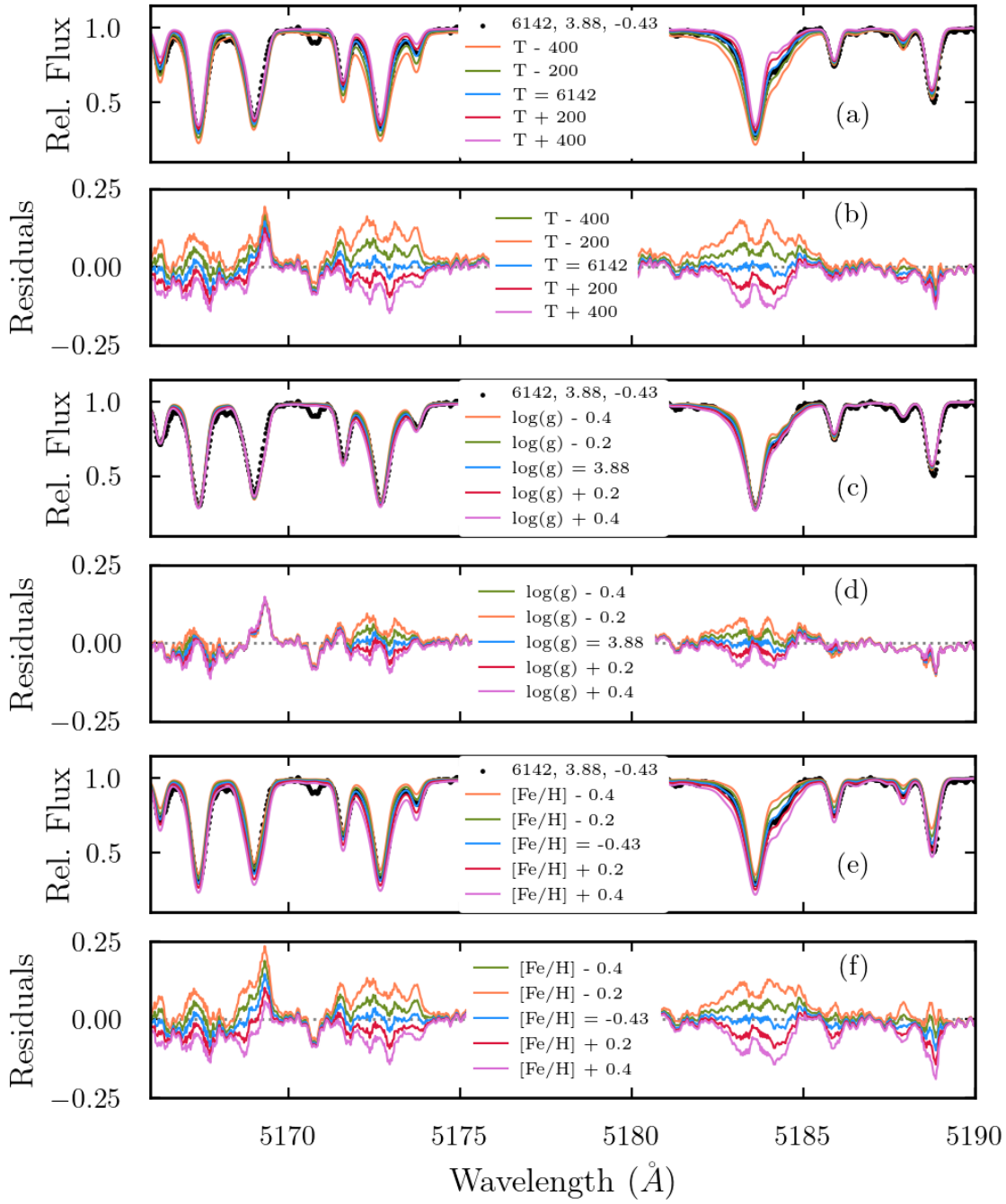

Figure 1.6: Broadening mechanism effects on a stellar spectrum of a star. Panels (a), (c), and (e) display a portion of the spectrum from HD 156432 around the Mg b lines, with synthetic spectra of varying stellar parameters. Panel (a) shows how the absorption features change with temperature, with residuals in Panel (b). Panel (c) displays the effect of changing surface gravity on the spectrum, with residuals in Panel (d). Panel (e) shows how changing the chemical abundance (in this case, of Fe) affects the spectral features, with residuals in Panel (f).

results in broadened Lorentzian wings. Stark broadening is especially significant in hydrogen lines, or in hot ionized atmospheres with $T_{eff} > 7500$ K. Van der Waals broadening arises from interactions with neutral atoms, and is more dominant in cooler stellar atmospheres. An example of pressure broadening is seen in the middle panels of Figure 1.6. Panel (c) shows how changes in $\log(g)$ affect the spectrum, with residuals in Panel (d). The Mg b lines around 5180 Å are sensitive to pressure broadening.

With sufficiently high-resolution observations, instrumental broadening becomes the main contributor, which is typically corrected for by applying a Gaussian broadening kernel.

Curve of Growth Strong absorption features are the result of high opacities, where photons of these wavelengths are readily absorbed. The line core forms higher up in the atmosphere at lower temperatures and densities, where the damped wings form deeper in the atmosphere. Weak absorption lines have low opacity, so photons at the line center escape before being absorbed.

With an increase in the abundance of the absorbers, the line strength is expected to increase. An example of this behavior is seen in the bottom panels of Figure 1.6. Panel (e) shows how changes in metallicity, or the chemical abundance of [Fe/H], affect the strength of absorption features, with residuals in Panel (f).

The change in line profile depends on the optical depth within the line. In "weak" lines, the Gaussian core dominates. The atmosphere is relatively transparent to radiation with low optical depth, and the equivalent width of the line increases logarithmically with the number of absorbing atoms ($\log(EW) \propto \log(A)$). As the central depth of the line approaches its minimum value, the line becomes "saturated". With the increasing number of absorbers, the optical depth increases and the atmosphere becomes less transparent. The curve flattens, the equivalent width increases more slowly, proportional to the square root of the log of the number of absorbers, $\log(EW) \propto \sqrt{\log N}$. As the optical depth in the wings becomes significant compared to the continuum, the line becomes "strong", and the line strength is proportional to $A^{1/2}$. The transition between these three regimes specifying the relation between equivalent width and abundance is known as the curve of growth. The curve of growth relates to the strength of a spectral line to the number of absorbing atoms in the atmosphere contributing to the production of the line. This reveals

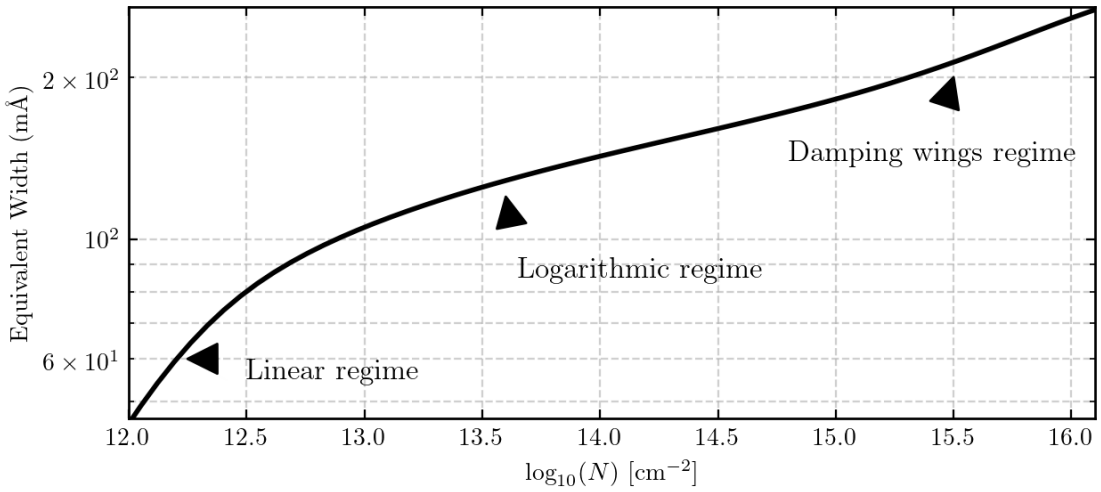

Figure 1.7: Theoretical curve of growth for computing the abundance of an element using the equivalent width of a spectral feature. Log-linear, logarithmic, and square-root regimes are highlighted with increasing width and abundance.

information about the physical conditions and composition of the atmosphere and distinguishes between weak, saturated, and strong lines. A theoretical example of the curve of growth is seen in Figure 1.7.

In addition to the abundance of an absorber, there are other chemical properties that influence the strength of a spectral feature. Hyperfine splitting (HFS) arises from properties of the atomic nucleus and interactions between the magnetic field. This occurs when the nucleus has an odd number of protons or neutrons and leads to the splitting of energy levels. This causes the broadening and weakening of absorption lines, where the absorption is spread across several closely spaced lines. Isotopic splitting comes from different isotopes having different masses and charge distributions leading again to slightly different energy levels. Line profiles become a blend of multiple isotopic components, broadening the line, and possibly causing asymmetry. Both hyperfine and isotopic splitting must be taken into account in chemical analysis of spectral features.

1.3.2 Stellar Atmospheric Parameters

The stellar temperature can be estimated with spectral techniques or broadband photometry (e.g. from Gaia (Gaia Collaboration et al., 2021), or The Two Micron All Sky Survey (2MASS) (Skrutskie et al., 2006)) and fitting a spectral energy distribution (SED). Wien's displacement law describes the shift of the peak of a black body spectrum with temperature $\lambda_{\max} = \frac{b}{T}$, with $\lambda_{\max}$ as the peak wavelength, T the temperature in Kelvin, and $b = 2.897 \times 10^7$ ÅK. The surface gravity can be computed using the parallax of the star and the position on the HR diagram, through spectroscopic methods, or asteroseismic techniques. The metallicity of a star can be roughly inferred by its color, but is more accurately measured with spectroscopy through the widths of Fe lines.

Light from the stellar photosphere is absorbed and re-emitted by atoms and ions, with each element imprinting its own characteristic features. These features provide direct information about the chemical and physical properties of the stellar atmosphere. From a stellar spectrum one can determine the temperature, surface gravity, and metallicity of a star, as well as the microturbulence, rotation velocity $v \sin(i)$, atomic and molecular abundances and, in some cases, isotopic abundances. A full optical spectrum of a star provides numerous diagnostic features sensitive to $T_{\rm eff}$, log(g), and [Fe/H], which can be fitted simultaneously, enabling high-precision parameter determination. Deriving the stellar parameters can be done through a number of techniques, such as comparing flux ratios in different parts of the spectrum, or excitation-ionization balance.

Flux Ratios Flux ratios are powerful tools for determining atmospheric parameters. By comparing fluxes measured at different wavelengths it is possible to extract information about physical conditions and the chemical composition of a stellar atmosphere Hanke et al. (2018). The flux emitted by a star at a particular wavelength depends on its temperature, surface gravity, and composition $T_{\rm eff}$, log(g), and [Fe/H].

Appropriate flux ratios in different parts of the spectrum are related to the parameters to which they are sensitive. For example, ratios of fluxes in the blue and red parts of the spectrum are used to estimate the temperature of a star. Using flux ratios provides precise measurements of atmospheric parameters, may be used

on both high and low resolution spectra, and can be applied to large datasets at low computational cost. Well-reduced and well-normalized spectra are extremely important in computing the correct flux ratios. Tools like ATHOS (A Tool for Homogenizing Stellar parameters) (Hanke et al., 2018) use flux ratios to estimate stellar parameters, and are fast and efficient methods to obtain initial guesses for further refinement.

Ionization - Excitation Equilibrium By analyzing absorption features of both neutral and ionized iron (Fe I and Fe II), atmospheric parameters can be determined. In stars, the distribution of electrons among different energy levels within an atom is governed by the local temperature through the Boltzmann equation. Excitation equilibrium implies that the abundances derived from lines of different excitation levels of the same element should be consistent. Tools like Xiru are used to compute stellar parameters using ionization-excitation balance (Alencastro Puls, 2023).

The ionization state of an element in the atmosphere of a star is determined by the balance between ionization and electronic recombination through the Saha equation. Ionization balance implies that the abundances derived from neutral and ionized lines of the same element should match. The surface gravity of the star affects the electron pressure in the atmosphere, which influences ionization equilibrium. This is a standard method for determining the surface gravity of a star.

The metallicity is determined by analyzing the overall strength of the iron absorption features. By ensuring there is no trend between the abundance of Fe I and the effective equivalent width (w / λ), the microturbulent velocity can be determined. Iron has many well studied spectral features, but this technique may also be performed using other elements with many absorption features exhibiting different ionization states, such as titanium.

This process relies on the assumption of local thermodynamic equilibrium (LTE), where the energy distribution with a small volume of the atmosphere is determined by the local temperature and where collisions between the particles in the atmosphere dominate the transfer of energy. The classical 1D-LTE approximation provides a fast and effective way to estimate the elemental abundances from a stellar spectrum. Grids of 1D-LTE atmospheric models exist (for example, the MARCS models or the ATLAS models) and are commonly used for comparison to observed spectra. Post-processing corrections for non-LTE (NLTE) effects and 3D convective

inhomogeneities can be computed to further refine derived abundances.

1.3.3 Atmospheric Abundances

From the wide wavelength coverage of echelle spectroscopy, many individual features are available for computing high precision abundances. The derived abundances of key s-process elements allow comparison with nucleosynthesis model predictions. Accurate stellar parameters are crucial for this comparison, where uncertainties in the effective temperature or surface gravity directly impact abundance determinations by 0.1-0.3 dex. To derive elemental abundances, one calculates the strength of a spectral line and derives the abundance through the curve of growth. When more than one element is present in a special feature, the lines must be de-blended where the equivalent width contributions from each of the blended features can be computed. Spectral synthesis is required in the cases of hyperfine or isotopic splitting within a spectral line.

Equivalent Width There are different ways to measure the strength or equivalent width (W) of a spectral line, which are used to infer elemental abundances. To use this technique, the lines must be clean un-blended features, or de-blending of the lines must be performed. The equivalent width of a spectral line is defined as

$$W = \int \frac{F_c - F_\nu}{F_c}\, d\nu, \tag{1.19}$$

where F_c is the continuum flux level, and F_ν is the flux at the given wavelength within the line. This integral returns the width of a rectangular feature of continuum height equal to one and an area equal to that of the absorption line. Numerically, one can isolate the absorption line and, assuming symmetry, fit a Gaussian, Lorentzian, or Voigt profile to the line and compute the equivalent width of the fitted feature. We define the total flux removed by the line

$$w = \frac{\text{const}}{\kappa_\nu} \int l_\nu d\nu. \tag{1.20}$$

Using $l_\nu \rho = N\alpha$, with the mass density, ρ, the number of absorbers, N, the atomic absorption coefficient $\alpha = (\pi e^2/mc)\lambda^2/c$, and including f,

$$w = \text{const}\frac{\pi e^2}{mc}\frac{\lambda^2}{c} f \frac{N}{\kappa_\nu}. \tag{1.21}$$

The number of absorbers can be written using the excitation equation,

$$N = A\frac{N_j}{N_E} N_H \frac{g_n}{u(T)} \exp(-\chi/kT)$$

with N_j/N_E is the ionization fraction of element E, A is the abundance of element E relative to hydrogen, and N_H is the number of hydrogen particles. The statistical weight divided by the partition function is $\frac{g_n}{u(T)}$, and χ is the excitation potential. We then find

$$\log\left(\frac{w}{\lambda}\right) = \log C + \log A + \log g_n f\lambda - \theta_{ex}\chi - \log\kappa_\nu. \tag{1.22}$$

The temperature is contained in $\theta_{ex} = 5040/T$, and the constant C contains the ionization fraction, the statistical weight, and the partition function, and is constant for any given star and for any given ion. For fixed θ_{ex}, κ_ν, $g_n f\lambda$, and χ, changes in line width correspond to changes in abundance.

There exist automated tools like IRAF and ARES (Automatic Routine for line Equivalent widths in stellar Spectra) (Sousa et al., 2015) where equivalent widths of spectral features can be quickly computed for across a spectrum, provided an input list of wavelengths and atomic data. Provided a line list containing wavelengths and atomic data like the excitation potential and oscillator strengths, and the measured equivalent width of line features, the MOOG program computes the chemical abundance by solving the radiative transfer equations for an input model atmosphere and computing the curve of growth. From each spectral line, an abundance A is obtained. The abundance is then computed with

$$\Delta\log A = \log(g_n f/g_n^1 f_1) + \log(\lambda/\lambda_1) - \log(\kappa_\nu/\kappa_1) - \theta_{ex}(\chi - \chi_1) \tag{1.23}$$

where the subscript denotes values used in generating the standard curve. By visualizing the observed $\log(W/\lambda)$ versus $\Delta\log A$, each line is reduced to the same standard curve of growth.

Spectral Synthesis In cases where spectral features consist of multiple contributing elements, suffer from molecular blending, or where hyperfine splitting or isotopic shifts are significant, simple equivalent width measurements are insufficient to compute individual elemental abundances. Synthetic spectra must then be computed to match the observations.

In spectral synthesis, a 1D-LTE model atmosphere with the observationally derived atmospheric parameters is adopted, using a pre-defined elemental abundance scaled to that of the Sun. To generate a spectrum from the stellar atmosphere model, one dimensional radiative transfer is computed under the assumption of LTE. There are many tools to choose from to generate synthetic spectra and derive atmospheric abundances (e.g. MOOG, Turbospectrum). The chemical abundance of the element of interest is then varied, and synthetic spectra are generated for the relevant wavelength region.

To derive the elemental abundance in the observed spectrum, one varies the abundance in synthetic spectra to match the observed spectrum. A goodness of fit parameter is computed for each synthetic spectrum to find the best localized fit. In this case, it is extremely important to have a well-characterized continuum.

When deriving abundances, one may use either the absolute abundance A or $\log \varepsilon$, or the abundance ratio of two elements, usually hydrogen or iron. The relation between the abundance ratios and the absolute abundance is $[\mathrm{Fe/H}] = \log A(\mathrm{Fe}) - \log A_{\odot}(\mathrm{Fe})$.

Uncertainties Sources of uncertainty in derived abundances stem from both statistical and systematic contributions. Statistical errors arise from the signal to noise ratio of the spectrum which manifest in a noisy continuum, line fitting precision, and line-to-line scatter when multiple lines of a single element are measured. Typical statistical errors for high SNR and high resolution spectra range from 0.05-0.20 dex.

Systematic errors arise from uncertainty in atmospheric parameters. Temperature uncertainties affect the excitation balance, and uncertainty in the surface gravity affects the ionization balance, particularly important for ionized species (e.g., Ba II). Microturbulent velocity uncertainties affect strong line saturation and the computation of the widths of the lines. Uncertainties in the metallicity propagate directly into computed abundance ratios [X/Fe]. Sensitivity studies are commonly used by varying each parameter independently and recalculating the abundance to estimate

the impact. The final abundance uncertainty is the square root of the quadrature sum of the statistical and systematic components.

It is also important to consider non-local thermodynamic equilibrium (NLTE) effects. In essence, NLTE is a deviation from the LTE source function being the Planck function. Deviations from local thermodynamic equilibrium change the profile and shape of lines in synthetic spectra, and in some cases lead to significant differences in derived abundances. As stellar atmospheres get hotter, radiative transport becomes more efficient, and collisional transport no longer dominates the energy exchange between particles.

1.3.4 Radial Velocities

Precise radial velocity measurements are essential for confirming the binarity of a star system, and are extremely useful for constraining orbital parameters. Monitoring changes in radial velocity over time provides a direct method for detecting orbital motion and revealing the presence of binary companions, even if they are not directly visible in the spectrum. Echelle spectrographs are well-suited to the task of measuring radial velocities through their wide wavelength coverage, split over multiple spectral orders. This allows for the observation of many spectral features for a statistical value of the radial velocity.

A common method to determine the stellar radial velocities from a spectrum is the cross-correlation technique. A synthetic or observed template spectrum, matched in spectral type and resolution to approximate the rest-frame spectrum of the star, is compared to the target spectrum. The cross-correlation function is the integral product of the two signals. When the two signals overlap, the cross correlation function increases. By shifting the template spectrum for a range of velocities, we compare the signals in velocity space. The peak of the cross-correlation function will be offset from zero by the shift of the observed spectrum, which directly translates to its radial velocity through the Doppler formula. Converting to log-wavelength, the correction becomes linear with RV, simplifying the calculation:

$$\Delta \log \lambda = \log \left(1 + \frac{v}{c}\right), \tag{1.24}$$

with $\Delta \log \lambda$ being a shift of the spectrum from the rest frame, v the radial velocity of the observed component, and c the speed of light.

With high-resolution spectrographs and sufficient SNR, RV precision of 10–100 m/s can be achieved, sufficient to resolve orbital motions in binary systems with periods of hundreds to thousands of days. If only one component is visible in the spectrum due to brightness differences, the system is identified as an SB1, or single-lined binary. If both components appear in the spectrum, it is an SB2, or double-lined binary. In the SB1 case, single-template cross-correlation can be used to constrain the RVs and the orbital parameters. Spectra of SB2 stars must be disentangled before performing a cross-correlation on each of the components, out of the scope of this work.

Interpreting observational signatures requires detailed modeling of stellar evolution.

1.4 Astrophysical Simulations: Stellar Evolution Models

Stars evolve as a response to their interior composition progressively changing over their lifetimes. Theoretical modeling is crucial to interpret observations of stars and to understand stellar evolution and nucleosynthesis. Modern stellar evolution models track the structure and composition of stars from their formation into the final stages of their evolution. In binary systems, additional complexities can arise due to mass transfer. Modeling mass accretion onto a companion is essential for reproducing observed abundance patterns in extrinsic stars.

1.4.1 Stellar Structure Equations

A set of four coupled first-order equations describes how the internal conditions of stars evolve in hydrostatic equilibrium. These are each defined with respect to radius or mass. Under the assumptions of spherical symmetry, no rotation, no magnetic fields, and time-independence (quasi-static equilibrium), these equations define how mass M, pressure P, temperature T, and luminosity L vary from the center of a star to its surface. Time dependent modeling includes tracking the changing composition of the star.

The mass continuity equation describes how total mass increases with radius,

$$\boxed{\frac{dM_r}{dr} = 4\pi r^2 \rho}, \tag{1.25}$$

with mass M_r enclosed within a radius r, and a density ρ, which may also vary with radius. This ensures the increase in enclosed mass comes from the volume of the shell at a given radius r.

Hydrostatic Equilibrium

Hydrostatic equilibrium describes the balance between the inward acceleration due to gravity and the outward acceleration due to the gas pressure,

$$\boxed{\frac{dP}{dr} = -\frac{GM_r\rho}{r^2}}, \tag{1.26}$$

for a pressure P at a radius r. In hydrostatic equilibrium, the mass elements within a star experience a net force of zero. This is required to prevent a star from collapsing under its own gravity or from dispersing into space. Converting to the Lagrangian form of the expression, we adopt mass coordinates using Equation 1.25. The expression for the pressure becomes

$$\frac{dP}{dm} = -\frac{Gm}{4\pi r^2}, \tag{1.27}$$

for an element with mass m at a radius r. For an ideal gas with an equation of state of the form $\rho = \mu P/\Re T$, with mean molecular weight μ and gas constant $\Re = 8.314 \times 10^7\,\mathrm{ergs\,mol^{-1}\,K^{-1}}$, we can estimate the central values of P_c and T_c as

$$P_c \approx \frac{2GM^2}{\pi R^4}, \text{ and } T_c \approx \frac{8\mu}{3\Re}\frac{Gm}{R}\frac{\bar{\rho}}{\rho_c} \leq \frac{8G\mu M}{3\Re R}. \tag{1.28}$$

This formalism allows us to define the hydrostatic free-fall timescale. If the pressure disappears, the star will collapse on the free-fall timescale of

$$\tau_{ff} \approx \left(\frac{R}{g}\right)^{1/2}. \tag{1.29}$$

Correspondingly, if the gravity is turned off, the star will explode on a timescale following the sound speed through the interior

$$\tau_{exp} \approx R\left(\frac{\rho}{P}\right)^{1/2}. \tag{1.30}$$

If the star is near hydrostatic equilibrium, then $\tau_{ff} \approx \tau_{exp}$, and we define the dynamical timescale on which a star will react to a perturbation of hydrostatic equilibrium

$$\tau_{dyn} \approx \frac{1}{2}(G\bar{\rho})^{-1/2}. \tag{1.31}$$

The virial theorem connects two important energy reservoirs within stars and enables predictions of stellar evolutionary phases. The gravitational energy is defined as

$$E_g = -\int_0^M \frac{Gm}{r} dm, \tag{1.32}$$

for a mass m at position r inside the star. Integrating this expression, E_g is total gravitational potential of the star. Assuming an ideal gas,

$$\frac{P}{\rho} = \frac{\Re T}{\mu} = (c_P - c_v)T = (\gamma - 1)c_v T, \tag{1.33}$$

where c_P and c_v are the specific heats at constant pressure and volume per unit mass. For a monatomic gas, $\gamma = 5/3$, and we can write

$$\frac{P}{\rho} = \frac{2c_v T}{3}. \tag{1.34}$$

We see that the total internal energy of a star is then proportional to the gravitational energy following $E_g = -2E_i$. This is the virial theorem for a perfect monatomic gas. For a generalized equation of state, we may write

$$\zeta c_v T = 3\frac{P}{\rho}, \tag{1.35}$$

where for an ideal gas $\zeta = 3(\gamma - 1)$, and since for a monatomic gas $\gamma = 5/3$, $\zeta = 2$. We may define the total energy of our star as $W = E_g + E_i$, but the values of the total, gravitational, and internal energies are coupled. A gas of finite temperature must radiate, and the total energy W decreases with the luminosity L through radiation,

$$L = (\zeta - 1)\frac{dE_i}{dt}. \tag{1.36}$$

In an ideal gas, the luminosity is $L = \dot{E}_i = -2\dot{E}_g$. This means that half of the energy released by the contraction of the star is radiated away, and half is used to heat the star; the star heats up as it loses energy. As a star expands or contracts, the gravitational energy increases or decreases, respectively. Under the conditions of hydrostatic equilibrium, this process is slow compared to τ_{dyn}. The timescale for a contracting or cooling a star under the influence of gravity is the Kelvin-Helmholz timescale,

$$\tau_{KH} = \frac{|E_g|}{L} \approx \frac{E_i}{L} \approx \frac{GM^2}{2RL}. \tag{1.37}$$

Thermodynamic Relations

Thermodynamics relates the heat, dq, and internal energy, du, of a star, with a dependence on the pressure P and volume $v = 1/\rho$ through

$$dq = du + Pdv. \tag{1.38}$$

Assuming general equations of state $\rho = \rho(P, T)$ and $u = u(\rho, T)$, the derivatives α and δ, and specific heats c_P and c_v are

$$\alpha = -\frac{P}{v}\left(\frac{\partial v}{\partial P}\right)_T \tag{1.39}$$

$$\delta = \frac{T}{v}\left(\frac{\partial v}{\partial T}\right)_P \tag{1.40}$$

$$c_P = \left(\frac{\partial u}{\partial T}\right)_P + P\left(\frac{\partial v}{\partial T}\right)_P \tag{1.41}$$

$$c_v = \left(\frac{\partial u}{\partial P}\right)_T, \tag{1.42}$$

with

$$du = \left(\frac{\partial u}{\partial v}\right)_T \partial v + \left(\frac{\partial u}{\partial T}\right)_v dT. \tag{1.43}$$

We define the specific entropy $ds = dq/T$, which translates here to

$$ds = \frac{dq}{T} = \frac{1}{T}\left[\left(\frac{\partial u}{\partial v}\right)_T + P\right]dv + \frac{1}{T}\left(\frac{\partial u}{\partial T}\right)_v dt. \tag{1.44}$$

Since ds is in differential form, we use the identity $\partial^2 s/\partial T\partial v = \partial^2 s/\partial v\partial T$ and differentiate for the expression

$$\left(\frac{\partial u}{\partial v}\right)_T = T\left(\frac{\partial P}{\partial T}\right)_v - P. \tag{1.45}$$

We derive an expression for $(\partial u/\partial T)_P$, decoupling the temperature and pressure artificially such that they behave as independent variables

$$\begin{aligned}\frac{\partial u}{\partial T} &= \left(\frac{\partial u}{\partial T}\right)_v + \left(\frac{\partial u}{\partial v}\right)_T \left(\frac{dv}{dT}\right)_P \\ &= \left(\frac{\partial u}{\partial T}\right)_v + \left(\frac{\partial u}{\partial v}\right)_T \left[T\left(\frac{\partial P}{\partial T}\right)_v - P\right].\end{aligned} \tag{1.46}$$

The difference in the specific heats of our ideal gas, c_P and c_v, is written as

$$\begin{aligned}c_P - c_v &= P\left(\frac{\partial v}{\partial T}\right)_P + \left(\frac{\partial u}{\partial T}\right)_P - \left(\frac{\partial u}{\partial T}\right)_v \\ &= \left(\frac{\partial v}{\partial T}\right)_P \left(\frac{\partial P}{\partial T}\right)_v T,\end{aligned} \tag{1.47}$$

and, using the α and δ derivative definitions, we find $(\partial P/\partial T)_v = P\delta/T\alpha$. Therefore,

$$\begin{aligned}c_P - c_v &= T\left(\frac{\partial v}{\partial T}\right)_P \frac{P\delta}{T\alpha} \\ &= \frac{P\delta^2}{\rho T\alpha}.\end{aligned} \tag{1.48}$$

We write the expression in Equation 1.38 in the form

$$dq = du + Pdv = \left(\frac{\partial u}{\partial T}\right)_v dT + \left[\left(\frac{\partial u}{\partial v}\right)_T + P\right] dv$$
$$= \left(\frac{\partial u}{\partial T}\right)_v dT + T\left(\frac{\partial P}{\partial T}\right)_v dv. \tag{1.49}$$

Using our derivations of $(\partial u/\partial v)_T$ and $(\partial P/\partial T)_v$ with the specific heats c_v and c_P we write

$$dq = c_v dT - \frac{P\delta}{\rho\alpha}\left(\alpha\frac{dP}{P} - \delta\frac{dT}{T}\right)$$
$$= \left(c_v + \frac{P\delta^2}{\rho T\alpha}\right) dT - \frac{\delta}{\rho} dP$$
$$= c_P dT - \frac{\delta}{\rho} dP. \tag{1.50}$$

We define the adiabatic temperature gradient for a constant entropy

$$\nabla_{ad} = \left(\frac{d\ln T}{d\ln P}\right)_s. \tag{1.51}$$

Entropy has to remain constant for adiabatic changes, i.e. $ds = dq/T = 0$, and we see that

$$0 = dq = c_P dT - \frac{\delta}{\rho} dP, \tag{1.52}$$

or

$$\nabla_{ad} = \left(\frac{PdT}{TdP}\right)_s = \frac{P\delta}{T\rho c_P}. \tag{1.53}$$

Energy Conservation

The equation of energy conservation describes how luminosity changes with radius due to the generation of energy:

$$\boxed{\frac{dL_r}{dr} = 4\pi r^2 \rho\epsilon}, \tag{1.54}$$

with luminosity L_r at radius r, and energy generation rate ϵ per unit mass. This can also be written in mass coordinates, as

$$\frac{dL}{dm} = \epsilon_n - \epsilon_\nu + \epsilon_g. \tag{1.55}$$

The luminosity is the energy output per unit time, with contributions from nuclear reactions in the core ϵ_n and gravitational energy ϵ_g, and losses from neutrinos ϵ_ν. The bulk of the energy is generated from nuclear reactions within the star, linking nuclear physics to the stellar structure. If a star is radiating with a constant luminosity L, we can define the nuclear timescale on which this nuclear energy is released

$$\tau_{nuc} = \frac{E_n}{L}. \tag{1.56}$$

The most important reaction in estimating the lifetime of a star is the PP-chain hydrogen burning. Comparing the three timescales we have derived, we see that $\tau_{nuc} \gg \tau_{KH} \gg \tau_{dyn}$.

1.4.2 Energy Transport in Stellar Interiors

Radiative Transport

Within the star, energy is transported from the nuclear core to the surface. The temperature changes with the radius, depending on the mechanism of energy transport. The mean free path $l_{ph} = 1/\kappa\rho$ of a photon in a star is inversely proportional to the absorption coefficient and the density. In the dense and opaque interiors of stars, l_{ph} is short. Photons generated in the core diffuse outwards through the stellar atmosphere, gradually losing energy as they are absorbed, emitted, and scattered before escaping the photosphere. The diffusive flux j between places within the star of different density n is

$$j = -D\ \nabla n, \tag{1.57}$$

where $D = (1/3)vl_{ph}$ is the diffusion coefficient. The radiative energy flux F can be obtained using the energy density of radiation $U = aT^4$, where $a = 4\sigma/c$ is the radiation energy constant, and σ is the Stefan-Boltzmann constant. With spherical symmetry, there is only the radial component, and we find

$$F = -\frac{4ac}{3}\frac{T^3}{\kappa\rho}\frac{\partial T}{\partial r}. \tag{1.58}$$

This can be seen in the heat transfer equation of the form

$$F = -k_{rad}\nabla T, \text{ with } k_{rad} = \frac{4ac}{3}\frac{T^3}{\kappa\rho}. \tag{1.59}$$

Using the luminosity and flux relation $l = 4\pi r^2 F$ locally, we find

$$\boxed{\frac{dT}{dr} = -\frac{3\kappa\rho l}{16\pi acT^3 r^2}}, \tag{1.60}$$

for a temperature T and opacity κ, where a is the radiation energy constant, and c is the speed of light. In mass coordinates, the changing temperature throughout the star is written

$$\frac{dT}{dm} = -\frac{GmT}{4\pi r^4 P}\nabla, \tag{1.61}$$

with the energy transfer gradient ∇. If energy is carried by radiation or convection, the term is substituted for the corresponding transfer gradient. Operating under the assumptions of hydrostatic equilibrium, we define the radiative transfer gradient as

$$\nabla_{rad} \equiv \left(\frac{d\ln T}{d\ln P}\right)_{rad} = \frac{3\kappa Pl}{16\pi GacmT^4}. \tag{1.62}$$

Convective Transport

When radiative transport is inefficient, convective energy transport takes over. The Schwarzschild criterion determines if the form of energy transport is radiative or convective Schwarzschild (1956). We compare the radiative temperature gradient with the adiabatic temperature gradient

$$\nabla_{ad} \equiv \left(\frac{d\ln T}{d\ln P}\right)_{ad} \approx \frac{\gamma - 1}{\gamma}, \tag{1.63}$$

for a rising fluid element that expands or contracts adiabatically, where for an ideal monatomic gas the adiabatic index $\gamma = 5/3$, so $\nabla_{ad} \approx 2/5$, or 0.40. This comparison, known as the Schwarzschild criterion, determines if a region within a star is unstable to convection. If $\nabla_{rad} < \nabla_{ad}$ in a region of homogeneous chemical composition, the

region will transport energy through convection. If $\nabla_{rad} < \nabla_{ad} + \nabla\mu$, with $\nabla\mu$ being the molecular weight gradient, the fluid parcel is cooler and denser after displacement and sinks back to its original position for stable radiative energy transport.

Mixing-length theory (MLT) simplifies this using transport particles in place of parcels of gas, whose mean free path is the mixing length Prandtl (1925). The local convective energy flux is given by

$$F_{con} = \rho v c_P DT, \tag{1.64}$$

where DT is the temperature excess of the convecting element, and v is the velocity of the particle. Due to differences in temperature gradients and buoyancy forces, DT and v increase with the rising of the element until, after a mixing-length distance l_m, the element mixes with its surroundings, transporting its heat energy and composition to its new position. The prescription of MLT provides a robust and fast way to numerically compute convective transport and mixing processes.

1.4.3 Chemical Composition

The time dependence of stellar evolution arises from the changing chemical composition of the star. The composition of a star directly influences the absorption or generation of energy by nuclear reactions, which in turn further alters the composition. The total mass can be written as the sum of the mass fractions consisting of a nucleus of type i:

$$\sum_i X_i = 1. \tag{1.65}$$

Relevant nuclei follow time dependent functions $X_i = X_i(m, t)$ on the mass interval $[0, M]$. With this, we describe the chemical composition of a star at time t. The particle number per unit volume n_i of nuclei with mass m_i is related to the mass abundance by

$$X_i = \frac{m_i n_i}{\rho}. \tag{1.66}$$

The elements that play the most significant roles are H and He, denoted as $X = X_H$ and $Y = X_{He}$, and the remaining 'metals' are denoted with $Z = 1 - X - Y$.

Nuclear reactions within the star will change the relative mass fractions of X, Y, and Z.

In radiative regions, the composition X_i only changes with the synthesis or destruction of nuclei through fusion reactions. The frequency of a reaction is described by the reaction rate r_{ab}, for a reaction transforming element a to element b. Generally, the abundance of an element can be affected by many reactions through creation r_{ji} or destruction r_{ik}. Following Equation 1.66, we sum the relative contributions

$$\boxed{\frac{\partial X}{\partial t} = \frac{m_i}{\rho}\left[\sum_j r_{ji} - \sum_k r_{ik}\right], \quad i = 1, ..., I} \tag{1.67}$$

for any of the elements involved in the reaction scheme. The transformation of a nucleus may be connected with a release of energy e_{ab}. The rates of energy generation ε are proportional to the reaction rates

$$\varepsilon = \sum_{a,b} \varepsilon_{ab} = \frac{1}{\rho}\sum_{a,b} r_{ab} e_{ab}. \tag{1.68}$$

We define the energy generated relative to the mass of the parent nucleus $q_{ab} = e_{ab}/m_a$. If all reactions provide a positive contribution to ε, we write Equation 1.67 as

$$\frac{\partial X}{\partial t} = \sum_j \frac{\varepsilon_{ji}}{q_{ji}} - \sum_k \frac{\varepsilon_{ik}}{q_{ik}}, \tag{1.69}$$

Convective Mixing in Stellar Atmospheres

There exist many mechanisms that mix and homogenize material within stellar interiors and envelopes, altering surface abundances and affecting evolution. Here we focus on mixing due to turbulent convective motion. Convection occurs when a region is thermally unstable to convection following the Schwarzschild criterion and, as heat is transferred by the bulk movement of parcels of fluid, the chemical composition of the fluid is transported along the temperature gradient. This process is rapid compared to the slow change in composition, and we can assume that the composition within a convective region remains homogeneous,

$$\frac{\partial X_i}{\partial m} = 0. \tag{1.70}$$

Stellar convection is described in one-dimensional (1D) stellar models using MLT (Prandtl, 1925; Canuto and Mazzitelli, 1991). The mixing-length parameter, or scale factor, α is proportional to the pressure scale height, and effectively expresses the convective flux, viscosity, and temperature gradient of the convective elements in the stellar medium. The mixing-length parameter is determined by comparing stellar models to some calibrator, often the Sun or hydrodynamical models.

Updated models of convection incorporate the effects of convective penetration, where convective elements overshoot into radiative zones Deng et al. (1996). The convecting parcels can penetrate the boundary where the convective motion theoretically stops. Overshoot can be treated as an extension of the convective region using $l_{ov} = \alpha_{ov} H_P$, with α_{ov} on the order of 0.1 - 0.2 in modern models, where H_P is the pressure scale height.

Convective mixing becomes the dominant source of mixing with the advance of the convective envelope as the star ascends the giant branch. Convection plays a key role in dredge-up processes during stellar evolution, particularly in red giant and AGB stars, where surface abundances (of, e.g, s-process elements) are altered. The third dredge-up is more efficient at lower metallicities, making overall s-process enrichment weaker in the metal-rich Ba stars Cristallo et al. (2011). Three-dimensional numerical simulations that solve the hydrodynamic equations for convection offer a more physically accurate representation of turbulent convection, at the cost of the computation time Magic et al. (2015).

These equations, along with the equation of state that relates pressure, temperature, and density, nuclear reaction rates for ϵ, and an opacity law for κ, describe the internal structure of a star. Solving this system of equations allows for the modeling of stellar interiors and evolutionary pathways. Modern stellar evolution codes (e.g., STARS (Eggleton, 1971, 1972; Pols et al., 1995), and MESA (Paxton et al., 2011)) use these fundamental equations as their core framework.

1.4.4 Evolution of Low-mass Stars

In this section, we follow the evolution of a 1 $M_\odot$ star with approximately solar composition ($X = 0.70$, $Y = 0.28$, $Z = 0.02$) modeled using the STARS code. A

stellar evolutionary track is shown in Figure 1.8 where the colorbar shows the age throughout the star's evolution. The interior structure is shown in a Kippenhahn diagram in Figure 1.9, with time on the x axis and the mass coordinate from the center to the surface on the y axis. Colors ranging from yellow to purple show the computed difference between the radiative and adiabatic transfer gradients, marking regions of radiative and convective energy transport, respectively.

Stars form from the gravitational collapse of molecular clouds. If the mass of a molecular cloud exceeds the Jeans mass $M_J = T^{3/2}/\rho^{1/2}$ for its temperature and density, the cloud will dynamically collapse and form a proto-star. The central temperature increases until the point where nuclear fusion takes place, marking the birth of the star and the beginning of the main-sequence (MS) evolution. The proto-star phase is indicated in the center of Figure 1.8.

On the MS, this star hydrostatically fuses available H fuel in its core, creating He through the PP chain. At higher masses above ~ 1.3 $M_\odot$, the CNO cycle dominates the He production in the core. The temperature and luminosity of the star do not change significantly over the MS lifetime, as seen in the bottom left of Figure 1.8, and between model numbers 400 - 550 in Figure 1.9. This is the longest and most stable evolutionary phase of a star. The age of this star before the MS is a few $\times 10^8$ years, and upon leaving the MS the age has increased to more than 10^{10} years.

With the exhaustion of H fuel in the core, the star evolves off the MS and crosses the sub-giant branch, identified in Figure 1.8. Without nuclear fusion providing radiation pressure to support the star, the star contracts on a thermal timescale, and gravitational energy is radiated away. The internal temperature and density correspondingly increase until H-fusion is ignited in a shell around the inert He core. The outer layers of the star expand as the star becomes a red giant. The luminosity increases following the Stefan-Boltzmann law, despite a drop in temperature.

On the RGB, the H-burning shell continues to produce energy causing the envelope to expand, and the luminosity increases dramatically with the increasing radius. The ascent of the RGB is seen in the central part of Figure 1.8. Convection extends deep into the envelope with the onset of FDU around model number 550 in Figure 1.9, and the surface chemical composition is altered with the cycling of C, N, and Li. The H shell-fusion produces He ash that settles on the inert core. The core density reaches a point where the core is supported by electron degeneracy pressure, beyond which the He core contracts further with the addition of mass.

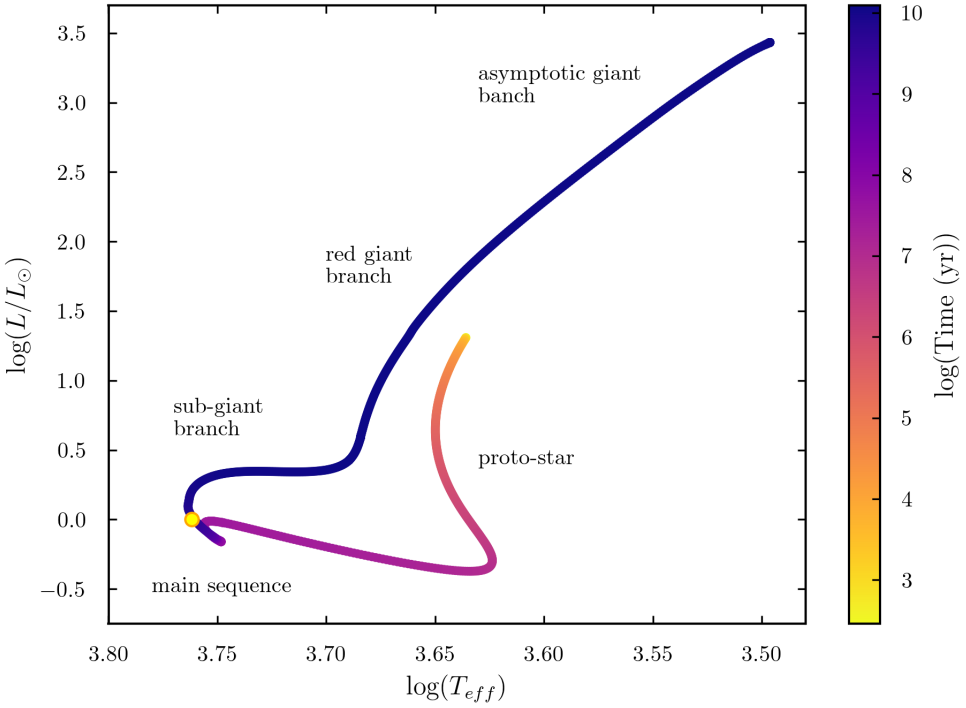

Figure 1.8: Evolution of a 1 $M_\odot$ star with solar metallicity, from a proto-star to an AGB star in the HR diagram. Progressing evolutionary phases are identified. The colorbar represents the age of the star. The position of the Sun is shown in the yellow data point on the MS.s

When the degenerate core reaches $\sim$ 0.40 $M_\odot$ and the temperature reaches $T \sim 10^8$ K, He ignites in a thermonuclear runaway reaction called the He flash. The majority of energy released goes into lifting the degeneracy condition of the core, as the temperature across the core changes simultaneously. On the surface, however, there is little noticeable change. The star settles into core He-burning via the triple-α process, while H-burning continues in a shell around the core on the horizontal branch and the red clump. This 1 $M_\odot$ star does not experience a significant departure from the first ascent of the giant branch, although more massive stars will traverse the horizontal branch.

By fusing He, a star will develops an inert carbon-oxygen core. Further He-burning occurs in a shell around the core, while maintaining a H-burning layer. The AGB phase is shown in the upper right corner of Figure 1.8. Toward the end of the

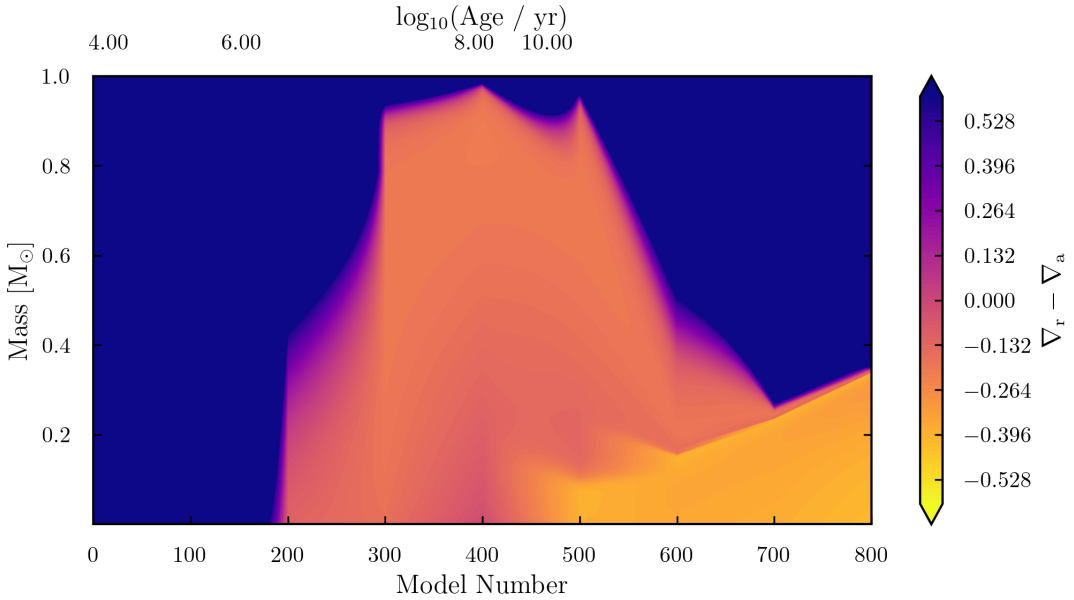

Figure 1.9: Kippenhahn diagram displaying the evolving internal structure of a 1 $M_\odot$ star from a proto-star to the AGB phase. The mass coordinate is plotted on the y axis. Model number is shown on the lower x axis and stellar age in log(yrs) on the upper x axis. Yellow and orange regions indicate radiative energy transport, and purple indicates convective regions.

AGB phase, the envelope again becomes deeply convective with further dredge-up events. Unstable He-shell flashes lead to thermal pulses (TPs) and third dredge-up events (TDUs) as the star expands and contracts. With the TPs, strong mass loss episodes shed the outer envelope of the star, forming a planetary nebula. The star maintains a high luminosity with an increase in temperature, mmoving left across the HR diagram. By this point, the star has lost most of its envelope and the exposed, compact core of the star is left behind as a white dwarf.

1.4.5 Binary Stars

Binary stars are an ideal laboratory to study stellar physics and gravitational orbital dynamics. More information can be obtained from a binary system compared to that of a singular star due to measurable interactions with another gravitational body. These interactions reveal information about stellar masses, internal structures, and

mass exchange.

Binarity (or higher-order multiplicity) in star systems is observed through a number of techniques dictated by the properties of the observed system. They are detected through radial velocity variation in spectroscopic binaries, through light curve photometry in eclipsing binaries, or through tracking their motion on the sky for astrometric binaries. The distance between the observer and the star and the orbital period of the binary play the largest role in determining how the system may be observed. The inclination, relative brightness of the two components, and the mass ratio also play important roles in the observability of binarity using any given technique. Different observational techniques probe different kinds of information about the system and its components. It is therefore advantageous to combine multiple types of observations when possible to more completely characterize a binary system. Astrometric missions like Gaia can detect orbital motion via proper motion anomalies, while photometric monitoring identifies eclipses or variability that reveal orbital inclinations or orbital radii.

An example binary system, HD 48767, is shown in Figure 1.10. In this image both stars are resolved, but atmospheric seeing and instrumental resolution blur the point sources over many pixels, making them appear non-spherical. At a distance of only 42.69 parsec (Gaia Collaboration et al., 2021), this star is quite close to the Sun, and both stellar components are easily observed. Its close proximity contributes to its relative brightness of 6.23 magnitudes in the V-band (Fabricius et al., 2002). Within the image, the two-arcsecond square represents the width of an optical fibre connected to a spectrograph. For binaries that have shorter orbits or are farther away, other techniques are required to characterize the system, as they cannot be spatially resolved. With a favorable orbital orientation, this system is simultaneously an astrometric, eclipsing, and spectroscopic binary.

Single-lined spectroscopic binaries, where one star in the system dominates the flux, allow measurements of the radial velocity of one of the binary components. With a modest number of short-exposure spectra, the binary orbit can be determined and characterized in terms of the period and eccentricity, as well as the radial velocity amplitude of the primary component. If both components are bright enough to be simultaneously observed, double-lined binaries display information about both stars in the system. Reduction of this data requires spectral disentangling to identify and isolate each of the stellar components.

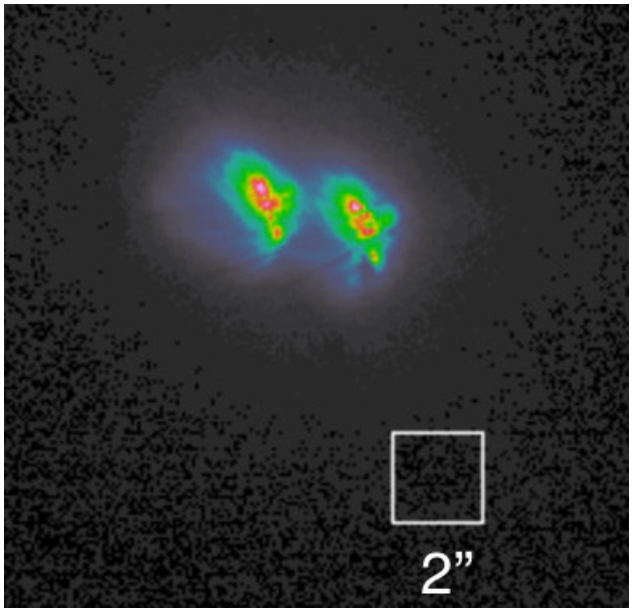

Figure 1.10: Image of the binary star HD 48767, captured with the object finder scope at Moletai Observatory in Lithuania. Each component of the binary is visible and easily resolved. A two-arcsecond square is included for reference.

Orbital Dynamics

The stars in a binary will exert their gravitational influence on each other, and Kepler's Laws, Newton's Laws, and Einstein's general relativity predict and can be used to model their dynamics. There are six Keplerian orbital parameters that uniquely describe a binary system: the orbital period P, the eccentricity e, the argument of periastron ω, the time of periastron T_0, the longitude of the ascending node Ω, and the orbital inclination i. These parameters are visualized in Figure 1.11.

Kepler's Laws of Planetary Motion By studying apparent motion of the planets in the solar system, Kepler was able to deduce three laws of planetary motion. Kepler's first law states that planets orbit their host stars in ellipses, with the host star at one focus of the ellipse. Kepler's second law expresses that, as the orbital radius and angular velocity of the planet in the elliptical orbit vary, a line joining the planet and the star sweep over equal areas in equal amounts of time. This is equivalent to the conservation of momentum for any body experiencing a radially

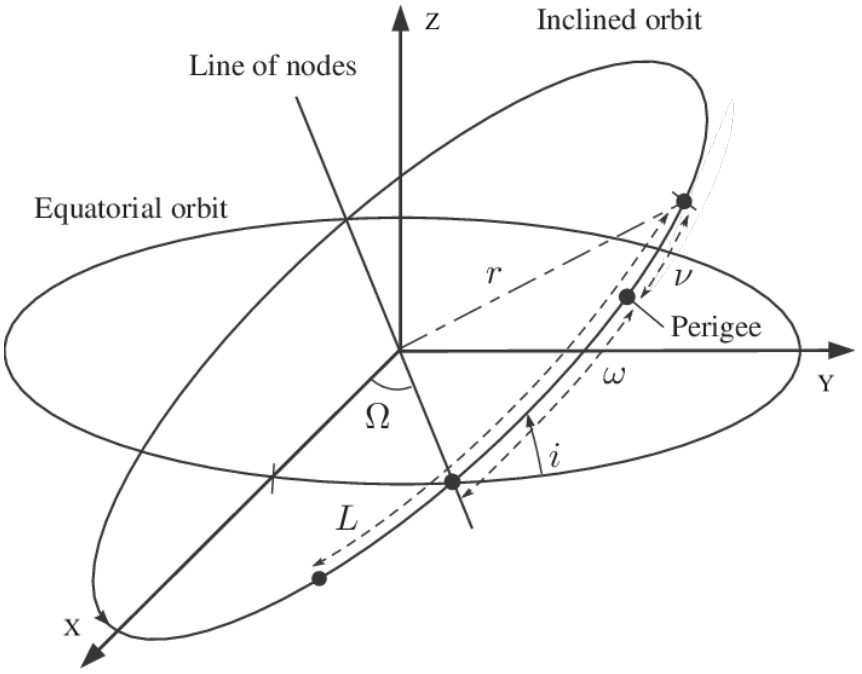

Figure 1.11: Schematic of an orbit, with orbital parameters identified.

symmetric force, such as gravity. Kepler's third law describes the relation between the orbital period P and the orbital separation a, and is mathematically written as

$$P^2 = \frac{4\pi^2 a_0^3}{G(M_1 + M_2)}, \tag{1.71}$$

where a_0 is the semi-major axis of the eccentric binary orbit, G is Newton's gravitational constant, and M_1 and M_2 are the masses of the primary and secondary. The primary is the more massive or more luminous of the two objects. For fixed component masses, we can expect an increase in the orbital period with an increase in the semi-major axis. If the masses of the components are known, then the ratio of the orbital period to the semi-major axis can be determined, and vice versa.

While Kepler studied planets within the solar system, these laws of orbital motion also apply to binary stars and other gravitational interactions. The total mass and the mass function $f(m)$ can be estimated with the orbital period and inclination, and the radial velocity semi-amplitude of the primary K_1. The mass function is defined as

$$f(m) = \frac{M_2^3 \sin^3(i)}{(M_1 + M_2)^2} = \frac{PK_1^3}{2\pi G} \tag{1.72}$$

where K_1 is the RV semi-amplitude of the primary star, and i is the orbital inclination. This provides a lower limit on the companion mass, since it depends on $\sin^3(i)$. In SB1 systems, the mass function provides the only constraint on the mass of the unseen companion.

Newton's Laws of Motion and Gravitation Newton's first law, also known as the law of inertia, describes that a body at rest will remain at rest, and bodies and motion will remain in motion unless acted upon by an external force. In Newton's second law, the net force on a body is equal to the mass of the object times its acceleration, mathematically written as $\vec{F} = m\vec{a}$. In terms of gravity, Newton's second law can be written as $\vec{F} = m_p\ddot{\vec{r}} = -m_p\alpha r^{-2}\hat{r}$, where m_p is the mass of the planet, and α is the same for all planets in the solar system. Newton's third law states that for every action there is an equal and opposite reaction. By Newton's third law, the sun experiences a force equal in magnitude to that it enacts on the planet, so $\alpha = Gm_\odot$ where G is the gravitational constant.

1.4.6 Mass Transfer

Material can be transferred from one binary companion to the other through a number of channels depending on the orbital configuration and the evolutionary states of the stars. Mass transfer can be fully conservative, where all of the material lost from the donor star is accreted. In reality, mass transfer is likely highly non-conservative, where a significant portion of the material escapes the system entirely. This affects the orbital evolution through the loss of angular momentum, and can inhibit efficient accretion onto the companion.

The observed chemical peculiarities in Ba, CH, and CEMP-s stars require a mechanism for transferring enriched material from an evolved AGB star to a less-evolved companion. In the framework of post-mass-transfer binaries, the more massive primary TPAGB star loses mass and pollutes the atmosphere of the less evolved companion (Roriz et al., 2024). Modeling efforts in binary mass loss and accretion have been successful in generalizing the effects of interacting binaries (Karakas et al.,

2000), but the amount of material transferred and the mass transfer mechanism is generally poorly constrained for these post-accretion systems.

Gravitational Capture In the Bondi-Hoyle-Lyttleton (BHL) accretion regime Bondi and Hoyle (1944); Hurley et al. (2002); Edgar (2004), mass is gravitationally captured from a stellar wind, and early models predict inefficient accretion. Han et al. (1995) investigated the formation of Ba and CH stars via binary interactions, considering wind accretion, stable RLOF, and common-envelope evolution followed by envelope ejection.

Roche-lobe Overflow (RLOF) The Roche-lobe of a star is a surface in the gravitational potential energy field at which material is no longer gravitationally bound. In a binary star system, the gravitational potential energy distribution of the two bodies has local minima and maxima, called the Lagrange points. Due to tidal interactions between the binary components, material can be pulled from the primary to the secondary. Stable RLOF occurs in close binaries when the primary star fills its Roche lobe and transfers mass to the secondary star through the L1 inner Lagrange point. This allows for efficient mass transfer from one star to its companion. In AGB binaries, the envelope of the AGB star is loosely bound, and can easily be pulled away by a close-orbiting binary companion.

Models suggest RLOF can efficiently transfer s-process elements while avoiding excessive dilution; Boffin and Jorissen (1988) showed that RLOF is a likely mass transfer mechanism for some Ba stars. However, RLOF is expected in short-period systems, whereas many observed Ba, CH, and CEMP-s stars have long orbital periods.

AGB Winds In the AGB phase, low- to intermediate-mass stars ($\sim 1 - 8\mathrm{M}_{\odot}$) experience substantial mass loss through slow, dense stellar winds. This mass loss is driven by a combination of stellar pulsations and radiation pressure acting on dust grains that have formed in the cool and extended atmospheres of AGB stars. These winds can reach mass-loss rates up to 10^{-4} $\mathrm{M}_{\odot}\,\mathrm{yr}^{-1}$ Höfner and Olofsson (2018). An empirical formula from van Loon et al. (2005) describes the mass loss of oxygen-rich AGB stars (C/O < 1) as a function of luminosity and temperature

$$\log \dot{M}_{AGB} = -5.65 + 1.05 \log \left(10^{-4} \frac{L}{L_\odot} \right) - 6.3 \log \left(\frac{T_{\rm eff}}{3500K} \right), \tag{1.73}$$

and an expression for carbon-rich (C/O > 1) AGB stars made by fitting the luminosity, temperature, and mass to theoretical carbon-dust models comes from Wachter et al. (2002),

$$\log \dot{M}_{AGB} = -4.52 + 2.47 \log \left(10^{-4} \frac{L}{L_\odot} \right) - 6.81 \log \left(\frac{T_{\rm eff}}{2600K} \right) - 1.95 \log \left(\frac{M}{M_\odot} \right). \tag{1.74}$$

The mass loss from AGB stars plays a crucial role in redistributing the heavy elements synthesized via the s-process back into the interstellar medium. In wide binary systems, some of the lost wind material can be gravitationally captured by the companion through BHL accretion, but early versions of this accretion mechanism predict inefficient accretion. Accretion from an AGB significantly alters the surface composition of the companion, leaving an observable chemical fingerprint as a record of past binary interaction. Mass transferred through AGB winds is generally non-conservative, with a significant portion escaping the system.

Wind Roche-lobe Overflow (WRLOF) The concept of WRLOF was proposed by Mohamed and Podsiadlowski (2007), suggesting that WRLOF could be an efficient mass transfer mechanism in binaries. The slow, dense wind of an AGB star can itself fill the stars Roche-lobe and be channeled onto the secondary. This allows enhanced mass transfer rates higher than that of the Bondi-Lylleton-Hoyle accretion regime, approaching the efficiency of the stable RLOF regime, and modern hydrodynamical simulations (e.g., Theuns et al. (1996)) show that wind Roche-lobe overflow (WRLOF) can significantly increase accretion efficiency. Abate et al. (2013, 2015b); Krynski et al. (2025) demonstrated that WRLOF may explain the enrichment observed in Ba, CH, and CEMP-s stars in moderate- to wide binary systems. This can also result in the formation of a circumbinary disc.

Accretion Disc Formation Some models suggest that accreted material forms a circumstellar disc around the companion Chen et al. (2017). The secondary may not be able to accrete material at its inner boundary as fast as it accretes material

at the outer boundary of its disc. Material will then pile up in the accretion disc. The accretion disc of a low-mass main-sequence star is generally not luminous, but theoretically allows enhanced retention of accreted material from a companion and a sink for angular momentum transfer.

Using nucleosynthetic material produced by AGB stars to model mass transfer requires accurate AGB yields. Yield models rely on experimental results, including neutron capture cross-sections and reaction rates, which can introduce significant uncertainties. Therefore, experimental measurements are vital to constrain these inputs and are indispensable for validating predictions, thus motivating dedicated experimental efforts.

1.5 Nuclear Physics Experiments

While observations and theory provide powerful tools to study stellar nucleosynthesis, laboratory nuclear physics experiments supply the fundamental data needed to model the s-process. Nuclear theory has been developed to describe atomic nuclei and the forces governing their structure, and it plays a fundamental role in modeling nucleosynthesis. To understand neutron-capture processes and to measure neutron-capture cross-sections, we examine the radioactive decay of a nucleus generated through activation experiments in the laboratory.

1.5.1 Neutron Reactions

Plasma in stellar interiors is considered to be in thermodynamical equilibrium, where particles are thermalized and their velocities follow a Maxwell-Boltzmann distribution, depending on the mass of the particle and the ambient temperature Reifarth et al. (2014). The Maxwell-Boltzmann velocity distribution is written as

$$\phi(v_x)\,dv_x = 4\pi v_x^2 \left(\frac{m_x}{2\pi k_B T}\right)^{3/2} \exp\left(-\frac{m_x v_x^2}{2k_B T}\right) dv_x \tag{1.75}$$

where ϕ denotes the probability of finding a particle with a velocity between v_x and $v_x + dv$, and $k_B = 1.380649 \times 10^{-16}\ \mathrm{erg\,K^{-1}}$ is the Boltzmann constant.

For interacting nuclei x and y, the reaction rate per particle pair can be written as

$$\langle \sigma v \rangle = \int_0^\infty \phi(v)\, \sigma(v)\, v\, dv = 4\pi \left(\frac{\mu}{2\pi k_B T} \right)^{3/2} \int_0^\infty \sigma(v)\, v^3 \exp\left(-\frac{\mu v^2}{k_B T} \right) dv \quad (1.76)$$

where v is the relative velocity between the particles and $\mu = m_x m_y/(m_x + m_y)$ is the reduced mass. Maxwellian average cross-sections (MACS) are defined as the reaction rate scaled by the most probable velocity (in the Maxwellian case, the average thermal velocity $v_T = \sqrt{k_B T/\mu}$) of the distribution,

$$\langle \sigma \rangle = \frac{\langle \sigma v \rangle}{v_T} = \frac{2}{\sqrt{\pi}} \frac{1}{(k_B T)^2} \int_0^\infty \sigma(E)\, E \exp\left(-\frac{E}{k_B T} \right) dE. \quad (1.77)$$

The 'Kadonis Astrophysical Database of Nucleosynthesis in Stars' (KADoNiS) (Bao, 2009) provides experimental and theoretical data for nuclear cross-sections for different nuclear processes. Because free neutrons are unstable and have short decay times of about 880 seconds (around 15 minutes), it is not yet possible to perform neutron capture experiments in inverse kinematics. Therefore, experiments are limited to direct measurements of (n, γ) cross sections on reasonably long-lived samples.

1.5.2 Interaction of Radiation with Matter

Photons Photons can interact with matter through the photoelectric effect, Compton scattering, and electron-positron pair-production. These processes transfer energy from the photon to an electron in an absorbing atom. In the photoelectric effect, a photon is absorbed by a bound electron, ionizing the host atom and releasing a photoelectron. The electron has an energy equal to the difference between the energy of the incident photon E_γ and the binding energy of the electron E_b, $E_e = E_\gamma - E_b$.

In the Compton effect, photons are scattered by electrons within an absorbing material. A portion of the photon energy is transferred, and the photon is deflected at some angle θ. The scattered photon energy depends on the incident energy and angle,

$$E'_\gamma = \frac{E_\gamma}{1 + \frac{E_\gamma}{m_e c^2}(1 - \cos\theta)}. \quad (1.78)$$

For a scattering angle of $\theta = 0$, the energy loss is minimized and the scattered photon has the same energy as the incident photon. For high scattering angles $\theta = 180$, the energy loss is maximized. For sufficiently energetic photons ($E_\gamma \geq 1022$ keV), interactions with the Coulomb field can produce electron-positron pairs. The positron will be annihilated by an electron, resulting in two photons with an energy equal to that of the rest mass of the electron (511 keV).

Electrons The interaction rate of charged particles (e.g., electrons) is higher than that of neutral particles (e.g., photons). As they are deflected by the Coulomb field of a material, they release bremsstrahlung radiation. Because of their low mass, electrons are inelastically scattered when they collide with atomic shells, changing their velocity and momentum. Electrons can lose a large fraction of their energy when they interact with heavy atoms. The energy loss due to scattering depends on the particle charge and the density of the absorber. The Bethe-Bloch formula, written as

$$\left\langle \frac{dE}{dx} \right\rangle_{\text{coll}} = \frac{2\pi N_A r_e^2 m_e c^2 \rho Z}{A} \frac{z^2}{\beta^2} \left[\ln \left(\frac{2 m_e c^2 v^2 \gamma^2 W_{\max}}{I_{\text{pot}}^2} \right) - 2\beta^2 - \delta(\beta) - \frac{2C}{Z} \right] \tag{1.79}$$

describes the energy loss of a charged particle moving linearly through matter, or the stopping power. Here dE/dx is the energy loss per unit path length, r_e is the classical electron radius, m_e is the rest mass of the electron, c is the speed of light, ρ is the material density, Z and A are the nuclear charge and the mass number of the absorber material (Bethe, 1954; Knoll, 2010). Avogadro's constant is written with $N_A = 6.022 \times 10^{23}$ particles per mole. The variables z, v, and β are the charge, velocity, and relativistically scaled velocity of the incident particle, and γ here is the Lorentz factor. The quantity $W_{\max}$ is the maximum energy transfer for a single collision. Equation 1.79 contains an important parameter in the average ionization potential I_{pot}. This value is difficult to compute, but can be parameterized using

$$I_{\text{pot},Z} = (12 + 7\,Z)\ \text{eV}, \quad Z < 13 \tag{1.80}$$

for low atomic numbers, and for high atomic numbers,

$$I_{\mathrm{pot},Z} = \left(9.76 + 58.8\, Z^{-1.19}\right)\ \mathrm{eV}, \quad Z \geq 13. \tag{1.81}$$

The total stopping power of an electron in an absorbing material is the sum of the collisional and radiative stopping powers. At low velocities ($\beta \ll 1$), the energy loss due to inelastic collisions follows the form $\langle dE/dx \rangle \propto \beta^{-2}$ through the velocity dependence of the Coulomb interaction. With increasing velocities ($\beta\gamma > 4$), relativistic effects lead to increasing energy loss $\langle dE/dx \rangle \propto \ln(\gamma^2 v^2)$. Radiative effects become significant at even higher velocities $\beta\gamma \sim 50$.

When high-energy electrons are decelerated in an absorber, electromagnetic energy is emitted as bremsstrahlung radiation. The radiative energy loss increases with the incident electron energy. Since the cross-section for bremsstrahlung depends on the mass $\sigma_{\mathrm{brems}} \propto e^4/m_e^2c^2$, this contribution is insignificant for heavy particles at low energies. For low-mass charged particles (e.g., electrons), the probability of bremsstrahlung emission is higher. The main energy loss due to bremsstrahlung is directly proportional to the energy of the incident particle, and to the square of the nuclear charge of the absorber material,

$$\left\langle \frac{dE}{dx} \right\rangle_{\mathrm{rad}} \propto T_e, \quad \left\langle \frac{dE}{dx} \right\rangle_{\mathrm{rad}} \propto Z^2. \tag{1.82}$$

For low energy electrons, or in absorbers with low atomic weight, radiative energy loss due to bremsstrahlung can typically be neglected. The ratio of the specific energies dE/dx from bremsstrahlung and inelastic collisions can be approximated as:

$$\frac{(dE/dx)_{brems}}{(dE/dx)_{col}} \approx \frac{E_{through} Z}{800} \tag{1.83}$$

where $E_{through}$ is the kinetic energy of the electron in MeV and Z is the atomic number of the absorber (Krieger, 1989). Since experimental determination of stopping powers for many materials and energy ranges is impractical, computational databases such as ESTAR (`https://www.physics.nist.gov/PhysRefData/Star/Text/ESTAR.html`) provide tabulated and interpreted values of computed collisional and radiative stopping powers Berger (1992). Using data from the ESTAR database, we estimate electron energy loss through different materials as a function of electron energy.

1.5.3 Beta Electron Spectroscopy

Electrons penetrating matter lose energy primarily through inelastic collisions with atomic electrons, and at sufficiently high energies, through interactions with atomic nuclei. Electrons, being charged particles with finite rest mass, undergo multiple scattering events, resulting in a total path length that is significantly longer than their net penetration depth. The rate of energy loss depends on the charge of the particle, its velocity, and the density and atomic composition of the absorbing medium. The mean energy loss per unit path length is described by the Bethe–Bloch formula in Equation 1.79.

The Continuous Slowing Down Approximation (CSDA) range through a material is the idealized path length taken as the particle slows down to rest, assuming continuous and gradual energy loss through the material projected in a straight line Pal et al. (1987). In practice, scattering events shorten the penetration depth. This can be expressed as

$$R_{CSDA}(E_0) = \int_0^{E_0} \left(-\frac{dE}{dx}\right)^{-1} dE, \tag{1.84}$$

where E_0 is the initial energy of the particle and dE/dx is the stopping power. High-Z materials (e.g., Pb) will stop particles more readily.

Semiconductor Detectors

Materials can be characterized in terms of their electrical properties. The permitted and forbidden energy states of an electron within a material can be described using an energy band model, distinguishing between insulators, semiconductors, and conductors. These materials vary in their energy band gap between the valence band and the 'conduction' band. In semiconductors, the band gap ranges from 0.1 eV to 3 eV (Schreckenbach, 1979).

The detection principle of incoming radiation is based on the production of electron-hole pairs. Particles or photons with high enough energy will penetrate the semiconductor and excite an electron from the valence band to the conduction band, leaving a hole in the valence band. The electron-hole pairs within the semiconductor then drift to the anode or cathode and register an event. The size of the voltage difference is proportional to the energy of the incident particle.

Semiconductors with large atomic numbers (e.g., germanium or gallium crystals) are used to achieve a high probability of detection (Knoll, 2010). To maximize the signal-to-noise ratio by reducing thermal electron excitation within the crystal, semiconductors are often cooled using liquid nitrogen.

The GEometry ANd Tracking (GEANT) simulation software theoretically describes the transmission of elementary particles through matter using Monte Carlo methods (Brun et al., 1978). Handling geometric effects and particle tracking, GEANT is used to model detector response functions and particle transport in laboratory setups.

1.5.4 Cross-sections and Reaction Rates

The interaction cross-section $\sigma(v)$ depends on the relative velocity v between the projectile and the target. It follows that the reaction rate $r = N_X v N_Y \sigma(v)$ is the number of reactions between two particle number densities N_X, N_Y per unit volume per unit time. To determine the reaction rate for a pair of particles $\langle \sigma v \rangle$, the cross-section $\sigma(v)$ is convolved with the velocity distribution $\phi(v)$,

$$\langle \sigma v \rangle = \int_0^\infty \sigma(v) v \phi(v) dv, \tag{1.85}$$

resulting in the total reaction rate

$$R = \frac{N_X N_Y \langle \sigma v \rangle}{(1 + \delta_{XY})}, \tag{1.86}$$

with the correction term $(1 + \delta_{XY})$ applied to prevent double counting. Using the Maxwell-Boltzmann velocity distribution from Equation 1.75, the cross-section under stellar conditions is written as the MACS.

1.5.5 Activation Experiments

Activation experiments are widely used to measure neutron interaction cross-sections and are used to investigate reactions relevant in the nucleosynthetic s-process. In these experiments, a stable target is bombarded with neutrons of a known energy distribution. The induced radioactivity is then measured, allowing for a determination of the capture cross-section. The decay products from the radioactive isotopes

can be γ photons or β^- electrons; both may be detected using broad-energy germanium detectors (BEGe) or high-purity germanium detectors (HPGe). To obtain stellar cross-sections from an activation experiment, the neutron spectrum should ideally correspond to the thermal spectrum at the respective s-process site. At low energy accelerators, the reaction ^{7}Li(p,n)^{7}Be fulfills this requirement as the neutron source. Setting the proton energy to $E_p = 1912$ keV, 30 keV above the reaction threshold of 1882 keV, yields a neutron spectrum with an energy dependence close to that of a Maxwellian,

$$\Phi(E) = E \exp\left(-\frac{E}{k_B T}\right), \tag{1.87}$$

almost perfectly mimicking the conditions during He shell flashes in AGB stars. This quasi-stellar neutron source is ideal for the determination of MACS data.

The cross-section is a measure of the probability that a reaction will occur under given circumstances. Cross-sections are determined by the reaction rate R, the areal density of a sample μ_A, and the incident particle flux Φ,

$$\sigma = \frac{R}{\mu_a \Phi}. \tag{1.88}$$

To determine the reaction rate, it is imperative to understand the time dependent activity A of the produced radioisotope

$$\frac{dN}{dt} = -\lambda N = -A, \tag{1.89}$$

where the decay constant λ times the number of present nuclei N defines the number of decays per second A. The decay constant λ is related to the half-life $t_{1/2}$ through $\lambda = \ln(2)/t_{1/2}$. The general nuclear decay law can be recovered by integrating Equation 1.89 with respect to time,

$$N(t) = N_0 \exp(-\lambda t), \quad \text{and} \quad A(t) = A_0 \exp(\lambda t). \tag{1.90}$$

Connecting the detected counts to a reaction rate requires considering the time dependent evolution of the activity of the sample during all stages of the experiment. There are three main stages to an activation experiment: irradiation, transport, and measurement. During the irradiation phase, the decay of the radioisotope competes

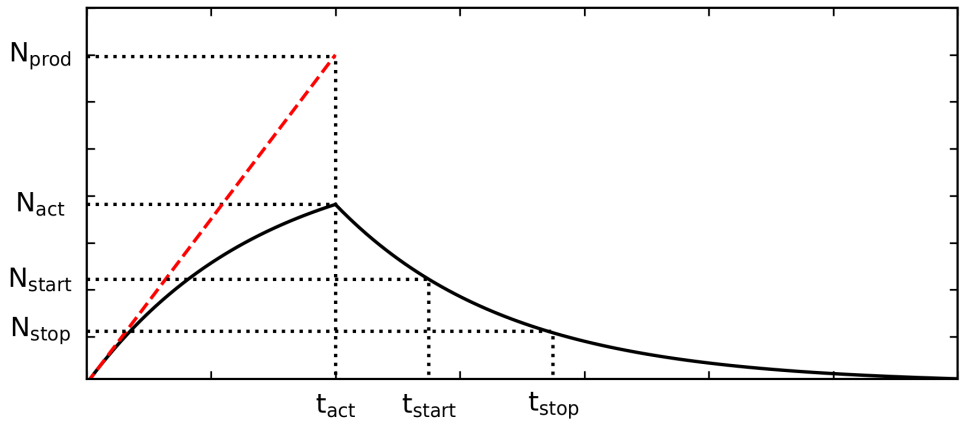

Figure 1.12: Evolution of the number of nuclei in an activation experiment. Important experimental times, t_{act}, t_{start}, t_{stop} are shown, and the number of active nuclei at these times, N_{prod}, N_{act}, N_{start}, N_{stop}, are marked.

with its production, and a term $\sigma\Phi N_0^{sample}$ is added to Equation 1.89. In reality N_0^{sample} changes with time, but practically the conversion rate is small compared to the number of nuclei within the sample, and N_0^{sample} is assumed to be constant. At time $t = 0$, the number of produced active nuclei is zero, leading to

$$\begin{aligned} N_{\text{prod}}(t_b) &= \sigma\,\Phi\,N_0^{\text{sample}}\,\frac{1}{\lambda}\left(1 - e^{-\lambda t_b}\right) \\ &= \sigma\,\Phi\,N_0^{\text{sample}} f_{b,\text{const}}, \end{aligned} \tag{1.91}$$

where t_b is the beam time in the irradiation phase and N_{prod} is the number of product nuclei at the end of the irradiation. A varying particle flux has to be taken into account by segmenting the irradiation time into intervals, and solving iteratively.

$$\begin{aligned} N_{\text{prod}}(t_b) &= \sigma\,N_0^{\text{sample}} \sum_{i=0}^{n} \Phi_i\,\frac{1 - e^{-\lambda t_i}}{\lambda}\,e^{-\lambda t_i (n-i)} \\ &= \sigma\,N_0^{\text{sample}} f_b. \end{aligned} \tag{1.92}$$

After the irradiation, the sample is transported to the detectors. In this phase, radioactive isotopes decay without being measured. This leads to another correction

factor f_w, where t_w is the waiting time between the irradiation and measuring phases.

$$N_{\text{decay}}(t_w) = N_{\text{prod}}\, e^{-\lambda t_w} = N_{\text{prod}}\, f_w. \tag{1.93}$$

The final stage of the activation experiment is the measurement phase. By integrating the solution of the decay equation across the measurement time t_m we find

$$N_{\text{meas}}(t_w) = N_{\text{prod}}\, e^{-\lambda t_m}(1 - e^{-\lambda t_m}) = N_{\text{prod}}\, f_w\, f_m. \tag{1.94}$$

In Figure 1.12, the time evolution of produced nuclei in an activation experiment is shown. Using γ or β^- spectroscopy to determine the number of decaying nuclei comes with limitations, leading to the correction factors. Applying the correction factors, we connect the number of counted events C to the number of produced nuclei N_{prod} through

$$C = N_{prod}\, \kappa\, \epsilon\, I\, f_{DT}\, f_b\, f_w\, f_m. \tag{1.95}$$

Further correction factors for self-absorption κ, detection efficiency ϵ, intensity I, and dead time correction f_{DT} are specific to the experimental setup. The self-absorption factor κ takes into account emitted radiation that does not reach the active detector material, or loses energy and does not contribute to the observed spectrum. The detection efficiency ϵ takes into account that not all emitted particles reach the active parts of the detector. This is dependent on the distance between the sample and the detector, the angular cover coverage of the detector, and the detector geometry. The intensity I is the probability that the particle of interest is emitted during the nuclear decay. If the time between the emission of two or more particles is shorter than the time resolution of the detector, their deposited energy is summed by the detector. The dead time correction factor f_{DT} takes into account that, for a short time after an event is registered, the detection system cannot detect another event. Taking these expressions together, we find an equation for the cross-section

$$\sigma = \frac{C}{\mu_a\, \Phi\, \kappa\, \epsilon\, I\, f_b\, f_w\, f_m\, f_{DT}} \tag{1.96}$$

The activation method is limited to cases where a neutron capture results in an unstable isotope with a half life longer than about a second. The quasi-stellar

neutron spectrum is not precisely thermal, and the respective corrections require knowledge of the energy dependence of the cross-section. Historically, the quasi-stellar spectrum could only be produced for a few temperatures using a few reactions: at $k_BT = 25$ keV with ^{7}Li$\rightarrow^7$Be, at $k_BT = 5$ keV with^{18}O(p,n), and at $k_BT = 52$ keV with ^{3}H reactions, each becoming more energy-demanding and producing lower neutron yields. This means that the MACS values have to be extrapolated to cover the full range of s-process temperatures (Reifarth et al., 2014).

Because the target sample can be placed directly at the neutron production target, the neutron flux is orders of magnitude higher than that which can be achieved in other experimental setups. This results in a gain in sensitivity, allowing for the measurements of very small cross-sections. In activation experiments, the background contamination is also strongly reduced using semiconductor detectors, and the short measurement times allow the study of systematic uncertainties by repeated activations. This technique allows for good accuracy, as demonstrated by the 1.4% uncertainty on MACS of ^{197}Au (Ratynski and Käppeler, 1988).

The Ring Method

The ring method takes advantage of the wide opening angle (120°) of the neutron cone produced by the ^{7}Li(p,n)^{7}Be reaction, where higher energy neutrons are concentrated towards the center of the cone ($k_BT = 25$ keV), and lower energy neutrons towards the edges. By constructing a target with a ring shape to capture an annulus of the neutron beam, neutron energies down to $k_BT = 5$ keV can be probed (Heftrich et al., 2022). Astrophysically, the ^{13}C(α,n)^{16}O reaction produces neutrons at energies around $k_BT = 5 - 8$ keV in the He intershell region in AGB stars, and is the main neutron source for the strong component of the s-process.

1.6 Structure of the Thesis

Chapter 1 presents an overview of current research into the s-process from the three astronuclear disciplines. Observational techniques and their applications to characterize binary stars, their atmospheres, and their surface chemistry are summarized. The evolution of low-mass stars, binaries, mass transfer, and the nucleosynthetic s-process are discussed from the modeling perspective, and methods commonly used

to model stars are presented. Experimental nuclear physics is discussed as an avenue to explore the s-process. The importance of each of these pillars is noted within the wider field of nuclear astrophysics. In the following chapters, we describe projects that continue the development and implementation of data and tools to better understand the s-process from the comprehensive astronuclear perspective.

In Chapter 2, we introduce an observational campaign to measure and monitor the orbits of binary stars enriched in heavy material produced by the s-process in AGB stars. We derive stellar atmospheric parameters, heavy element abundances, and orbital parameters from high-resolution, high signal-to-noise spectra for a sample of intrinsic and extrinsic stars.

Chapter 3 discusses stellar evolution modeling and binary accretion. We present a grid of stellar evolution models including accretion across a range of metallicities, AGB donor masses, initial masses, and accretion masses. We simulate the effects of accretion onto a stellar surface, including the mixing of accreted material, and we track observable surface chemical abundances through the stellar lifetime.

In Chapter 4, we present experimental efforts to measure the neutron interaction cross section of the double magic number element ^{208}Pb. We use the ring-activation method to mimic the conditions of stellar interiors and investigate the cross section of the species marking the end point of the s-process.

Chapter 5 summarizes the work and provides an outlook for follow-up and directions in which the following projects may be pursued.

2 Observations of the s-process in Stars

2.1 Motivation

The details of how s-process elements are synthesized in AGB stars and are subsequently imprinted on their binary companions remain uncertain. Observations of chemically peculiar stars - such as Ba, CH, and CEMP-s stars - provide direct constraints on surface abundance patterns resulting from mass transfer. High-resolution spectroscopy allows us to derive precise atmospheric parameters and elemental abundances, which serve as empirical benchmarks for stellar evolution and nucleosynthesis models. By systematically analyzing a large sample of post-accretion stars, we test theoretical predictions for s-process yields, identify signatures of different nucleosynthesis pathways, and constrain the mass of the AGB star that produced the observed abundance pattern. This observational foundation is essential for connecting nuclear physics reaction rates to the chemical evolution of stars. This chapter is based closely on the work detailed in Dimoff et al. (2024), *S-Process Nucleosynthesis in Chemically Peculiar Binaries*.

What's New: We generate a large spectral database of 404 stars. We measure their radial velocities and have computed orbital parameters for 50 stars. We have derived homogeneous stellar parameters for a large sub-sample of 312. For the highest quality sub-sample of 30 stars, we have computed surface abundance patterns of 12 elements. We add new abundance patterns to the literature, and make new detections of Mo and Pb in stellar atmospheres. We classify stars based on their abundance patterns and overall metallicity.

2.2 Abstract

We study the s-process by observing the luminous components of binary systems polluted by a previous AGB companion. Our radial velocity (RV) monitoring program establishes an ongoing collection of binary stars exhibiting enrichment in s-process material for the study of elemental abundances, production of s-process material, and binary mass transfer. From high resolution optical spectra, we measure radial velocities (RVs) for 404 stars and derive stellar parameters for 312 stars using ATHOS. For a sub-sample of 25 chemically interesting stars we refine our atmospheric parameters using ionization and excitation balance with the Xiru program. We use the MOOG code to compute one-dimensional local thermodynamic equilibrium (1D-LTE) abundances of C, Mg, s-process elements (Sr, Y, Zr, Mo, Ba, La, Ce, Nd, Pb), and Eu to investigate neutron capture events and stellar chemical composition. We estimate dynamical stellar masses via orbital optimization using Markov chain Monte Carlo (MCMC) techniques in the ELC program, and we compare our results with low-mass AGB models in the FUll-Network Repository of Updated Isotopic Tables & Yields (FRUITY) database. We compute surface parameters for a sample of 5 AGB stars, and derive surface abundance patterns. We estimate the mass and evolutionary phase of the AGB stars by comparing surface parameters and abundances to the FRUITY database. In our abundance sub-sample, we find enhancements in s-process material in spectroscopic binaries, a signature of AGB mass transfer. We add the element Mo to the abundance patterns, and for 12 stars we add Pb detections or upper limits, as these are not known in the literature. Computed abundances are in general agreement with the literature. Comparing our abundances to dilution-modified FRUITY yields, we find correlations between s-process enrichment and AGB mass, supported by dynamical modeling from RVs. From our high-resolution observations, we expand heavy element abundance patterns and highlight binarity in our chemically interesting systems. We find trends in s-process element enhancement from AGB stars and agreements in theoretical and dynamically modeled masses. We investigate evolutionary stages for a small sub-set of our companion stars.

2.3 Stars with s-process Enhancements

2.3.1 AGB Stars

AGB stars are evolved low-mass stars that synthesize heavy elements via the s-process in their interiors. Convective mixing and TDU events bring this material to the surface where it can be observed in the AGB star. In binary systems, this enriched material is shared with and accreted by a companion. The signature of the AGB star is preserved in the atmosphere of the binary companion where it can be observed on the surface of a less-evolved star.

The binaries enriched by an AGB star have different names depending on their metallicity and carbon enrichment. They are called barium (Ba) stars, CH stars, or Carbon-Enhanced Metal-Poor (-s) (CEMP-s) stars. In these systems, the star we observe is not the star that itself made the elements, but rather has received material through mass transfer from an AGB companion. The vast majority of these stars are binaries - possibly all of them - and some of them reside in systems with very long periods, up to hundreds or thousands of days.

2.3.2 Ba Stars

At high metallicities, AGB nucleosynthesis and mass transfer in binary systems are followed by studying the Ba stars. Primarily found in the Galactic disk, the Ba stars characteristics include moderate to high metal content ([Fe/H] > -1.0), s-process element enrichment, and mild carbon enrichment. These stars were first identified as a distinct class of chemically peculiar stars in the 1950s due to their unusually strong singly-ionized Ba II spectral lines at 4554 Å, along with other features of s-process elements like Sr, Y, and La, and Pb (Bidelman and Keenan, 1951). Initially described as first ascent giants, Ba stars are primarily G and K type giants, and were initially thought to be intrinsically enriched in heavy elements. However, subgiants and dwarfs fitting these chemical properties have been discovered and, being in such evolutionary states, are not able to produce s-process material and self-enrich their envelopes. Detailed chemical abundance analyses have confirmed the s-rich nature of the Ba stars (Warner, 1965; Allen and Barbuy, 2006; Pereira et al., 2011; de Castro et al., 2016; Cseh et al., 2018; Karinkuzhi et al., 2018; Roriz et al., 2021b,a).

Unlike their metal-poor counterparts, Ba stars were not originally suspected to be

binaries until after their binary nature was recognized spectroscopically (McClure et al., 1980; McClure, 1984). It was later confirmed that Ba stars share common orbital properties, supporting a binary mass transfer scenario (Jorissen and Mayor, 1988; McClure and Woodsworth, 1990; Udry et al., 1998). More recent studies have contributed to the compilation of orbital properties and component parameters for increasingly large samples of Ba stars (Escorza et al., 2019; Jorissen et al., 2019).

The mass distribution of Ba stars was studied by Escorza et al. (2017) and is described by two Gaussians with a main peak at 2.5 $M_{\odot}$ with a standard deviation of 0.18 $M_{\odot}$, and a broader tail at higher masses (up to 4.5 $M_{\odot}$), which peaks at 3 $M_{\odot}$ with a standard deviation of 1 $M_{\odot}$. A complementary study in Jorissen et al. (2019) found a similar distribution of masses with compatible metallicities for Ba stars. Post-accretion binaries play a crucial role in stellar population synthesis and binary population synthesis modeling.

2.3.3 CH Stars

At lower metallicities ([Fe/H] $<$ -1) we trace the s-process in the early Galaxy through the CH and CEMP-s stars. The CH stars were first recognized as a distinct class of chemically peculiar stars in the late 1940s and early 1950s by Keenan (1942) from strong molecular CH absorption bands in their spectra near 4308 Å, distinguishing them from ordinary carbon stars. The CH stars were further classified based on their enhanced carbon and s-process elements (e.g., Ba, Sr, La, and Pb) Bidelman and Keenan (1951). These stars also show strong molecular C-N-O bands, and are important to understand the detailed composition of the early s-process and binary accretion at early cosmic times (Hansen et al., 2019).

Photometric surveys Bond (1974) expanded the known population of CH stars, confirming that they are primarily found in the Galactic halo. Their key characteristics include low metallicities ([Fe/H] $\approx$ -1.0 to -2.5), strong CH molecular bands (e.g., the G-band (near 430 nm)), high levels of carbon enhancement ([C/Fe] $>$ +0.5), and enrichment in s-process elements showing elevated levels of e.g., Ba, Sr, La, and Pb. Most CH stars are red giants, but some are subgiants or main-sequence stars.

CH stars were suspected to be binary systems early on, and radial velocity monitoring in the 1980's and 1990's confirmed their binary nature. The CH stars exhibit

long-term radial velocity variations and present a very high binary fraction within the population (> 80%) McClure (1984). It has been established that CH stars have orbital properties consistent with mass transfer from an evolved AGB star McClure and Woodsworth (1990), providing direct evidence of binary evolution.

Recent studies have expanded on heavy element abundance patterns in both number of elements and number of stars (Goswami et al., 2006; Karinkuzhi and Goswami, 2014, 2015; Goswami et al., 2016; Purandardas et al., 2019). The CH stars help link chemically peculiar stars across different metallicity regimes by bridging the gap between CEMP-s and Ba stars. CH stars are important because they trace early galactic chemical enrichment, as their abundances help to better understand the s-process contribution of early stars.

2.3.4 CEMP-s Stars

Carbon-Enhanced Metal-Poor (CEMP) stars were first identified in the 1980's and 1990's during large-scale surveys of metal-poor stars. Norris et al. (1997) identified stars with unusually high carbon and neutron-capture element abundances in the halo of the Milky Way. Ryan et al. (1996) found metal-poor stars with strong Ba and Eu features, linking them to possible binary interactions. Beers and Christlieb (2005) formally defined the differing CEMP classes and their abundance patterns.

CEMP-s stars belong to the broader CEMP class, defined by their low iron content and high carbon enhancement. They are characterized by having low metallicities of [Fe/H] < -1.0 (although it may be much lower, < -2.0), high carbon-to-iron ratios of [C/Fe] > +0.7, and exhibiting overabundances in s-process elements such as Ba, Sr, and other s-process elements (e.g., [Ba/Fe] > +1.0). Evolutionarily, these stars are typically giants, but more recently subgiant and even dwarf CEMP-s stars have been discovered. Large-scale surveys, such as the HK Survey (Beers et al., 1992) and the Hamburg/ESO Survey (Frebel et al., 2006) significantly expanded the sample of known CEMP-s stars.

One of the most significant discoveries regarding CEMP-s stars is that nearly all of them are in binary systems, with a binary fraction near 100%, providing strong evidence of mass transfer as the source of their chemical enrichment, rather than intrinsic nucleosynthesis (Lucatello et al., 2005; Starkenburg et al., 2014; Hansen et al., 2016b). The binary nature of CEMP-s stars is widely supported by data ac-

Spec. Type	[Fe/H] [dex]	Mass [$M_\odot$]	Gal. Pos.
Ba	$[Fe/H] > -1.00$	~ 2.50	disc
CH	$-0.15 > [Fe/H] > -2.50$	~ 1.00	halo
CEMP-s	$-1.00 > [Fe/H] > -2.50$	~ 0.80	halo

Table 2.1: General properties of post-accretion systems.

quired from extensive programs of radial velocity monitoring, where orbital periods range from hundreds to tens of thousands of days (Jorissen et al., 1998; Hansen et al., 2016b). With refined orbital parameters of the observed population, Izzard et al. (2010), Starkenburg et al. (2014), Hansen et al. (2016a), Hansen et al. (2016b), and Abate et al. (2018) show consistency with binary mass transfer models. The primary star in the binary system was originally an AGB star, which produced carbon and s-process elements through nucleosynthesis, and transferred enriched stellar material to the present-day CEMP-s star. The AGB star continued its evolution into a white dwarf, leaving behind an enriched CEMP-s star.

Studying the orbital properties of both CH and CEMP stars, Jorissen et al. (2016) found no discernible differences in the period-eccentricity distribution of the two groups. They remark that the two classes of stars should not be treated separately from the orbital perspective, but as one population.

Ba stars, CH stars, and CEMP-s stars are recognized as post-accretion binaries showing enrichment in carbon and elements synthesized mainly through the s-process (Keenan, 1942; Bidelman and Keenan, 1951; Burbidge et al., 1957; Käppeler et al., 2011; Lugaro et al., 2023). As testbeds of binary interactions and evolution, these classes of stars constrain models of mass transfer. Being similar post-mass-transfer systems but at different metallicities, these three populations of stars provide valuable observational constraints on s-process nucleosynthesis models in AGB stars at different metallicities (Hansen et al., 2016a,b; Cseh et al., 2018; Hansen et al., 2019; Cseh et al., 2022). When viewed from a Galactic chemical evolution perspective, the Ba, CH, and CEMP-s stars trace how subsequent generations of stars enrich the Milky Way with heavy elements.

2.4 Observational Campaign

We observe warm to cool (spectral types A, F, G, K, M) dwarfs, subgiants, and giants, focusing on AGB, CEMP, Ba, C, CH, CEMP-s, using a set of high-resolution (R = 30000 - 67000) echelle spectrographs available through the Trans-National Access program (TNA) within the Chemical Elements as Tracers of the Evolution of the Cosmos INFRAstructures (ChETEC-INFRA) framework. For most of our stars, the spectral lines are generally narrow and deep, and sufficient pseudo-continuum windows are available within each spectral order. This approach would not work well for very hot or rapidly-rotating stars, where spectral lines are broadened across several echelle orders.

2.4.1 Telescopes and Observatories

Vilnius University Moletai Astronomical Observatory (MAO)

The Moletai Astronomical Observatory (MAO) at Vilnius University in Lithuania hosts a 1.65m Ritchey-Chretien telescope, with the fibre-fed Vilnius University Echelle Spectrograph (VUES) at the Cassegrain focus (Jurgenson et al., 2014, 2016). With a resolution of $R = 37000$ in the "low" resolution mode, and a wavelength range of $4000 - 8800$ Å, VUES is an excellent instrument to measure RVs with high precision. Estimated velocity uncertainty with the VUES instrument for an average signal-to-noise (SNR) ~ 15 is on the order of 1.0 km/s. With the smallest aperture in our network, this instrument is mostly used for RV monitoring, and the only highest SNR spectra are of abundance measurement quality. A refurbished mirror coating applied in the summer of 2022 resulted in higher quality data through the remainder of the campaign. Spectra are collected by local astronomers.

Astronomical Institute of the Czech Academy of Sciences (ASU) Ondřejov Astronomical Observatory

The Ondřejov Observatory is part of the Astronomical Institute of the Czech Academy of Sciences (ASU), which operates the 2m Perek telescope on which the Ondřejov Echelle Spectrograph (OES) is mounted (Koubský et al., 2004). The OES instrument is a high-dispersion white-pupil design, stationed at the Coude focus of the Perek telescope, with a resolution of $R \sim 51600$ at 5000 Å and a broad spectral

range covering 3753-9195 Å. This instrument is well-suited to perform radial velocity measurements, and spectra of high SNR are used for chemical abundance estimations.

Bulgarian National Astronomical Observatory Rozhen

The Echelle Spectrograph Rozhen (ESpeRo) (Bonev et al., 2017) is a cross-dispersed fibre-fed instrument obtaining spectra from 3900 Å to 9000 Å at high resolution from $R \sim 30000 - 45000$. This presents another ideal instrument for RV measurements and abundance derivations due to the similarities between the ASU and IANAO telescopes.

Roque de los Muchachos Observatory, Instituto Astrofisico de Canarias (IAC)

Located on the island of La Palma in las Canarias in Spain, in accordance with the IAC, the 2.65m Nordic Optical Telescope (NOT) is the home of the high-resolution FIbre-fed Echelle Spectrograph (FIES). The FIES instrument is a cross-dispersed high-resolution echelle spectrograph mounted in an independent building for thermal and mechanical stability, and is fully described in Telting et al. (2014). We use the highest resolution setting of $R \sim 67000$ on the high-resolution 1.3 arcsecond fibre number 4. The optical range is from $3700 - 8300$ Å, without gaps. Our average RV uncertainty from FIES is on the order of 0.01 km/s. Data is automatically reduced using the nightly calibration frames (biases, flats, ThAr lamps) through the FIEStool reduction software. A drawback is the low UV sensitivity, due to Rayleigh scattering within the fibre. We find FIES to be a consistent instrument and useful in our abundance investigation.

La Silla Observatory, European Southern Observatory (ESO)

The Fiber-fed Extended Range Optical Spectrograph (FEROS) (Kaufer and Pasquini, 1998; Kaufer et al., 1999) is a temperature and humidity controlled echellograph mounted at the MPG/ESO 2.2m telescope at the La Silla Observatory in Chile. With a resolution of $R \sim 48000$, the radial velocity accuracy is ≈ 20 m/s over a two month baseline with consistent observations. Our measured average RV uncertainty from this instrument is of this order, $\langle \sigma_{RV} \rangle \sim 0.03$ km/s. High-SNR FEROS spectra are suitable to compute stellar abundances.

These spectrographs provide high-resolution spectra allowing for accurate and precise stellar parameters and abundances, together with the long baseline radial velocity monitoring crucial in determining orbital parameters.

2.4.2 Target Selection

We select our targets from multiple catalogs including Stephenson (1984), Alksnis et al. (2001), Escorza et al. (2020), Yoon et al. (2016), Čotar et al. (2019), Karinkuzhi et al. (2021b), and Cseh et al. (2018). These catalogs contain stars of spectral classifications that are of interest: AGB, Ba, CEMP-s, C, and CH type stars. From large surveys, we select targets based on binarity indicators, heavy element enrichment, and atmospheric parameters. These stars will construct our radial velocity database, to be observed multiple times over four years. A subset of these stars are selected for high-SNR observations to investigate their surface chemical composition.

The Apache Point Observatory Galactic Evolution Experiment (APOGEE) survey samples major populations of the Milky Way with moderate resolution ($R \sim 22500$) and high SNR (> 100) infrared ($\lambda = 1.5 - 1.7\mu$m) spectra (Majewski et al., 2017). The catalog includes stellar parameter estimations, radial velocities, metallicities, and sparse heavy element abundances. We query the Gaia data release 3 (DR3) database for targets with more than 10 observations, radial velocity uncertainties >5 km/s, and astrometric reduced-unit weight-error ≥ 1.4 to increase the chances of selecting binaries (Gaia Collaboration et al., 2023). Gaia DR3 includes radial-velocity spectrograph data ($R \sim 11000$) in the near-IR around the Ca triplet, which also provides indicators of enrichment in s-process material (e.g., Ce and Nd). We use this information as another selection criterion to find stars that are possibly enriched in heavy metals. We further select targets based on output from secondary data products such as the The Final Luminosity Mass Age Estimator (FLAME, Creevey and Lebreton, 2022), including estimates of the masses, ages, and orbital parameters of stars in Gaia DR3. The Galactic Archeology with Hermes (GALAH) survey provides a wealth of spectroscopic data for bright stars in the southern hemisphere in relatively high resolution ($R \sim 28000$) (Buder et al., 2019). Chemical compositions and orbital properties of this sample are available for reference and comparison. GALAH allows selection of targets identified as Ba-enhanced, CEMP-s, or other C-enhanced stars, and we select candidates in both confirmed and sus-

pected binary systems. We selected stars from the Large Sky Area Multi-Object Fiber Spectroscopic Telescope (LAMOST) catalog (Cui et al., 2012) that show heavy element features in their spectra and display binary star characteristics.

We compose a sample of ~ 500 targets (limited to stars brighter than $\sim$14th magnitude) visible by our suite of telescopes. For observed stars in our sample, we show right ascensions (RA) and declinations (DEC) on the sky in Galactic coordinates in the left panel of Figure 2.1 and Gaia DR3 parallax distances in the right panel of Figure 2.1. Gaia DR3 magnitudes and colors are displayed in a Hertzsprung-Russell (HR) diagram in Figure 2.2. Our sample is a combination of warm to cool stars (spectral types (A),F,G,K); either dwarfs or giants; that have binary star characteristics; and that exhibit s-process enrichment. We make distinctions between giant stars known to produce (AGB) or exhibit the presence of s-process material (Ba, CEMP, C, CH). Our targets are either in known binaries, or suspected to be in binary systems based on RV measurements and relative uncertainties.

As we source our targets from catalogs and surveys, some have already been observed with high spectral resolution. Large spectroscopic and photometric surveys often include estimates of atmospheric parameters, and we use the existing literature data as a consistency check and benchmark for our own observations and analysis. A list of observed stars, their spectra, computed radial velocities and abundances (where applicable) is available at the Milne Centre Barium Star Repository at `https://github.com/Milne-Centre/Barium-Star-Repository`.

This work uses spectroscopic data to extract information about the studied systems. Other techniques, including photometry and astrometry, provide baseline data from which orbital, atmospheric, and physical parameters are estimated.

2.4.3 Observing Strategy

Our observing program is split into two components. We obtain high SNR (≥ 50 at 4500 Å) spectra from stars either with peculiar abundance patterns or in known binaries with the intent to derive abundances of neutron capture elements accurate to within ± 0.2 dex. We also collect snapshot spectra of SNR $\sim 10-20$ of stars with peculiar abundances that may reside in binary systems, or know binary systems that may show peculiar abundances, suitable for precise RV measurements and long-term monitoring. Precise RV data over a long baseline is crucial to determining binary

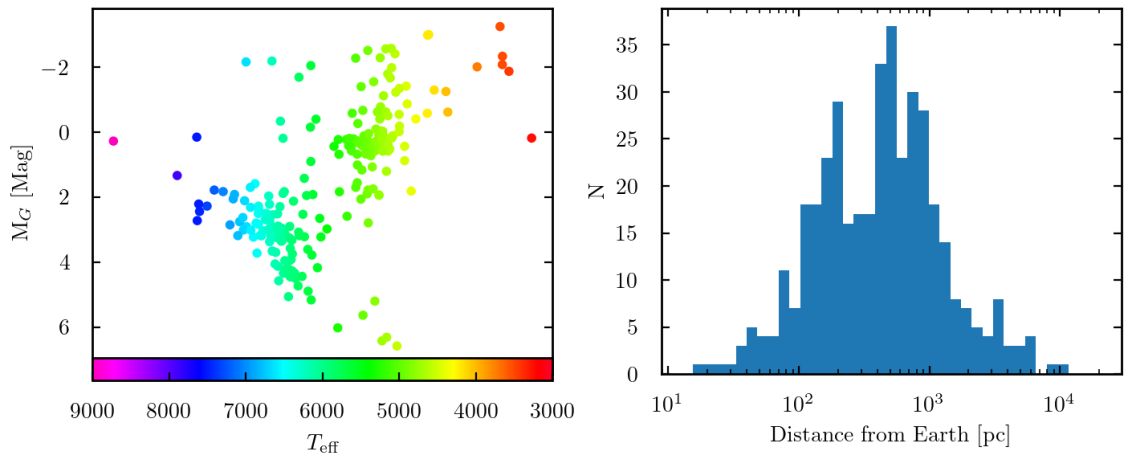

Figure 2.1: Left: HR Diagram for stars in our sample, using Gaia photometric data and parallax. Stars are generally split between main-sequence dwarfs and giants from 4000 - 7000 K. Right: Histogram of stellar distances for our sample, using Gaia DR3 parallaxes. Adapted from Dimoff et al. (2024).

parameters in systems with long orbital periods.

To date, most approaches are made in small samples ($<$ 20 stars) with a long baseline or larger samples over a short period of time. We improve on previous approaches by monitoring the radial velocities in a large sample (hundreds of stars) over the long baseline of four years. It is important to monitor radial velocities over a long baseline in time (Hansen et al., 2016b) to confirm if *all* Ba, CH, and CEMP-s stars are indeed binaries, to characterize their orbits, and to investigate the binary fraction of AGB stars in the field.

2.4.4 Campaign Results

Table 2.2 lists the number of nights at each of the observatories in the program. For the TNA telescopes, there were four proposals calls each year on a quarterly basis, but proposals were not submitted for each call. For the MPG telescope, observation proposals were submitted on a six-month basis. In total, we obtained 187 nights across the five observatories over a period of four years.

Of the total number of requested stars in our full target list to be observed for radial velocity monitoring ($\sim$ 500), the number of observed targets is 404, with an

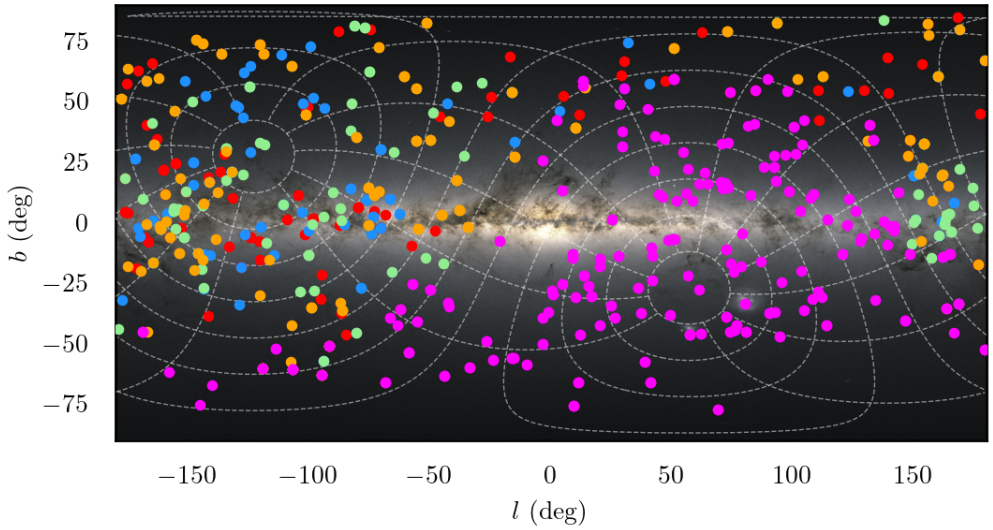

Figure 2.2: Position of sample stars on the sky, in galactic coordinates. Different colors symbolize different instruments.

average of about six observations per star. We have focused our RV monitoring efforts on stars showing heavy element enhancements, which are expected to be in binaries that yet have only a few observed RVs in the literature. Additions to the RV literature are shown in Figure 2.3. Further RV follow up is planned for stars where abundances have only recently been measured. We note that not all of the stars with measured RVs or abundances are analyzed in this work. The full RV and abundance samples will be analyzed and presented in the future.

2.5 Data Reduction

Because we collected data from multiple sources, data are reduced in different ways corresponding to the instrument. The raw VUES spectroscopic data are reduced using a spectroscopic reduction pipeline written in Interactive Data Language (IDL). The bias is first subtracted, spectral orders are traced using halogen lamp (flat field)

Table 2.2: Awarded observation nights between 2021 and 2025. This list includes nights lost due to bad weather conditions, Target of Opportunity programs, or other reasons.

Instrument	Resolution (R)	Telescope Size [m]	Obs. Nights
VUES	37000	1.65	57
OES	40000	2.00	46
ESpeRo	30000	2.00	39
FIES	67000	2.65	10
FEROS	48000	2.20	36
Total			188

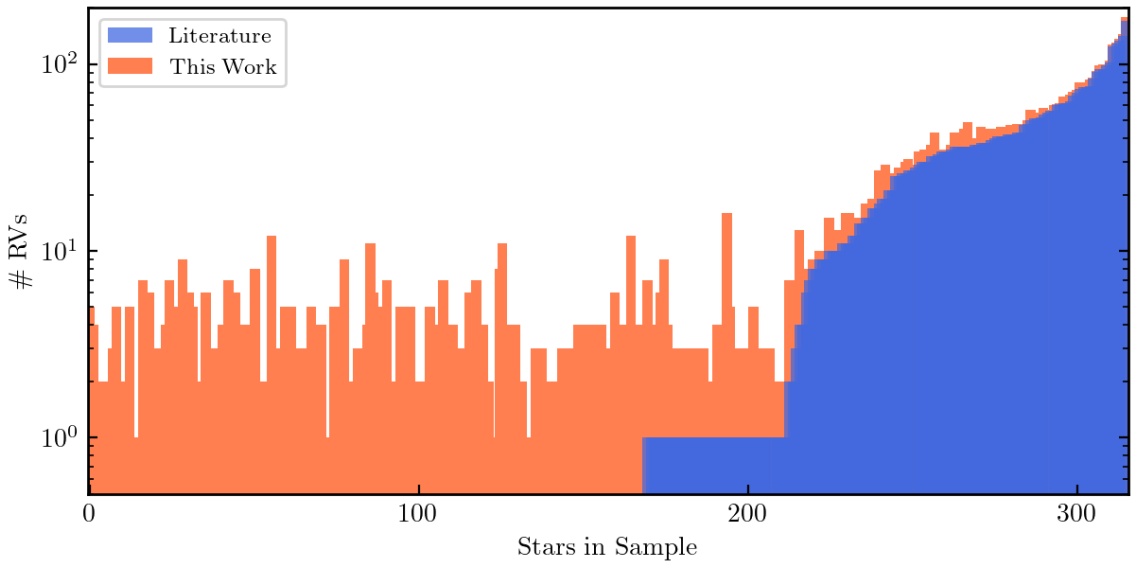

Figure 2.3: Contributions from RV monitoring program to the literature. Each bin is one observed star, and the y-axis value is the total number of RV data points for the given star. Blue data is the available literature data, and orange is the contribution from our monitoring program. Adapted from Dimoff et al. (2024).

images, a flat-field correction is applied, and the wavelengths are calibrated using Thorium-Argon (ThAr) lamp spectra. Finally the science spectra are extracted along traced orders, and the wavelength dispersion solution is applied. Data from the VUES instrument is provided to the end user in a pre-reduced .fits file format. For a final step in the data reduction, we normalize the spectra by performing a blaze correction using the flat field frame, and fitting the resulting continuum with a low-order polynomial.

Data from OES are reduced using the Ondřejov Echelle Spectrograph REDuction (OESRED) semi-automatic reduction pipeline written in IRAF, tailored to reduce the 2D OES spectra (Cabezas et al., 2023). The biases, halogen lamp flat fields, and thorium-argon frames are combined for their respective master images. The master bias is subtracted from the master flat field and the science frames. The apertures for the spectral orders in the master flat, lamp, and science frames are determined by fitting high-order polynomials. Wavelength calibration with the master lamp is done for each night of observation. Flat correction effectively removes the blaze function from all orders as well as fringing effects in the reddest orders. Final normalization of the individual orders is done with high-order splines (~ 10) in batches.

Raw CCD data from the ESpeRo spectrograph at the Rozhen observatory is reduced by the observing staff following standard spectral reduction procedures in IRAF. The bias subtraction, flat field correction, and wavelength calibration steps are all performed before the data is sent to the user. The master bias is removed from the master flat field and sciences frames. Individual echelle orders are extracted from the master flat, the best obtained stellar spectrum, or a standard (RV or photometric) bright star that has been observed. The orders are extracted for the stellar spectra, master flat, and ThAr images. Science orders are divided by the flat field, and wavelengths are calibrated using the ThAr lamps. Additionally, a heliocentric correction is applied to the spectra. We normalize the spectra in-house with a polynomial fitting routine in IRAF.

Data from FIES is received in both raw form and a preliminarily reduced form, using the FIEStool pipeline; however, we are cautioned against using this 'reduced' data for scientific studies, and are encouraged to perform our own reduction. FEROS data is received in raw form. Full spectral reduction for the data collected from FIES and FEROS is performed using the Collection of Elemental Routines for Echelle Spectra (CERES) pipeline (Brahm et al., 2017). We use tools and routines for CCD

image reduction, tracing of the echelle orders, optimal extraction of the wavelength solution, and RV estimation. The CERES pipeline provides normalized optical spectra from the FEROS and FIES data.

For all of our echelle spectra, we merge the continuum-normalized spectral orders for a complete 1D spectrum by interpolating the overlapping spectral regions at the native resolution.

2.5.1 Spectral Normalization

Spectral normalization is of extreme importance for accurate RV cross-correlation, stellar parameter estimation, and accurate abundance determinations. Echellogram spectra have a curved 'blaze' shape, where they receive more flux in the middle of the chip compared to the edges. After extraction and reduction, this feature remains in the science spectra. To flatten and normalize the spectra, we fit a polynomial to corresponding to the apertures in the flat field frame, and then the science apertures are divided by this function to remove the blaze. This also removes any fringing effects in higher order apertures, but may not fully flatten the spectrum. For each night of observation, we perform a flat-correction to the calibrated data. We use cubic splines of high order ($\sim 8-10$) to flatten the spectrum and obtain a continuum value of ≈ 1.

Additional spectral features may be present after normalization. In general, the spectra are noisy on edges of the orders, and there are large regions of spectral overlap between orders on some instruments. We exercise caution when merging the spectral orders to generate a full 1D spectrum by taking the weighted mean of the flux at resolution-consistent wavelength intervals. Other features could be related to the quality of the flat-field calibration or may be related to a change in polarization along the fibre Škoda et al. (2008). We avoid regions where spurious spectral features may affect our measurements.

2.6 Data Analysis

2.6.1 Radial Velocities

From the normalized stellar spectra, we measure the Doppler shift to move the spectra into the rest-frame. In doing so, we compute the radial velocity (RV) of the observed star and adjust for the motion of the Earth around the Sun with the barycentric correction. To compute the RV of our targets, we used the cross-correlation method by comparing the observations to rest-frame template spectra.

We generated synthetic spectra of the same spectral types covered in our observational campaign using MOOG and use them as templates for the cross-correlation comparison Sneden et al. (2012). Additionally, for each spectrograph, we used observed spectra of varying spectral types as templates for comparison. We manually shift them to the rest frame using absorption features at known wavelengths: H-α (6563 Å), H-β (4381 Å), Mg b triplet (5183 Å), and the Na D doublet (5980 Å). We opt to use the observed stellar spectral templates that we have manually shifted to the rest frame, as they preserve the instrumental profile and result in more consistent and precise RV.

For the spectroscopic data from VUES, OES, and ESpeRo, we used the Python package PyAstronomy and the RVCorr function to compute cross-correlation functions (CCFs) on the reduced data. From the CCF results, we compute radial velocities as the shift of the peak of the CCF. We verify our results using the IRAF (Image Reduction and Analysis Facility) functions for the Doppler correction of a spectrum DOPCOR, and cross-correlation of a spectrum FXCOR, within the NOAO (National Optical Astronomy Observatory) package.

We computed the CCFs on the entire sample of observed stars for each spectral order before merging. To determine the goodness-of-fit of the cross-correlation, we computed both the statistical 'r' (TDr) value Tonry and Davis (1979) and a χ^2 between the observed and template spectra. In the TDr comparison,

$$\epsilon = \frac{N}{8B}\frac{1}{1+r}, \tag{2.1}$$

where N is the number of bins in the cross-correlation, B is the wavenumber at the center of the peak, and r is

$$r = \frac{h}{\sqrt{2}\sigma_a}, \tag{2.2}$$

where h is the height of the cross-correlation peak and σ_a is the root mean square average of the cross-correlation, or the average height of the CCF background. We compared RV results using the TDr approach and the χ^2 metric and we find that the best TDr value is not always consistent with the best χ^2 value, and the CCF background may be poorly constrained in noisy spectra. In the majority of instances, we found the CCF with the highest peak compared to the background consistent with the χ^2 metric. Since this is case, we determined the χ^2 method is sufficient in finding the best template spectrum. We computed the RV for each spectral order before merging to provide a statistical value of the RV. We remove outlying RV values beyond 3σ of the median. Such deviations may arise from noisy spectral orders in the bluer regions or from low SNR.

2.6.2 Stellar Atmospheric Parameters

Stellar atmospheric parameters are important for characterizing the internal structure and evolutionary state of a star. Knowing the effective temperature $T_{\rm eff}$, surface gravity $\log(g)$, and metallicity [Fe/H] is vital for computing synthetic stellar atmospheres for the derivation of elemental abundances.

ATHOS To homogenize our samples from different instruments, we used ATHOS (A Tool for HOmogenizing Stellar spectra) from Hanke et al. (2018), because it is a fast and automated code needed for our sample size. The ATHOS program estimates the stellar effective temperature $T_{\rm eff}$, surface gravity $\log(g)$, and metallicity [Fe/H] from spectra by computing analytical relations between flux ratios (FRs) within designated wavelength regions of interest. The temperature estimates come from FRs around the Balmer lines Hα and Hβ, and the metallicity and surface gravity FRs come from regions of interest within the optical spectrum between $\sim$ 4800Å and $\sim$ 6500Å that include the Mg b triplet and many Fe features between 5000 and 5500 Å.

The ATHOS program works on stellar spectra with resolution within the range $R \sim 2000 - 67000$. ATHOS is a machine-learning algorithm trained on chemically

normal stars, operating effectively within temperatures $4000 - 6500$ K, surface gravities from $1 - 5$, and metallicities between -4.5 and +0.3 dex, covering spectral types F, G, and K. There exist stars in our dataset outside of these boundaries, and we find the code performs poorly when used on data outside of the training set. ATHOS does not require a fully stitched 1D spectrum; only that the regions of interest be in the spectrum. The code can also be parallelized, enabling fast and efficient analysis of very large datasets.

ATHOS quickly determines atmospheric parameters for a large sample of stars, provided their parameters are within that of the training set. Since the program depends on flux ratios from a set of wavelength ranges, it suffers degeneracies when stars are chemically peculiar or have appreciable rotational velocities.

Uncertainties in the parameters determined by ATHOS stem from statistical uncertainties within the training set. The parameters are estimated in order: first temperature, then surface gravity, and finally metallicity. If the estimate of the temperature is highly uncertain, this will propagate to the estimation of the surface gravity, which further compounds into the estimate of the metallicity (Hanke et al., 2018).

We tested ATHOS on odd- and even- numbered spectral orders, on combined orders that contain the only the regions of interest, and on merged 1D spectra for our data sets. For the majority of the instruments used, we find no significant difference between using odd and even orders, compared to isolating the regions of interest. For the OES sample, the regions of interest are split unequally between the odd and even orders, and choosing this method results in inaccurate estimation of the atmospheric parameters with large uncertainties. The $T_{\rm eff}$ estimation often comes close to literature, but can have large errors on the order of > 500 K. To mitigate these effects, we merge the spectral orders after shifting them to the rest frame. Using merged 1D spectra provides the best results with the lowest uncertainties. ATHOS performed well on our data, provided that the atmospheric parameters of the stars are within the operational limits of the program.

ATHOS does not provide an estimate of the microturbulence parameter ξ. In this case, we computed the microturbulence using the empirical relation from Mashonkina et al. (2017),

$$\xi_t = 0.14 - 0.08\,[\mathrm{Fe/H}] + 4.90\frac{T_{\mathrm{eff}}\,(\mathrm{K})}{10^4} - 0.47\,\log(g). \tag{2.3}$$

While this formula is designed to work with metal-poor giants, we found it sufficient to estimate the microturbulence of our sample.

Our full observational sample slightly exceeds the parameter limits of the ATHOS program, so we apply ATHOS to a trimmed sample of our 360 observed stars. Not all of our spectra are of high enough quality to estimate accurate parameters using ATHOS; we estimate accurate parameters in a high-quality sub-sample of about 312 stars.

ARES The ARES (Automatic Routine for Equivalent widths of Spectra) program (Sousa et al., 2015) is a tool for quickly measuring equivalent widths of spectral features. We used separate line lists for metal-rich stars (Alves-Brito et al., 2010; Koch et al., 2016) and metal-poor stars (Hansen et al., 2012a; Koch et al., 2016) with ARES to quickly compute equivalent widths of Fe I and II features in our observed stars. In preparing the line lists, we visually inspected the features to ensure they are not blended or asymmetric. To verify our results using ARES, we selected a number of lines and computed the equivalent widths 'by hand' using IRAF. We find good agreement, and deem it safe to use the ARES results when performing the excitation and ionization balance to determine atmospheric parameters.

Xiru The Xiru code (Alencastro Puls, 2023) is a program to find spectroscopic parameters of a star, including the microturbulent velocity ξ, from excitation/ionization balance, given a set of equivalent widths of Fe I and Fe II spectral lines. To find the best fit stellar atmospheric parameters, Xiru interpolates the grid of model atmospheres in four-dimensional T_{eff}, $\log(g)$, [Fe/H], and ξ space using Broyden's method to quickly optimize the spectral solution. Choosing a high quality, high SNR subset of our stars analyzed by ATHOS, we refined the stellar parameters by using the Xiru program using equivalent widths measured with ARES, using the ATHOS values as input for iteration.

AGB Stars

A known characteristic of AGB stars is their cool extended atmospheres. In cool stellar atmospheres, the neutral and ionized states of atomic species are not in equilibrium and may not display the same abundance for a given model atmosphere Campbell et al. (2017). In this light, we opted to use different methods to estimate the surface parameters for our sample of AGB stars.

We collected photometric data in Johnson-Cousins UBVRI bands and 2MASS JHK_s bands, with corrections, are collected from SIMBAD for our set of AGB stars (Chen et al., 2019). To account for extinction, we used an individual determination of the line of sight reddening for each of our stars from the dust map hosted by CalTech (`https://irsa.ipac.caltech.edu/applications/DUST/`) (Schlafly and Finkbeiner, 2011). For each of the available photometric bands, we applied extinction corrections to reduce the systematic errors in our parameter estimates; we rely on the relative reddening with respect to a known reference point.

We computed the metallicity by measuring the equivalent widths of Fe I spectral features. We formed a line list of features >7000 Å using lists provided in Neyskens et al. (2015); Shetye et al. (2018, 2019, 2020, 2021), and supplement it with 5500<7000 Å by choosing Fe lines that are not included in molecular features or strongly blended with other features.

The stellar temperature was computed using the infrared flux method (IRFM), using photometric data and empirical scaling relations Alonso et al. (1999). This method has a metallicity dependence, and we use our derived metallicities.

We computed the surface gravities $\log(g)$ using the parallax, luminosities, and mass estimates (Nissen et al., 1997), through the expression

$$\log(g/g_{\odot}) = \log(M/M_{\odot}) + 4\log(T/T_{\odot}) + 0.4V0 + 0.4BC + 2\log(\pi) + 0.12. \quad (2.4)$$

Using this method the surface gravity depends on the stellar temperature and mass of the star. We estimate AGB masses using our temperature and luminosity estimations and fitting evolutionary tracks from Bressan et al. (2012) and Chen et al. (2014).

2.6.3 Abundances

To focus our abundance measurements on the highest-quality spectra, we made cuts on spectral SNR ($>$ 40 around $\lambda \sim$ 4500 Å) and parameter uncertainties ($\Delta T_{\rm eff} < 300$ K, $\Delta \log(g) < 0.5$, Δ[Fe/H] < 0.3 dex). In addition to high SNR, we choose stars that stars satisfy at least one of our criteria of interest: they are known chemically interesting stars (Ba, C/CH, CEMP-s stars), or are flagged as chemically peculiar candidates; they are in known binaries, or they are known to be chemically interesting and are in suspected binaries. We used Xiru to compute parameters on our high-quality sub-sample. The average uncertainties in $T_{\rm eff}$, $\log(g)$, and [Fe/H] are 89 K, 0.35, and 0.16 respectively. We used our stellar parameters from Xiru to generate synthetic spectra from the ATLAS9/Kurucz stellar atmosphere models (Heiter et al., 2002; Castelli and Kurucz, 2003), and we compared them to our observations.

We computed 1D-LTE abundances from spectral features using the MOOG software (Sneden et al., 2012; Sneden, 2023), with the PyMOOGi[1] implementation (Adamow, 2017). We used the drivers *abfind* and *synth* to determine the atomic abundances through equivalent width fitting and synthetic spectra comparison. For clean lines, we determined the strength of the absorption feature by measuring the equivalent width and using it as input for *abfind*. We used the *synth* driver to compute abundances via synthetic spectra comparison for blends and hyperfine split lines. A χ^2 routine within the *synth* driver indicates the best fit synthetic spectrum to the localized observations.

In both cases of computing abundances, a continuum correction is first applied across larger wavelengths (∼40-50 Å) for a verification of the continuum around the line(s) in question. When determining abundances, we generated a (2-5 Å) region centered around the line of interest.

Elemental abundances from the s-process have been previously studied in parts of our sub-sample, although not always at such high resolution, nor for all of the elements we probe in this study. The elements Sr, Ba, and Eu are relatively well measured in the literature and provide a good basis for comparison in most cases.

The $\log \varepsilon$ abundance scale is customary in astronomy, and is computed using the expression

[1] `https://github.com/madamow/pymoogi/`

$$\log \varepsilon_X = \log(N_X/N_H) + 12, \tag{2.5}$$

where $\log \varepsilon_H = 12$. The MOOG abundance outputs are in the form oflog ε abundances, which we convert to the logarithmic 'square-bracket' [X/Fe] notation, scaling chemical abundances in our stars to the sun. To convert this value to [X/Fe], we subtract the solar abundance $\log \varepsilon_{X,\odot}$ and then the stellar metallicity $[\mathrm{Fe/H}]_*$,

$$[\mathrm{X/Fe}] = \log \varepsilon_{X,*} - \log \varepsilon_{X,\odot} - [\mathrm{Fe/H}]_*. \tag{2.6}$$

We computed the total abundance of an element by averaging the abundances measured from multiple spectral lines when available. A line list for our atomic species is in Table A.1, with wavelengths, excitation potentials, and oscillator strengths $\log(gf)$, compiled with data from `linemake`. NIST[2] data quality flags are included where available. Lines with hyper-fine or isotopic splitting are marked accordingly, with (hfs).

AGB Stars

For the AGB stars, we interpolated a grid of 1D-LTE MARCS model atmospheres specifically designed for evolved S-type stars Van Eck et al. (2017). These models cover lower temperatures down to 2700 K, variable C/O ratios, and the overall enhancement of s-process elements. They consider the important molecular contributions to the absorption spectrum. AGB stellar spectra suffer from significant molecular absorption, mainly from C, TiO and ZrO.

In AGB spectra, the lines of interest are typically heavily blended, especially in the blue region. We selected lines > 5500 Å, since bluer regions of AGB spectra are dominated by ZrO and TiO absorption. We compile our line list for AGB stars from Meléndez and Barbuy (2009); Neyskens et al. (2015); Shetye et al. (2019, 2020, 2021).

2.6.4 Orbital and Physical Elements

We used the ELC program to model the binary orbits with collected and available RVs. The ELC program is a photodynamical modeling software for binary stars

[2] `https://physics.nist.gov/`

(Orosz and Hauschildt, 2000). The code is general, and the orbits of a variety of binary systems can be directly modeled, including RV variable systems. The program computes the Cartesian positions and velocities of the stars from the Keplerian orbital parameters in a 6-to-6 conversion, and integrates the Newtonian equations of motion. Further details are found in Orosz et al. (2019) and Dimoff and Orosz (2023).

We collected available RV data and orbital parameters for our targets from literature sources, including Gaia DR3, The RAdial Velocity Experiment (RAVE) Steinmetz et al. (2006) the 9th Catalogue of Spectroscopic Binary Orbits (SB9) Pourbaix et al. (2004), and references therein. With our RV time-series data and informed priors from the literature, we used ELC to optimize and refine the orbital and physical parameters of the binaries with a differential evolution Markov chain Monte Carlo (DEMCMC) routine to best fit the input data (Ter Braak, 2006).

In an eccentric orbit, the RV semi-amplitude of the primary component K_1 is measured from spectroscopic observations (Marcy and Butler, 1992; Mayor and Queloz, 1995), and is expressed as

$$K_1 = \left(\frac{2\pi G}{P}\right)^{1/3} \frac{M_2 \sin i}{(M_1 + M_2)^{2/3}} \frac{1}{(1-e^2)^{1/2}}, \tag{2.7}$$

where P is the orbital period of the binary, M_1 and M_2 are the masses of the primary and secondary components, i is the orbital inclination with respect to the observer, and e is the orbital eccentricity. The same expression exists for the secondary component, with the subscripts switched.

From a single-lined spectroscopic binary with one visible component, the individual masses of the components cannot be measured directly Instead, component masses are approximated through the mass function via Kepler's third law:

$$f(m) = \frac{M_2^3}{(M_1 + M_2)^2} \sin^3 i = 1.0385 \times 10^{-7} K_1^3 (1-e^2)^{3/2} P. \tag{2.8}$$

where i is the inclination in the observer's frame, M_1 and M_2 are the primary and secondary masses, e is the eccentricity, and P is the orbital period. Both component masses and the inclination are degenerate, and depend on one another to keep the mass function constant for the system. The observable parameters K_1, e, and P allow the computation of the mass function. For an eccentric orbit, the mass function

is derived from

$$f(m) = 1.0385 \times 10^{-7} K_1^3 (1 - e^2)^{3/2} P, \tag{2.9}$$

where P is the orbital period in days, K_1 is the radial-velocity semi-amplitude of the observable (primary) component, and e is the eccentricity. These parameters were determined from our DEMCMC modeling. These two expressions are then combined for

$$\frac{M_2^3}{(M_1 + M_2)^2} \sin^3 i = 1.0385 \times 10^{-7} K_1^3 (1 - e^2)^{3/2} P. \tag{2.10}$$

To estimate the masses of the binary components through the mass function, we need the inclination i of the system. Since our systems generally do not eclipse, we impose upper limits on the inclination, where $i \leq 85^\circ$ and we estimate a lower limit of $i \geq 15^\circ$ because we detect significant RV variations.

The inclination is further constrained by assuming rotational synchronization of the stars with their orbit; i.e. they rotate in the plane of the orbit, and at the same rate that the stars orbit each other. Since our sample is mostly older stars typically with long periods, we assume enough time has passed such that tidal interactions have synchronized the stellar rotation, and the rotational rate of the star $v \sin i$ is equal to that of the orbit P. In reality, this may not be the case, as mass transfer will likely disrupt the orbital system.

With Gaia DR3 parallaxes we estimated the luminosity from the radius using the temperature through $L = 4\pi R^2 T_{\rm eff}^4$. The parallax angle π and semi-major axis a are used to compute a relation between the period and masses, following Escorza et al. (2017):

$$\frac{a}{\Pi} = P^{2/3} \frac{M_2}{(M_1 + M_2)^{2/3}}. \tag{2.11}$$

This allows estimation of the luminous mass, which we use as input for the ELC program. Where available, we use mass estimates from the FLAME pipeline and mass information from literature references within Table 2.7 as informed priors for our orbital optimization. It is noted that the estimated mass of evolved stars from the FLAME pipeline generally are less accurate and have larger uncertainties.

From Escorza et al. (2017) and Jorissen et al. (2019), the average mass of a Ba

giant is $\sim 2.5\ M_{\odot}$, and varies between about 1.5 - 3.0 $M_{\odot}$; we initialize our visible components using this mass range in our higher metallicity systems in our dynamical modeling. For low metallicity stars, we initialize with a mass of approximately $0.80 M_{\odot}$ because the average mass of a CEMP star is about $0.80 M_{\odot}$. If the unseen component in the binary is indeed an AGB remnant, it should be a white dwarf. From AGB stars with initial masses between 0.85 and 7.5 $M_{\odot}$, white dwarf remnant masses are typically $0.5\ M_{\odot} < m < 1.1\ M_{\odot}$ (El-Badry et al., 2018), and we use this lower limit in our optimization. We set an upper limit for the mass of white dwarfs with the Chandrasekhar mass $M_{*} \leq 1.44\ M_{\odot}$ (Chandrasekhar, 1931).

2.7 Results

2.7.1 Atmospheric Parameters

High-resolution spectra allow for good estimation of atmospheric parameters, an important step in determining abundances in stellar atmospheres. Making cuts on our full sample of 404 stars, we arrive at a refined sample of about 312 stars.

A Kiel diagram in the left panel Figure 2.4 shows surface gravities and effective temperatures of our sample. Stellar parameters of our large sample analyzed with ATHOS and of our abundance sub-sample from Xiru are shown in solid and open circles respectively. In the right panel, metallicity is plotted against temperature. Blue data points are known Ba stars, red data points are C-enhanced stars, and green data points are "other" stars, yet unclassified by their abundances or chemical peculiarity. Parameters for the AGB stars are shown with solid orange circles. Error bars in the figure are the average uncertainties across our samples.

Typically, Ba stars have metallicities between $-1.0 \leq$ [Fe/H] $\leq +0.15$, where about 75% of our sample lies. Some CH stars in our sample also have metallicities in this range. About 25% of our sample stars have lower metallicity ([Fe/H] < -1), including CH and CEMP-s stars. After trimming our sample to be compatible with ATHOS, the effective temperatures range from 4100-6500 K, surface gravities from 0.65-4.97 dex, and metallicities from -2.6-$+0.20$ dex. A summary of the parameters for our abundance-quality sub-sample is in Table 2.3, where the first line for each star has our Xiru parameters and the second line has those from the literature, with references in the last column.

Table 2.3: Estimated atmospheric parameters for our abundance sample using Xiru. Literature values are provided for comparison, with references. From Dimoff et al. (2024)
(1) Soubiran et al. (2022) (2) Jorissen et al. (2019) (3) Purandardas et al. (2019) (4) Ting et al. (2019) (5) Karinkuzhi et al. (2018) (6) Zhang et al. (2023) (7) Pereira et al. (2012) (8) Karinkuzhi et al. (2021a) (9) Limberg et al. (2021) (10) Jönsson et al. (2020) (11) Buder et al. (2018) (12) Karinkuzhi et al. (2021b) (13) Gaia Collaboration et al. (2023) (14) Guillout et al. (2009) (15) Steinmetz et al. (2020a)

Star	$T_{\rm eff}$ [K]	σ_T	$\log(g)$ [dex]	$\sigma_{\log g}$	[Fe/H] [dex]	$\sigma_{\rm [Fe/H]}$	ξ [km/s]	σ_ξ	Ref.
HD 105671	4700	200	4.50	0.25	0.10	0.25	1.19	0.28	
	4617		4.55		0.07				(1)
HD 196673	4825	66	0.94	0.37	0.00	0.14	1.81	0.13	
	4914		2.50		0.12				(2)
HD 50264	5972	45	4.24	0.12	-0.17	0.07	0.86	0.08	
	5900		4.60		-0.13				(3)
HRCMa	5063	75	1.98	0.36	-0.23	0.12	1.82	0.14	
	4822		2.40		-0.23				(4)
PV UMa	5058	74	2.28	0.34	-0.32	0.13	2.00	0.13	
	5050		2.50		-0.13				(2)
HD 104979	5007	53	2.08	0.20	-0.35	0.10	1.65	0.09	
	4933		2.68		-0.33				(1)
HD 31487	4964	80	1.94	0.40	-0.38	0.24	2.08	0.13	
	4960		3.11		-0.04				(5)
HD 101581	5366	51	3.82	0.64	-0.55	0.29	3.18	0.12	
	4738		4.46		-0.52				(1)
BD+41 2150	4828	84	1.73	0.51	-0.48	0.18	1.77	0.16	
	4707		2.16		-0.67				(6)
CD-621346	5318	78	1.40	0.28	-1.35	0.10	1.81	0.10	
	5300		1.70		-1.57				(7)
HD 135148	4573	130	1.26	0.60	-1.41	0.24	1.95	0.21	
	4237		0.66		-1.89				(1)
HD 209621	4850	443	1.64	0.33	-1.60	0.40	2.06	0.45	
	4740		1.75		-2.00				(8)
TYC 1987-753-1	6047	200	4.00	0.25	-1.80	0.25	0.98	0.20	
	6126		3.45		-2.09				(9)
HE 0414-0343	5204	118	2.00	0.62	-1.89	0.15	0.80	0.14	
	4863		1.25		-2.24				(1)
BD+04 2466	5021	220	1.68	0.15	-1.93	0.30	1.66	0.20	
	4991		1.43		-1.97				(1)
HD 103545	4960	121	1.51	0.79	-2.02	0.17	2.14	0.19	
	4807		1.70		-1.99				(1)
HD 116514	6247	127	4.25	0.58	-0.04	0.17	2.93	0.18	
	5687		4.11		0.02				(10)
TYC 8258-1189-1	5158	63	2.64	0.23	-0.08	0.08	1.20	0.12	
	5171		2.77		-0.14				(11)
TYC 2250-1047-1	5853	97	3.55	0.56	-0.31	0.19	2.13	0.17	
	5335		3.71		-0.55				(12)
HD 51273	6412	103	3.46	0.43	-0.31	0.12	1.75	0.17	
	6249		3.87		-0.79				(13)
HD 33363	4947	61	2.07	0.42	-0.35	0.18	2.25	0.12	
	4660		2.92		-0.06				(14)
TYC 2866-338-1	4837	78	2.78	0.35	-0.51	0.13	1.86	0.12	
	4475		1.91		-0.60				(6)
BD-193868	4402	95	1.55	0.45	-0.67	0.13	1.32	0.18	
	4451		1.39		-0.54				(15)
HD 276679	5934	115	3.18	0.50	-0.90	0.18	1.05	0.18	
	6467		4.12		-1.31				(13)

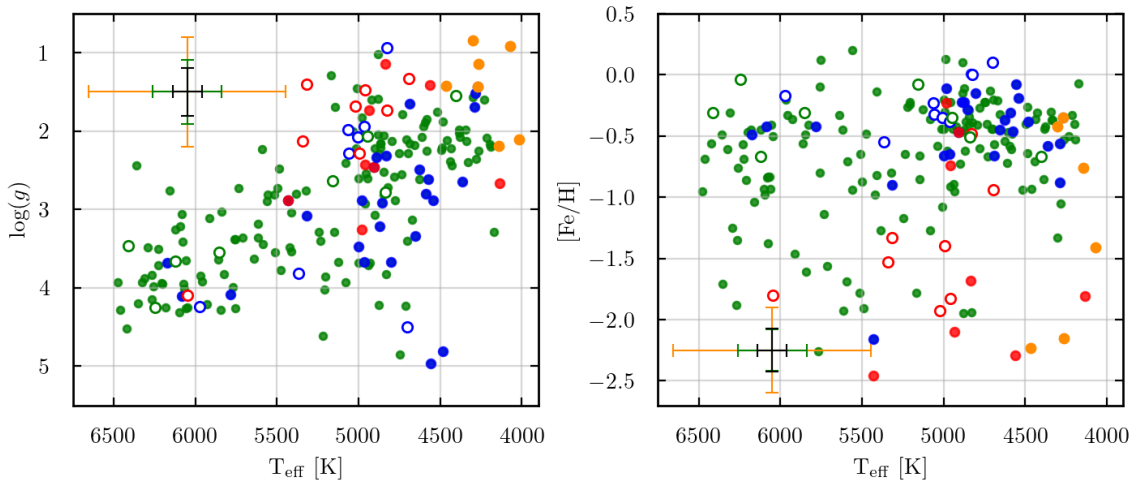

Figure 2.4: Left: Kiel diagram of our estimated stellar parameters from ATHOS and Xiru. Open circles are parameters estimated by Xiru. Blue data points are Ba stars, red are carbon enhanced stars, green are "other" stars, and orange are AGB stars. Floating error bars are averages for Xiru (black), ATHOS (green), and our AGB parameter averages (orange). Cool giants are in the upper right, and warm dwarfs are in the lower left. Right: Metallicity vs temperature for our this sub-sample, with ATHOS operational limits as the dashed grey box. Colors are the same as the top panel. Adapted from Dimoff et al. (2024).

We find Xiru estimates slightly higher temperatures and metallicities compared to ATHOS and other studies when determining atmospheric parameters. This may be due to imposing the restriction of ionization balance between Fe I and Fe II, where higher temperatures increase the relative abundance of Fe II. Over-ionization of Fe II is a known problem in cool giants, and Fe suffers from NLTE effects at low metallicities. This has a small but noticable effect when comparing our computed abundances to those in the literature. Our sample of ATHOS stellar parameters for 312 stars is made available on Zenodo[3].

AGB Stars

For our sample of AGB stars, we present derived atmospheric parameters in Table 2.4. We make note of the large uncertainties in the temperatures; From the grid

[3] `https://zenodo.org/communities/chetec-infra-wp6/records?q=&l=list&p=1&s=10&sort=newest`

Table 2.4: Stellar parameters of AGB stars in our sample.

Name	$T_{\rm eff}$ [K]	$\sigma_{T_{\rm eff}}$	$\log(g)$ [dex]	$\sigma_{\log(g)}$	[Fe/H] [dex]	$\sigma_{\rm [Fe/H]}$
V1139Tau	3503	96	0.215	0.112	-0.21	0.17
TVAur	3505	150	0.112	0.111	-0.61	0.24
V365Cas	3597	40	0.191	0.103	-0.3	0.20
SUMa	3748	25	0.263	0.099	-0.24	0.30
HRPeg	3543	125	0.277	0.119	-0.18	0.25

of MARCS models for late type stars described in Van Eck et al. (2017), we find the best matching model to our stellar parameters using a χ^2 maximum-likelihood method, and adopt this model when computing elemental abundances. In Figure 2.4, our sample of AGB stars are cooler than 4500 K and typically have surface gravities around $\log(g) \sim 1.0$.

2.7.2 Abundances

We investigated signals of enrichment from AGB nucleosynthesis through s-process abundance patterns in AGB stars themselves and the binary companions of former AGB stars. Here we present our relative abundances and patterns for a sub-sample of 25 stars. Additionally, we identify and verify signatures of s-process nucelosynthesis in the atmospheres of 5 AGB stars. We constructed atomic and molecular line lists using `linemake` including the elements we want to derive, as well as potential molecular contaminants in blended lines.

We computed abundances for the elements C, Mg, Fe, Sr, Y, Zr, Mo, Ba, La, Ce, Nd, Eu, and Pb. When we cannot compute abundances, we identify upper limits. Abundance ratios [X/Fe] for our sub-sample are compared to the literature star-by-star in Table 2.5, where the upper row for each star is our derived abundances, and the lower row is that of the literature, with references. Quoted uncertainties are the average statistical uncertainties between lines of the same element.

An example of a synthetic spectrum fit for the CEMP-s star HE 0414-0343 is seen in Figure 2.5, where black data points are the observed spectrum, and multi-colored solid lines are generated synthetic spectra. While carbon dominates the spectrum in this blended line, there is a significant contribution from La. The carbon abundance

Table 2.5: Computed abundances [X/Fe] for our sub-sample of stars, compared to literature values. Upper limits are indicated with <. For the stars HD 33363, HD 51273, HD 276679, HD 116514, TYC 2866-338-1, and BD-07 3076 we were unable to find abundance information in the literature. Units are expressed in [dex] compared to the Sun. Adapted from Dimoff et al. (2024).

Star	[Fe/H]	C	Mg	Sr	Y	Zr	Mo	Ba	La	Ce	Nd	Eu	Pb
HD	0.10 ± 0.25	0.01 ± 0.09	0.01 ± 0.11	0.19 ± 0.11	-0.06 ± 0.12	0.16 ± 0.14	0.21 ± 0.14	-0.03 ± 0.13	0.17 ± 0.16	-0.07 ± 0.2	0.31 ± 0.16	0.26 ± 0.14	0.21 ± 0.18
105671	-0.03[8]	- -	0.03[8]	0.03[8]	0.01[8]	0.06[8]	- -	-0.10[8]	- -	0.00[8]	- -	- -	- -
HD	0.00 ± 0.14	-0.05 ± 0.13	0.14 ± 0.2	0.15 ± 0.12	-0.35 ± 0.23	-0.07 ± 0.17	0.15 ± 0.19	-0.35 ± 0.22	-0.15 ± 0.13	-0.1 ± 0.14	-0.05 ± 0.14	-0.15 ± 0.16	- -
196673	0.12[2]	- -	- -	- -	0.00[2]	0.25[2]	- -	- -	0.39[2]	0.31[2]	- -	- -	- -
HD	-0.17 ± 0.07	0.31 ± 0.09	0.07 ± 0.11	0.84 ± 0.09	0.41 ± 0.13	0.93 ± 0.10	0.96 ± 0.15	0.99 ± 0.11	1.0 ± 0.089	0.89 ± 0.06	0.78 ± 0.14	0.26 ± 0.11	1.2 ± 0.18
50264	-0.13[10]	0.21[10]	0.14[10]	1.90[10]	0.88[11]	1.29[11]	- -	1.25[11]	1.30[10]	1.66[10]	1.35[10]	0.44[11]	- -
HR CMa	-0.23 ± 0.12	0.21 ± 0.071	0.25 ± 0.11	0.94 ± 0.18	0.85 ± 0.18	1.0 ± 0.11	0.81 ± 0.13	1.4 ± 0.13	1.0 ± 0.13	0.97 ± 0.089	1.0 ± 0.14	0.31 ± 0.11	1.1 ± 0.18
	-0.36[1]	0.25[1]	-0.30[1]	1.21[1]	1.08[1]	1.45[1]	- -	1.88[1]	1.56[1]	1.50[1]	1.40[1]	0.54[1]	- -
PV UMa	-0.32 ± 0.13	-0.13 ± 0.1	0.19 ± 0.2	0.47 ± 0.15	0.14 ± 0.13	0.04 ± 0.19	0.37 ± 0.19	0.62 ± 0.12	0.62 ± 0.13	0.27 ± 0.14	0.47 ± 0.16	-0.08 ± 0.16	- -
	-0.13[2]	- -	- -	- -	0.73[2]	0.75[2]	- -	- -	0.76[2]	0.68[2]	- -	- -	- -
HD	-0.35 ± 0.10	-0.02 ± 0.09	0.08 ± 0.16	0.53 ± 0.14	0.20 ± 0.14	0.38 ± 0.13	0.56 ± 0.14	0.66 ± 0.12	0.74 ± 0.12	0.65 ± 0.11	0.55 ± 0.17	0.25 ± 0.11	1.1 ± 0.18
104979	-0.26[2]	0.03[4]	-0.23[3]	0.99[5]	0.71[2]	0.85[2]	- -	0.52[3]	1.11[2]	1.06[2]	1.13[5]	0.40[5]	- -
HD	-0.38 ± 0.24	0.09 ± 0.071	0.22 ± 0.2	0.29 ± 0.17	0.59 ± 0.14	0.62 ± 0.14	0.64 ± 0.15	1.0 ± 0.13	0.92 ± 0.14	0.69 ± 0.14	0.84 ± 0.14	0.15 ± 0.18	- -
31487	-0.04[1]	0.13[1]	- -	- -	- -	1.11[1]	- -	- -	- -	- -	- -	- -	- -
HD	-0.55 ± 0.29	0.4 ± 0.07	0.46 ± 0.06	0.46 ± 0.11	0.35 ± 0.11	0.20 ± 0.15	0.50 ± 0.18	0.42 ± 0.13	0.7 ± 0.23	0.70 ± 0.15	0.52 ± 0.11	0.55 ± 0.25	0.40 ± 0.22
101581	-0.44[12]	0.34[12]	0.04[13]	0.13[12]	-0.06[12]	0.08[12]	- -	-0.10[12]	0.48[12]	0.41[12]	0.58[12]	0.29[13]	- -
BD	-0.48 ± 0.18	0.37 ± 0.05	0.04 ± 0.16	0.52 ± 0.15	0.60 ± 0.15	0.91 ± 0.13	0.89 ± 0.13	1.40 ± 0.12	1.40 ± 0.14	1.2 ± 0.10	1.20 ± 0.10	0.32 ± 0.16	0.92 ± 0.18
+41 2150	-0.77[18]	0.46[18]	- -	0.85[18]	1.06[18]	0.78[18]	- -	1.65[18]	- -	- -	1.42[18]	- -	- -
CD	-1.35 ± 0.10	0.91 ± 0.071	0.31 ± 0.11	0.54 ± 0.14	0.41 ± 0.11	0.51 ± 0.16	< 0.81	1.40 ± 0.13	1.00 ± 0.11	1.00 ± 0.11	1.3 ± 0.18	0.51 ± 0.11	2.10 ± 0.14
-62 1346	-1.59[24]	0.86[24]	0.69[24]	- -	0.46[24]	0.86[24]	- -	1.58[24]	1.18[24]	1.24[24]	1.25[24]	- -	2.05[24]
HD	-1.41 ± 0.24	0.61 ± 0.11	0.27 ± 0.06	0.37 ± 0.26	-0.06 ± 0.15	0.04 ± 0.16	0.24 ± 0.26	0.14 ± 0.13	0.12 ± 0.16	0.07 ± 0.11	0.14 ± 0.14	0.14 ± 0.18	- -
135148	-2.17[6]	0.80[7]	- -	- -	- -	- -	- -	0.30[7]	0.31[9]	- -	- -	0.71[9]	- -
HD	-1.60 ± 0.40	1.50 ± 0.21	0.76 ± 0.20	1.10 ± 0.23	0.95 ± 0.25	1.5 ± 0.11	< 1.30	1.50 ± 0.11	< 1.80	1.90 ± 0.18	1.90 ± 0.20	1.10 ± 0.20	2.06 ± 0.22
209621	-1.99[15]	1.26[15]	0.17[17]	1.02[16]	0.36[16]	1.80[16]	- -	1.76[15]	2.41[16]	2.04[16]	1.87[16]	1.35[16]	1.88[16]
TYC	-1.80 ± 0.25	0.61 ± 0.11	0.22 ± 0.16	-0.02 ± 0.21	-0.06 ± 0.13	< 0.61	< 0.81	0.76 ± 0.12	0.56 ± 0.16	0.71 ± 0.14	< 0.41	< 0.36	1.4 ± 0.27
1987-753-1	-2.05[15]	2.39[15]	- -	- -	- -	- -	- -	0.75[15]	- -	- -	- -	0.04[15]	- -
HE	-1.89 ± 0.15	0.95 ± 0.07	0.35 ± 0.14	0.78 ± 0.2	0.65 ± 0.25	1.00 ± 0.16	0.59 ± 0.26	1.40 ± 0.13	1.30 ± 0.15	1.30 ± 0.16	1.30 ± 0.13	0.85 ± 0.11	2.20 ± 0.18
0414-0343	-2.50[23]	1.3[23]	0.49[22]	0.48[22]	0.20[22]	0.52[22]	- -	1.9[23]	1.48[22]	1.42[22]	1.63[22]	1.23[22]	2.53[22]
BD	-1.93 ± 0.30	0.90 ± 0.10	0.33 ± 0.05	0.36 ± 0.14	0.27 ± 0.11	0.60 ± 0.17	0.70 ± 0.22	1.2 ± 0.11	1.10 ± 0.089	1.10 ± 0.11	0.91 ± 0.098	0.50 ± 0.16	1.70 ± 0.18
+04 2466	-1.90[15]	1.24[15]	0.24[17]	- -	0.49[19]	- -	- -	1.63[15]	1.31[19]	- -	1.23[19]	0.37[19]	1.92[17]
HD	-2.02 ± 0.17	0.47 ± 0.07	0.44 ± 0.11	0.30 ± 0.26	0.12 ± 0.19	0.44 ± 0.11	< 1.10	-0.17 ± 0.16	0.17 ± 0.09	0.21 ± 0.16	-0.13 ± 0.16	0.37 ± 0.22	< -0.33
103545	-2.45[9]	-0.04[9]	- -	- -	-0.26[14]	- -	- -	- -	0.17[14]	- -	- -	0.37[14]	0.65[14]
HD	-0.04 ± 0.17	0.00 ± 0.19	0.20 ± 0.11	0.12 ± 0.14	-0.26 ± 0.10	0.20 ± 0.11	< 0.50	-0.23 ± 0.13	0.30 ± 0.20	-0.20 ± 0.19	< 0.30	-0.20 ± 0.20	< 0.90
116514	-0.15[21]	- -	- -	- -	- -	- -	- -	- -	- -	- -	- -	- -	- -
TYC	-0.08 ± 0.08	-0.24 ± 0.11	0.01 ± 0.16	0.21 ± 0.15	-0.02 ± 0.11	0.14 ± 0.13	0.31 ± 0.2	0.29 ± 0.12	0.26 ± 0.14	0.26 ± 0.14	0.36 ± 0.14	0.21 ± 0.16	< 0.41
8258-1189-1	-0.14[25]	-0.05[25]	0.01[25]	- -	0.14[25]	-0.03[25]	1.37[25]	0.66[25]	0.00[25]	-0.10[25]	- -	0.09[25]	- -
TYC	-0.31 ± 0.19	0.28 ± 0.094	0.31 ± 0.16	0.71 ± 0.10	0.38 ± 0.13	0.40 ± 0.11	0.74 ± 0.18	0.98 ± 0.12	0.96 ± 0.10	0.83 ± 0.10	0.93 ± 0.11	0.38 ± 0.11	1.2 ± 0.18
2250-1047-1	-0.55[20]	0.37[20]	- -	1.07[20]	0.44[20]	0.77[20]	- -	1.17[20]	1.18[20]	0.97[20]	- -	- -	- -
HD	-0.31 ± 0.12	0.11 ± 0.21	0.08 ± 0.09	-0.14 ± 0.17	-0.24 ± 0.12	0.16 ± 0.25	< 0.46	-0.13 ± 0.2	0.26 ± 0.14	< -0.32	0.29 ± 0.25	< 0.46	- -
51273	-0.80[21]	- -	- -	- -	- -	- -	- -	- -	- -	- -	- -	- -	- -
HD	-0.35 ± 0.18	-0.51 ± 0.16	0.47 ± 0.045	-0.18 ± 0.18	-0.45 ± 0.18	-0.12 ± 0.19	0.25 ± 0.18	-0.36 ± 0.13	-0.05 ± 0.16	-0.37 ± 0.08	-0.1 ± 0.2	-0.05 ± 0.25	- -
33363	-0.05[21]	- -	- -	- -	- -	- -	- -	- -	- -	- -	- -	- -	- -
TYC	-0.51 ± 0.13	-0.02 ± 0.11	0.18 ± 0.12	0.1 ± 0.16	0.19 ± 0.16	0.53 ± 0.16	0.53 ± 0.17	1.0 ± 0.12	0.91 ± 0.13	0.93 ± 0.13	1.1 ± 0.14	0.33 ± 0.14	< 1.0
2866-338-1	- -	- -	- -	- -	- -	- -	- -	- -	- -	- -	- -	- -	- -
BD	-0.67 ± 0.13	-0.06 ± 0.16	0.44 ± 0.16	0.17 ± 0.17	-0.18 ± 0.15	0.31 ± 0.13	0.34 ± 0.18	0.04 ± 0.13	0.14 ± 0.13	0.04 ± 0.15	0.27 ± 0.13	0.34 ± 0.11	0.14 ± 0.14
-19 3868	-0.63[26]	- -	0.27[26]	- -	- -	- -	- -	- -	- -	- -	- -	- -	- -
HD	-0.90 ± 0.18	0.72 ± 0.16	-0.05 ± 0.22	0.63 ± 0.12	0.53 ± 0.14	< 0.66	< 0.73	0.76 ± 0.22	0.96 ± 0.26	0.88 ± 0.2	< 1.1	< 0.93	- -
276679	- -	- -	- -	- -	- -	- -	- -	- -	- -	- -	- -	- -	- -
BD	-0.11 ± 0.07	-0.1 ± 0.094	0.2 ± 0.11	0.13 ± 0.16	0.25 ± 0.19	0.35 ± 0.16	0.4 ± 0.18	0.35 ± 0.13	0.58 ± 0.17	0.4 ± 0.16	0.6 ± 0.2	0.55 ± 0.11	0.7 ± nan
-07 3076	- -	- -	- -	- -	- -	- -	- -	- -	- -	- -	- -	- -	- -

References: (1)Karinkuzhi et al. (2018), (2)Jorissen et al. (2019), (3)Jofré et al. (2015), (4)Cristallo et al. (2016), (5)Karinkuzhi and Goswami (2015), (6)Placco et al. (2014b), (7)Suda et al. (2011), (8)Soto and Jenkins (2018), (9)Simmerer et al. (2004), (10)Purandardas et al. (2019), (11)Pereira and Junqueira (2003), (12)Luck (2018), (13)Delgado Mena et al. (2017), (14)Roederer et al. (2010), (15)Yoon et al. (2016), (16)Goswami and Aoki (2010), (17)Bisterzo et al. (2011), (18)Zamora et al. (2009), (19)Ishigaki et al. (2013), (20)Karinkuzhi et al. (2021b), (21)Gaia Collaboration (2022), (22)Hollek et al. (2015), (23)Hansen et al. (2016a), (24)Pereira et al. (2012), (25)Buder et al. (2021), (26)Steinmetz et al. (2020b)

is first determined from the 5156 Å Swan band, and this is then used while deriving the La abundance. The blue line is set with an absolute abundance of $\log \epsilon_{La} = -5$ for effectively no La contribution to provide a baseline. The green line is the best fit for La, with $\log \epsilon_{La} = 0.45$. This corresponds to a [La/Fe] ratio of 1.30 at a metallicity of [Fe/H] ≈ -1.90, which we find compatible with the heavy element abundances found by Hansen et al. (2016a) considering differences in atmospheric parameters.

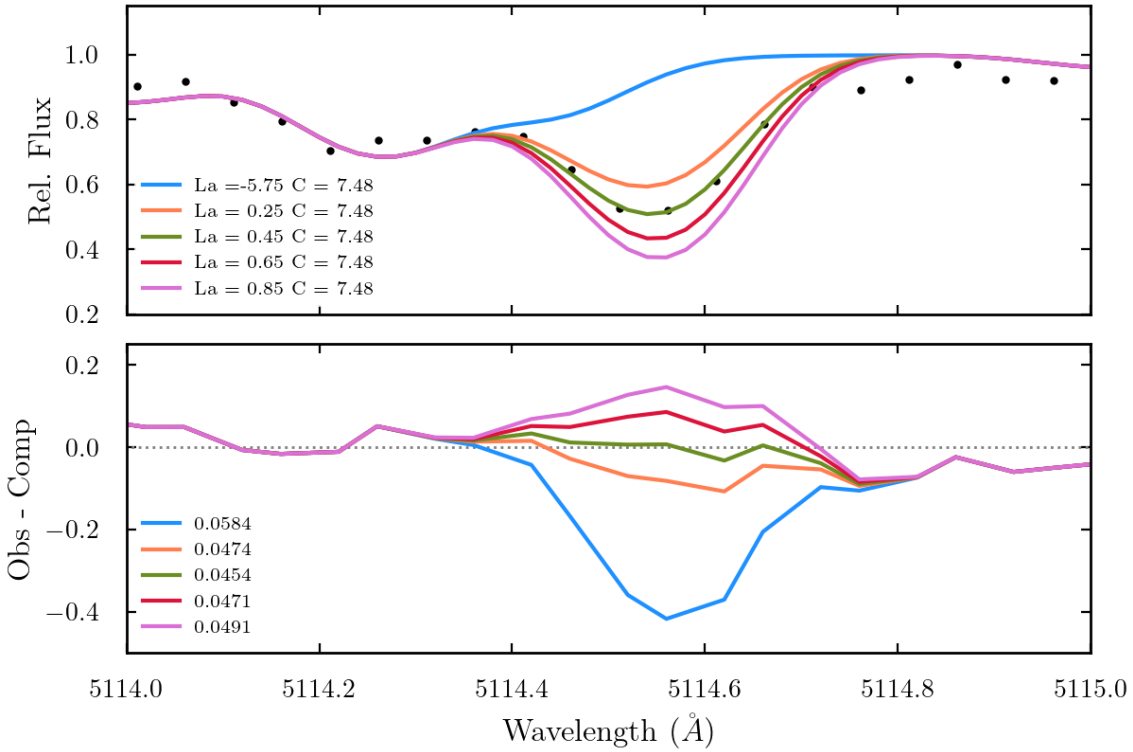

Figure 2.5: Top Panel: Synthetic fits to a C and La blend at 5114.5 Å in the CEMP-s star HE 0414-0343, varying the abundance of La. Bottom Panel: Residuals between the synthetic spectral fits and the observed data points, and relative goodness-of-fit values for the spectral region. Adapted from Dimoff et al. (2024).

Abundances as functions of metallicity for our sample are plotted in Figure 2.6, where red circles are carbon-enhanced (CEMP-s/-no, CH) stars, blue squares are known Ba stars, and green x's are "other" stars, yet unclassified by their heavy metal content or carbon enrichment.

Abundance patterns for our sample are displayed in Figure 2.7. Stars are cate-

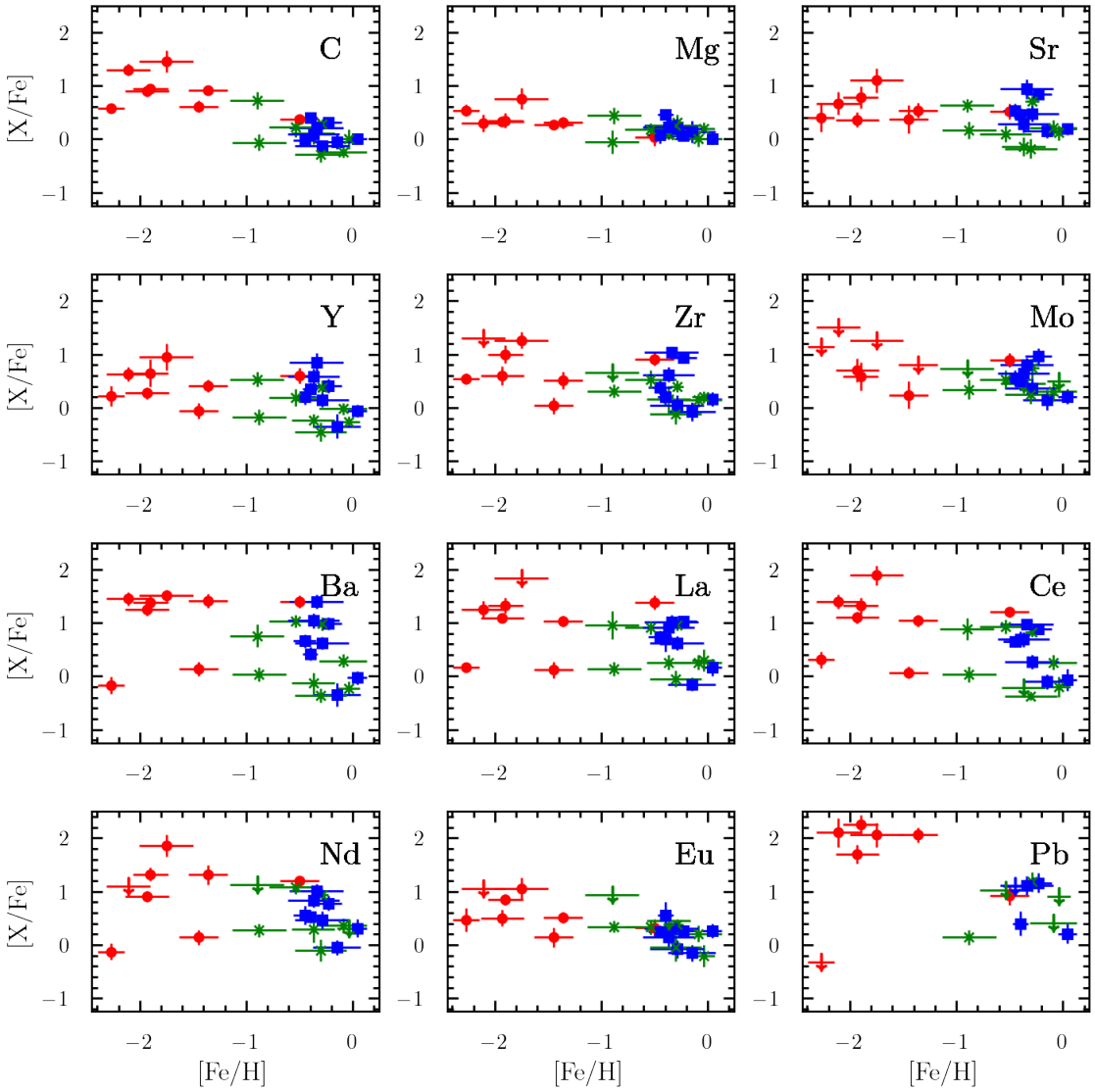

Figure 2.6: Abundances for our sample of stars by element. Blue squares are Ba stars, red circles are carbon-enhanced (CEMP-s/-no or CH) stars, and green x's are "other" or unclassified stars. Inverted arrows are upper limits on the abundance of [X/Fe]. From Dimoff et al. (2024).

gorized by class: carbon-enhanced stars in the top panel, Ba stars in second panel, "other" stars in the third panel, and AGB stars in the bottom panel. We improve upon the patterns of all stars in our sample by adding elements. Stars that are candidates based on their carbon and heavy element enhancements are HD 116514, TYC 2250-1047-1, HD 51273, HD 276679, TYC 2866-338-1, and TYC 9244-8667-1,

but these stars have not yet been fully classified. On average, we extend existing abundance patterns by about 50%. Stars in the third panel

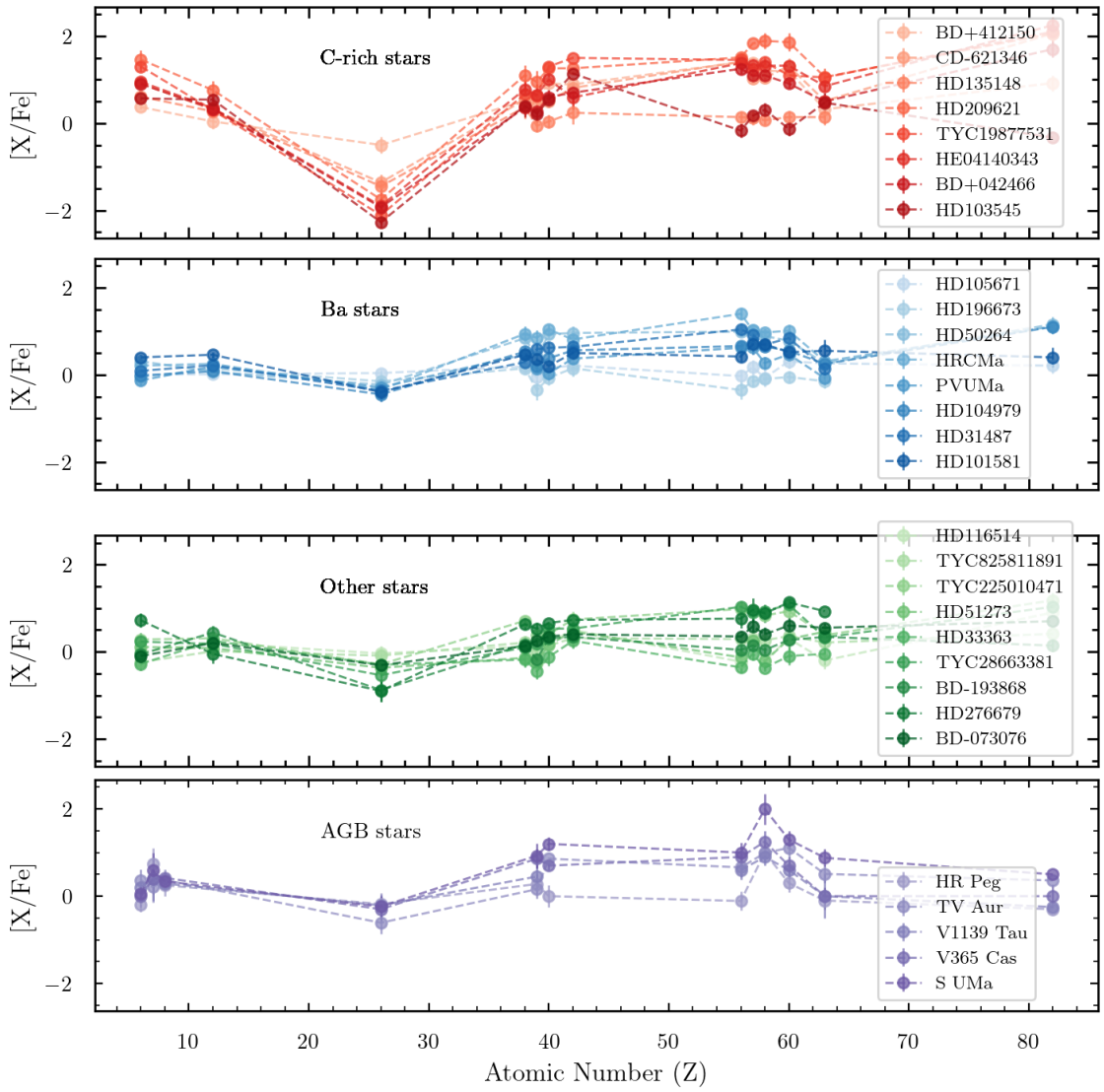

Figure 2.7: Abundance patterns for our sample of stars by stellar classification; carbon enhanced stars, Ba stars, "other" stars, and AGB stars. There is minor spread in metallicity within each population. Adapted from Dimoff et al. (2024)

Carbon: We derive the carbon abundance in our stars from synthetic spectrum analysis of the C_2 swan band at 5165 Å and the CH band at 4308 Å. The steep

change in flux and the sensitivity of the C_2 band makes it a robust feature to precisely determine the C abundance in our high-resolution spectral data, and the CH band provides a verification to the carbon abundance from the C_2 band. By selection bias in our sample of metal-poor stars, we see large enhancements in C at lower metallicities. For eight stars in our sample (CD-62 1346, HD 135148, HD 209621, TYC 1987-753-1, HE 0141-0343, BD+04 2466, HD 276679, and HD 103545) we observe large enhancements in [C/Fe] $\geq +0.5$ dex. Many other features in the spectra are blended with molecular carbon lines, and understanding the carbon content ensures our other computed abundances are robust.

Nitrogen: For only the AGB stars, we used spectral synthesis on a large region in the red part of the spectrum, between 8000 and 8100 Å. With less absorption in this region, and fitting TiO and ZrO band features, we roughly constrain the N abundances. This is helpful in computing other abundances that are blended with CN features, and is useful in determining the evolutionary state of the AGB star. Despite large uncertainties, we find relatively consistent N abundances, typically higher than the derived C abundance in our AGB stars. The abundance of N can also be important for computing the O abundance.

Oxygen: Deriving the O abundance using unblended spectral features or spectral synthesis proved difficult due to large amounts of molecular absorption in our spectra, and the degeneracy with Ti and Zr abundances. We compare our synthesis estimates by scaling the oxygen abundance to the metallicity and the N abundance [N/Fe] $- 0.4$ [Fe/H] $\approx$ [O/Fe]. The C/O ratio in our stars allows the determination of age, as AGB stars produce more oxygen later in their evolution.

Magnesium: Abundances of Mg are computed by measuring the equivalent widths of the Mg lines at 5528 and 5711 Å. These lines are weaker than the Mg b lines and remain unsaturated. The 5711 Å line is very weak and, in cases where [Mg/Fe] $\sim$ 0.0 may be indistinguishable from the continuum, even at higher metallicities. For our sub-sample of stars, we find [Mg/Fe] values close to the solar value at high metallicities ([Fe/H] $>$ -1) with some expected scatter. At lower metallicities, our results are in agreement with Buder et al. (2019), following a flat α-enhancement trend with some scatter.

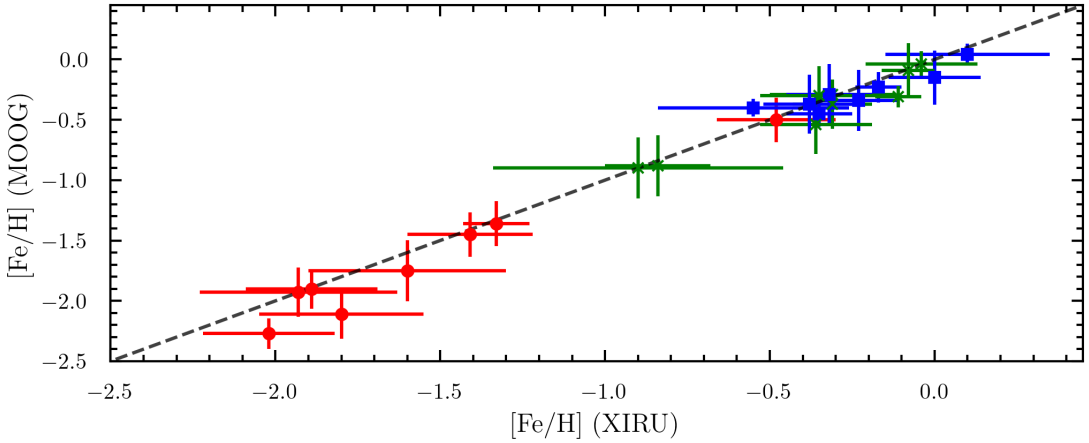

Figure 2.8: Comparison of [Fe/H] abundances between ionization and excitation balance from Xiru and spectral synthesis abundances using MOOG. There is good agreement between Xiru and MOOG, with only two metal-poor stars slightly outlying from the one-to-one trend. From Dimoff et al. (2024).

Iron: We determined spectroscopic iron abundances using the equivalent widths of Fe I and II lines determined by ARES and verified with Xiru and ATHOS. In determining the atmospheric parameters, Xiru computes a metallicity from the Fe features. We also compute Fe abundances using spectral synthesis in the region between 5180 and 5250 Å, where many Fe I and II features exist. We compare the values from Xiru and MOOG synthesis in Figure 2.8. Xiru metallicity estimates in our abundance sample are in close agreement to the determined spectroscopic value. Lines of Fe I and Fe II should display the same abundance in the stellar spectrum; if the temperature or surface gravity is not well constrained, there may be a disagreement between the abundances in the two ionization states of iron. This effect is minimized when using ionization balance, for example in Xiru. While discrepancies in Fe I and II could be due to NLTE effects in some of the lines, particularly at lower metallicities, this provides another check on the estimates of $T_{\rm eff}$ and $\log(g)$ from Xiru.

s-Process: Abundances of light s-process elements all follow a similar trend in Figure 2.6. We observe a tight grouping in the [Mo/Fe] abundance in our abundance sub-sample, with [Mo/Fe] generally between 0 and +1.0 dex. Abundances of the

heavy s-process elements Ba, La, Ce, and Nd exhibit more scatter in the metal-poor regime [Fe/H] ≤ -1.0 (François et al., 2007; Hansen et al., 2012b, 2014). There is visible scatter in the s-process element abundances in our sample, indicating different enrichment pathways in some of our targets. Two of the carbon-enhanced stars (red data points in the figure) are CEMP-no stars, and do not exhibit significant s-process enhancement.

The [Pb/Fe] space is more sparsely filled compared to other elements, where not all of our stars had Pb detections. The Pb line at 4057 Å is blended with C and Mg features, and is easily washed out at lower SNR. For some of our metal-poor stars and Ba stars, we observed large enhancements with [Pb/Fe] > 1, a key signature of the strong s-process in AGB stars. We observed one star HD 103545 with a low Pb abundance, and note that this star is a CEMP-no star.

The abundances of Sr, Y, Zr, La, and Eu have been previously derived for a large part of our sub-sample, and we find our results in general agreement with the literature. Some stars show large enhancements in s-process elements and are likely to have been enriched by an AGB companion, where some have lower enhancements and are likely to have been enriched by the parent molecular cloud.

Table 2.6 displays the metallicity, carbon enrichment, and relative s-process enhancement for our abundance sample, organized by nucleosynthetic classification (Ba, C-rich, unknown), and ordered by decreasing metallicity. Contributions from light ([ls], $\langle \mathrm{Sr, Y, Zr, Mo} \rangle$) and heavy ([hs], $\langle \mathrm{Ba, La, Ce, Nd} \rangle$) s-process enrichment, and the ratio of heavy-to-light s-process ([hs/ls]) elements, are shown. Stars with positive [hs/ls] are likely to have received this material from an AGB companion.

Europium: Computed abundances of the canonically r-process-produced element Eu in Figure 2.6 show a general trend with little scatter, suggesting a more singular enrichment channel for r-process material in our stars that are predominantly s-process enriched. Since this is the case, we assert that our Mo enhancements are mainly from the s-process and not the r-process. Lower metallicity stars show [Eu/Fe] abundances typical of r-I type stars.

Uncertainties in our abundances vary slightly between spectral features and, on average, the atmospheric parameters contribute an uncertainty of 0.15. With the average statistical uncertainty in our lines of 0.10, we arrive at a combined average uncertainty of $\langle \sigma \rangle = 0.25$.

Sensitivity Study

We perform a sensitivity study to determine the relative change in the abundance for a small change in each of the atmospheric parameters. We vary the stellar temperature by ±200 K, the surface gravity by ±0.3 dex, the metallicity by ±0.3 dex, and the microturbulence by ± 0.2 dex to determine the effect changing each of the parameters has on the abundance.

For example, $\partial \log \epsilon / \partial \xi$: varying the microturbulence ξ by ±0.2 km/s alters the abundances of Sr, Ba, and La by ≤ 0.05 dex, and in specific cases (e.g. strong lines or low surface temperatures) up to a maximum of 0.1 dex. We find this acceptable, as it is within the combined uncertainties in our abundance computations, and assume similar variations from the microturbulence in other elements.

If the abundances of different ionization states of iron are not compatible within the spectra (i.e. > 0.3 dex separation), this may be indicative of NLTE effects in some of the lines, or a poorly fit atmospheric model. Broadening of spectral lines due to stellar rotation hinders the derivaiton of accurate abundances of weak lines. Spectral features will be blended together which removes finer details, even at high resolution. We find rotation becomes an issue with rotational velocities $v \sin i \geq 15$ km/s. If the rotation velocity is not known, we visually inspect the spectrum for rotational broadening effects. To this end, we chose stars for our abundance sample that have low rotation velocities.

2.7.3 Orbital Parameters

A list of input parameters is presented in Table 2.7 in the second line for each star. Combining our computed heliocentric RVs with available literature data, we optimized binary orbits to estimate orbital and physical parameters of the star systems. Measured RVs from our observations are electronically available on Zenodo[4]. We add low-error data points to existing stellar RV curves with our high-resolution snapshot spectra, with a typical improvement on the order of a factor of 5 compared to previous RV uncertainties.

Systems enriched by a previous AGB companion may have long orbital periods and are old enough such that the AGB has faded to a white dwarf, providing time

[4] `https://zenodo.org/communities/chetec-infra-wp6/records?q=&l=list&p=1&s=10&sort=newest`

Table 2.6: Ratios of s-process elements for each star in our abundance sub-sample, organized by increasing metallicity. Total s-process [s/Fe], light s-process ('ls' $\langle \mathrm{Sr, Y, Zr, Mo} \rangle$) and heavy s-process ('hs' $\langle \mathrm{Ba, La, Ce, Nd} \rangle$) enrichment are compared. Units are expressed in [dex] compared to the Sun. From Dimoff et al. (2024).

Star	[Fe/H]	[C/Fe]	[s/Fe]	[ls]	[hs]	[hs/ls]
HD105671	0.10	0.01	0.12	0.13	0.09	-0.03
HD196673	0.00	-0.05	-0.10	-0.03	-0.16	-0.13
HD50264	-0.17	0.31	0.89	0.79	0.92	0.14
HRCMa	-0.23	0.21	1.02	0.91	1.10	0.19
PVUMa	-0.32	-0.13	0.37	0.25	0.49	0.24
HD104979	-0.35	-0.02	0.60	0.42	0.65	0.23
HD31487	-0.38	0.09	0.70	0.54	0.87	0.34
HD101581	-0.55	0.40	0.47	0.38	0.59	0.21
BD+412150	-0.48	0.37	1.00	0.73	1.29	0.56
CD-621346	-1.35	0.91	1.01	0.57	1.20	0.63
HD135148	-1.41	0.61	0.13	0.15	0.12	-0.03
HD209621	-1.60	1.46	1.55	1.19	1.77	0.58
TYC19877531	-1.80	1.30	1.27	1.03	1.30	0.28
HE04140343	-1.89	0.95	1.18	0.76	1.34	0.58
BD+042466	-1.93	0.90	0.89	0.48	1.09	0.60
HD103545	-2.02	0.57	0.24	0.57	0.04	-0.53
HD116514	-0.04	0.00	0.18	0.14	0.04	-0.10
TYC825811891	-0.08	-0.24	0.25	0.16	0.29	0.13
TYC225010471	-0.31	0.28	0.79	0.56	0.93	0.37
HD51273	-0.31	0.11	0.06	0.06	0.05	-0.01
HD33363	-0.35	-0.38	-0.17	-0.13	-0.22	-0.09
TYC28663381	-0.36	-0.02	0.70	0.34	0.99	0.65
BD-193868	-0.67	-0.06	0.14	0.16	0.12	-0.04
HD276679	-0.90	0.72	0.79	0.64	0.93	0.30

for orbital circularization. Most of our binary systems with abundance patterns indicative of AGB mass transfer have low eccentricity orbits, and the orbital periods vary from a few hundred days to a few thousand days. Figure 2.9 displays phase-folded RV curves for selected systems CD-62 1346, HD 50264, HR Peg, and HD 31732. For the CEMP-s star CD-62 1346, we added eight data points to the RV curve and refined orbital parameters. Notably, we modeled the orbit of the long period binary CD-62 1346 for the first time, with our data in good agreement

Table 2.7: Orbital parameters and estimated stellar masses, where sufficient data exists, from model orbits derived using ELC. Uncertainties in the parameters are taken from the widths of the posterior distributions after MCMC optimization. For each star, the first line is the results of our analysis and the second line is the data from the literature.

Star	# Obs. # Lit.	ω [°]	e	P (d)	k_1 [km/s]	T_0 [BJD-2400000]	$a \sin i$ [10^9m]	$f(m)$ [$M_\odot$]	M_1 [$M_\odot$]	M_2 [$M_\odot$]	Ref.
HD 105671	1	244.46 ±	0.138 ± 0.050	817.60 ± 95.75	0.75	60605.361 ± 284.127	111.94	3.2e-5	5.33 ± 0.75	0.34 ± 0.25	
	6	- -	- -	- -	- -	- -	- -	- -	7.40	- -	(6,7)
CD-62 1346	6	184.50 ± 4.16	0.137 ± 0.105	30928.29 ± 5515.11	4.16	59933.235 ± 16.78	70.76	3.9e-4	2.283 ± 1.61	0.98 ± 0.38	
	12	- -	- -	- -	- -	- -	- -	- -	- -	- -	- -
HD 50264	5	249.25 ± 8.37	0.011 ± 0.006	912.40 ± 0.38	9.52	49579.283 ± 20.442	271.76	0.069	1.25 ± 0.89	0.66 ± 0.32	
	11	230	0.091	909.90	9.52	49541	- -	- -	0.90	0.60	(6)
HD 196673	1	116.19 ± 1.49	0.589 ± 0.016	7784.88 ± 75.12	3.58	51697.923 ± 77.760	1823.0	0.019	5.08 ± 0.32	1.05 ± 0.04	
	79	116	0.590	7780.00	3.70	51698	314.0	0.020	5.00	1.10	(4,6)
HD 104979	2	164.34 ± 9.59	0.075 ± 0.022	18189.37 ± 621.76	1.65	60297.864 ± 149.790	1466.92	0.008	2.99 ± 0.65	1.10 ± 0.34	
	128	- -	0.080	19295.02	- -	- -	- -	- -	2.70	0.75	(6)
HR CMa	6	180.80*	0.055 ± 0.020	457.32*	6.79	47357.722 ± 55.167	180.13	0.014	1.87 ± 0.95	0.60 ± 0.15	
	38	- -	0.013	457.40	- -	- -	- -	0.035	2.10	0.75	(5,6,10)
PV UMa	3	22.69 ± 2.10	0.110 ± 0.004	80.52 ± 0.001	8.48	55155.728 ± 0.061	32.48	0.005	2.20 ± 0.64	1.01 ± 0.10	
	140	- -	0.090	80.00	- -	- -	- -	0.005	3.90	0.94	(6,8,9)
HD 31487	1	246.02 ± 60.45	0.049 ± 0.008	1086.80 ± 72.23	7.86	49432.182 ± 123.928	255.57	0.060	1.95 ± 0.98	0.73 ± 0.33	
	36	238	0.050	1066.40	7.00	45173	- -	0.038	3.40	1.59	(4,5)
BD+41 2150	3	358.86 ± 1.60	0.057 ± 0.001	306.82 ± 2.04	10.78	56323.099 ± 1.822	187.69	0.040	1.69 ± 0.94	0.88 ± 0.31	
	70	315	0.055	323.0	11.80	56114	- -	- -	1.27	- -	(8,12,13,14,15)
HD 135148	11	261.04 ± 18.45	0.114 ± 0.020	1405.19 ± 2.78	4.87	47477.107 ± 67.530	496.36	0.016	2.72 ± 1.73	0.72 ± 0.35	
	36	273	0.123	1416	4.79	47534	- -	- -	0.80	0.26	(1)
HD 209621	1	15.66 ± 10.55	0.005 ± 0.005	407.81 ± 0.42	11.98	45877.766 ± 15.605	247.32	0.072	2.30 ± 1.10	1.15 ± 0.24	
	27	- -	0.000	407.4	12.05	45858	- -	- -	3.60	- -	(4,8,11,12,13)
BD+04 2466	2	319.91 ± 2.23	0.166 ± 0.022	4762.26 ± 20.12	5.53	59908.329 ± 12.918	1131.9	0.080	2.40 ± 1.20	1.18 ± 0.21	
	42	- -	- -	4600	- -	- -	- -	- -	- -	1.10	(11,16)

References: (1)Carney et al. (2003) (2)Eker et al. (2008) (3)Fekel and Eitter (1989) (4)McClure and Woodsworth (1990) (5)Van der Swaelmen et al. (2017) (6)Jorissen et al. (2019) (7)Delgado Mena et al. (2019) (8)Escorza et al. (2017) (9)Katoh et al. (2013) (10)Udry et al. (1998) (11)Bisterzo et al. (2011) (12)Jorissen et al. (2016) (13)Escorza et al. (2020) (14)Platais et al. (2003) (15)Sperauskas et al. (2016) (16)Abate et al. (2015a) (17)Fekel et al. (1999) (18)Griffin and Beggs (1991)

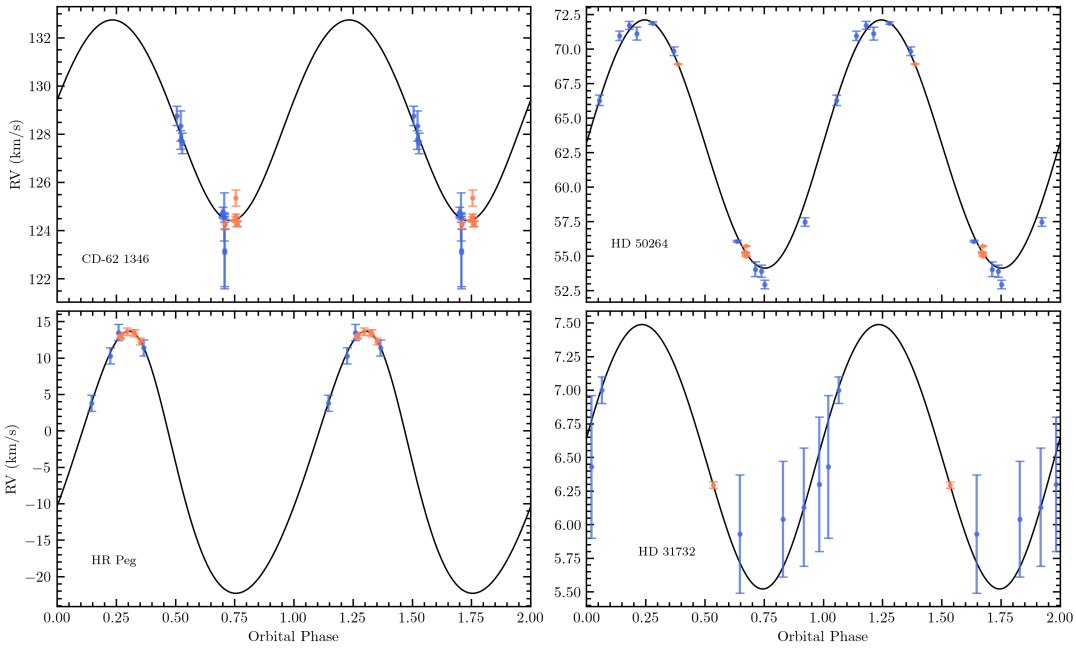

Figure 2.9: Phase-folded RV curves for the post-accretion binaries CD-62 1346, HD 50264, HR Peg, and HD 31732. We use available literature RV data (blue) in conjunction with our own observations (orange). These four stars have few literature data points, and with our provide enough data to characterize their orbits and constrain component masses. Adapted from Dimoff et al. (2024).

with the existing literature data from CORrelation-RAdial-VELocities instrument (CORAVEL)Baranne et al. (1979) and South African Large Telescope High Resolution Spectrograph (SALT-HRS) Tyas (2012).

The individual masses and the mass ratio are key outputs of our study, along with the standard binary orbital parameters. A sub-sample of orbital and physical parameters from ELC are presented in Table 2.7. The # Obs. column is the number of data points added to each system from our RV observations, and the # Lit. column is the number of literature data points used in the orbital analysis. Individual component masses are approximated and are included in the table where available. We note that our masses are dependent on the assumption of the orbital inclination, and we observe large scatter across the subset. In HR CMa, the parameters with an asterisk are fixed values for the best fitting model. Here, M_1 refers to the visible component, and M_2 refers to the companion, typically a white dwarf.

2.8 Discussion

2.8.1 Abundances

Across the sub-sample, our computed abundances generally agree with the literature within combined uncertainties, and larger differences arise from scaling of the metallicity. At higher metallicities, with [Fe/H] > -0.5, some of our derived abundances do not agree with the literature. This may be due to NLTE effects, particularly in the AGB stars, differences in model atmosphere parameters, or higher spectral resolution Placco et al. (2014a).

In Figure 2.10, we compare our stellar abundance distributions to one another and investigate correlations in abundance space. We eliminate metallicity dependencies by using the abundance compared to hydrogen, [X/H]. Tight relations with a slope of one indicate co-production of the elements; scatter in these relations or deviation from the slope-one line is indicative of multiple nucleosynthetic production pathways. We observe general correlations in all panels of Figure 2.10. We expect tight relations within the light- and heavy s-process element groups (e.g., Y and Sr, or Ba and La), and between both light- and heavy s-elements. A corner plot of the derived s-process abundances is shown in Figure 2.11. We attempted to apply machine learning techniques and perform Gaussian mixture modeling on our sample of stars to distinguish between groups in abundance space. However, we found that with only 25 data points we lack the statistical depth required for this analysis.

We find scatter in the relations when comparing s-process element Ce with the r-process element Eu in Figure 2.10, as Ce is produced $\approx 80\%$ by the s-process. Similar scatter exists in the Eu-Nd panel, indicating the multiple formation pathways of Nd ($\approx 50\%$ s versus $\approx 50\%$ r), with Eu being produced $\approx 94\%$ by the r-process.

The average of our Mo distribution ($\langle$[Mo/Fe]$\rangle = 0.57$) is between that of the heavy s-elements ($\langle$[hs]$\rangle = 0.66$) and the light s-elements ($\langle$[ls]$\rangle = 0.45$). We find correlations between Mo and Zr, and Mo and La; one each of the light and heavy s-process elements, although there is scatter with higher Mo / Zr / La abundances, and with decreasing metallicity. This suggests that, at lower metallicities, Mo is produced by multiple channels. Pignatari et al. (2013) investigated the impact of ^{12}C fusion in massive stars and its effect on the production of Mo. Hansen et al. (2014) investigated the production of Mo in a sample of 52 stars and found

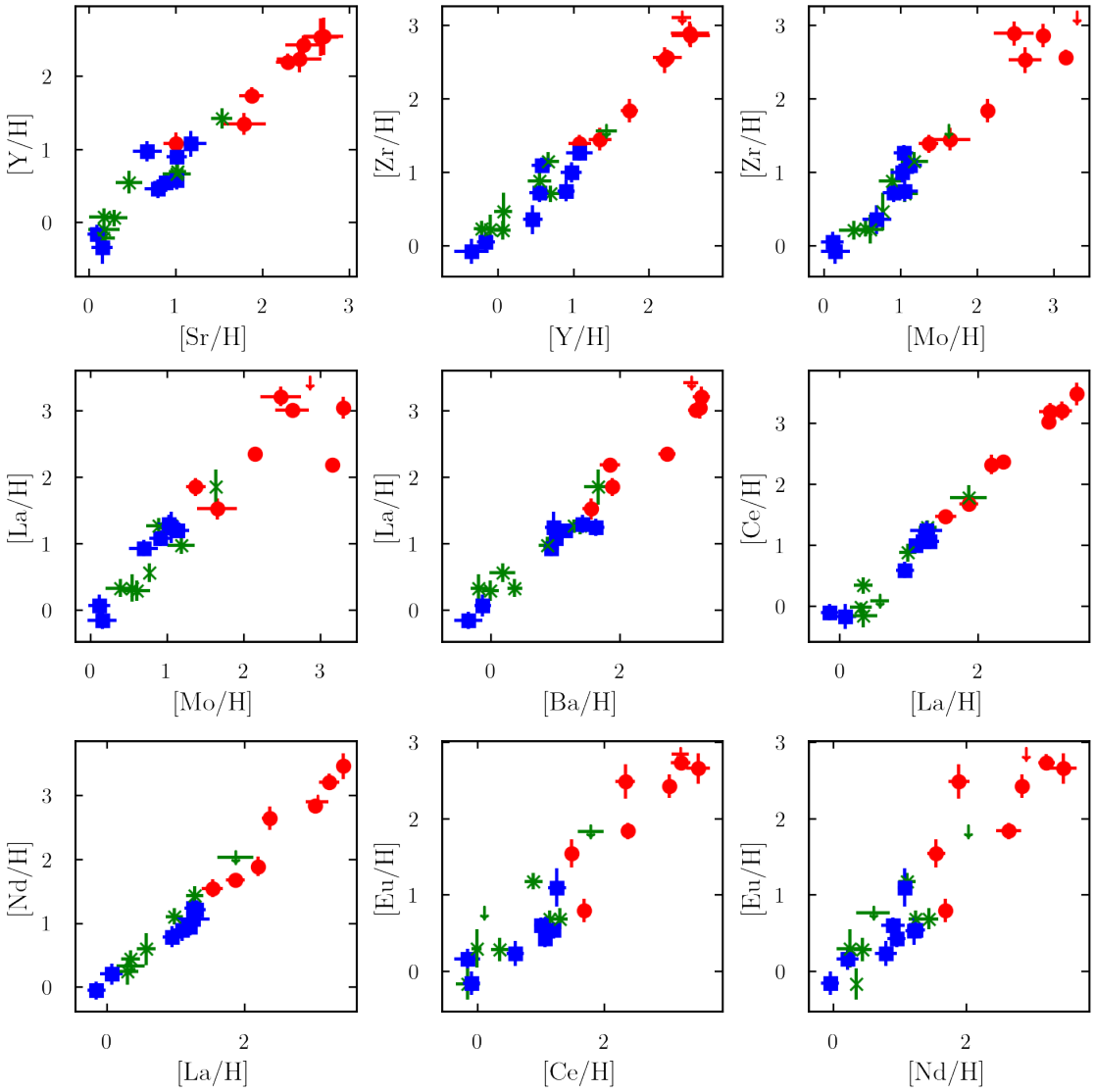

Figure 2.10: Elemental comparison between light- and heavy s-process elements. We compare [X/H] values to remove metallicity dependent biases in the abundances. We observe general correlations in all shown comparisons, with trends between s-process elements following tight correlations (Dimoff et al., 2024).

multiple pathways to increased Mo abundances. Both groups found that Mo is highly convolved with other elements and receives contributions from both the s- and r-processes. At higher [Fe/H], Mo may be produced by the p-process and, at lower metallicities, from the early weak s-process in massive stars. We find tighter

correlations between Mo and light s-elements, and more scatter when comparing with heavy s-elements.

de Castro et al. (2016) provides a definition of a Ba star as [s/Fe] $> +0.25$ and [Fe/H] > -1, based on high-resolution spectra. For simplicity, we adopt this same definition. We confirm the large s-process enhancements and Ba-star nature of TYC 2250-1074-1, and we add the stars TYC 8258-1189-1 and TYC 2866-338-1 to this category. We suggest HD 276679 is a CH type star with large enhancements in carbon ([C/Fe] = 0.72) and s-process elements ([s/Fe] = 0.79).

2.8.2 AGB Stars

Circumstellar dust provides a source of intrinsic reddening, in addition to typical ISM reddening. Dust disks are more prominent around highly variable S-stars with higher mass-loss rates. We limit our sample to intrinsic S-stars with low levels of variability. Oxygen-rich dust contributes to reddening through the relation $A_\lambda = -1.086\tau_\lambda$.

In Tc-rich stars, IR excess from dust grains is observed in the literature. The level of IR dust excess increases with decreasing temperature. Lower temperatures will result in more dust condensation in the upper atmosphere, indicating a more evolved star. This is observed in the C/O ratio, where lower temperatures correlate with lower C/O ratios, and is often used as an indicator for AGB evolution. There is also a known correlation with decreasing temperatures and s-process enrichment, but in our small sample we do not observe this trend.

2.8.3 Comparison to Models: the FRUITY models

The FUll-Network Repository of Updated Isotopic Tables & Yields (FRUITY) models (Straniero et al., 2006; Cristallo et al., 2011; Domínguez et al., 2011; Cristallo et al., 2015) provide updated s-process element yields from AGB stars at different masses and metallicities. These models are useful for predicting s-process abundance patterns in AGB stars and their polluted binary companions, in turn determining neutron source efficiency, comparing observed physical parameters, and comparing stellar abundances to theoretical yields.

We compare our abundance measurements to the FRUITY yields to investigate

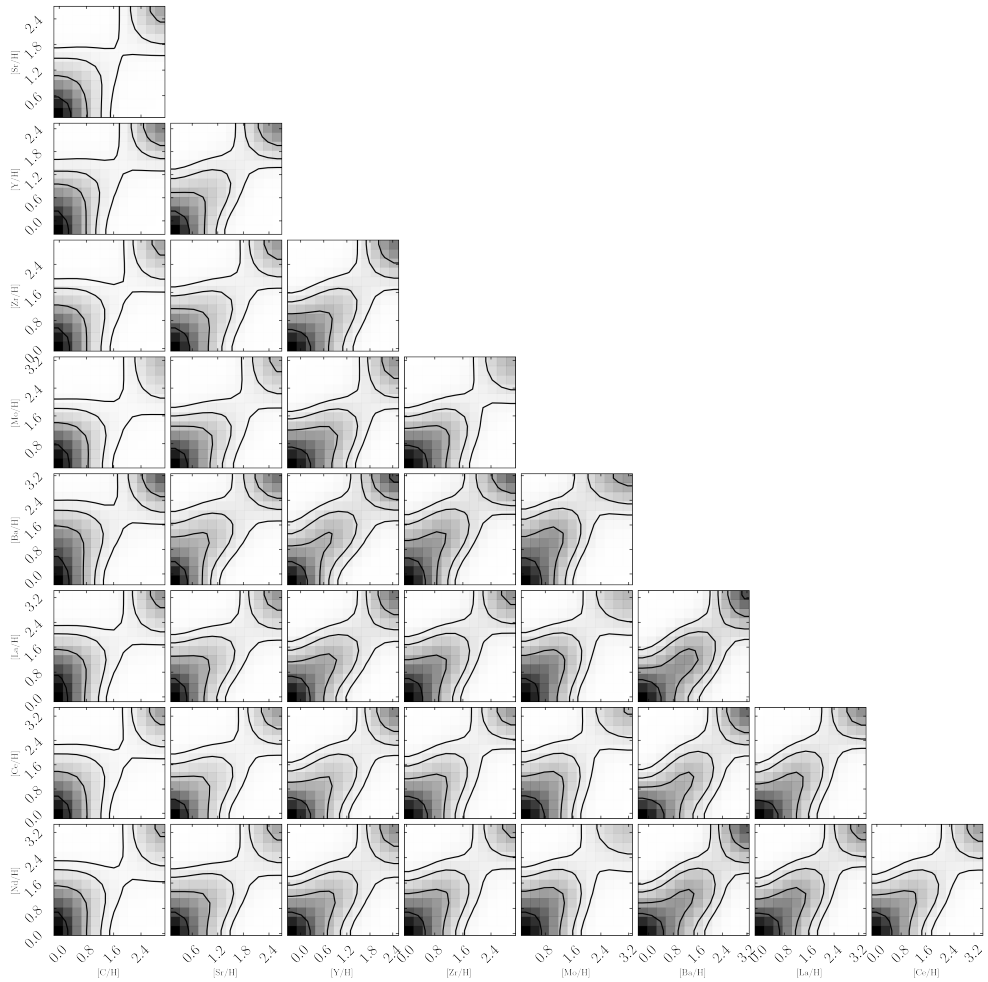

Figure 2.11: Corner plot of s-process elements in our sample. We observe correlations between s-process elements within the light s-process elements and the heavy s-process elements. Dimoff et al. (2024)

the origins of our observed abundance patterns. The FRUITY database contains around 120 models that range in initial mass from 1.3 - 6.0 $M_{\odot}$, metallicities from $Z = 2 \times 10^{-5}$ to 0.03 ([Fe/H] = -3.33 to 0.33), and initial rotational velocities of 0, 10, and 30 km/s. FRUITY allows for the free creation of the ^{13}C pocket by parameterization of physical mixing processes through the thermal pulses.

Since the FRUITY models simulate AGB surface abundances, this material is

diluted upon accretion onto a binary companion through convective and thermohaline mixing processes. We approximate the mixing of the stellar abundances and FRUITY abundances using a prescription identical to den Hartogh et al. (2023). The material accreted onto the stellar surface is diluted such that

$$\left[\frac{\mathrm{X}}{\mathrm{Fe}}\right] = \log_{10}\left[(1-\delta) \times 10^{[\mathrm{X/Fe}]_{\mathrm{ini}}} + \delta \times 10^{[\mathrm{X/Fe}]_{\mathrm{AGB}}}\right], \tag{2.12}$$

where $[\mathrm{X/Fe}]_{\mathrm{ini}}$ is the initial abundance of element X, $[\mathrm{X/Fe}]_{\mathrm{AGB}}$ is the final surface abundance of the AGB model, and δ is the dilution factor. Higher dilution factors imply the observed stellar envelope is less mixed, and signatures of AGB material are more visible. A dilution factor of zero (0) results in a flat abundance profile, and no indication of heavy element enhancement from an AGB star.

We determine the model to best fit our observed stellar abundances using a least-squared fitting method by comparing the abundances measured in our sample to those produced by the model AGB stars within a range of masses, metallicities, initial rotation rates, ^{13}C pocket formation, and dilution factors. For each star, the abundance pattern and best fit model are displayed in Figure 2.12, organized by chemical composition and decreasing metallicity, with the most metal-rich stars in each group at the top of the plot. Colors in Figure 2.12 correspond to to stellar classification, following other figures in this work.

For most of the Ba, CH, and CEMP-s stars in our abundance sub-sample, we find good fits to the FRUITY AGB yield models with s-process signatures, visible in the two (or three) peaks around Sr and Ba (and Pb where available). The weak Ba stars HD 105671 and HD 196673 show less pronounced peaks around Sr and Ba. The CEMP-no stars HD 135148 and HD 103545 show flat abundance patterns with an AGB mass of $M_{\mathrm{AGB}} = 6.0$, indicating that these stars have not been enriched by the s-process from a reasonable AGB companion. Some of our stars are metal-poor, where chemical enrichment processes at low metallicities may operate differently than those that produced the solar abundance pattern. Contributions from the nucleosynthetic i-process may explain discrepancies in these patterns.

The amount of material transferred from an AGB star depends on the orbital separation, where wide binaries will have low mass transfer efficiencies, and close binaries will likely experience higher mass transfer efficiency through Roche-Lobe overflow (RLOF).

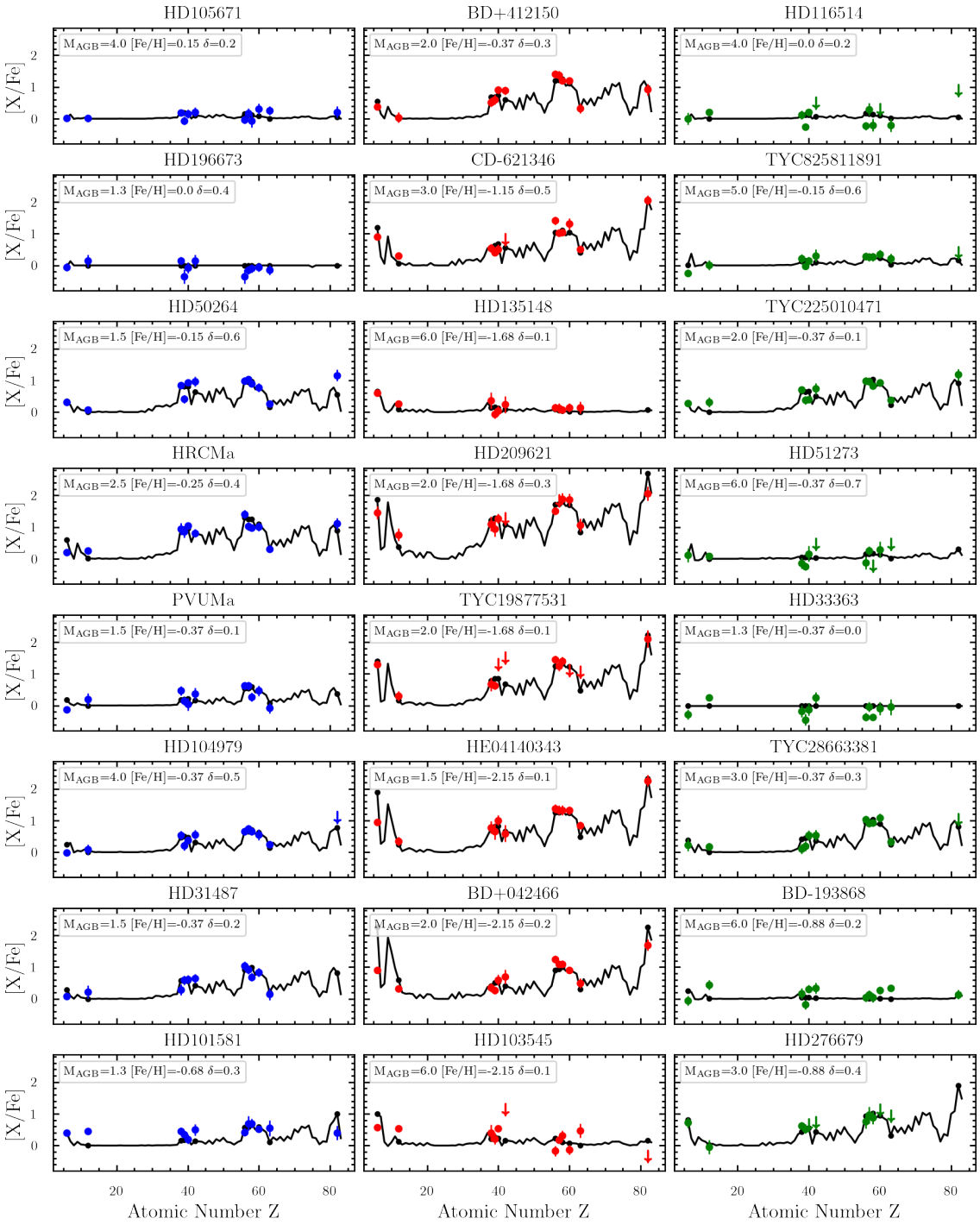

Figure 2.12: FRUITY models compared to computed abundances for our high-quality abundance sample, organized by decreasing metallicity. Blue data points correspond to Ba stars, red to C-enriched stars, and green to "other" stars. Inverted triangles in the plots are upper limits from our abundance computations. FRUITY model data is shown in black (Dimoff et al., 2024).

While we have focused this study on s-process signatures of low mass AGB stars, the s-process also occurs in rapidly-rotating massive stars (Frischknecht et al., 2012). Rotation rates required to induce internal mixing and the weak s-process in these massive stars are on the order of half of the critical rotation velocity. These massive stars may have polluted the ISM in regions of the galaxy where some of our stars have formed, which could explain why some of our stars show only mild enhancements in [s/Fe] and do not fit well to FRUITY yields.

2.8.4 RV Variability

To characterize binary orbits of stars in our sample, we use the ELC program to model systems with sufficient RV data. Generally, six to eight data points are sufficient if they are well spread across the orbit. Collected RV data is of good quality, with an average precision of $\sim$ 0.5 km/s for the ChETEC-INFRA TNA instruments, and $\sim$ 0.05 km/s for FIES and FEROS.

Our measured RVs are in good agreement with literature data, and systematic offsets have been corrected using observations of RV standard stars and making the heliocentric correction. Velocity variability for known binaries is within the expected ranges, giving confidence in observed variability in binary candidates. Computed mass functions $f(m)$ in Table 2.7 are sensible, and in good agreement with corresponding literature values.

The stars TYC 8258-1189-1, TYC 2250-1047-1, TYC 2866-338-1, HD 276679, and the CEMP-s star TYC 1987-753-1 show promising abundance patterns (Figure 2.7) for s-process enrichment from an AGB companion but, with only a few time-series data points, they do not show appreciable RV variability. We have scheduled follow up observations to characterize the binarity of these targets. We do not detect appreciable radial velocity variation in the CEMP-no star HD 103545 or in the mild Ba star HD 101581.

We find that stars with sufficient RV data in our abundance sub-sample generally have lower eccentricities ≤ 0.15. This is expected for older systems, where they have had enough time to circularize their orbits. This is further evidence that Ba, CH, and CEMP-s stars obtain their heavy element signatures from an AGB companion where the system has had enough time to evolve the AGB to a white dwarf. However, we note this may be selection bias; mass transfer will disrupt the initial orbital

configuration, and there have been many high-eccentricity post-accretion systems observed. For more, see Chapter 3

2.8.5 Stellar Masses and Ages

The masses of the AGBs that produced the s-process elements should be greater than or roughly equal to the initial mass of the observable star for evolutionary reasons, with some allowances for accreted mass. The AGB masses estimated from the abundances patterns are compared to the mass estimates from the binary orbit modeling in the left panel of Figure 2.13. As the AGB evolves into a white dwarf, its mass cannot exceed the Chandrasekhar limit of 1.44 $M_{\odot}$. We find white dwarf masses (m_{WD} or M_2, dashed red line) less than those of the initial AGB mass from FRUITY (black line), and less than those of the visible components (m_{vis} or M_1, solid red line). For the stars HD 31487, PV UMa, HD 209621, BD+04 2466, the visible component is slightly more massive than the AGB donor, although the AGB mass is within the error bars of the estimated visual mass. For the star HD 105671, we did not find a reasonable AGB mass estimate from the flat abundance pattern.

In the right panel of Figure 2.13 we compare the estimated AGB donor mass from FRUITY (black line) and the level of s-process enrichment from our abundance analysis (green lines). With the exception of the mild Ba star PV UMa, we observe more s-process enrichment from low- and intermediate-mass AGB stars, with masses between $2 - 3$ $M_{\odot}$. The exception of PV UMa could be related to the orbital configuration, where PV UMa has a short orbital period compared to other stars in these classes. mass transfer may have proceeded via RLOF, transferring significant angular momentum and shrinking the orbit of the binary. This may have ejected the AGB envelope, and resulted in an overall reduced accretion mass. Alternatively, the accretion may have occurred long in the past, and the mixing processes in this star have strongly diluted the surface abundances. In the extreme cases of $m_{AGB} \sim 4-6$ $M_{\odot}$ such as HD 104979, HD 105671, and HD 196673, we observe comparatively less s-process enrichment.

With our derived stellar masses and atmospheric parameters, we approximate the ages of our program stars. Using PARSEC isochrones (Bressan et al., 2012; Chen et al., 2014, 2015; Tang et al., 2014; Marigo et al., 2017) for metallicities comparable to those in our abundance sub-sample, we investigate the ages for eight

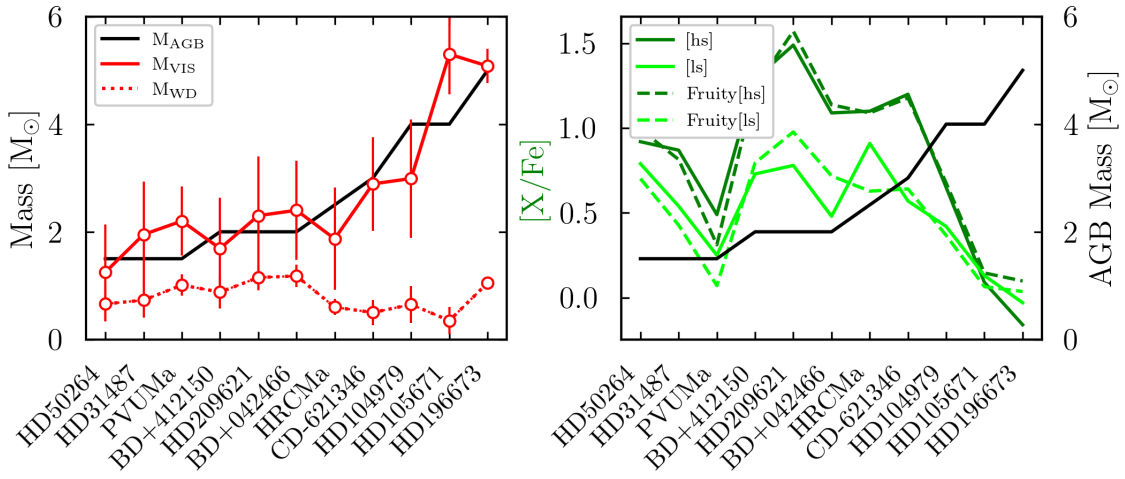

Figure 2.13: Top: Estimated masses for AGB donor stars from FRUITY (black line), and dynamically derived visible (solid red line) and white dwarf (dashed red line) masses from ELC. Bottom: AGB donor mass (black) compared with observed s-process enrichment (shades of green). Dashed green lines are predicted s-process enrichment from the FRUITY models. Adapted from Dimoff et al. (2024).

of our best-fit stellar systems: HD 50264, HR CMa, HD 104979, BD+41 2150, HD 31487, HD 209621, CD-62 1346, and BD+04 2466. We chose these systems because they display strong s-process enhancement and show good agreement between AGB mass, dynamical mass, and white dwarf masses. We initialize our isochrones using an IMF from Kroupa et al. (2013), which corrects for unresolved binaries. We compare our stars to the isochrones based on our dynamical mass estimates, effective temperature, surface gravity, and extinction-corrected absolute G magnitudes (G_0) from Gaia DR3.

For a given metallicity bin, we determine on which isochrone our star sits by minimizing the distance between our data and the isochrones in a least-squares fitting routine. We perform comparisons in $T_{\rm eff}$-mass space, $\log(g)$-mass space, and G_0-mass space, and compare these results to the standard HR diagram of $T_{\rm eff}$-G_0. Approximated ages of our systems are in Table 2.8.

In Figure 2.14 we plot our stars against isochrones in the HR-Diagram parameter space (magnitude vs temperature), organized by metallicity. The color bar represents the age of the isochrones ranging from 10^8 to 10^{10} years, with our stars plotted on top. For these eight selected stars, stellar ages from the HR diagram are all

Table 2.8: Stellar metallicities, masses, and estimated ages. Ages are based on fitting stellar parameters on PARSEC isochrones (HR) and using the dynamical stellar masses derived using ELC (M).

Star	[Fe/H] [dex]	$\sigma_{[Fe/H]}$	Mass [$M_{\odot}$]	σ_M	log(Age$_M$ yrs)	σ(Age$_M$)	log(Age$_{HR}$ yrs)	σ(Age$_{HR}$)
HD 50264	-0.17	0.07	1.25	0.85	9.55	0.11	9.71	0.33
HR CMa	-0.23	0.12	1.87	0.95	9.12	0.07	9.47	0.42
HD 104979	-0.35	0.10	2.99	1.10	9.36	0.16	9.50	0.33
HD 31487	-0.38	0.14	1.95	0.98	9.19	0.07	9.42	0.47
BD+41 2150	-0.48	0.18	1.69	0.94	9.19	0.08	9.42	0.47
CD-62 1346	-1.33	0.10	2.89	0.87	8.52	0.14	9.79	0.30
HD 209621	-1.60	0.40	2.30	1.10	8.63	0.49	9.45	0.36
BD+04 2466	-1.93	0.30	2.40	0.92	8.49	0.51	9.55	0.33

over 10^9 years, with the oldest around 6.2×10^9 years. The ages derived using mass estimates are between 3.3×10^8 and 3.5×10^9 years. For more metal-poor stars, we find a systematic offset of about 0.7 dex toward younger ages when using our derived masses. One would generally not expect a metal-poor ([Fe/H] ~ -2) star to be less than $\sim 10^9$ years old; however, one would also not expect a two-solar-mass star to be older than about 1.7 Gyr. In the cases where the age estimates from the stellar mass disagree strongly with those from the HR diagram, we find the ages determined from our dynamical mass estimates to be more robust.

The metal-poor star BD+04 2466 sits on the RGB, but the low surface gravity of $\log(g) = 1.68$ may suggest the possibility of being a second-ascent giant, where uncertainties in the stellar temperature overlap with the AGB. The CEMP-s star CD-62 1346 lies on the RGB, between the first ascent RGB and the red clump. The low surface gravity may indicate advanced evolution from the RGB toward the horizontal branch (HB). The Ba star HD 104979 is on the RGB, or advancing onto the HB in the HR diagram. The surface gravity $\log(g) = 2.08$ does not suggest this star is an AGB star. The star BD+41 2150 is definitively on the first ascent of the RGB, undergoing hydrogen shell fusion. While we find a $\log(g) < 2$, the error bars are not small; we do not suggest this star is an AGB. The Ba star HD 31487 is also on the RGB, in a similar evolutionary state as BD+41 2150. The Ba star HD 209621 sits in a similar place to HD 104979, between the RGB and HB phases. The lower surface gravity of $\log(g) = 1.64$ indicates advanced evolution, and He burning on the second ascent of the giant branch may be beginning. The Ba star HR CMa sits in the red clump region of the HR diagram, possibly undergoing helium fusion in the core before ascending the AGB. The lower surface gravity of $\log(g) = 1.98$ indicates advanced RGB or HB evolution. The Ba dwarf star HD 50264 has a high

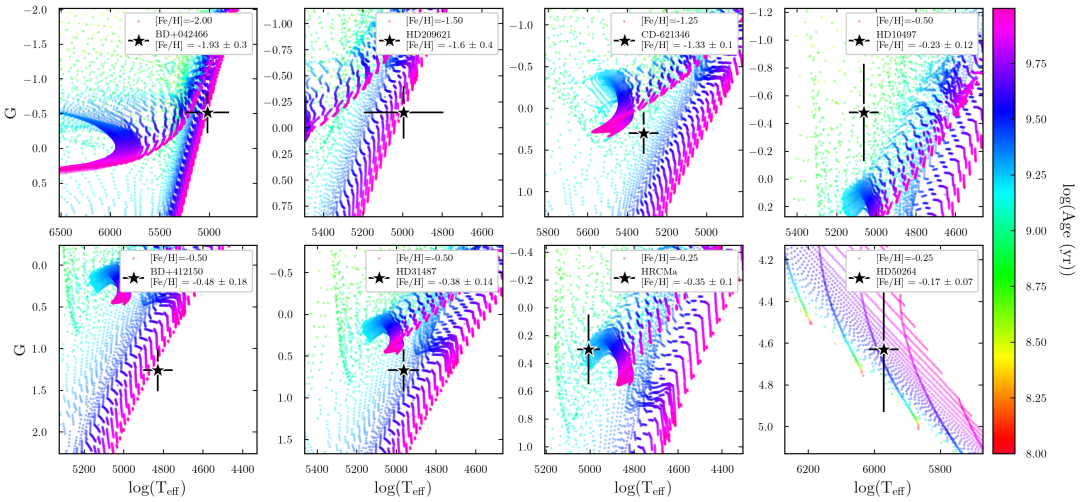

Figure 2.14: PARSEC isochrone fits for systems where we have dynamical masses, shown in compatible mass and metallicity bins. Adapted from Dimoff et al. (2024).

surface gravity $\log(g) = 4.24$, and lies on the main sequence at the bottom of the HR diagram.

2.8.6 Galactic Chemical Evolution

We visually compare our abundances [X/Fe] to the galactic nucleosynthesis analysis of Kobayashi et al. (2020), and find similar trends in increasing s-process enrichment [s/Fe] with decreasing metallicity. This is the result of a higher ratio of available neutrons to seed nuclei. The same trend can be observed in [C/Fe], where more metal poor stars are more enriched in carbon than their metal-rich counterparts. Our Mg abundances follow the same general α-element trend with near-solar values at higher metallicities, and with slight enhancements at lower metallicities. The heavy element trends show increased scatter at lower metallicities.

Uncertainties

To determine the uncertainties in the radial velocities, we fit a Gaussian profile to peak in the CCF and take the half-width at the half-maximum of the Gaussian fit for each cross-correlation. Uncertainties in the RVs are taken as standard deviation across all spectral orders. Uncertainties in the radial velocities from the OES

instrument are numerically approximated using the equation

$$\sigma_{RV} = C \times (SNR)^{-1} \times \Delta\lambda^{-0.5} \times R^{-1.5}, \tag{2.13}$$

where $\Delta\lambda = 5900$ Å, $R = 51600$ for the high-resolution fibre, and the instrument-specific constant $C = 6.5 \times 10^{12}$ Kabáth et al. (2020). For a SNR of $\sim 10-15$, deemed adequate for RV observations, a RV accuracy of ≈ 0.8 km/s is estimated. Our OES observations typically have SNR ~ 30, and using our multi-CCF approach we find an average uncertainty of ~ 0.5 km/s. Due to the similarities between the ASU and IANAO telescopes, we estimate the average RV uncertainty of our observations is ~ 0.8 km/s for observations with SNR $\sim 10 - 15$. Our observations with ESpeRo have consistently high SNR on the order of 30, resulting in likely more precise RV measurements than predicted.

We estimated uncertainties for data collected from the FIES and FEROS instruments using the CERES pipeline. The reduction code additionally calculates the error in the computed radial velocities using the SNR of the observations and includes the statistical deviation across the spectral orders.

Uncertainties in our atmospheric parameters stem from spectral qualities SNR, the spectral normalization, and cross correlation. Additionally, each derivation method comes with its own set of uncertainties. Using flux ratios, the spectral uncertainties play the most significant role, as the statistical uncertainties from ATHOS are small. Balancing excitation and ionization levels requires the widths of many Fe spectral features, whose uncertainties add to those of the overall spectrum. However, at high resolution, the uncertainty in fitting a well-defined spectral feature is small, provided well-reduced data.

The average uncertainty in our abundance derivations is a combination of the statistical scatter measurement between lines and the uncertainties in the atmospheric parameters. Abundance uncertainties are calculated for all elements using the methodology described in Karinkuzhi et al. (2018, 2021b), following Equation (2) from Johnson (2002) or Equation (A20) from McWilliam et al. (1995), where σ_{ran} is the statistical uncertainty in the line measurements, and σ_T , $\sigma_{\log g}$, $\sigma_{[Fe/H]}$, and σ_ξ are the uncertainties on the atmospheric parameters:

$$\sigma_{tot}^2 = \sigma_{ran}^2 + \left(\frac{\partial \log \epsilon}{\partial T}\right)^2 \sigma_{T_eff}^2 + \left(\frac{\partial \log \epsilon}{\partial \log g}\right)^2 \sigma_{\log g}^2 + \left(\frac{\partial \log \epsilon}{\partial \xi}\right)^2 \sigma_{\xi}^2 + \left(\frac{\partial \log \epsilon}{\partial [Fe/H]}\right)^2 \sigma_{[Fe/H]}^2 + 2\Bigg(\left(\frac{\partial \log \epsilon}{\partial T}\right)\left(\frac{\partial \log \epsilon}{\partial \log g}\right)\sigma_{T,\log g} + \left(\frac{\partial \log \epsilon}{\partial \log g}\right)\left(\frac{\partial \log \epsilon}{\partial \xi}\right)\sigma_{\log g,\xi} + \left(\frac{\partial \log \epsilon}{\partial \xi}\right)\left(\frac{\partial \log \epsilon}{\partial T}\right)\sigma_{\xi,T} + \left(\frac{\partial \log \epsilon}{\partial\, T}\right)\left(\frac{\partial \log \epsilon}{\partial [Fe/H]}\right)\sigma_{\log g,\xi} + \left(\frac{\partial \log \epsilon}{\partial \log g}\right)\left(\frac{\partial \log \epsilon}{\partial [Fe/H]}\right)\sigma_{\log g,\xi} + \left(\frac{\partial \log \epsilon}{\partial \xi}\right)\left(\frac{\partial \log \epsilon}{\partial [Fe/H]}\right)\sigma_{\log g,\xi}\Bigg).$$

2.9 Conclusions

It is understood that AGB stars produce s-process elements in the He-intershell boundary region outside the core. Convective mixing processes and thermal flashes resulting in pulses and dredge-up events bring this material to the surface where it is observable. Binary AGB stars share their enriched envelope material through TPs, strong stellar winds, or by overflowing their Roche lobe. The polluted companion is either a main-sequence or a giant star with s-process material visible on the surface, even long after the AGB itself has faded to a white dwarf and disappeared from view. This results in a single-lined spectroscopic binary enriched in s-process material. By understanding element ratios produced by AGB stars of different masses, we aim to better understand the nuclear physics of the s-process, mass transfer processes in binary systems, and galactic chemical evolution.

We observed spectroscopic binaries with high-resolution spectrographs to trace AGB nucleosynthesis patterns in the now-visible extrinsic binary companions. We derived atmospheric parameters estimated with ATHOS and Xiru, and computed 1D-LTE photospheric abundances in a sample of 25 extrinsic stars with MOOG. We added Mo and Pb to abundance patterns, useful in determining the initial AGB mass in binary systems polluted with s-process material. We see similar trends between both light and heavy s-process elements and Mo, and note correlations in elemental abundances produced by the s-process. For 5 AGB stars, we determined

atmospheric parameters using scaling relations and derive abundances of s-process elements with MOOG.

We use our derived s-process signatures to infer the mass of the former AGB companion star that produced the heavy elements through comparison to FRUITY model AGB yields. We find a narrow range of initial AGB masses corresponding to enrichment in s-process material and observe a general trend between s-process enhancement and donor AGB mass, where low- and intermediate-mass AGB stars produce more heavy s-process material compared to higher mass AGB stars. With RV monitoring, we model binary orbits to further investigate the estimated stellar masses of our sample. We find general agreement in the observed stellar masses, initial AGB masses, and calculated white dwarf masses.

3 Simulating Stellar Evolution with Accretion from a Binary AGB Companion

3.1 Motivation

It is not yet precisely known how or how much asymptotic giant branch (AGB) stars enrich their binary companions. To this end, we present a large grid of 2691 stellar stellar evolution models, including accretion from a binary AGB companion. By modeling the evolution of these polluted stars through the accretion phase, we estimate the amount of material necessary to reproduce the observed surface abundance patterns. For a large and diverse set of chemically enriched stars, we compute accretion efficiencies and infer how material is transferred in these binary systems. We rule out accretion mechanisms for some classes of stars. We trace evolutionary links through cosmic time between different classes of chemically peculiar stars and comment on convective mixing and mass-transfer efficiencies. This chapter closely follows the work in Dimoff et al. (2025), *Modeling the Progenitors of Low-Mass Post-Accretion Binaries*.

What's New: We generate a new grid of binary stellar evolution models including accretion for a broad range of metallicities, AGB donor masses, initial stellar masses, and accretion masses. This is the first time such modeling has been performed at low metallicities ([Fe/H] = -2.15). We find distinctions in accretion mass for populations of stars. Different groups in metallicity formed at different times, hinting at trends in accretion and mixing efficiencies with cosmic age.

3.2 Abstract

About half of the mass of all heavy elements with mass number A > 90 is formed through the slow neutron capture process (s-process), occurring in evolved asymptotic giant branch (AGB) stars with masses $\sim 1-6$ $M_\odot$. The s-process can be studied by modeling the evolution of barium (Ba), CH, and carbon-enhanced metal-poor (CEMP)-s stars. Comparing observationally derived surface parameters and 1D-LTE abundance patterns of s-process elements to theoretical binary accretion models, we aim to understand the formation of post-accretion systems. We explore the extent of dilution of the accreted material and describe the impact of convective mixing on the observed surface abundances. We compute a new grid of 2691 stellar evolution models including accretion from an AGB companion for low-mass post-accretion systems. A maximum-likelihood comparison of surface parameters and derived abundances determines the best fit model. We find consistent AGB donor masses in the mass range of $2-3$ $M_\odot$ across our sample of post-accretion stars. Our modeling shows CH and CEMP-s stars have low final masses (~ 1.0 $M_\odot$) and small amounts of transferred material (~ 0.1 $M_\odot$). We find the formation scenario for weak Ba stars is an AGB star transferring a moderate amount of mass (≤ 0.5 $M_\odot$) resulting in a $\sim 2.0-2.5$ $M_\odot$ Ba star. The strong Ba stars are best fit with lower final masses $\sim 1.0-2.0$ $M_\odot$ and significant accreted mass (≥ 0.5 $M_\odot$). We find that metal rich Ba stars generally accrete more material than metal poor CEMP-s and CH stars. We also find that strong Ba stars must accrete more than 0.50 $M_\odot$ to explain their abundance patterns, and in this limit we are unable to reproduce the observed mass distribution of strong Ba stars. The mass distributions of the weak Ba stars, CEMP-s, and CH stars are well reproduced in our modeling.

3.3 Modeling the Progenitor AGB Stars

When modeling the effects of mass transfer, the nucleosynthetic signatures depend heavily on the nature of the original AGB star. Significant effort has been made to model the s-process nucleosynthesis within AGB stars.

The FUll-Network Repository for Updated Isotopic Tables and Yields (FRUITY) Straniero et al. (2006); Cristallo et al. (2011) provides results of modeling AGB yields of s-process elements. They found that low-mass (1-3 $M_\odot$) AGB stars present

the best match to the observed s-process abundance patterns in CEMP-s, CH, and Barium stars. Karakas and Lattanzio (2014) modeled the yields of s-process elements in AGB stars in the MONASH models, and found similar results, in that low-mass (1-3 $M_{\odot}$) AGB stars are primarily responsible for the chemical signatures observed in these post-mass-transfer systems.

The peculiar abundance patterns in the populations of Ba, CH, and CEMP-s stars are understood to be the result of AGB mass-transfer in binary systems. To explain the origins of the chemical enhancements in these stars, various models of accretion and mass transfer have been developed with the aim of determining how AGB stars enrich their binary companions, the efficiency of accretion, and evolutionary links between classes of chemically peculiar stars. Boffin and Jorissen (1988) showed that for some Ba stars with short orbits, Roche-lobe overflow (RLOF) is a likely mechanism of mass transfer. However, many observed Ba, CH, and CEMP-s stars have long orbital periods ($P > 1 \times 10^4$ days, where RLOF is unlikely to occur.

The observable surface abundances of these stars are strongly dependent on the amount of mass transferred ΔM, when the mass is transferred during the evolution of the secondary, and the mixing processes within the accretor star. One of the outstanding questions is how much material is actually accreted by the companion, which provides a direct link to the efficiencies of AGB mass transfer. Stancliffe (2021) has modeled Ba star progenitor systems at a fixed metallicity of [Fe/H] $= -0.25$ and a fixed post-accretion Ba star mass of 2.5 $M_{\odot}$, corresponding to the average mass of Ba giants determined by Escorza et al. (2017). Under these assumptions, Stancliffe (2021) found that the amount of accretion in Ba star systems is typically small, on the order of 0.10 $M_{\odot}$.

3.4 Observational Data

We compare our models to stellar parameters and surface abundances derived from high-resolution ($30000 < R < 60000$) spectroscopic observations. We include the homogeneously analyzed sample of Ba, CH, and CEMP-s stars from Dimoff et al. (2024). We collect further data from the large sample of strong and weak Ba stars from de Castro et al. (2016), supplemented by additional heavy element abundances from Roriz et al. (2021a). We extend our analysis to the metal-poor regime and

include CH and CEMP-s stars from Goswami et al. (2006); Karinkuzhi and Goswami (2014, 2015); Goswami et al. (2016, 2021). For each of our observational samples, we collect stellar surface parameters $T_{\rm eff}$, $\log g$, and [Fe/H] (see Figure 3.1) and surface abundances of C and heavy elements produced via the s-process, as well as the r-process tracer Eu.

These observational data are non-homogeneous and do not contain the same elemental abundances, as we draw our observed data from different sources. In some cases, the observable Ba lines are saturated and are not used for abundance derivations. By comparing our models to different populations of stars believed to have accreted material from a previous AGB companion, we make predictions about AGB masses, stellar masses, and accretion masses, and we make distinctions between metal-poor and metal-rich populations.

We take note of stellar labels from the literature, and we apply corresponding labels based on metallicity and chemical enrichment. The original CEMP classification scheme from Beers and Christlieb (2005) and Masseron et al. (2010) defines metal poor stars as those with [Fe/H] < -1.00. Within this category, we define CEMP stars in our sample as stars with [C/Fe] > 0.70. Further classifying the stars in our sample, we define [ls/Fe] as the average abundances of Sr, Y, Zr, and Mo with respect to Fe, and [hs/Fe] as the average abundances of Ba, La, Ce, and Pr with respect to Fe. According to Bisterzo et al. (2014), Nb is mostly produced by the s-process, but Nb abundances in the de Castro et al. (2016) dataset are systematically higher than the models. Given this information, we choose to exclude Nb from the computation of [hs/Fe].

Following Hansen et al. (2019), we classify our CEMP population based on carbon and relative ratios of light- and heavy- s-process element abundances. We substitute [ls/Fe] for [Sr/Fe] and [hs/Fe] for [Ba/Fe] to account for observations where derivations of these elements are missing. If the CEMP star has enhancements in both light and heavy s-elements ([Sr/Fe] or [ls/Fe] > 0.30 and [Ba/Fe] or [hs/Fe] > 0.30) and does not have significant r-process enhancements ([Eu/Fe] < 0.50), it is a CEMP-s star. Otherwise, we exclude any -r/s enriched stars from our investigation. The CH stars also have high carbon enhancements [C/Fe] > 0.70, and are expected to have enhancements in s-process material with [ls/Fe] > 0.30 or [hs/Fe] > 0.30, but may have metallicities up to [Fe/H] $<$ -0.15. If there are no enhancements in either r- or s- elements, the star is labeled as a CEMP-no star. From our accretion

modeling, we omit the CEMP-r, -r/s, and -no stars, as they are not believed to have accreted pure s-process signatures from a former AGB companion.

Ba stars have higher metallicities ([Fe/H] > -1.00) and are generally not as enhanced in carbon as the CEMP and CH populations. Ba stars are split into two categories: strong and weak Ba stars. Karinkuzhi et al. (2021b) provides a classification of the Ba stars based on heavy element abundance ratios. We use the [ls/Fe] and [hs/Fe] ratios to satisfy the criterion that more than three elements in the light- and heavy- s-process peaks are included. A star is a 'Ba-no' star if both [hs/Fe] and [ls/Fe] < 0.20. A 'mild' (or weak) Ba star has either [hs/Fe] or [ls/Fe] in the range $0.20 <$ [hs/Fe] *or* [ls/Fe] < 0.80, and a strong Ba star has either [hs/Fe] or [ls/Fe] > 0.80. Our observational sample is displayed in Figure 3.1, where the stars are colored following these classification schemes.

We use a statistical treatment for upper limits in our comparison. When explicitly stated, or when the uncertainties are not provided in the source material, we treat upper limits on abundance by the following: the value of the abundance is consistent with zero (0), and the observed 'upper limit' is taken as the 2-σ uncertainty, so the true uncertainty in the abundance is $\frac{1}{2}$ of the upper limit. For an example upper limit of [Sr/Fe] < 3.00, the value [Sr/Fe] $= 0.0$ and the uncertainty $\sigma_{\rm [Sr/Fe]} = 1.50$.

3.5 Modeling Methods

We compute a grid of stellar evolution models using the `STARS` code (Eggleton, 1971, 1972; Pols et al., 1995; Stancliffe and Eldridge, 2009), including the addition of mass to simulate binary accretion. The code requires inputs of an opacity table for a specific metallicity, and a starting stellar structure, which the code also generates. The program solves the equations of stellar structure with the chemical evolution of seven energetically important species: ^{1}H, ^{3}He, ^{4}He, ^{12}C, ^{14}N, ^{16}O, and ^{20}Ne. At the convergence of every time step in the model, a network of 40 isotopes is computed (Stancliffe, 2005). Our models use 499 mesh-points, no additional mass-loss, a mixing length of $\alpha = 2.025$ following Stancliffe (2021), and a prescription for convective overshoot following Schroder et al. (1997), using $\delta_{ov} = 0.15$ from Stancliffe et al. (2015). We define the primary star to be the AGB donor star, and the secondary star to be the accreting Ba, CH, or CEMP-s star.

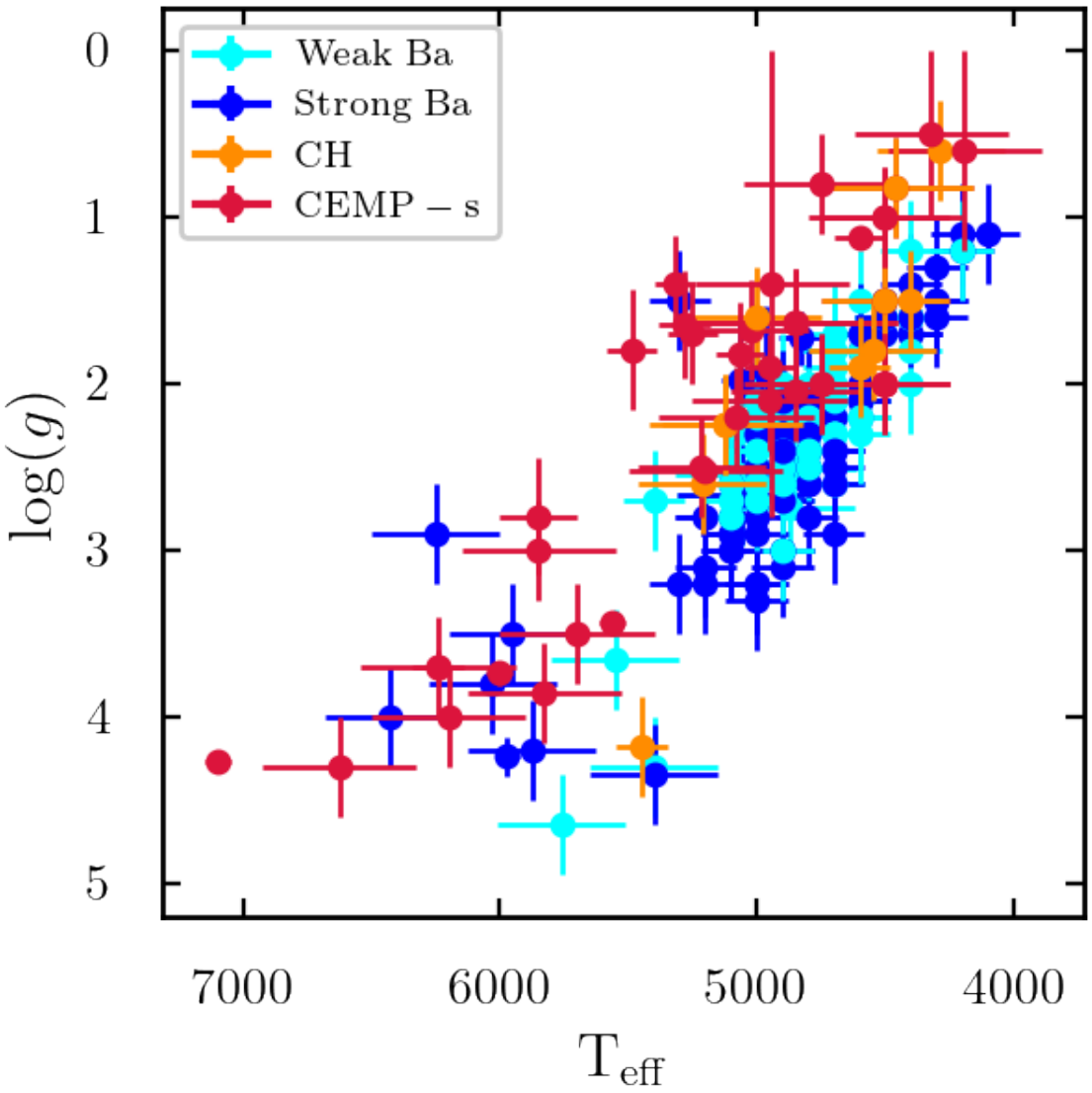

Figure 3.1: Kiel diagram showing surface gravities and effective temperatures for the collected observational sample. Blue data points are strong Ba stars, cyan data points are weak Ba stars, orange data points are CH stars, and red data points are CEMP-s stars. Surface parameters and abundances are collected from Dimoff et al. (2024), de Castro et al. (2016), Roriz et al. (2021b), Goswami et al. (2006), Karinkuzhi and Goswami (2014), Karinkuzhi and Goswami (2015), Goswami et al. (2016), Goswami et al. (2021). From Dimoff et al. (2025).

The code uses a prescription for convection using mixing length theory with a mixing-length parameter $\alpha = 2.025$, includes atomic diffusive mechanisms, and ther-

mohaline mixing (THM). The effects of radiative levitation and gravitational settling are included in the code but are not considered in our modeling. While THM is more important in the dwarfs and stars on the upper giant branch (Stancliffe, 2015), most of our stars are giants, and we opt to not include THM for convergence purposes. This choice plays a role when fitting dwarf star abundance patterns. Without THM, there is no significant mixing occurring on the main sequence so, until accretion occurs, the accreted material will remain in a layer on the surface until the convective envelope advances.

In our models, the main mixing processes occur due to convection as the accretor star ascends the giant branch. We do not consider thermohaline mixing, and note that thermohaline mixing has been shown to be an effective means of changing the surface composition of low-mass stars on the upper part of the giant branch (Stancliffe, 2015), but our observational sample contains generally less evolved stars. While Stancliffe et al. (2007) found that thermohaline mixing is effective on the main sequence, a follow-up study found that the effects of gravitational settling can inhibit thermohaline mixing at low metallicities and, in cases where a small quantity of material is accreted, may be suppressed almost completely (Stancliffe and Glebbeek, 2008). Stancliffe (2021) showed that THM plays an overall less significant role in diluting surface abundances compared to convective mixing upon first dredge-up (FDU) in metal-rich stars.

The grid of stellar evolutionary tracks is parameterized by the metallicity, the AGB donor mass, the initial mass, and the amount of accreted material. Metallicities range from $Z = 0.0001$ ([Fe/H]=-2.15) to $Z = 0.010$ ([Fe/H]=-0.15), complementary to the set of barium star models from Stancliffe (2021) who computed models for a metallicity of [Fe/H] = -0.25. It is assumed that the AGB donor and companion are the same metallicity. Our models cover a post-accretion final mass range to include low- and intermediate-mass stars with final masses from 0.80 to 5.0 $M_\odot$. The initial masses of the models are determined by subtracting the prescribed amount of accreted material. For any given final mass, the initial masses range from $M_f - 0.50\ M_\odot$ to $M_f - 0.05\ M_\odot$, with accretion masses equal to 0.05, 0.10, 0.20, 0.30, 0.40, and 0.50 $M_\odot$. In total, we generated 2691 stellar evolution models.

Following Stancliffe (2021), each model was evolved up to an age that is determined by the lifetime of the AGB companion, where material from the AGB is added to the stellar surface at a constant rate until the final target mass is achieved.

The composition of the AGB ejecta is taken from the FRUITY database Domínguez et al. (2011); Cristallo et al. (2011, 2015). The FRUITY database contains around 120 models that range in initial mass from 1.3 - 6 $M_\odot$ and metallicities from Z = 0.0001 ([Fe/H]=-2.15) to 0.03 ([Fe/H]=+0.32). After the accretion phase has ended, the secondary star continues to evolve, taking the new surface composition into account. Surface abundances are diluted following mixing processes in the accretor star. We use a tracer element 'arbitrarium' to define how the AGB material is mixed into the secondary star. If the material originates from the AGB star, the value of arbitrarium is set to one, and it is set to zero if it originates within the secondary. We quantify the mixing following

$$X_i^{actual} = X_{arb} X_i^{acc} + (1 - X_{arb}) X_i^{original}, \tag{3.1}$$

where X^{actual} is the surface abundance, i is the timestep, X_{arb} is the value of arbitrarium, X^{acc} is the ejecta abundance, and $X^{original}$ is equal to the elemental abundance in a star of solar metallicity, scaled by the metallicity of the star. We use the solar abundances from Asplund et al. (2009). The effects of mixing due to convection become more prominent with lower surface gravities and the inward advance of the convective envelope as the star ascends the giant branch.

The time of accretion changes with the mass and metallicity of the AGB donor star, with more massive and more metal rich AGBs donating their material earlier than lower mass and more metal-poor stars. To this end, we first evolve single stars using the `STARS` code with masses of 1.3, 1.5, 2.0, 2.5, 3.0, 4.0, and 5.0 $M_\odot$, compatible with the AGB masses in the FRUITY database. Evolution in the `STARS` code continues past the core helium burning phase and begins the ascent of the AGB, past the evolutionary states of our observed sample stars. The AGB phase is very short compared to the lifetime of a lower mass companion, and we find this acceptable for our purposes.

A selection of evolutionary tracks from our grid of models is seen in Figure 3.2, where in the left panel the evolutionary tracks are offset from one another in the Kiel diagram. The accretion phase is highlighted in blue where, for the lowest initial mass tracks, there is a noticeable change in temperature between the beginning and end of the accretion phase. The right panel of Figure 3.2 shows the surface abundance of [Ba/Fe], an element produced in AGB stars, as a function of model number, a

proxy for time. Our models are parameterized such that after the star accretes the specified amount of mass, the surface abundances are changed to reflect that of the transferred AGB material. Beyond this, the convective envelope mixes and dilutes the surface abundances.

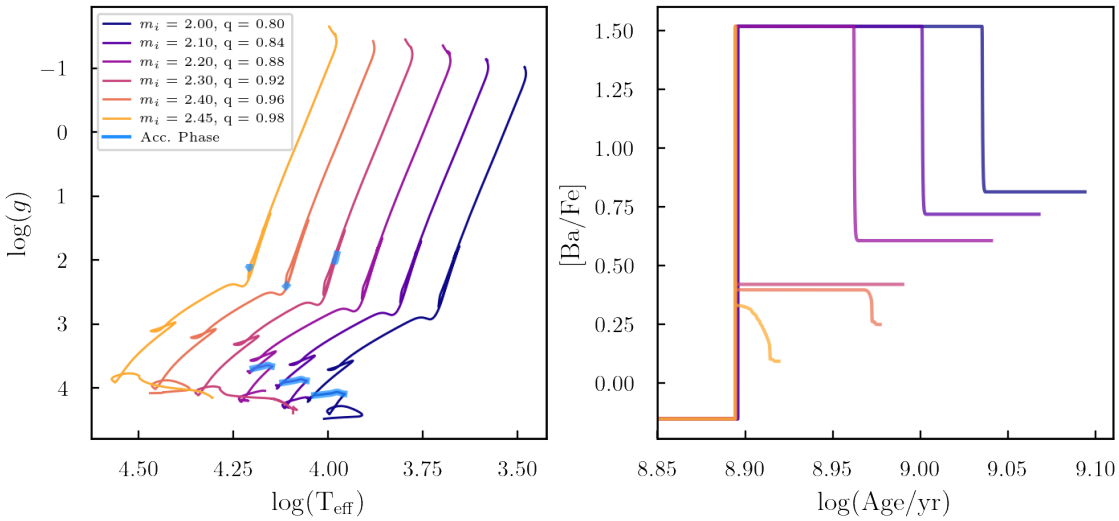

Figure 3.2: Left: Evolutionary tracks for a sample of stars with m_{final} = 2.50 $M_\odot$ at [Fe/H] = -0.15 with varying initial masses and accretion masses, with accretion phases for each model highlighted in blue. Right: Relative surface abundance of the s-process element Ba with $\log_{10}$ (Age/yr). The abundance is elevated after the accretion phase, and after the onset of first dredge-up the surface abundance is diluted. From Dimoff et al. (2025).

An example Kippenhahn diagram is shown in Figure 3.3. In this example, we display the structure of a 2.0 $M_\odot$ star accreting 0.5 $M_\odot$ of material from a 2.5 $M_\odot$ AGB primary. The total mass is plotted against the model number, a proxy for time. The logarithm of the stellar age in years is included on the upper x-axis. The purple and green regions denote radiative and convective zones respectively, determined by computing the difference between the radiative and adiabatic transfer gradients, shown in the color bar. The onset of FDU is visible in the advance of the convective envelope towards the core as the star ascends the giant branch around model number 4500, as well as the onset of core He burning as the star begins to ascend the AGB around model number 5250. The accretion phase is shown as an increase in the overall mass of the star. In this case, accretion occurs while the

secondary star is on the main sequence.

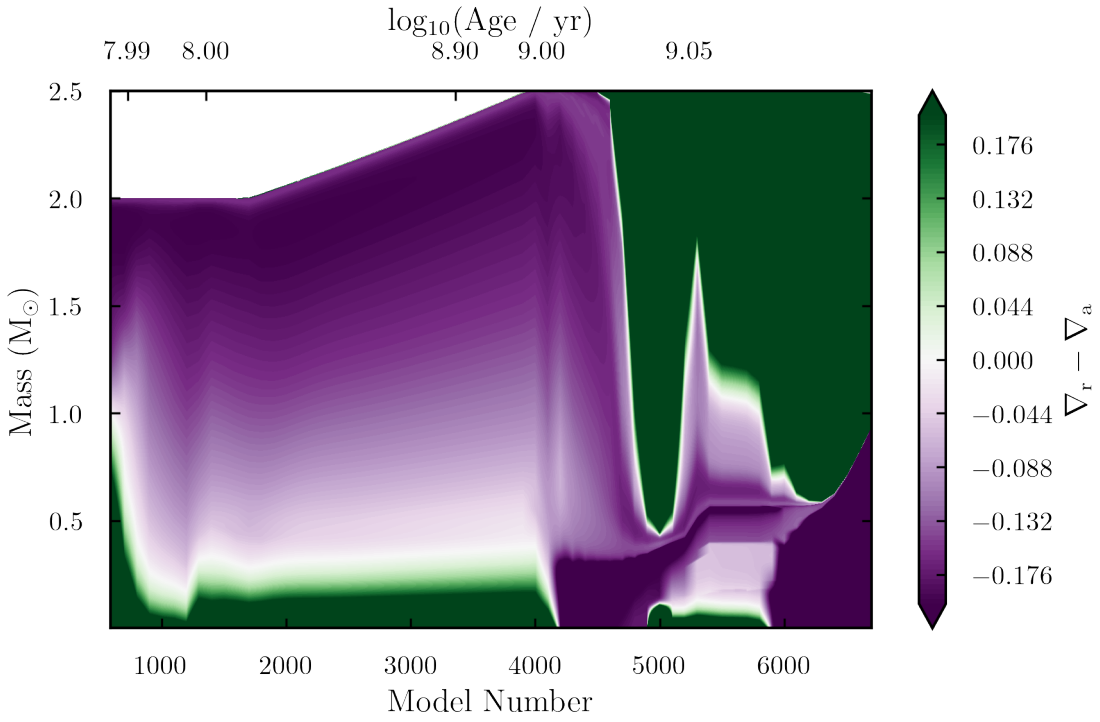

Figure 3.3: Example Kippenhahn diagram for a 2.00 $M_\odot$ star accreting 0.50 $M_\odot$ of material from a 2.50 $M_\odot$ AGB star at a metallicity of [Fe/H] = -0.15. Green colors denote convective regions, and purple colors denote radiative regions, determined by the computed difference in the radiative and adiabatic transfer gradients. In the total mass on the y-axis, the accretion phase is identified by the steady increase in mass. The upper x-axis shows $\log_{10}$ (Age/yr), and the lower x-axis shows the model number, which is highly non-linear with respect to time. From Dimoff et al. (2025).

We describe the general features of our models by focusing on the case of a 2.00 $M_\odot$ star accreting 0.5 $M_\odot$ from a 2.50 $M_\odot$ AGB star at a metallicity of [Fe/H] = -0.15. This evolution is shown in Figure 3.3. The accretion phase starts at a stellar age of around 780 Myr. At this point, the 2.00 $M_\odot$ star reaches a core helium abundance of $X_{He} \sim 0.48$, and the convective core contains around 0.64 $M_\odot$ of material. As accretion progresses, the convective core expands to reach a mass coordinate around 0.77 $M_\odot$, where the core helium abundance is reduced as fresh hydrogen is ingested into the core of the now more-massive star. Since we

only account for convective mixing, the accreted layer remains on the surface until the onset of FDU. At its maximum depth, the convective envelope reaches a mass coordinate of around 0.50 $M_\odot$, and penetrates the outer layers of the core. This signifies the maximum dilution of the accreted material, as the envelope will not reach this depth for the remainder of the lifetime of the star. As in Stancliffe (2021), we can define the dilution factor

$$d = M_{acc}/M_{mix},$$

where M_{acc} is the mass of the accreted material and M_{mix} is the mass through which it is mixed. At this point, $d = 0.25$. While expressed in different notation, this is analogous to the dilution factor described in den Hartogh et al. (2023).

As the initial mass ratio q of the binary approaches one, accretion occurs later in the evolution of the secondary star (see Figure 3.2). A secondary with an initial mass of 2.40 $M_\odot$ accretes after it has left the main sequence and is going through the core-He burning phase, shown in the orange evolutionary track in Figure 3.2. At this point, the convective envelope is considerably shallower than at the onset of FDU, and has a thickness of only about 0.70 $M_\odot$. Convective mixing quickly dilutes the accreted material. During this time, the maximum mass contained in the envelope is $\sim$ 1.90 $M_\odot$.

- AGB masses: 1.3, 1.5, 2.0, 2.5, 3.0, 4.0, 5.0 $M_\odot$ consistent with FRUITY models, so we can reliably use their yields.
- Accretion masses: 0.5, 0.4, 0.3, 0.2, 0.1, 0.05 $M_\odot$
- Metallicities [Fe/H] = -2.15, -1.68, -1.15, -0.68, -0.37, -0.15, allowing coverage from metal-rich Ba stars to metal-poor CEMP-s stars.
- Initial stellar masses: unequally spaced bins from 0.45 - 4.95 $M_\odot$ pre-accretion.

The evolution of the surface abundances generally follows that of the dilution factor, since temperatures in the envelope are not high enough to process the heavy elements accreted from the AGB star. In the right panel of Figure 3.2, the surface abundances of the s-process element [Ba/Fe] are displayed. With only convection acting, the abundance of Ba in models with earlier accretion times is unchanged from

the end of the accretion phase until the onset of FDU. With the inward advance of the convective envelope, the accreted material is mixed and diluted within the stellar interior, and the surface abundance falls dramatically. With the increase of the mass of the accretor star, the mass of the convective envelope increases, and through this the surface abundances are diluted more effectively.

3.6 Results

Our grid of stellar evolution models spans a wide range in mass and metallicity, compatible with both metal-poor and metal-rich post-accretion systems. Such models give insight into initial the mass of the primary AGB donor, how much material is transferred, and the initial mass of the observed polluted star. We compare observationally derived stellar surface parameters and abundances to our evolution models. When viewed together as multiple populations formed through similar scenarios, these systems trace changes in nucleosynthesis, accretion, and mixing processes through cosmic time.

3.6.1 Comparison to the Models

When comparing to our observational sample, we consider models in the grid that have mass ratios $q = M_2/M_1 \leq 1.00$. Otherwise, the companion would be more massive than the AGB star and would have evolved first. We require that each observed star have measured surface parameters $T_{\rm eff}$, $\log(g)$, and [Fe/H], and computed 1D-LTE abundances for at least one s-process element in each s-process peak. Many evolutionary tracks exist on the HR diagram during periods of rapid evolution (i.e. the red giant branch (RGB), where many stars in our sample lie), and the density of model data points in these regions can be preventative in selecting a single model that is physically representative of the observed system. Since this is the case, we exercise caution when addressing the best fit models using this method.

To quantify the comparison between our models and observations, we computed the likelihood for each model at each time step, comparing the observed values of the stellar surface temperature, surface gravity, metallicity, and available abundances to those within the models. To find the best fit model, we minimize the χ^2 difference between the models and observations. One caveat to the χ^2 method is that it

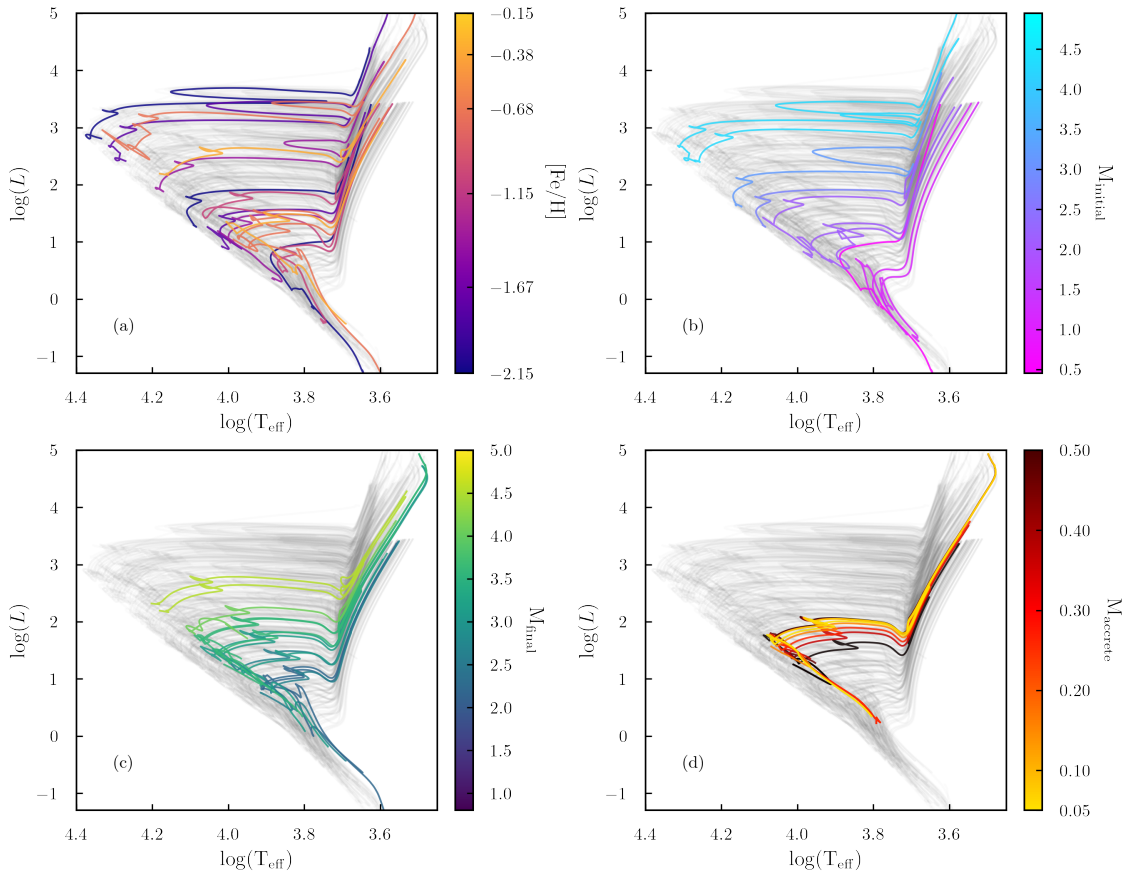

Figure 3.4: Our computed grid of evolutionary models in the HR diagram, displaying every 5th model in gray. Selected models are highlighted to show the range of parameters across the grid. Panel (a) shows the varying metallicities of our models, with purple models at lower metallicity and orange models at higher metallicities. These are spread across the Kiel diagram. On the giant branch, metal-rich evolutionary tracks fall to the right side of the giant branch towards cooler temperatures, where metal-poor giants are on the left side at higher temperatures. Panel (b) shows the range of initial masses, with lower initial masses in blue and higher initial masses in pink. Lower initial-mass models appear towards the bottom and right of the panel, and higher initial-mass models to top and the left. Panel (c) shows the range of final masses. The highlighted evolutionary tracks are for a fixed metallicity of -0.15, with green and yellow models showing higher mass and blue models showing lower mass. This parameter follows the same general trend as the initial masses. Panel (d) displays an example of the varying accretion mass in our models. The highlighted tracks begin at different initial masses all resulting in $m_{\rm final}$ = 2.50 $M_\odot$, at a metallicity of [Fe/H] = -0.15. Black tracks show higher accretion masses, and yellow tracks show lower amounts of accretion. From Dimoff et al. (2025).

generally assumes that the parameters being fit are uncorrelated; in our comparison, this is not true. The relative abundances of heavy elements are highly correlated with one another as well as the surface parameters. In many cases, the difference in χ^2 between best-fit models is small, indicating only subtle differences between them.

We computed probability distributions to estimate uncertainties in our modeling efforts. By calculating the distance between adjacent data points in each of the model parameters, we compute and normalize the volume of each grid cell $d\theta$ and integrate for the full volume of the grid θ,

$$d\theta = \frac{dZ}{\sum dZ} \frac{dM_{acc}}{\sum dM_{acc}} \frac{dM_i\, dM_{AGB}}{\sum dM_i\, dM_{AGB}}. \tag{3.2}$$

Using our calculated χ^2 values, we calculate the likelihood function $L(\theta)$ for each model. The probability is calculated by convolving the likelihood function with prior distributions for each fitting parameter,

$$P(Z) = \frac{\sum L(\theta)\Delta Z}{\sum \Delta Z} \tag{3.3}$$

where $L(\theta)$ is the likelihood function and ΔZ is the grid spacing in metallicity space, for example. This is performed for each model parameter Z, M_{AGB}, M_{init}, and M_{acc}, and provides an error envelope within the model space based on the likelihood where we can determine confidence intervals. The width of the probability distribution can be taken as representative uncertainties in the models. The condition we impose such that the AGB star must be more massive than the accretor imposes a prior on M_{init} and M_{AGB}, and for the other parameters we maintain a flat prior.

3.6.2 Validating the Model Fits

We compare one of the grid models to the grid as a fiducial set of observational parameters. This should result in a zero-value chi-squared and 100% model probability. In this comparison, we recover the inputs as the best fit model. Furthermore, we test sets of constraints and priors within our model comparison.

We first test by fitting only the stellar parameters, leaving surface abundances as free parameters, and vice versa. We find that this does not adequately find a single best-fit model. Considering the stellar parameters, single models are difficult to identify in dense regions of stellar parameter space, for example, on the RGB.

Considering the abundances, for a given AGB mass, we model accretion onto all initial masses within the grid lower than that of the AGB. Thus, there exist dense regions in abundance space as well. We find that stellar parameters and surface abundances are both necessary in making this comparison.

We test two conditions on the metallicity. First, we only allow comparison with models within metallicities set by three-sigma observational uncertainties around the observed [Fe/H]. This prevents many systems from finding best fit models, as the grid is widely spaced in metallicity. Second, we allow the comparison to probe metallicities only within in closest [Fe/H] bins. In both cases, we generally recover our input metallicities and the resulting populations are not significantly affected. Ultimately, we do not constrain our metallicities in our comparison, and we still recover input metallicities.

From stellar theory, we test visible mass constraints by setting priors on the preferred final mass of our stars to be either 0.8 $M_{\odot}$ for the metal-poor population or 2.50 $M_{\odot}$ for the metal-rich population. We find that these constraints too sharply confine our results. We do not impose any strict boundaries in the masses, as this is a key output parameter in our study. We opt to fit our models across the full range of stellar masses with only a flat prior.

We test the dependence on individual abundances. We test the removal of C, Mg, Pb in turn to determine if they make a significant difference. We find that C is important, particularly for the metal-poor population. Some of our observational datasets contain alpha elements, including Mg. We find observed Mg abundances consistently higher than the AGB yield predictions, and the inclusion of Mg and other alpha elements is a hindrance in finding the best fit model, decreasing the likelihood and probability that any given model fits the observed data. Previous studies on Galactic chemical evolution have also observed problems where the observations of Mg are systematically higher than the model predictions Romano et al. (2010); Prantzos et al. (2018); Jost et al. (2024). By this justification, we omit Mg and other alpha elements in the fitting routine, and focus on C and the s-process material that is produced in AGB stars.

As the end of the s-process, we find that any derived Pb abundances or upper limits are helpful in finding a best fit model. For the light- and heavy s-process elements, we test fitting the abundances individually as separate parameters or together in groups of [ls] and [hs]. The choice of which elements to include in the

groups (e.g., Nb within the [ls] group or Dy within the [hs] group) makes a difference in the quality of the fits. To remain agnostic to these choices, we treat the surfaces as individual parameters in our comparison.

3.6.3 Fits to Known Ba, CH, and CEMP-s Stars

We compare our model grid to the properties of known Ba, CH and CEMP-s stars. Comparing the effective temperature, surface gravity, metallicity, stellar mass, and elemental abundance patterns, we determine the most probable initial configuration to have produced the observations. We estimate the mass of the AGB star that transferred mass to the observed star, the initial and final mass of the chemically peculiar star, and the amount of accreted material required to reproduce the observed chemical signatures. We are able to recover the metallicity of the observed system with high accuracy. For each star, we visually examine the three best fit models according to their χ^2 values. In many cases, there is only a small difference in χ^2 between the best fit models. Before discussing the sample as a whole and the constituent populations of stars within our sample, we describe individual objects. Stancliffe (2021) analyzed a subset of 74 Ba stars from de Castro et al. (2016), although with fewer abundances compared to our inclusion of the data from Roriz et al. (2021b).

PV UMa We find a very good fit for this weak Ba star in both the Kiel diagram and abundance space, shown in the top panels of Figure 3.5. Our best fit to this star is a 2.40 $M_\odot$ star accreting 0.10 $M_\odot$ of material from a 2.50 $M_\odot$ AGB star at a metallicity of [Fe/H] = -0.37. The observed temperature The two best fit models could each be likely scenarios to produce this and other weak Ba star systems. Recently observed and studied by Dimoff et al. (2024), PV UMa is best fit on the second ascent of the giant branch, after the onset of core He burning. Computed abundances including carbon are well represented in the models, except for an over-abundance of Sr and an under-abundance of Ce. The low accretion mass and significant mixing on the giant branch results in relatively low surface abundances compared to the Ba strong stars.

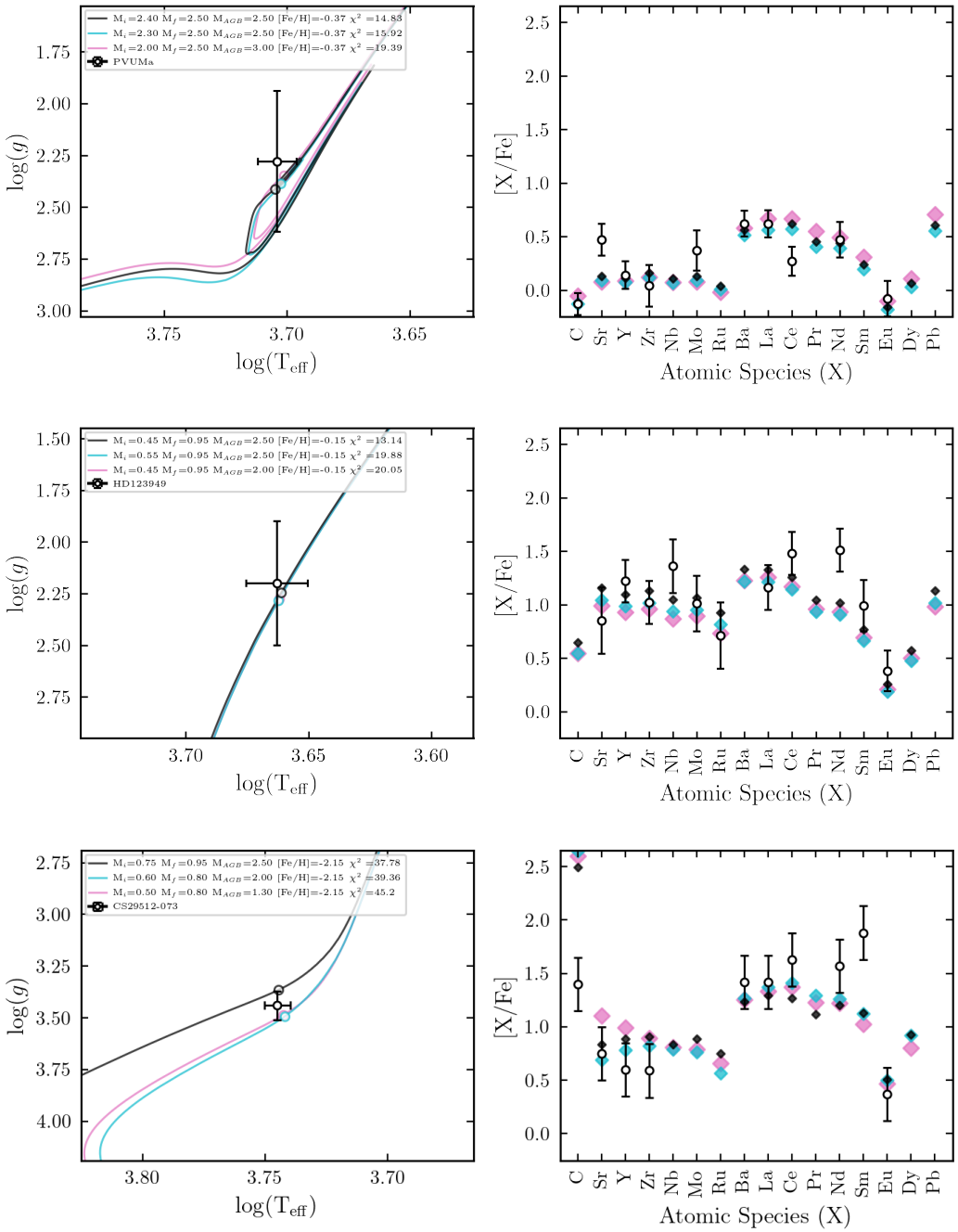

Figure 3.5: Kiel diagrams and abundance patterns for selected stars within our sample. We show the weak Ba star PV UMa, the strong Ba star HD 123949, and the CEMP-s star CS 29512-073, each showing the three best-fitting models and their associated χ^2 values. From Dimoff et al. (2025).

HD 123949 This object is representative of a large portion of the strong Ba stars in the de Castro et al. (2016) sample in both the Kiel diagram and in abundance space. An acceptable fit is obtained for this system, shown in the middle panels of Figure 3.5. This star lies directly on the evolutionary track for a 0.95 $M_\odot$ star and the abundances are well-fit, save for slight over-abundances in Nb and Nd. The low χ^2 values indicate a good fit, given the number of fitting parameters. We find best fit models to be low initial mass stars $M_i \sim 0.45 - 0.55$ $M_\odot$, accreting significant (> 0.40 $M_\odot$) amounts of material from a 2.50 $M_\odot$ AGB star, resulting in a 0.95 $M_\odot$ Ba giant. This does not fully agree with estimated Ba star masses from Escorza et al. (2017). More massive stars will have more massive convective envelopes, which will more efficiently mix and dilute surface abundances on the ascent of the giant branch, and a less massive accretor star will retain higher surface abundances.

CS 29512-073 In this CEMP-s star, we find an excellent match in metallicity with both observed and modeled [Fe/H] = -2.15. The precise observed stellar parameters are in good agreement with low-mass stellar evolution tracks on the sub-giant branch, with best fit final masses between $M_f = 0.80$ and 0.95 $M_\odot$. These values are in good agreement with theoretical masses of metal-poor stars. Carbon is over-produced by the models compared to the observations; thermohaline mixing on the main sequence could dilute the surface abundance of C to explain the observations. Abundances of heavy elements are generally well fit by our modeling, aside from a slight overabundance in Nd and an overabundance in Sm past the second s-process peak. The best fit AGB mass is 2.50 $M_\odot$, and our modeling suggests around 0.20 $M_\odot$ of material is accreted from the former AGB companion.

We present histograms of the main parameters of our models for our complete sample in Figure 3.6, where different populations are represented in different colors. The weak Ba stars are shown in cyan, the strong Ba stars in blue, the CEMP-s stars in red, and the CH stars in orange. While our grid is neither continuously nor equally spaced in initial and final mass, we are nonetheless able to make generalized statements about the progenitors of these post-accretion systems. We recover the metallicity distribution of stars in our sample, and since our model grid is limited to metallicities above [Fe/H] = -2.15, we make a cut on the observed stars at [Fe/H] $>$ -2.50.

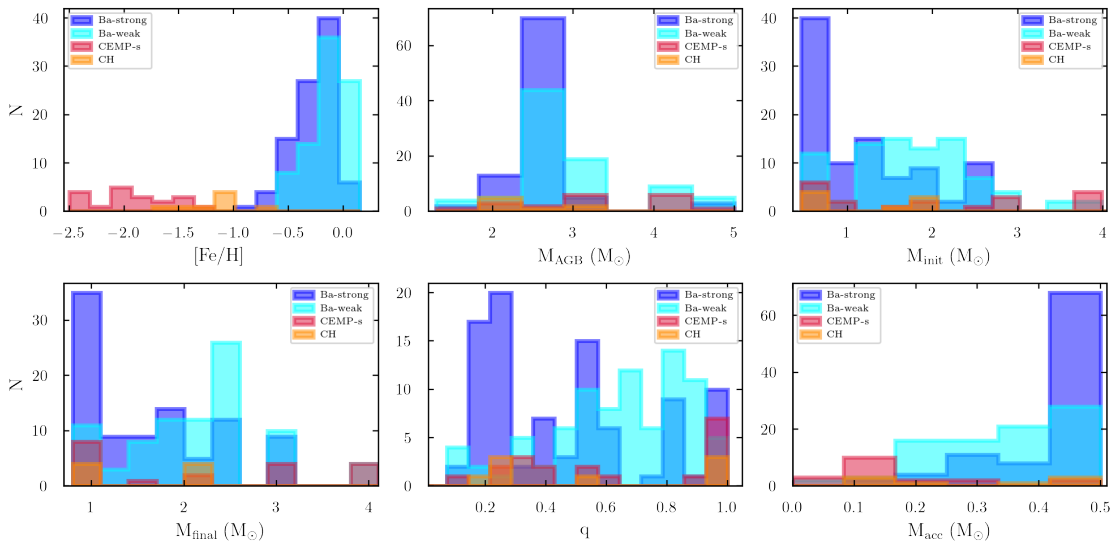

Figure 3.6: Histograms of model parameters for the different classes of stars in our investigation. Dark blue regions are strong Ba stars, cyan regions are weak Ba stars, red regions are CEMP-s stars, and orange regions are CH stars. From Dimoff et al. (2025).

Overall, there is a clear preference of donor AGB masses across all stellar classifications with a very strong peak at a mean AGB mass of $\langle M_{AGB} \rangle = 2.70$ $M_\odot$. This is expected, as the s-process production rates peak in this mass range. Fits to the strong Ba stars show a very pronounced peak at an AGB mass of 2.50 $M_\odot$, with a width of $\sigma = 0.52$ $M_\odot$. For the weak Ba stars, most of the fits suggest an average AGB mass of $\langle M_{AGB} \rangle = 2.80$ $M_\odot$. The distribution is broader compared to the strong Ba stars, with a width of $\sigma = 0.78$ $M_\odot$. For both the carbon-enhanced CH and metal-poor CEMP-s populations, the preferred AGB mass is $\langle M_{AGB} \rangle = 2.80$ $M_\odot$ with an even broader distribution ($\sigma = 0.88$).

Across the four different populations of post-accretion systems analyzed, all display non-gaussian behavior in their initial and final mass distributions. The weak Ba stars show a broad distribution in initial mass $\langle M_{init} \rangle = 1.70$ $M_\odot$ with a width of $\sigma_{M_{init}} = 0.74$, and final masses around $\langle M_{final} \rangle = 2.30$ $M_\odot$, and $\sigma_{M_{final}} = 0.75$. The mass ratios q of the weak Ba stars show a peak at higher values close to 0.90 with a tail down to low mass ratios of 0.10. The models suggest that weak Ba stars accrete moderate amounts of material; on average, they accrete about 0.35 $M_\odot$ from their AGB companion.

In the strong Ba stars, we find a very dominant peak at low initial masses around 0.5 $M_\odot$ with a tail extending up to 2.50 $M_\odot$. The final masses are concentrated at about 1.00 $M_\odot$ with a tail extending as high as 3.00 $M_\odot$. The mass ratios q of strong Ba stars are almost opposite that of the weak Ba stars, with most models fitting low q values of 0.20. There is a long tail extending to higher mass ratios, with a small peak at mass ratios close to $q = 1.0$. The models suggest that strong Ba stars accrete large amounts of material, with most fits showing $m_{\rm acc} = 0.50$ $M_\odot$. The distribution is strongly peaked at high accretion masses, with few systems indicating smaller amounts of accretion. This is more material compared to the weak Ba stars, which is reflected in the higher surface abundances observed in the strong Ba stars. We note this is the limit of our allowed accretion mass range.

At intermediate metallicities, the CH stars show initial masses with peaks at $\approx$ 0.50 $M_\odot$ and a small broader peak at $\approx$ 2.00 $M_\odot$. Final masses show corresponding peaks at $\approx$ 0.90 $M_\odot$ and around 2.10 $M_\odot$. Mass ratios in the CH stars are distributed between low ($\approx$ 0.20) and high ($\approx$ 0.98) values. The distribution of accretion masses in the CH systems display no clear preference in accretion masses. The number of CH stars in our sample is likely too low to make strong claims about the population as a whole.

At the lowest metallicities, the CEMP-s stars are somewhat scattered in initial and final masses. The majority of initial masses show peaks at $\approx$ 0.50 $M_\odot$ and $\approx$ 2.0 $M_\odot$ with a tail extending to higher initial masses. Most of the final masses show a peak around 0.90 $M_\odot$, with a second peak close to 2.70 $M_\odot$. As in the initial masses, there is a tail extending to higher masses. These could be dwarf stars in our sample, which are not as well modeled as the giant stars due to less intense convective mixing, or giant stars with very low surface gravities with values $\log(g) \leq 0.5$ and very high derived abundances [ls/Fe] or [hs/Fe] ≥ 1.50. Initial mass ratios for the metal-poor systems show two clear peaks at $q \approx 0.30$ and $q \approx 1.00$, with a preference for higher initial mass ratios. Our modeling finds low accretion masses around 0.10 $M_\odot$for the CEMP-s stars.

3.7 Discussion

The strong Ba stars almost always accrete the maximum amount of mass, and the final mass distribution we recover does not fully agree with that of Escorza et al. (2017), where we find lower initial and final masses for many strong Ba stars by about a full solar mass. At higher masses, the more massive convective envelope dilutes surface abundances more efficiently compared to lower masses, and to maintain the observed higher surface abundances in the strong Ba stars, lower masses are required. We note our sample of Ba stars is only from de Castro et al. (2016) and Dimoff et al. (2024), where the larger Escorza et al. (2017) sample includes the de Castro et al. (2016) data set, plus more Ba stars compiled from Lu et al. (1983); Lu (1991); Edvardsson et al. (1993); Bartkevicius (1996). The differences in average mass could be influenced by the larger sample.

We find that when accretion happens while the secondary is on the first ascent of the giant branch, the mixing processes within the advancing convective region have a significant effect in quickly diluting the surface abundances. Our models generally suggest higher accretion masses in secondary stars accreting on the main sequence or while first ascending the giant branch, compared to those accreting close to the tip of the RGB or near the onset of core He burning. This is also due to evolutionary reasons, where in systems with mass ratios $q \approx 1$ the primary and secondary stars are of near equal mass and can evolve nearly simultaneously.

Comparing our models and the observational data, we find better fits when observed abundances have lower uncertainties, and when there are more observed abundances available in the pattern. Overall, the CEMP-s and CH datasets have fewer observed abundances than the Ba stars in our sample. The average uncertainty in the Dimoff et al. (2024) abundances is $\sigma_{[X/Fe]} \sim 0.15$, where in the combined de Castro et al. (2016) and Roriz et al. (2021b) dataset it is $\sigma_{[X/Fe]} \sim 0.20$, and we find consistently smaller uncertainties approximately equally important when there are fewer computed abundances. The combined dataset from Cristallo et al. (2016) (and references therein) has average abundance uncertainties of $\sigma_{[X/Fe]} \sim 0.23$, and the CEMP-s stars dataset from Goswami et al. (2021) reports uncertainties of $\sigma_{[X/Fe]} \sim 0.25$, on average.

In the evolution of low-mass metal-poor stars, we generally find the accretion happens while the secondary star is on the main sequence. With initial AGB masses

much higher than accretor masses (2.50 $M_\odot$ vs. <1.00 $M_\odot$), the secondary star is on the main sequence when the AGB star begins thermal pulsations. Without thermohaline mixing, the surface abundances remain nearly constant until the onset of first dredge-up, making the differentiation between best fit models in this regime difficult (Stancliffe et al., 2007; Stancliffe and Glebbeek, 2008). Thus we find this set of models better for analyzing giant stars, and main sequence stars may not be as representative.

We find it unlikely that all barium stars are observed shortly after the accretion process has ended, as would need be the case for initial mass ratios very close to $q = 1$, where mixing on the giant branch is very effective and quickly dilutes surface abundances (see the right panel in Figure 3.2). Thus, larger accretion masses at lower initial mass ratios make sense for stars that exhibit large surface abundances of heavy elements. As the secondary star gains mass, it will alter its evolutionary path to follow that of the post-accretion mass. Some models in the grid have initial mass ratios $q > 1.0$ where the secondary star is more massive than the primary and would evolve more quickly. While these models could be useful in analyzing systems with multiple mass transfer events, we do not consider these models in this analysis, where mass transfer does not happen during the lifetime of the secondary.

A few stars in our sample are poorly fit due to relatively low surface gravities ($\log(g) \leq 0.50$), very high surface abundances of heavy elements where [ls/Fe] or [hs/Fe] ≥ 2.00, large amounts of Eu compared to the s-process elements, or some combination of these. For some observed systems, only one derived elemental abundance exists in each of the s-process peaks, providing only weak constraints within the fitting routine. Very few evolutionary tracks with high elemental abundances extend toward the upper part of the giant branch in the Kiel diagram, and the ones that do show in high masses close to 5.00 $M_\odot$ that do not agree with the theoretical masses of stars in our observational sample. These also correspond to AGB masses of 5.00 $M_\odot$, by the construction that the AGB mass must be larger than the initial mass of the observed star. Large χ^2 values on the order of ≥ 60 indicate poor fits in these instances. Fits resulting in high stellar masses often find flattened abundance patterns indicating the accreted material has been fully diluted, and the surface abundances have effectively returned to the un-enhanced values.

3.7.1 Mixing and Dilution

Matrozis and Stancliffe (2016) found that atomic diffusion does not have a substantial effect on the surface abundances of CEMP-s stars. As such, the dilution of the accreted material is most likely the same for all elements, and the mass ratios and overall pattern will be preserved. Thermohaline mixing on the main sequence will dilute the surface abundances to some extent. Stancliffe (2021) tested the inclusion and exclusion of thermohaline mixing in Ba stars, and after the onset of FDU the surface abundance ratios of heavy elements between the two cases are nearly identical. Convective mixing processes in metal-rich giant stars outweigh thermohaline mixing, and the overall level of mixing in both scenarios is the same after FDU.

In more metal-poor stars this is not always the case; Stancliffe et al. (2007) found that thermohaline mixing on the main sequence is effective for light elements C, N, and O, and predicts different surfaces abundances for CEMP-s stars compared to models with only convective mixing. Modeling additional mixing processes, Stancliffe and Glebbeek (2008) found that the effects of gravitational settling inhibit thermohaline mixing in CEMP-s stars and, in cases where a small quantity of material is accreted, mixing can be suppressed almost entirely. Low surface gravities indicate evolution on the upper part of the giant branch, where THM is effective in diluting surface abundances (Stancliffe, 2015).

The accretion phase in our models coincides with the AGB phase of the donor, so the initial mass ratio of the system effectively controls when the accretion happens during the lifetime of the secondary. If accretion occurs while the secondary is on the main sequence or on the sub-giant branch, the onset of first dredge-up (FDU) will severely deplete the surface abundances. If accretion happens after the onset of FDU, significant mixing will still occur within the convective envelope.

3.7.2 Angular Momentum

Matrozis et al. (2017) suggests that in the wind regime only about 0.05 $M_\odot$ of material is accreted before the star reaches critical rotation. The specific angular momentum of the accreted material should be be lower than the Keplerian value by about an order of magnitude, or significant angular momentum losses must occur for substantial accretion to take place. We find small amounts of mass transfer are able to explain the chemical enrichment of many CEMP-s stars, and this may happen in

the wind regime.

This may not be a significant issue for the weak-Ba stars, where the larger radius of the giant accretor star requires more angular momentum transfer to reach the critical rotation velocity, allowing more mass to be accreted. The strong Ba stars require more accreted mass to reproduce the patterns. The angular momentum transfer poses a problem for the strong Ba stars. The high amounts of required material for the Ba stars suggests that BHL wind mass transfer is not applicable to these systems.

3.7.3 Accretion Efficiencies

For our binary systems, we compute the accretion efficiency η_{acc} by dividing the amount of mass gained by the accretor by the total mass lost by the AGB star in the system:

$$\eta_{acc} = (m_{final} - m_{initial})/(m_{AGB} - m_{WD}) \times 100\ [\%]. \tag{3.4}$$

In this sense, we assume non-conservative mass transfer. We estimate white dwarf masses using tabulated H-exhausted core masses from Cristallo et al. (2015) for the given AGB mass and metallicity of the model. We compare the white dwarf masses from the FRUITY models used in this study to computed dynamical mass estimates from Dimoff et al. (2024) and find good agreement. Additionally, we find no significant differences between our samples of CH and CEMP-s stars in this analysis of accretion efficiencies and, in respect to accretion efficiencies, we treat them as one metal-poor and carbon-rich population following Jorissen et al. (2016). We note that the lack of chemical differences could be due to the relatively low number of CH stars studied.

In Figure 3.7 we compare our computed η_{acc} to 3D hydrodynamical wind mass-transfer models from Liu et al. (2017), where the black dashed and dotted lines are linear and 5th order polynomial fits from the 3D models respectively. These simulations generally result in low accretion efficiencies, with a trend toward higher efficiencies at higher mass ratios.

The models in our grid are discrete points, and often the same model is chosen to represent multiple systems. For this reason, we present our populations as density contours in $\eta - q$ space. We see a general trend of increasing efficiency η with de-

creasing mass ratio q across the different stellar populations. The metal-poor stars require less accretion in systems with initial mass ratios closer to $q = 1$ to reproduce the observed surface abundances, resulting in lower efficiencies. The bimodal distribution of the carbon-enhanced systems is well-shown in the density contours. At lower mass ratios below about $q \leq 0.5$, there are only a few carbon-enriched systems with relatively low mass-transfer efficiencies, $\approx 10\%$. Higher metallicity systems with lower mass ratios congregate in efficiencies around $\sim 25\%$; these are the strong Ba stars. Generally, we find that accretion masses greater than about 0.30 $M_\odot$ will result in efficiencies higher than the theoretical wind mass transfer regime described in Liu et al. (2017).

3.7.4 Orbital Properties

Orbital periods and eccentricities, collected from Jorissen et al. (1998), Udry et al. (1998), Lucatello et al. (2005), Hansen et al. (2016b), Karinkuzhi and Goswami (2014), Goswami et al. (2016), Jorissen et al. (2016), Goswami et al. (2021), and Dimoff et al. (2024), are shown in Figure 3.8, where cyan data points are weak Ba stars, blue data points are strong Ba stars, orange data points are CH stars, and red data points are the CEMP-s stars. There is significant scatter in the $e - P$ relation, even within single populations, and many systems show high orbital eccentricities. We compute and mark the centroids of the populations of stars. The strong Ba stars and weak Ba stars tend toward slightly higher eccentricities ($\langle e \rangle = 0.18$ and 0.25, respectively) compared to the CEMP-s and CH stars ($\langle e \rangle = 0.11$ and 0.12, respectively). The weak Ba stars and CH stars have on average longer periods ($P \approx 4500$ days) compared to the strong Ba stars and the CEMP-s stars ($P \approx 2300$ days), although the spread in these data overlap with each other. Mass transfer should aid in circularizing the binary orbits through tidal interactions and angular momentum transfer, and the older more metal-poor populations show orbital eccentricities closer to zero than the younger, more metal-rich populations. Krynski et al. (2025) have made progress explaining the spread of orbital eccentricities in these post-accretion systems with the inclusion of a circumbinary disc to assist in angular momentum transport and enhancing the orbital eccentricity.

When applying the accretion mass as a dimension to the $e - P$ plane, we find no significant trends with orbital period or eccentricity. In Figure 3.9, we see large

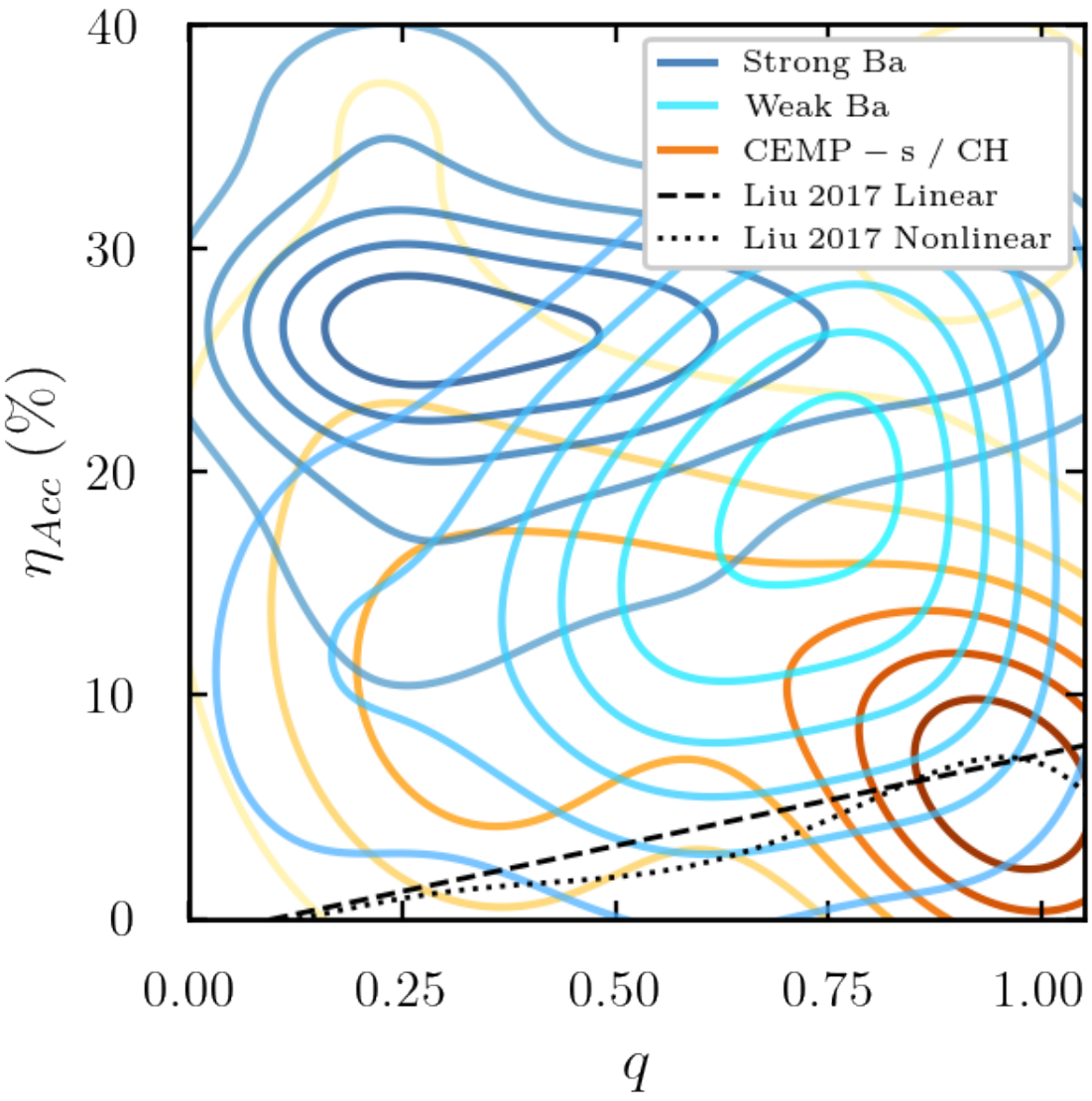

Figure 3.7: Computed accretion efficiencies for our sample populations. Dark blue contours are the strong Ba stars, and light blue contours are the weak Ba stars. Red-yellow contours represent our full carbon-enhanced sample, including both CH and CEMP-s stars. From Dimoff et al. (2025).

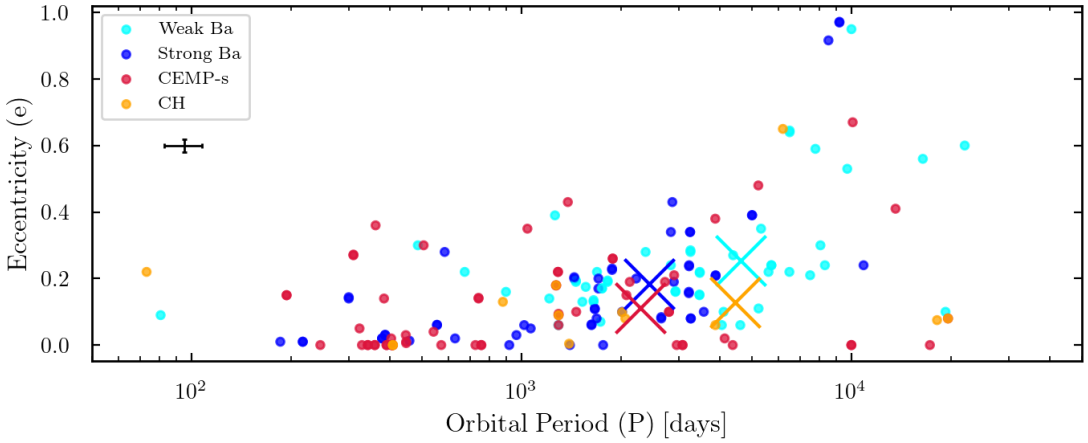

Figure 3.8: Eccentricity-period diagram for our combined sample of stars. Cyan data points are weak Ba stars, blue data points are strong Ba stars, orange data points are CH stars, and crimson data points are the CEMP-s stars. Centroids of the populations are marked with X's of corresponding colors. A characteristic errorbar is placed below the legend. From Dimoff et al. (2025).

scatter in the orbital period for all systems. We observe systems with high accretion masses at long and short orbital periods, and across eccentricity space. Systems with moderate and low accretion masses present no trend with orbital period. While there are more systems with lower accretion masses at lower eccentricities, this is likely an observational bias, where few data points exist at high eccentricities.

3.7.5 Possible Mass Transfer Scenarios

The mechanism of mass transfer in AGB stars is directly linked to the properties of the initial binary orbit and the relative velocity of the AGB wind compared to the orbital velocity. There are multiple regimes in which mass transfer can occur. With mass transfer comes angular momentum transfer, which will perturb the initial orbital configuration. The resulting orbit will likely not be the same as the initial orbit of the binary.

Krynski et al. (2025) suggest that WRLOF and non-conservative mass-transfer with the presence of a circumbinary disc provides mechanisms for both high accretion efficiencies and enhanced eccentricities, explaining the observed orbital geometries

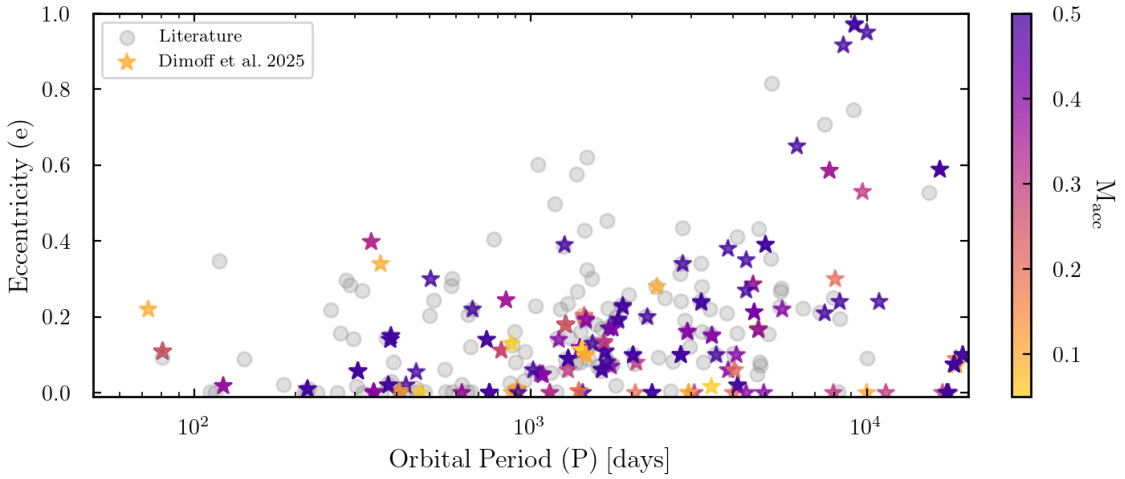

Figure 3.9: Eccentricity-period diagram with a third dimension of accretion mass indicated by the colorbar. Our sample is shown in the star-shaped data points, and the grey data in the background is compiled orbital data from the literature.

of these post-accretion systems. For slow and dense stellar winds with low wind velocities compared to the orbital velocity, structures resembling wind Roche-lobe overflow form as the stars approach periastron, indicating a form of tidally enhanced mass transfer (Mohamed and Podsiadlowski, 2007, 2012). Through this process, the circumstellar outflows are non-spherical and concentrated in the orbital plane of the binary. The non-symmetric flows contribute to maintaining or increasing the eccentricity of the binary system. Abate et al. (2013) discusses WRLOF in the context of binary population synthesis for the CEMP-s stars, finding that, pending the stability criterion, in short period systems, RLOF is likely to occur. However, most $> 70\%$ of the CEMP-s stars in their synthetic population have wide orbits and accrete through some form of wind-driven mass-transfer. In this work, we find that most CEMP-s stars accrete small amounts of material, consistent with the wind mass-transfer regime.

3.7.6 Mass Distributions of Post-Accretion Systems and their White-Dwarf Companions

In Ba stars, an empirical relation similar to the binary mass function has been proposed by Jorissen et al. (2019) to quantify correlations between the masses of

the two system components,

$$Q = \frac{M_{WD}^3}{(M_{Ba} + M_{WD})^2}, \tag{3.5}$$

where M_{Ba} is the mass of the barium star and M_{WD} is the mass of the white dwarf in solar masses. We tabulate our findings in Table 3.1. In our sample of strong Ba stars, we find the median value of $Q = 0.055$. Overall, the distribution is highly non-Gaussian, with the mode of the strong Ba stars at $Q = 0.041$ and a second peak around $Q \approx 0.100$. For the weak Ba stars, we find a median value of $Q = 0.032$, where the mode of the distribution is at $Q = 0.025$. Results from Jorissen et al. (2019) suggest the distribution of Q values at high metallicities is bimodal, with peaks at $Q = 0.057 \pm 0.009$ for the strong Ba stars and $Q = 0.036 \pm 0.027$ for the weak Ba stars. In our analysis, both classes of Ba stars are within the bounds of the wide distribution determined by Jorissen et al. (2019), and the median values of the distributions are in good agreement.

We extend this to the metal-poor regime and investigate trends in the value of Q with metallicity. To increase the statistics, we combine our samples of CH and CEMP-s stars. We find a median value of $Q = 0.043$, where there exists a prominent peak at a value of $Q = 0.037$, and a smaller secondary peak at values $Q = 0.120$. This suggests that lower metallicities overall have smaller Q values. As in our samples of Ba stars, the distribution in Q is non-Gaussian, where the median and mean averages are substantially different within each population. The secondary peaks in these populations could highlight the dwarf stars, where the models are less constrained by the lack of mixing and dilution of surface material.

Table 3.1: Computed Q values for the different populations of stars. From Dimoff et al. (2025).

Class	median(Q)	mode(Q)
Ba-weak	0.032	0.025
Ba-strong	0.055	0.041
CEMP-s + CH	0.043	0.037

3.8 Conclusions

In this study, we compute a large grid of binary accretion models to investigate the progenitor configurations of the Ba, CH, and CEMP-s stars. We find that the preferred model to explain weak Ba stars is a system that results in a $M_{final} = 2.50$ $M_\odot$ secondary, accreting a moderate amount of mass $m_{acc} \leq 0.40$ $M_\odot$ from a $2.00 - 3.00$ $M_\odot$ primary AGB star. We find that strong Ba stars tend to have lower initial masses $M_{init} \sim 0.6$ $M_\odot$ and accrete more material $m_{acc} \geq 0.50$ $M_\odot$ from 2.50 $M_\odot$ AGB stars, resulting in higher accretion efficiencies at lower initial mass ratios. Both subclasses of metal-rich Ba stars accrete moderate to high amounts of enriched material. This could be due to higher mass-loss efficiencies at higher metallicities, or higher masses where the convective envelope mixes more strongly than in lower mass stars. In both cases, we find that BHL wind mass-transfer models cannot explain the accretion masses and efficiencies.

The CH and CEMP stars are similar in many ways. Together, they share a preference for a $2.00 - 3.00$ $M_\odot$ AGB donor and both show bimodal behavior with peaks at lower (~ 0.80 / ~ 1.00 $M_\odot$) and higher masses ($\sim 2 - 3$ $M_\odot$) in initial and final mass respectively. The initial mass ratios for these metal-poor and carbon-rich systems are also bimodally split between $q \approx 0.2$ and $q = 1$, and they tend to accrete less material (~ 0.1 $M_\odot$) from their AGB companion compared to the metal-rich systems. These stars display lower accretion efficiencies, allowing better agreement with the BHL wind regime. Less massive convective envelopes do not mix the accreted material as thoroughly compared to the more massive and more metal-rich stars, allowing for less accretion while maintaining large enhancements in s-process material. Accretion in this regime is supported by their long orbital periods and comparatively lower eccentricities.

4 Measuring the Neutron Interaction cross section of ^{208}Pb

4.1 Motivations

Many reactions relevant to the s-process remain poorly constrained experimentally. The interpretation and modeling of observed s-process abundances in stars critically depends on accurate neutron-capture reaction rates under astrophysical conditions. We aim to better understand neutron capture reactions at low energies relevant to the strong component of the s-process taking place in low-mass asymptotic giant branch (AGB) stars. By performing activation experiments to obtain direct cross-section measurements, we provide essential nuclear physics inputs needed for stellar nucleosynthesis models. These experiments enable precise predictions of elemental and isotopic abundances and provide a robust connection between nuclear processes and the observed chemical signatures in AGB stars and post-AGB binaries. Accurate reaction rates also help identify which isotopes dominate branching points in the s-process path, improving our understanding of nucleosynthesis in low- and intermediate-mass stars.

What's New: Using the novel ring-activation method, we experimentally reproduce the conditions of stellar interiors. We measure the neutron interaction cross section of Pb at $k_BT = 25$ and establish an upper limit for the cross section at 5 keV.

4.2 Abstract

We investigate the neutron interaction cross section of ^{208}Pb at astrophysical energies relevant to the nucleosynthetic slow-neutron capture process (s-process), $k_BT = 5$

and 25 keV, by means of the ring-activation technique. The activation experiment was performed using a quasi-stellar neutron source at the Goethe University Frankfurt Van-de-Graff accelerator with a proton energy of 1918 keV. Protons were accelerated onto a Li target to produce neutrons with a quasi-Maxwellian energy distribution of $k_BT = 25keV$ via the reaction 7(Li,p)n7Be. Natural Pb samples are placed behind the Li target with Au neutron monitors. The neutron flux through the sample was determined relative to the well-known cross section $\langle\sigma^{Au}\rangle_{SACS}$. Through neutron capture, ^{208}Pb becomes ^{209}Pb and decays via β^--decay with a half-life of 3.257 hours. The induced activities were measured using β^- spectroscopy with broad-energy Germanium (BEGe) detectors, and we computed the number of activated nuclei in each Pb sample. The total β^- detection efficiency of the two detectors was estimated using the GEANT simulation. We measure the neutron capture cross section $\sigma_{25} = 18.87 \pm 6.18$ mb and the upper limit $\sigma_5 < 41.58$ mb. Within 3σ uncertainties, the cross section at 25 keV is in statistical agreement with literature values. Our upper limit of the cross section at 5 keV is larger than the computed literature value from et al. (1998). Together with our measurement at $k_BT = 25$ keV, Maxwellian-averaged capture (MACS) cross sections at the thermal energies of the s-process, i.e., at $k_BT = 8$ and 23 keV, can be interpolated.

4.3 Methods

4.3.1 PINO Simulations

We use the PINO (Protons In Neutrons Out) tool (Reifarth et al., 2009) to simulate the neutron flux through our samples at different energies. PINO is a Monte Carlo based program that simulates a neutron spectrum for an activation experiment from the 7(Li,p)n7Be reaction. It simulates the number of produced neutrons, as well as the σ_{SACS} for gold at different energies and geometries. The simulation requires the proton energy, the neutron production target including the thickness in microns and the target geometry, the activation sample geometry, and the distance between the sample and the neutron production Li target. We optimize the target size and distance to match a desired neutron energy spectrum.

We determine the optimal sample shape and distance from the beam source to the Pb target to capture the desired 5 keV neutron spectrum. Our targets have two

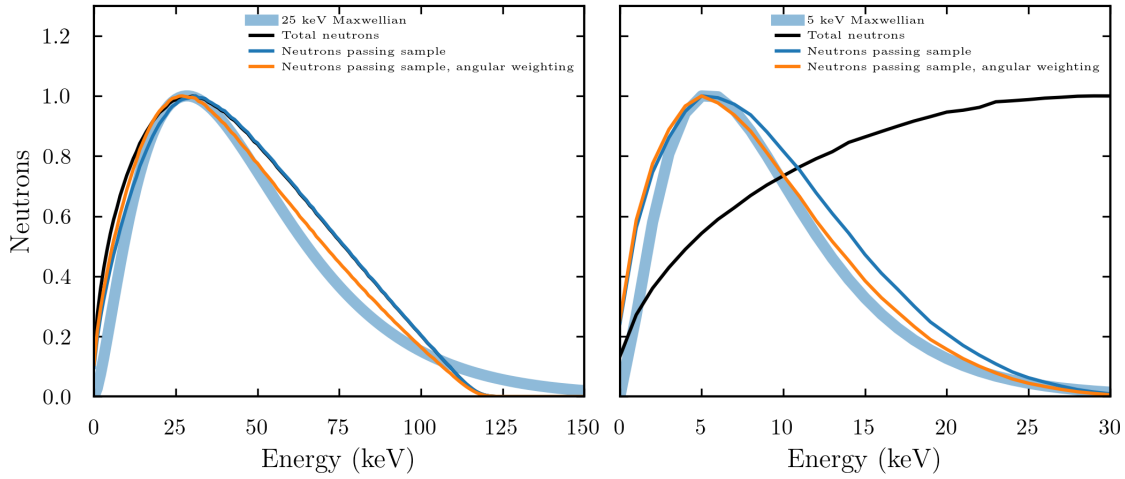

Figure 4.1: Simulated neutron spectra using PINO. Left: $k_BT = 25$ keV quasi-Maxwellian neutron spectrum for a disc shaped target. Right: $k_BT = 5$ keV quasi-Maxwellian neutron spectrum for a ring-shaped target.

components: the inner discs have an radius of 5 mm, and the outer rings have an inner radius of 5 mm with an outer radius of 10 mm. We find the best distance to produce the 5 keV neutron spectrum to be 2.25 mm, using an proton energy of 1918 keV. At this distance, we estimate a total number of 5.07×10^7 neutrons will pass through our Pb ring targets. In Figure 4.1 we compare Maxwellian distributions to the simulated neutron spectra. In each panel, the total neutron spectrum is shown in black, and the total number of neutrons passing through the sample are shown in blue and orange, including the geometric angular weighting.

4.3.2 Detector Setup

To measure the activity of the radionuclei, we use semiconductor broad energy germanium detectors (BEGe). These detectors have a high efficiency over a wide energy range of 3 keV - 3 MeV, ideal for γ-spectroscopy. Each detector is housed in a vacuum chamber, attached to a liquid nitrogen dewar. Germanium has a relatively small band gap at room temperature ($E_G = 0.7$ eV), and the detectors must be cooled using liquid nitrogen (77 K) to reduce the background current. To minimize the background noise during the measurement, the detectors are housed in a lead "castle". Background X-ray radiation is reduced by lining the castle with a copper tank. To measure the activity, samples and monitors are individually

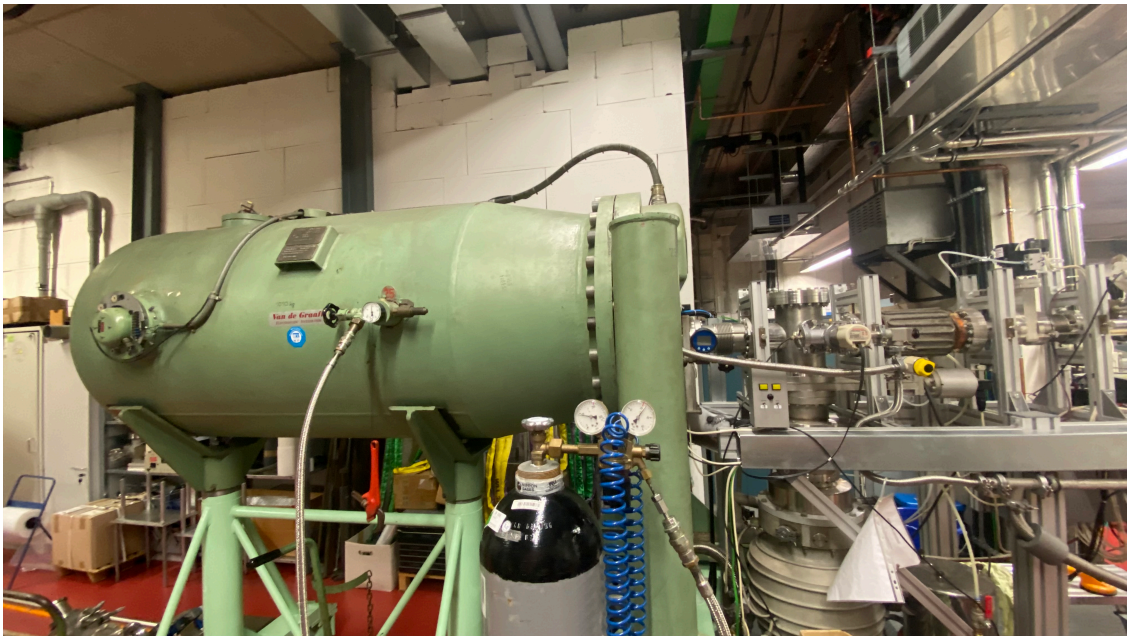

Figure 4.2: 2.5 MV Van-de-Graff accelerator at the Goethe University Frankfurt Institute for Nuclear Physics (IKF). The beamline continues to the right where the ^{7}Li target, our target samples, and the Li-glass scintillator are located.

inserted between the detectors. The two detectors are positioned on a movable rail, allowing the distance between the detectors and the sample to be adjusted. The distance indicator on the rail is not perfect, and requires further calibration. We place the sample close to the BEGe detectors at a nominal distance of 1.0 cm to maximize the detection rate of the escaping particles.

4.3.3 Experimental Setup

Proton Generation

Protons are extracted from a high frequency ion source and accelerated with an electrostatic 2.5 MV Van-de-Graff accelerator, seen in Figure 4.2. We accelerated protons to an energy of 1918 keV, and beam them onto a ^{7}Li target to produce thermal neutrons. We ensure a narrow energy distribution using an energy analyzing dipole with a spread of about 2 keV. Quadrupole magnets focus the beam onto the Li target position without major losses.

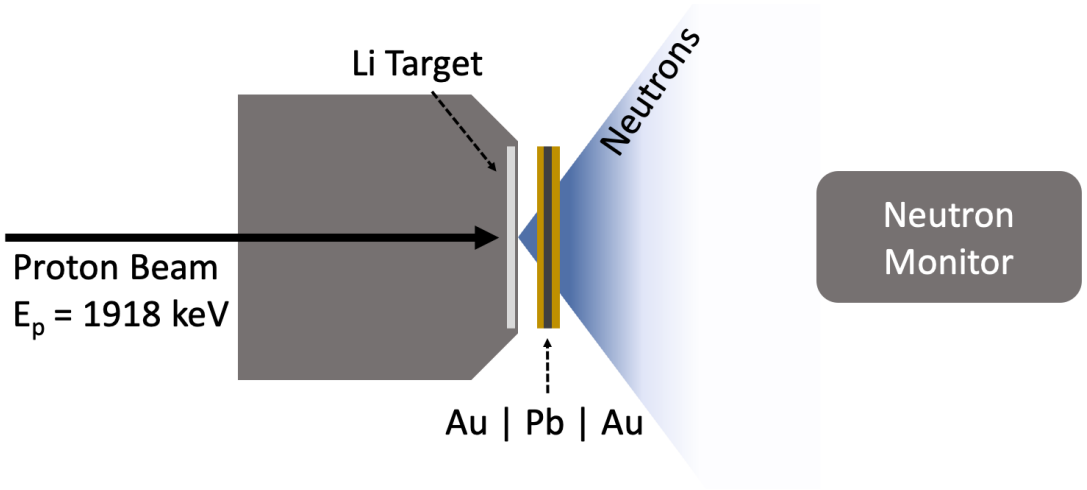

Figure 4.3: Setup for the activation measurements.

Neutron Generation

Neutrons from the ^{7}Li(p,n)^{7}Be reaction are emitted in a cone with an opening angle of $\sim 120°$ (Figure 4.3). The neutron energy decreases with radius from the center of the cone. The highest energy neutrons are more tightly beamed, and lower energy neutrons are only weakly beamed. Fluctuations in the neutron flux were determined using a Li-glass scintillator detector positioned behind the target. The scintillator is enriched in ^{6}Li and produces ions through an (n,α) reaction. When ionizing particles enter the scintillator, they excite electrons which, upon returning to their ground state, emit low-energy photons. These photons are collected in a photomultiplier via an optical fiber.

We use these neutrons to activate disc- and ring-shaped targets of ^{208}Pb. From the neutron bombardment, we form the radioisotope ^{209}Pb. The only way to detect the decay of ^{209}Pb to ^{209}Bi is through the detection of β^{-} particles, as there is no decay channel where γ photons are released. From our PINO simulations, the rings are designed to probe 5 keV neutrons, and combining the two target components probes neutron energies of 25 keV. This allows us to interpolate between for the 8 keV region.

4.3.4 Samples

The average energy of the β^- particles released from the ^{209}Pb decay is 197.5 keV, and the end-point energy, or maximum kinetic energy is 644 keV. We compute the maximum and the optimal thickness of our targets based on the kinetic energy and transmission of the β^- particles. In Figure 4.4, we see that with the maximum kinetic energy of 644 keV, the total stopping power is 1.12 MeV cm^2/g. At the average kinetic energy of 197.5 keV, the total stopping power is 1.43 MeV cm^2/g. At these energies, we remain in the collision-dominated regime. Radiative contributions from bremsstrahlung only become significant at higher kinetic energies, around ∼10 MeV.

Using the maximum stopping power and the formula $\frac{1}{\rho}\langle\frac{dE}{dx}\rangle = S(E)$ we calculate an upper limit of our target thickness $dx = 0.474$ mm for our ^{208}Pb foil target. A Pb target thicker than this will not allow electrons with energies lower than the maximum energy to traverse the width of the sample. Using the mean β^- particle energy of 197.5 keV, we compute a optimal target thickness of 0.12 mm.

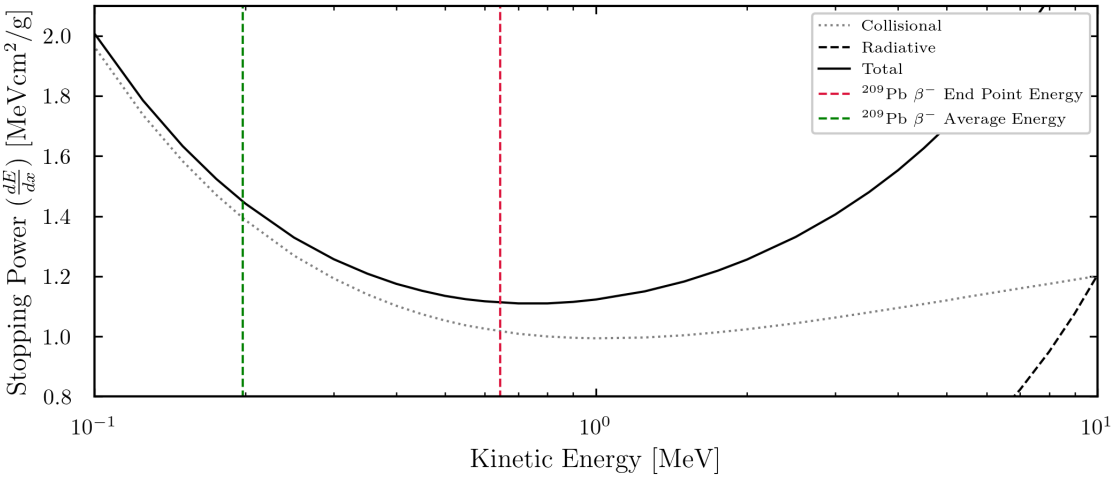

Figure 4.4: Total stopping power as a function of energy for electrons traveling through Pb, with contributions from collisions and bremsstrahlung shown in dotted and dashed lines respectively. Data collected from the ESTAR database (Berger, 1992).

Transmission Coefficients

The electrons emitted by the β^- decay can be self-absorbed by the ^{208}Pb target. If the target is too thick, the electrons will not be able to escape the Pb sample and make it to our detectors Eyring (1962). At low energies the transmission is dominated by the inelastic scattering of other electrons within the material, and the low-energy modified version of the Bethe-Bloch formula in Equation 1.79 is implemented, where we additionally consider the quantum indistinguishability of the incident and scattered electrons.

For a range of energies we compute the transmission coefficients $T(E)$, or the ratio of electrons that escape to those that are stopped within the material,

$$T(E) = E^{(-d/R(E))}, \tag{4.1}$$

where, in this expression, $R(E)$ is the Continuous Slowing Down Approximation (CSDA) range. The CSDA range is calculated following Equation 1.84, using

$$R(E) = 0.412 * E^{(1.265-0.0954*ln(E))} * \rho \tag{4.2}$$

where ρ is the density of the medium through which the particles are traveling. The CSDA range assumes a linear trajectory as the longest possible path length through a material as the particle slows down to rest, and is attenuated by the density of the material through which it is traveling. This is crucial in understanding how many particles escape the target and are available for detection. Figure 4.5 shows computed CSDA ranges for β^- particles traveling through Pb as a function of kinetic energy. These ranges correspond to the computed target thicknesses above.

In Figure 4.6 we show transmission coefficients as functions of energy for different thicknesses of Pb targets. We see that for thicknesses less than 0.1 mm, we retain $\sim$30% of the electrons with energies $E = 200$ keV, and $\sim$ 3% of electrons with energies $E = 100$ keV. Combining this with simulated expected β^- counts at different target thicknesses, we can optimize the two curves such that we maximize the produced β^- particles and minimize the particle self-absorption.

We simulate neutron counts for a theoretical activation of three times the half-life of ^{209}Pb for different thicknesses of a Pb target in Figure 4.7. The counts are estimated using a minimal waiting time of five minutes between activation and

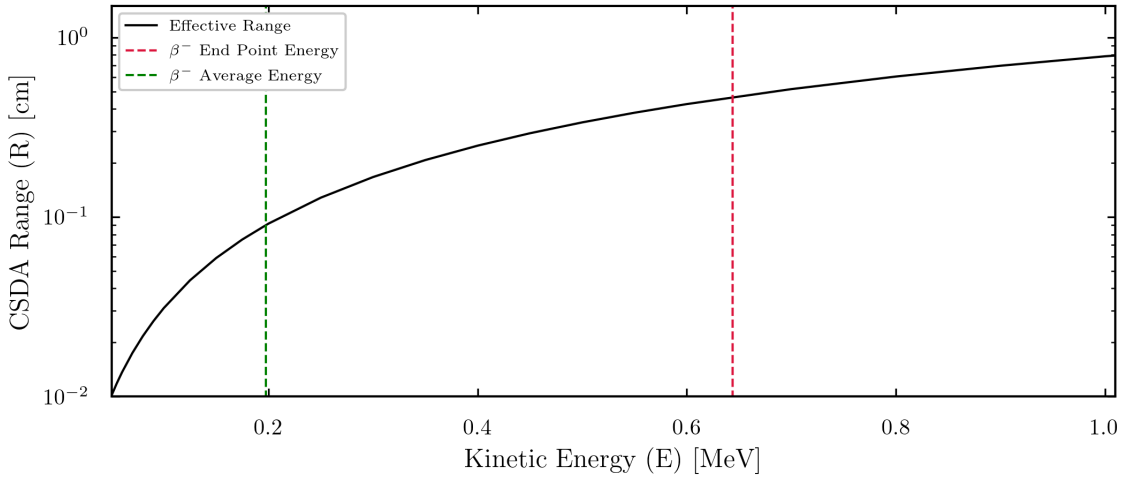

Figure 4.5: Continuous Slowing-Down Approximation (CSDA) range of β^- particles passing through Pb as a function of β^- kinetic energy.

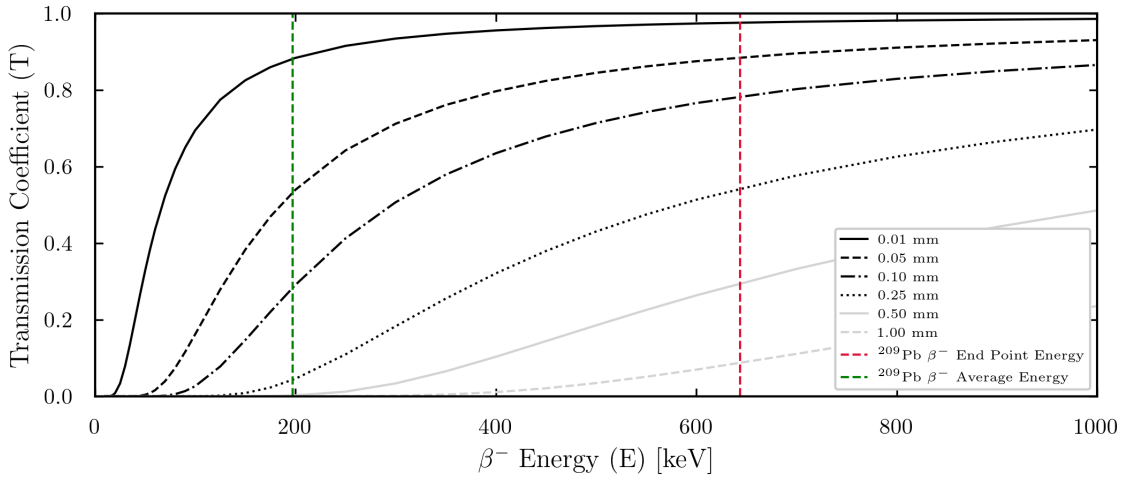

Figure 4.6: Transmission coefficients as functions of energy for electrons traveling through natural Pb. Different thicknesses of Pb are shown in different line-styles.

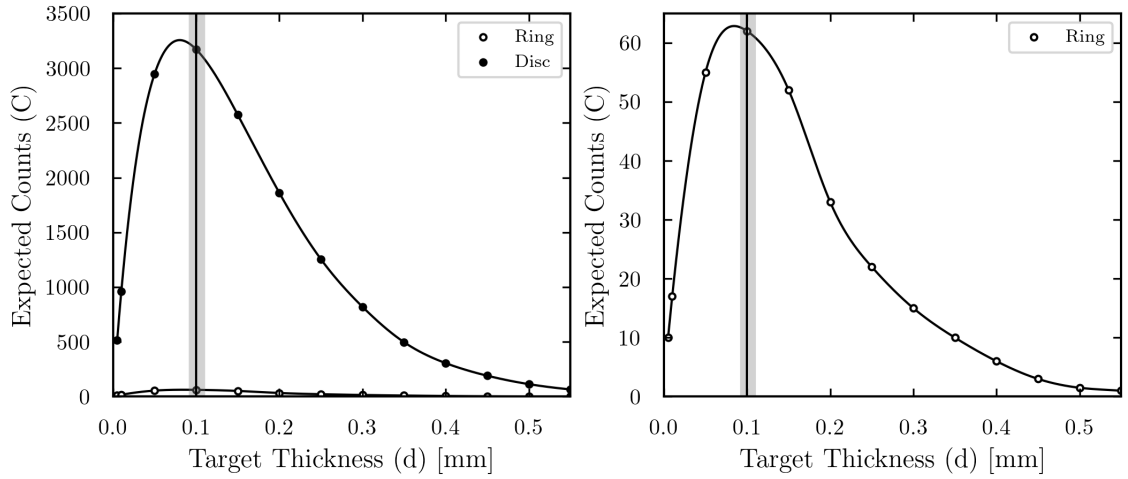

Figure 4.7: Simulated β^- counts as a function of target thickness for the inner disc (Left) and the outer ring (Right). Data points are the estimated counts at the given thickness, and the curves are cubic spline fits to the data. The outer ring captures the 5 keV neutron spectrum, where the full disc captures the 25 keV neutron spectrum.

measurement. In reality, the activity of the inner disc will be measured after the ring with a longer waiting time. There neutrons in the center of the beam are higher energy and more numerous, and we expect a higher activity from the disc.

The simulated counts for the Pb ring are about two orders of magnitude less than the disc, since the ring captures fewer neutrons at lower energies. From this data, we compute an optimal thickness of 0.08 mm. Since this thickness was not available from the manufacturer, we opted for the next closest value of 0.10 mm. This allows the β^- particles to traverse the sample width and escape on either side of the target toward the detectors, regardless of where in the sample the β^- is produced, and allows enough β^- particles to be produced such that we can expect to detect the decay products.

We choose a Pb target thickness of 0.1 mm to ensure the production of electrons in the target and to allow the escape of low-energy electrons. This is in agreement with the computed maximum target thickness of 0.5 mm, where virtually no low-energy electrons will escape. A thinner target would have allowed more electrons to escape, but the total number of activated nuclei would be lower as a result of there being less material to capture the neutrons.

The Pb samples used in this experiment were high purity (99.99%) metal foils of

natural composition obtained from Goodfellow Advanced Materials. Panel (a) of Figure 4.8 shows the unaltered Pb foil from the manufacturer with a side length of 5 cm. We cut our samples to the desired geometries using a metal stamp press, seen in Panel (b) of Figure 4.8. Specially machined stamp heads are designed to cut precise geometries. We stamp discs with a radius of 0.5 cm, and rings with an inner radius of 0.5 cm and an outer radius of 1.0 cm. Targets are prepared by suspending them in 3D-printed rings using Kapton® tape, a thin polyamide tape used for insulation and heat control. We prepare five sets of Pb targets, each consisting of an inner disc and an outer ring. Panel (c) shows a complete set of prepared Au, Pb, and Au samples. The Pb disc and ring can be distinguished within the 3D printed ring housing. The upstream gold monitor sits behind the Pb targets in this image. The downstream Au monitor is visible in the bottom of the image.

For each Pb sample, we assemble ^{197}Au foils to act as a neutron monitor to estimate the number of neutrons passing through our sample. During the activations, the Pb samples were sandwiched between two 0.03 mm gold foils of the same geometry, placed upstream and downstream of the Pb sample within the beam path. As such, all activation measurements are carried out relative to the gold cross section standard (see section 4.5).

Areal Surface Density

We compute the areal surface density μ_{areal} for our samples and monitors using their geometric and physical properties. The number of atoms of a chosen isotope within a sample is

$$N_{sample} = A_I \; m_{sample} \; N_{Avo} \; p/m_{mol} \tag{4.3}$$

where A_I is the abundance of the isotope of interest, m_{sample} is the mass in grams, p is the purity, and m_{mol} is the molar mass of the element. Our samples have the natural abundance of ^{208}Pb, 52.5%. The surface areas of our disc and ring samples were computed using $A_{sample} = \pi(r_{out}^2 - r_{in}^2)$, where for the discs the inner radius is equal to zero. The areal density is then equal to the number of atoms in the sample divided by the surface area,

$$\mu_{areal} = N_{sample}/A_{sample}. \tag{4.4}$$

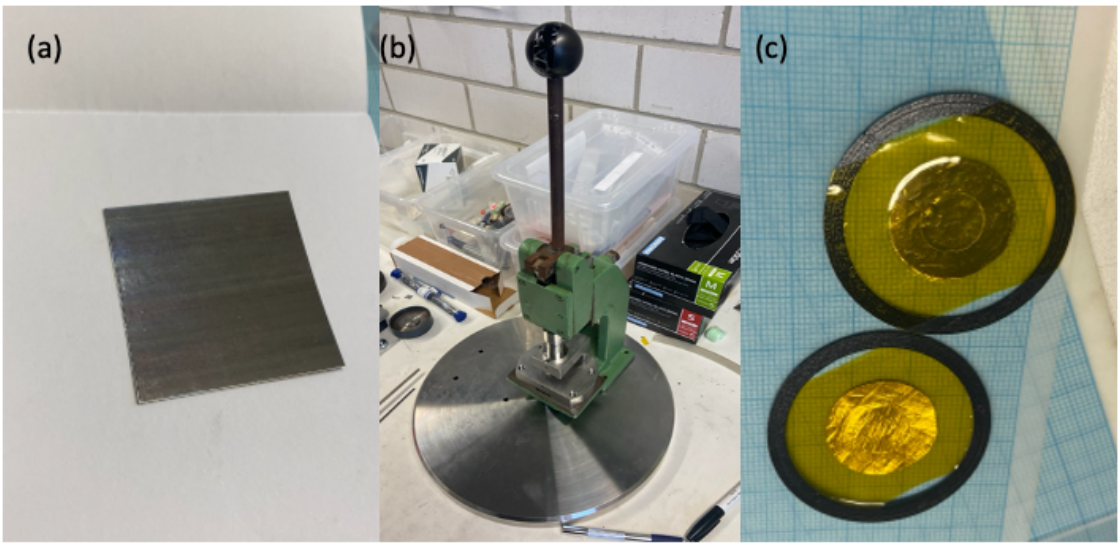

Figure 4.8: Sample preparation for the activation experiment. (a) Pb foil sheet from the manufacturer. (b) Stamp press used to cut disc and ring shapes fromo the foils. (c) Prepared Pb and Au samples suspended in 3D printed rings using Kapton tape.

4.4 Activation of ^{208}Pb

While the duration of the desired activation is three times the half-life of ^{209}Pb, the activation time is constrained by the working hours of the accelerator staff, and is limited to ~ 8 hours per day. After each activation, the number of activated nuclei in the samples and in the gold monitors are computed,

$$A = \phi_T \mu_A \sigma f_b, \tag{4.5}$$

where $\phi_T = \int_0^{t_b} \phi(t)dt$ is the time-integrated neutron flux, μ_A is the areal density, σ is the capture cross section, and f_b is the beam-time correction factor.

For a given γ-ray line, the number of counts in the BEGe detector is

$$C = A\kappa_\gamma \kappa_{casc} \epsilon_\gamma I_\gamma (1 - e^{-\lambda t_m}) e^{-\lambda t_w}, \tag{4.6}$$

where A is the number of activated nuclei, ϵ_γ is the efficiency of the BEGe detector and I_γ is the γ-ray intensity per decay. The correction factors κ_γ and κ_{casc} account for self-absorption of γ rays in the sample and the summing effect of the detector due

to cascade transitions, respectively. These correction factors have been calculated by means of Monte Carlo simulations using the GEANT-3 toolkit generously by Prof. Dr. Rene Riefarth, and are folded into in the computed ϵ detection efficiency. The same expression exists for detecting β^- particles, with subscripts γ replaced by β^-. Since all measurements are relative to the cross section of ^{197}Au, Equation 4.5 yields

$$\frac{A_i}{A_{Au}} = \frac{\sigma_i N_i f_{b_i}}{\sigma_{Au} N_{Au} f_{b_{Au}}}, \tag{4.7}$$

where A_i and A_{Au} are determined by the respective net counts registered in the detector.

4.4.1 Time Dependent Correction Factors

Decay of Nuclei during the Activation We compute the f_b correction factor using the time-dependent neutron flux measured using the Li-glass scintillator,

$$f_b = \frac{\int_0^{t_b} \phi(t) e^{-\lambda(t_b - t)} dt}{\int_0^{t_b} \phi(t) dt} \tag{4.8}$$

$$f_b = \frac{\sum_{i=0}^{T} r(i)\, e^{-\lambda(T-i)}}{\sum_{i=0}^{T} r(i)}, \tag{4.9}$$

where T is the full time period of the activation, i indicates the bin number of the time, and $r(i)$ is the count rate in the Li-glass scintillator for the respective time bin. Our neutron flux during one of the activation runs as measured by the Li-glass detector is shown in Figure 4.9.

To perform an analytical comparison for a constant neutron flux, we also compute f_b using the approximation

$$f_b = \frac{1 - e^{-\lambda t_b}}{\lambda t_b}, \tag{4.10}$$

for the decay constant λ and the beam time (or activation time) t_b. This term accounts for the decay of nuclei and variation of the neutron flux during the activation time. The neutron distribution within the samples, and therefore the cross sections, depends on the relative position of the of the samples to the neutron-producing Li

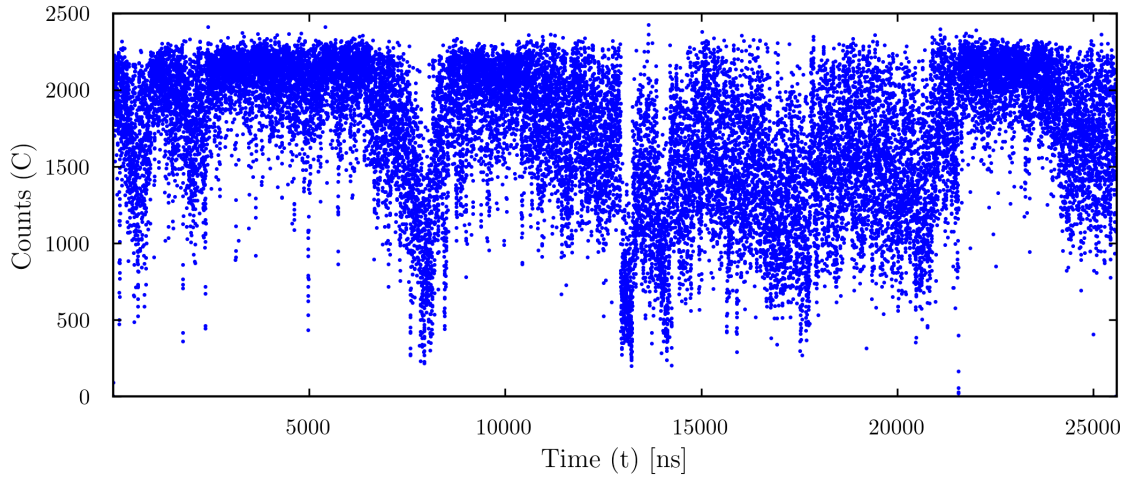

Figure 4.9: Neutron flux with time during one of the activation runs. Deviations in the neutron flux are accounted for by computing f_b.

target. Cross sections at different neutron energies and distributions for Au are computed with PINO.

Decay during the Waiting Time and Measuring Time After a waiting time t_w, the sample is placed within the BEGe detector setup, and γ-rays and β^- electrons are counted during a measuring time t_m. The two factors f_w and f_m correct for the number of decays that occur during the waiting and measurement phases, respectively. They are calculated with

$$f_w = e^{-\lambda t_w} \tag{4.11}$$

$$f_m = 1 - e^{-\lambda t_m}, \tag{4.12}$$

for waiting time t_w and measurement time t_m. The final time dependent correction factor is the dead time correction f_{DT}, intrinsic to the BEGe particle detectors. After an event is registered within the detector, a small period of time passes before another event can be registered. We correct for the counts missed by the detector by using the ratio of the live time and the wall-clock time during measurement, $f_{DT} = t_{live}/t_{real}$, where t_{live} and t_{real} are additional outputs from the measurements.

4.4.2 Number of Activated Nuclei

Radioactive isotopes decay according to the decay law following their nuclear decay constant λ, which is related to the half-life through $\lambda = \ln(2)/t_{1/2}$. The number of activated nuclei within a sample can be computed using the correction factors and the number of detected counts C,

$$N_{\text{active}} = \frac{C}{I(E)\,\epsilon(E)\,\kappa\,f_{\text{DT}}\,f_{\text{b}}\,f_{\text{w}}\,f_{\text{m}}}. \tag{4.13}$$

4.4.3 Pb Sample and Au Monitors

The β^- spectrum should be relatively smooth. However, the natural isotope distribution of Pb within the sample includes isotope ^{205}Pb, which will emit photons as decay products, which appear in the output spectra. We identify and remove the contributions from these photons in our β^- spectra. The γ spectra from the ^{197}Au monitors contains γ peaks and cascade effects at low energies.

4.5 Data Analysis

4.5.1 Detector Calibration

Energy Calibration

To calibrate the energy sensitivity range of the detector, we used radionuclides with well-known γ emission energies from Table 4.2. We placed the radionuclide in the detector configuration and measured the γ emission to calibrate the detector energy range. There are 4096 channels in each detector, and known γ peaks identify specific energy channels.

From the decay of ^{22}Na, we computed the positions of two prominent γ peaks and calibrated the detector energy channels. The energy range was set to a range of 0 - 1500 keV to capture the K background line ($E \sim 1459.7$ keV) emitted from the concrete blocks surrounding the detector bunker to serve as an additional calibration point. In Figure 4.10, we plot the γ peak energies as a function of detector channel for the set of calibration radioisotopes. The calibration energies follow a linear trend with detector channel. Our theoretical energy range of β^- particles from ^{209}Pb decay

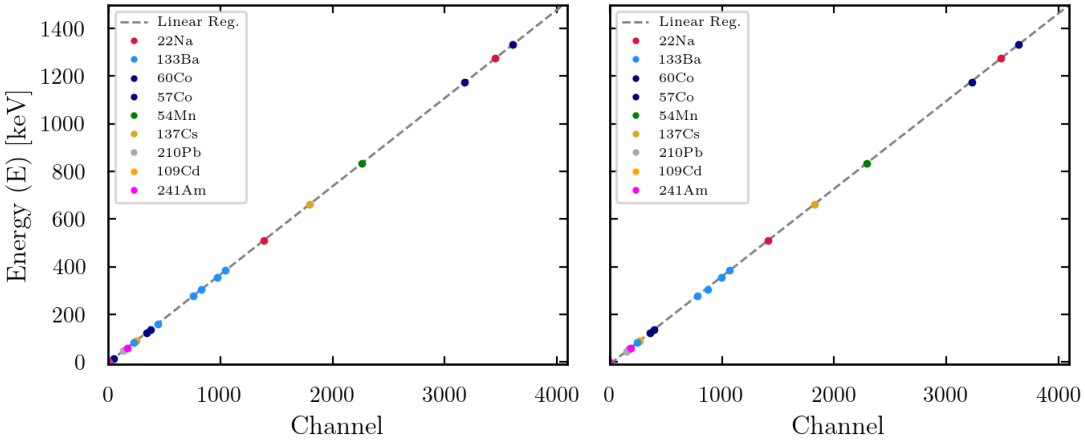

Figure 4.10: Detector energy calibration using a set of radioisotopes with known activities. The linear correlation is constructed using ^{22}Na data.

is 0 keV - 644 keV; however, we expect the higher energy β^- electrons to lose energy as they travel.

Distance Calibration

Using radioisotopes with known activities, we determined the true detector-sample distance by comparing to GEANT simulations. We computed the counts within each γ peak for each of the calibration samples. For a given measurement time, we expect a number of detected counts from the radioisotope. By simulating different distances and the known activities, we determined the true detector distance. Visually, this calibration is seen in Figure 4.11, for Detector 1 in the left panel and Detector 2 in the right panel. For Detector 2, the data points from ^{133}Ba emission were trimmed as extreme outliers. Calibrated distances are indicated in the lower right corner of each panel. Understanding the true distance from the sample to the detector is crucial in determining the particle detection efficiency, and may have a significant effect on the computed cross section. Where the detector setup distance scale reads 1 cm separation between the sample and the detectors, we found distances of 1.38 and 1.29 cm for Detectors 1 and 2, respectively. This feeds directly into the efficiency calibration of the detectors.

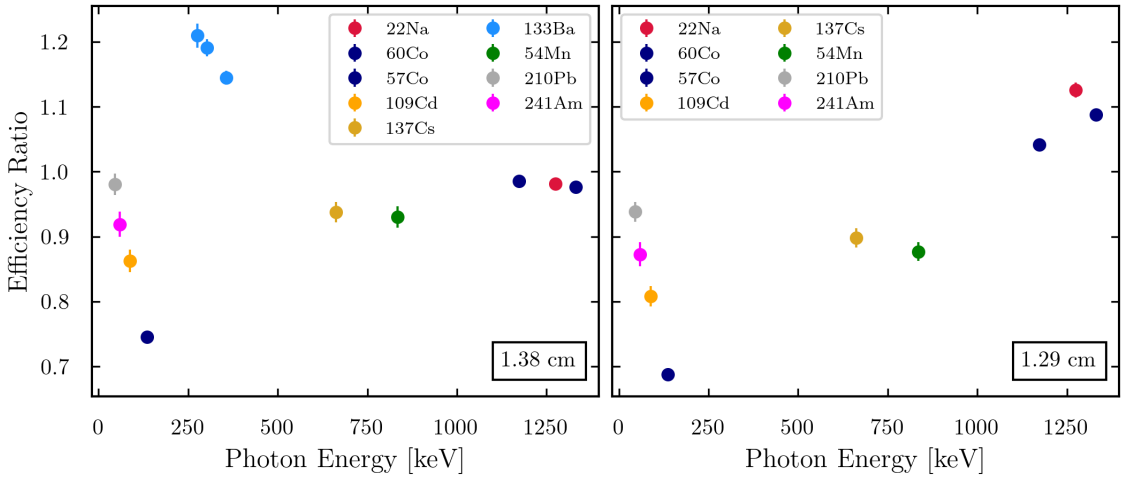

Figure 4.11: Calibrated detector distances using the efficiency ratio of the calibration radioisotopes, for detectors 1 and 2, respectively. Calibrated distances are in the boxes in the lower right of each plot.

Efficiency Calibration

A crucial factor to compute the cross section is the detector efficiency ϵ, which were estimated using GEANT-3 simulations, run by Prof. Dr. Rene Reifarth. The efficiency simulations were fitted to calibration source by varying geometric parameters, including the sample thickness and geometry, the detector dead layer thickness, and the distance to the detector. We estimated the efficiencies for both detectors at their calibrated distances, for our respective sample geometries, and for the different detected particles. The values for ϵ include the cascade and self-absorption coefficients κ, as well as the relative intensity of the emission I. We list our estimated efficiencies in Table 4.3 for our sample compositions and geometries.

To reduce our uncertainties, we integrated our simulated β^- counts within an energy range where most electrons are detected, from (20,200) keV. From the simulations, around 86% of the detected β^- particles were detected within this range, and we multiplied our total estimated efficiency by this factor. Our measured β^- counts are also calculated within this energy window for consistency.

4.5.2 Number of Detected Counts

The number of decays was determined by integrating the number of events within emission peaks or regions of characteristic energies. To prevent systematic deviations in the measured peak content, we ensure the contributions from other decays does not contaminate energy peak.

Background Calibration

We measured the environmental background radiation at the detection site using an empty detector setup and a measurement time of 2.54 days (58.87 hours). To remove the background contributions from our measured energy spectra we applied a scaling factor, SF, as the ratio of the measurement time to the background time $SF = t_m/t_{bkg}$. With this we ensure that no significant contribution from the background persists in our calibration spectra.

Lead

Energy spectra from our Pb samples are shown in Figure 4.12. The raw β^- spectra are shown in grey, where the background contribution is significant. The background subtracted spectra are shown in the black lines. To better visualize the shape of the extracted β^- spectra, we re-binned our sample at intervals of 10 keV. The disc samples show a characteristic curve at low energies with a soft peak near 100 keV. While the end-point energy of the ^{209}Pb β^- decay is 644 keV, the β^- particle energies are attenuated as they pass through both the sample and the detector. As such, few high-energy electrons were detected in this experiment. The ring samples show significant noise in the spectra.

Integrating the electron spectrum across the whole energy range will introduce noise and uncertainty to our computation of the cross section. Following our computation of the detector efficiency, we recover more signal by integrating our β^- spectra over a narrow energy range from (20,200) keV.

Gold

The γ spectra for the Au flux monitors is shown in Figure 4.13 in the energy range is 0 - 800 keV. There are prominent emission features visible in the spectra, where

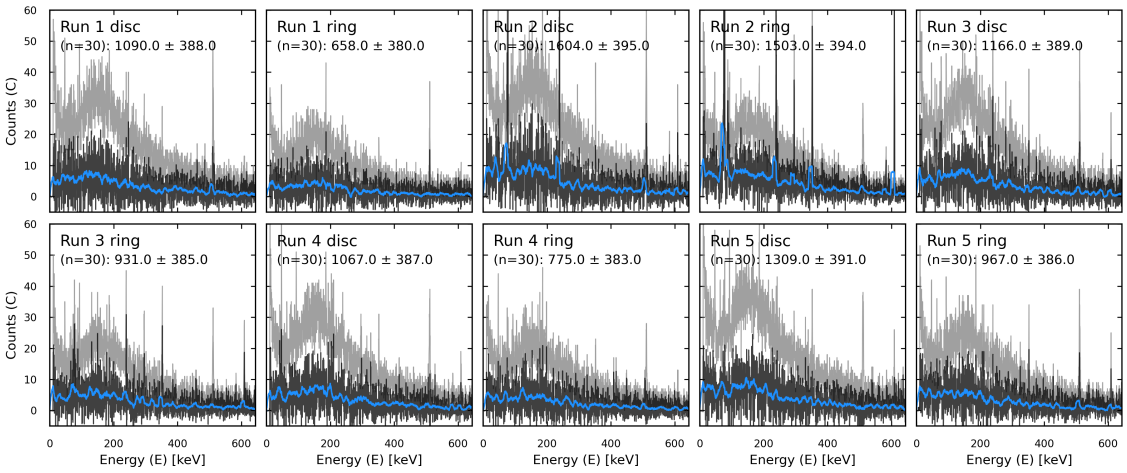

Figure 4.12: Energy spectra detected from our Pb samples. The grey lines are the raw spectra before background subtraction. In black are the background subtracted β^- spectra. Blue lines are the background subtracted spectra re-binned at 10 keV intervals.

peaks at 411.8 keV and at 675.9 keV correspond to the ^{198}Au $\rightarrow$ ^{198}Hg + γ decay products. The Compton continuum is seen in the sloping behavior of the spectra. A degraded γ-spectrum is seen in the Au ring spectra in Run 3 upstream ring, where the neutron flux was highly variable.

We used the γ-emission feature at 411.8 keV to compute the counts from our Au samples, and computed corresponding detection efficiencies from GEANT. As shown in Figure 4.14, we fit a Gaussian function (shown in red) to the γ peak in the background subtracted spectra (shown in black), with the same energy resolution as the detector. We integrated the Gaussian curve to obtain the number of counts within the peak.

From the detected number of counts, we computed the number of activated nuclei within the sample. We applied the correction factors for continuous decay during different phases of the experiment, and corrected for the detector efficiency.

4.5.3 Integrated Neutron Flux

The total neutron flux through the Pb samples cannot be measured directly; instead neutron flux through the sample was approximated by using the Au neutron monitors. Gold has the advantage of having a well-known neutron interaction cross

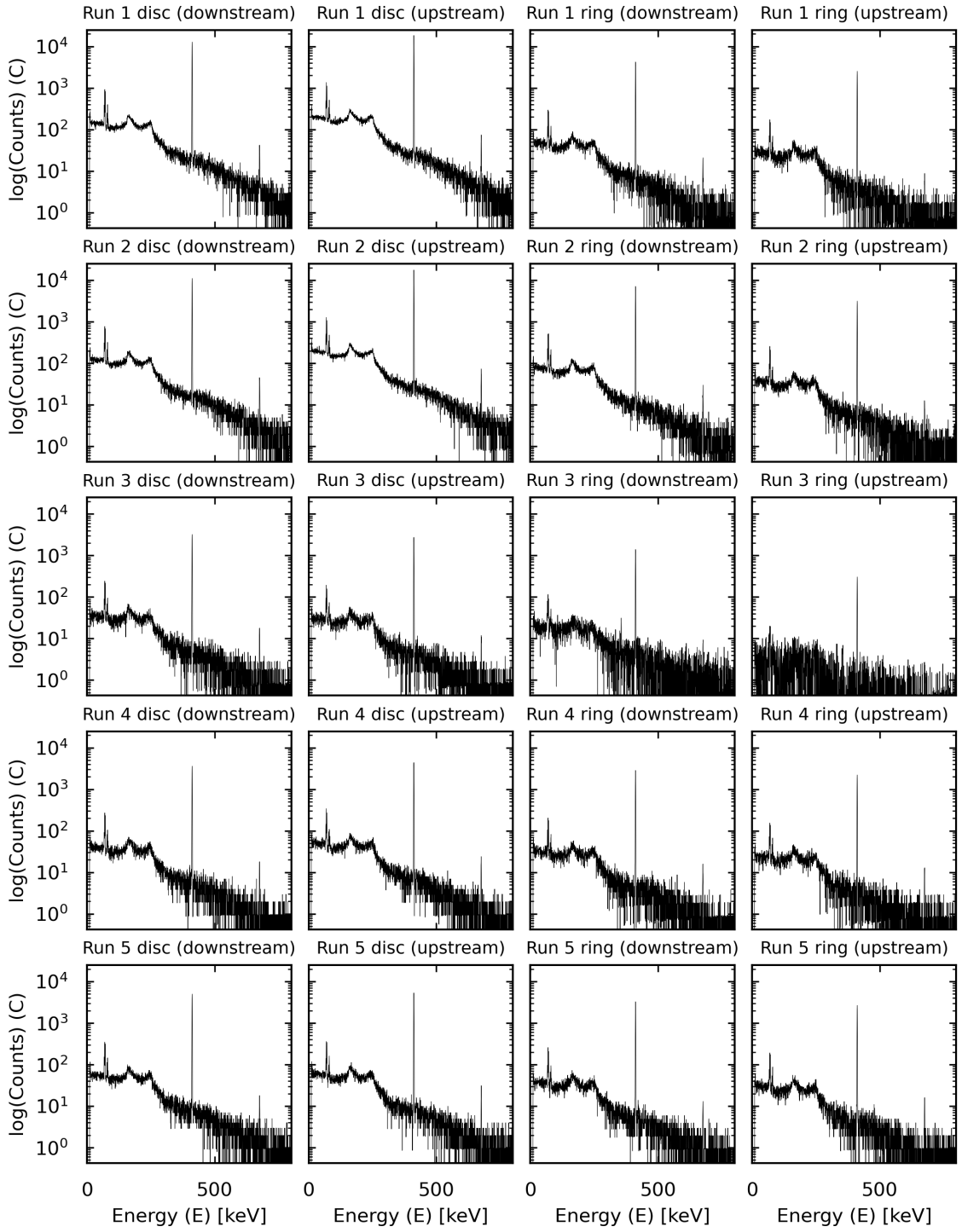

Figure 4.13: Energy spectra for our Au samples. Titles indicate which sample is presented. γ emission features and cascade features can be distinguished.

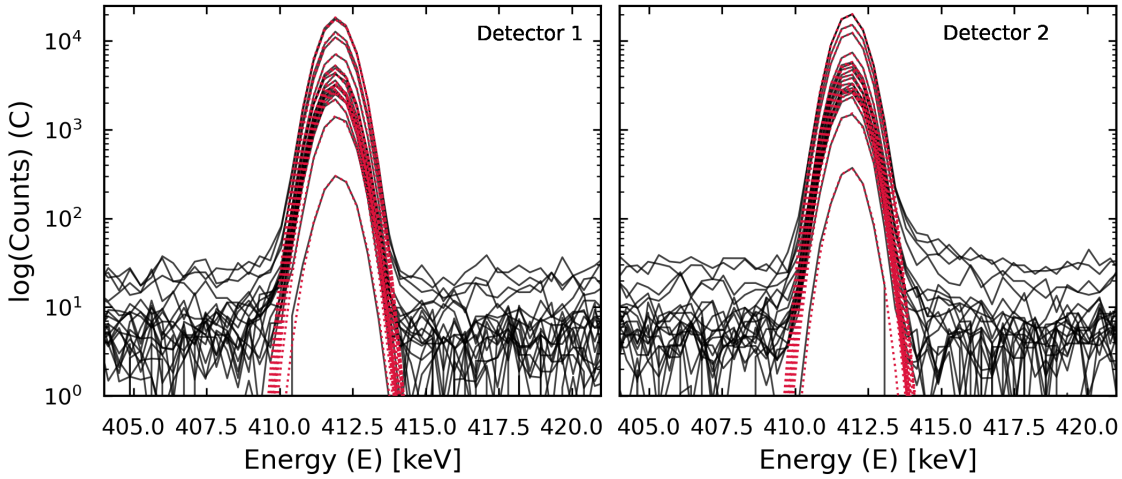

Figure 4.14: Energy spectra for our Au samples, stacked and focused on the 411.8 keV peak. Black curves are the Au spectra, and the red dotted curves are the Gaussian fits. The left and right panels show spectra from Detectors 1 and 2, respectively.

section, and is an established standard for cross-section measurements (Ratynski and Käppeler, 1988). Activities of the Au monitors were measured with BEGe detectors, and the integrated neutron flux through the Pb sample was determined by arithmetically averaging the computed neutron fluxes through the upstream and downstream monitors,

$$\Phi_T = \frac{1}{2}\left(\frac{C_1}{\mu_1\sigma_1\epsilon_{411}f_b f_w f_m f_{DT}} + \frac{C_2}{\mu_2\sigma_2\epsilon_{411}f_b f_w f_m f_{DT}}\right), \tag{4.14}$$

with T being the full time period of activation. The neutron distribution inside the samples, and therefore the cross sections σ, depend on the relative position of the samples to the neutron producing Li target. These energy-dependent cross sections for gold were simulated using PINO. Using the degree of activation R,

$$\begin{aligned} R_{upstream} &= \frac{\phi_{upstream}}{\phi_{upstream,sim}}, \\ R_{downstream} &= \frac{\phi_{downstream}}{\phi_{downstream,sim}}, \\ R_{sample} &= \frac{R_{upstream} + R_{downstream}}{2}, \end{aligned} \tag{4.15}$$

we rewrite the expression for the neutron flux through our Pb sample,

$$\Phi_T = \frac{\pi r^2}{2}\left(\frac{R_{upstream}}{\sigma_{upstream,sim}} + \frac{R_{downstream}}{\sigma_{downstream,sim}}\right). \tag{4.16}$$

4.5.4 Cross Section

Using the computed neutron flux and the activity of the Pb samples, we calculated the neutron interaction cross section using the expression,

$$\sigma = N_{\text{active}}/(n_a\,\Phi_T). \tag{4.17}$$

4.6 Results and Discussion

We tabulate our data and results for our measurement of the neutron interaction cross section of ^{208}Pb in Appendix A. Physical data include masses, geometrical properties, and areal densities. Simulated data for each sample include the SACS_{197Au} and ϕ_{sim} values from PINO, each listed by sample in Tables A.2 and A.7. Experimental timing for each sample is shown in Tables A.3 and A.8, followed by computed decay time correction factors in Tables A.4 and A.9. In Tables A.5 and A.6 for the Au samples, we list values for background scaling factors, detector efficiencies from GEANT, computed counts at 411.8 keV, the number of activated nuclei, and the computed neutron flux data. For the Pb samples, in Tables A.10a and A.10b we list the background scaling factors, detector efficiencies from GEANT, integrated β^- counts between 20 - 200 keV, the computed neutron flux, the number of activated nuclei, and neutron interaction cross sections in [cm^2].

We calculate the weighted mean of the cross sections across our five activation runs and between the two detectors. From our activation experiments of ^{208}Pb, we measure the spectrum-averaged cross sections (SACS) at $k_BT = 25$ keV $\sigma_{25} = 18.87 \pm 6.18$ mb.

We compare our results at $k_BT = 25$ keV to literature values from activation and time-of-flight (TOF) measurements in Table 4.4. There is scatter in literature values for the cross section at this energy, ranging from 0.32 to 0.75 mb. TOF measurements are, on average, higher than the activation experiments. We use this data as a check on our results and a measurement calibration point; if our results

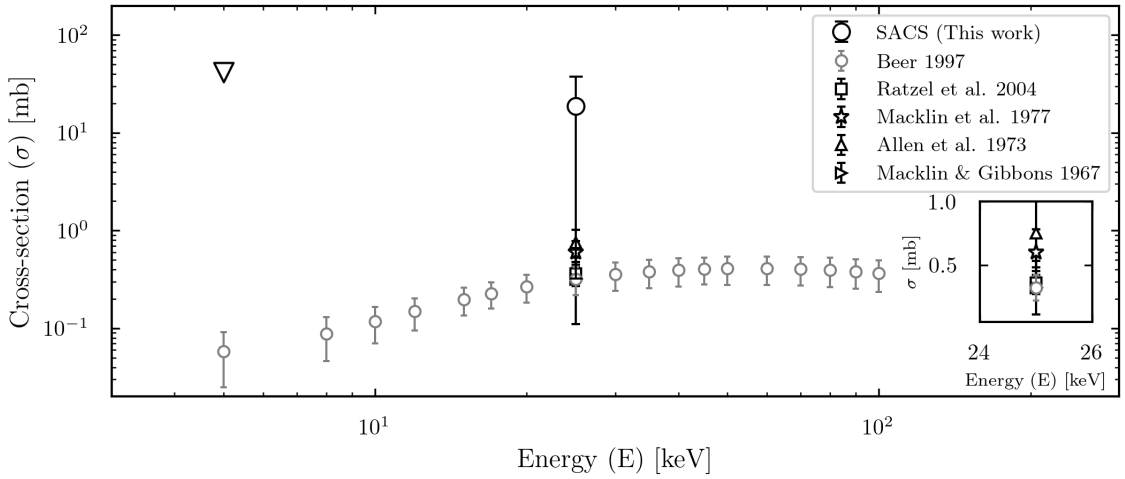

Figure 4.15: Experimentally measured SACS compared to computed total-capture cross sections from Beer et al. (1997) and other literature values. A zoom-in panel at 25 keV is shown to display the literature cross sections. At 25 keV, we find our result statistically consistent with the literature. At 5 keV, we establish an upper limit.

at this energy are sensible, then we may trust our results at lower energies. Our obtained experimental cross section is in statistical agreement and lies within 3σ of the literature data.

Our measured SACS value at 5 keV has large uncertainties of over fifty percent. Extending the uncertainties to cover the full confidence range, cross section values become negative, indicating our measurement is an upper limit. We establish the upper limit of $\sigma_5 < 41.58$ mb at $k_BT = 5$ keV, determined using the 2σ uncertainties in the computed value. This is much higher than the total-capture cross section $\sigma_{total,\,5\,keV} = 0.058$ mb, computed by Beer et al. (1997).

In Figure 4.15, we compare our results to the computed total-capture cross sections from Beer et al. (1997) and experimental results compiled in Table 4.4. All data are shown with 3σ uncertainties.

4.6.1 MACS

From the experiment we measure the SACS, which is used to approximate Maxwellian-averaged cross sections (MACS) through the relation $\sigma_{MACS} \approx (2/\sqrt{\pi})\,\sigma_{SACS}$. We compare our computed MACS values to theoretical predictions in Figure 4.16 to sets

of simulation data from Pritychenko et al. (2010); Chadwick et al. (1996); Chadwick et al. (2011); Plompen et al. (2025); Iwamoto and Iwamoto (2025); IAE (2022). In the figure, grey data identify the computed MACS at energies of $k_BT = 5$ and 25 keV. In this region, there is more than one order of magnitude discrepancy between the theoretical models. Our cross section at 25 keV lies between the theoretical curves, suggesting compatibility with models from Chadwick et al. (2011) and Iwamoto and Iwamoto (2025). The upper limit at 5 keV prevents us from ruling out any models.

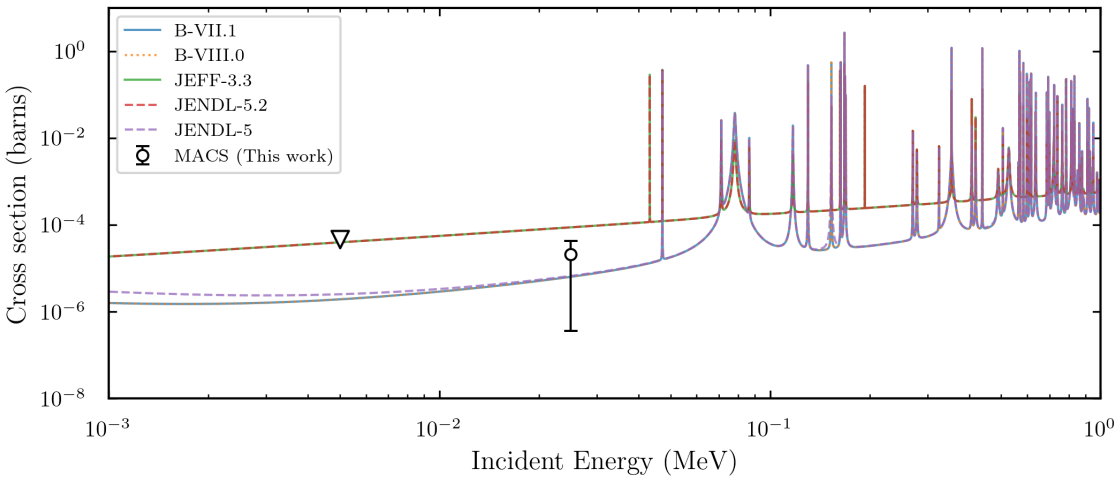

Figure 4.16: Theoretical MACS values for ^{208}Pb at energies from 1 keV to 1 MeV, from Pritychenko et al. (2010); Chadwick et al. (1996); Chadwick et al. (2011); Plompen et al. (2025); Iwamoto and Iwamoto (2025); IAE (2022). Computed MACS at 5 keV and 25 keV are shown in grey.

We note the relative success of our experiment, in that we are able to measure a cross section at astrophysical energies relevant to the s-process within statistical significance of the literature. However, we were not able to fully determine the n-interaction cross section of ^{208}Pb at 5 keV, due to low sensitivity in detecting low energy β^- particles.

4.6.2 Estimation of Uncertainties

Measurement methods cannot perfectly determine the true value of any quantity. Thus, a good understanding of the involved systematic and statistical uncertainties is important. Systematic uncertainties are the result of insufficient calibration

of the instrument, or experimental errors. If the cause of the systematic error is determined, it can be completely corrected for in the final result.

Statistical uncertainties are a product of the unpredictable behavior of statistical processes involved in the experiment and analysis. These can be reduced with repeated measurements. The direct measurements of the cross sections are calculated through analytical and numerical expressions through which we propagate statistical uncertainties. In general, the total uncertainty can be obtained by Gaussian error calculation,

$$\sigma = \sqrt{\sum_{i=1}^{m} \left(\frac{\partial y}{\partial x_i} \sigma_i \right)^2}, \tag{4.18}$$

assuming variables are independent. For multiple independent variables contributing to the computation of another, their uncertainties can be included following Equation 4.18. For dependent variables, the covariance is taken into account with the inclusion of cross-terms.

Uncertainties in the laboratory scales and calipers for measuring the geometry and mass of the samples were taken into account when computing computing the areal density μ_{areal}. The uncertainty in the measured masses is ± 0.05 mg, and the uncertainties in the measured radii is ± 0.05 mm.

$$\Delta\mu = \sqrt{\left(\frac{N_A \alpha}{M\, \pi r^2} \Delta m \right)^2 + \left(\frac{2 m N_A \alpha}{M\, \pi r^3} \Delta r \right)^2}. \tag{4.19}$$

The uncertainties in the detected counts are taken as the square root of the number of counts summed with the counts of the background, within the same energy range $\Delta C = \sqrt{C + C_{bkg}}$. On average, for the Au samples we compute uncertainties on the order of 0.6%. In the realm of large numbers, e.g., the γ spectra from our Au samples, we are in the statistical Poisson counting regime, and the contributions from the background are negligible. However, we observe few β^- counts from our Pb samples, and the background makes a significant contribution to the uncertainty in the counts. The uncertainty in our computed β^- counts is 38%. This is the dominant source of uncertainty in our computed cross sections.

The uncertainties in the neutron flux stem from the uncertainties in the Au cross section, the areal density of Au, the integrated counts within the 411.8 keV γ peak,

and the detector efficiency. The relative uncertainty in the neutron flux is given by

$$\frac{\Delta\Phi_T}{\Phi_T} = \sqrt{\left(\frac{\Delta\mu_{\mathrm{Au}}}{\mu_{\mathrm{Au}}}\right)^2 + \left(\frac{\Delta C_{Au}}{C_{Au}}\right)^2 + \left(\frac{\Delta\sigma_{\mathrm{SACS,Au}}}{\sigma_{\mathrm{SACS,Au}}}\right)^2 + \left(\frac{\Delta\epsilon}{\epsilon}\right)^2}. \tag{4.20}$$

Uncertainties in the activity are the combined contributions from uncertainties in the counts and correction factors

$$\frac{\Delta A}{A} = \sqrt{\left(\frac{\Delta C}{C}\right)^2 + \left(\frac{\Delta f_w}{f_w}\right)^2 + \left(\frac{\Delta f_b}{f_b}\right)^2 + \left(\frac{\Delta f_m}{f_m}\right)^2 + \left(\frac{\Delta f_{DT}}{f_{DT}}\right)^2}. \tag{4.21}$$

The uncertainty of the correction factor for the waiting phase f_w depends on the uncertainty of the waiting time t_w and the uncertainty of the decay constant λ of the respective isotope. The uncertainties in the measurement timings is negligibly small. The uncertainty in t_b is small, and the only source of uncertainty taken into account for the irradiation time correction factor t_b is the decay constant λ. The relevant source of uncertainty in the measurement time correction factor is the decay constant λ. The determination of the dead time correction factor has three sources of uncertainty occur, the dead time correction $f_{DT}(r)$ depending on the rate in the detector r and the uncertainty of the decay constant λ,

$$\Delta f_w = \sqrt{\left(t_w\, e^{-\lambda t_w}\, \Delta\lambda\right)^2 + \left(\lambda\, e^{-\lambda t_w}\, \Delta t_w\right)^2} \tag{4.22}$$

$$\Delta f_b = \left(\frac{e^{-\lambda t_b}}{\lambda} - \frac{1 - e^{-\lambda t_b}}{t_b \lambda^2}\right) \Delta\lambda \tag{4.23}$$

$$\Delta f_m = t_m\, e^{-\lambda t_m} \Delta\lambda \tag{4.24}$$

$$\frac{\Delta f_{DT}}{f_{DT}} = \sqrt{\left(\frac{\Delta f_{DT}(r)}{f_{DT}(r)}\right)^2 + \left(\frac{\Delta\left(e^{-\lambda t_m}\right)}{e^{-\lambda t_m}}\right)^2}. \tag{4.25}$$

Uncertainties in simulations are taken to be 5% for the γ energies, simulated cross sections, and electron energies and intensities,

$$\frac{\Delta f_{\rm sim}}{f_{\rm sim}} = \sqrt{\left(\frac{\Delta f_\epsilon}{f_\epsilon}\right)^2 + \left(\frac{\Delta I_\gamma}{I_\gamma}\right)^2 + \left(\frac{\Delta I_\beta}{I_\beta}\right)^2}. \tag{4.26}$$

The uncertainty in the cross section is the combination of the contributions from the areal density, the observed counts, the neutron flux, and the simulations,

$$\frac{\Delta\sigma}{\sigma} = \sqrt{\left(\frac{\Delta\mu}{\mu}\right)^2 + \left(\frac{\Delta C_\beta}{C_\beta}\right)^2 + \left(\frac{\Delta\Phi_T}{\Phi_T}\right)^2 + \sum_i \left(\frac{\Delta f_i}{f_i}\right)^2}. \tag{4.27}$$

4.7 Conclusion

The double-magic number nucleus ^{208}Pb marks the end point of the s-process. The cross section for neutron capture directly affects the produced ratio of Pb to Bi in stars. The rare capture of a neutron produces ^{209}Pb, which quickly decays to ^{209}Bi by releasing a β^- particle. In order to proceed with neutron captures beyond this reaction, the necessary neutron flux is much higher than that reached within thermally pulsing AGB stars.

To constrain the theoretical models and refine the rate of the s-process in AGB stars, the cross sections and reaction rate are measured. In this experiment, natural Pb was irradiated with pseudo-thermal neutrons, and the activated Pb samples were used to compute the interaction cross sections. Many direct measurements of the neutron capture cross section at $k_BT = 25$ keV have been made in the last 60 years, and our computed cross section $\sigma_{25} = 18.87 \pm 6.18$ mb is within 3σ agreement with the literature. However, below this energy, only theoretical predictions of the cross section have been used. We compute the upper limit $\sigma_5 =< 41.58$ mb in our investigation of neutron capture cross sections at low energies relevant to the strong component of the s-process. This is the first time a direct measurement has been made at $k_BT = 5$ keV for ^{208}Pb. These measurements together can be used to interpolate other astrophysically relevant energies and increase the reliability of the predicted production rates of s-process elements in AGB stars.

Table 4.1: Combined measurement runs including wait times and activation times.

Run	Sample	t_{wait} [s]	Start–Stop	Duration [s]
1	Pb ring	500	16:15:00 – 22:45:00	23400
1	Pb disc	24289	22:51:29 – 09:05:39	36850
1	Au ring downstream	65885	10:24:45 – 11:24:45	3600
1	Au ring upstream	61625	09:13:45 – 10:20:20	3995
1	Au disc downstream	72365	12:12:45 – 12:35:45	1380
1	Au disc upstream	69725	11:28:45 – 12:07:20	2315
2	Pb ring	833	15:44:45 – 22:25:45	24060
2	Pb disc	25198	22:30:00 – 10:10:15	42015
2	Au ring downstream	67513	10:15:15 – 11:16:45	3690
2	Au ring upstream	73238	11:50:40 – 13:50:40	7200
2	Au disc downstream	71378	11:19:40 – 11:45:10	1530
2	Au disc upstream	80603	13:53:25 – 14:30:25	5820
3	Pb ring	653	15:41:45 – 22:28:45	24420
3	Pb disc	25779	22:40:31 – 08:46:31	36360
3	Au ring downstream	62453	08:51:45 – 14:18:30	19605
3	Au ring upstream	82304	14:22:36 – 15:51:36	5340
3	Au disc downstream	158558	11:33:30 – 12:21:32	2882
3	Au disc upstream	161678	12:25:00 – 13:09:30	2670
4	Pb ring	750	16:01:40 – 23:01:40	25200
4	Pb disc	26331	23:08:01 – 08:47:46	34785
4	Au ring downstream	64635	09:46:25 – 10:23:25	2220
4	Au ring upstream	67010	10:26:00 – 11:02:30	2190
4	Au disc downstream	69320	11:04:30 – 11:15:00	870
4	Au disc upstream	70100	11:17:30 – 11:29:30	720
5	Pb ring	535	15:34:15 – 23:19:45	27930
5	Pb disc	28645	23:22:45 – 10:57:45	41700
5	Au ring downstream	70540	11:01:00 – 11:14:05	785
5	Au ring upstream	71500	11:17:00 – 11:27:30	630
5	Au disc downstream	72280	11:30:00 – 11:40:00	600
5	Au disc upstream	73000	11:42:00 – 11:52:20	620

Table 4.2: Gamma-ray energies of selected calibration isotopes.

Isotope	Gamma Energies [keV]
^{22}Na	511, 1274.54
^{54}Mn	834.85
^{57}Co	14.41, 122.06, 136.47
^{60}Co	1173.23, 1332.49
^{109}Cd	88.03
^{133}Ba	53.16, 79.61, 80.99, 160.61, 223.24, 276.39, 302.85, 356.01, 383.85, (1173.23, 1332.49)
^{137}Cs	661.66
^{210}Pb	45.539
^{241}Am	59.54

Table 4.3: Estimated efficiencies for β^- detection in our BEGe setup using the GEANT simulations.

Sample	Detector	Distance [cm]	ϵ	$\Delta\epsilon$
Pb Disc	1	1.38	0.010873	0.000451
Pb Disc	2	1.29	0.011249	0.000448
Pb Ring	1	1.38	0.010702	0.000436
Pb Ring	2	1.29	0.011037	0.000456
Au Disc	1	1.38	0.065485	0.000274
Au Disc	2	1.29	0.068699	0.000277
Au Ring	1	1.38	0.064063	0.000275
Au Ring	2	1.29	0.067805	0.000275

Table 4.4: Neutron capture cross sections at $k_BT = 25$ keV from sources in the literature. Results from activation and TOF experiments are compared.

σ [mb]	σ_σ	Comment	Ref.
18.87	6.18	VdG	This Work
0.36	0.03	VdG	Ratzel et al. (2004)
0.36	0.04	Linac, TOF	Beer et al. (1997)
0.60	0.06	Linac, TOF	Macklin et al. (1977)
0.75	0.09	Linac, TOF	Allen et al. (1973)
0.32	0.07	VdG	Macklin and Gibbons (1967)

5 Conclusion and Outlook

This thesis represents the culmination of a body of work through which I have obtained a comprehensive perspective on the s-process, and on how observational, computational, and experimental techniques are used to investigate nucleosynthesis in stars.

We observe spectroscopic binaries with high-resolution spectrographs to trace AGB nucleosynthesis patterns in the now-visible extrinsic binary companions displaying s-process element enhancements. We monitor spectroscopic orbits for a sample of 404 stars over the course of 4 years. For 312 of these stars, we have derived stellar atmospheric parameters using ATHOS and Xiru. We interpolate grids of stellar atmospheric models and generate synthetic spectra. We compute 1D-LTE photospheric abundances of C, the alpha element Mg, the s-process elements Sr, Y, Zr, Mo, Ba, La, Ce, Nd, Pb, and the r-process element Eu. Adding Mo and Pb to the abundance patterns, we determine the initial AGB mass in binary systems polluted with s-process material. We observe trends in Mo with both light and heavy s-process element production, and note correlations in elemental abundances produced by the s-process. We compare our abundance patterns to the FRUTIY models. For stars with good fits, we find a small range of initial AGB masses corresponding to a given level of enrichment in s-process material. We optimize binary orbits to further investigate estimated stellar masses. We find general agreement between the observed stellar masses, initial AGB masses, and white dwarf masses. We observe a general trend between s-process enhancement and donor AGB mass, where low- and intermediate-mass AGB stars produce higher [hs]/[ls] ratios compared to higher mass AGB stars. A natural extension to this project is to complete the analysis of the stars for the full sample. We plan to model and update the spectroscopic binary orbits of the entire catalog of stars. Further spectral analysis will be performed to derive stellar atmospheric parameters for the sample, and to calculate evolutionary states and ages. In addition, we plan to analyze the surface

chemistry of the sample whose observations have high enough SNR.

Modeling the accretion and evolution of extrinsic stars, we distinguish between different stellar populations and draw conclusions about the efficiencies of mass transfer over cosmic time. More carbon-rich and metal-poor (CH, CEMP-s) stars generally accrete less material from their companion star, whereas more metal-rich (Ba) stars tend to accrete more material from their AGB companion. The metal-rich population is typically of higher stellar mass, which may mean that the more massive envelope is more efficient at mixing the accreted material, requiring more accretion to produce the observed abundance pattern. Additionally, AGB mass loss may be more effective at higher metallicities due to the increasing effect of radiation pressure on the plasma, providing more material to be accreted. This project can be broadened by including more mixing mechanisms in the models, by extending to metallicities down to the theoretical limit of the s-process, and by refining the range of accretion masses to 0.10 step increments up to higher accretion masses, above 1 $M_{\odot}$. Further modeling considering these higher accretion masses may reveal a scenario that better describes the final mass distribution of the strong Ba stars. Evolution modeling including rotation is planned to track the angular momentum through the accretion process. The orbital evolution can also be taken into account, where a particular star system is investigated using binary stellar evolution and nucleosynthesis models, evolving the AGB star along with the companion in a focused case study. This exercise could also be performed for binary systems of higher mass.

Using the activation method, we beamed neutrons at pseudo-Maxwellian energies at a sample of ^{208}Pb. We measured the activity of the sample by counting the number of β^- decays from the produced ^{209}Pb. Applying corrections for the decay process and the experimental setup, we computed the neutron-interaction cross sections for ^{208}Pb at the s-process relevant energies of $kT = 25$ keV and $kT = 5$ keV. These cross sections have significant implications for modeling other neutron-capture processes, where both the i-process and the r-process extend their synthesis beyond Pb. We plan to compute corresponding upper limits on reaction rate constants and formation rates of Pb. This study may be improved using a detector setup specifically designed to detect β^- particles. A thinner Pb sample will also allow the release of more β^- particles to improve counting statistics. Using the ring method in activation experiments can probe energies intermediate to those already established, and may reveal energy dependent resonances in the cross section.

Acknowledgments This project has received funding from the European Union's Horizon 2020 research and innovation programme under grant agreement No 101008324 (ChETEC-INFRA). We graciously thank ChETEC-INFRA TNA program for providing the framework and infrastructure for the access to the telescopes and instruments used to accomplish data acquisition. Further support in funding comes from the State of Hesse within the Research Cluster ELEMENTS (Project ID 541 500/10.006). The Astronomical Institute Ondřejov is supported by the project RVO:67985815.

Results in this work are based on observations made using: the 1.65m Ritchey-Chretien telescope at Moletai Astronomical Observatory, the 2m Perek Telescope of Ondřejov observatory, run by Astronomical Institute of the Czech Academy of Sciences, and the 2m Rozhen Ritchie-Chretien-Coudé telescope at the National Astronomical Observatory – Rozhen, operated by the Institute of Astronomy, Bulgarian Academy of Sciences. Results are also based on observations made with the Nordic Optical Telescope at the Observatorio del Roque de los Muchachos, La Palma, Spain, of the Instituto de Astrofisica de Canarias. We thank the observers who worked to obtain our spectroscopic data at the ChETEC TNA infrastructures at Moletai, Ondrejov, and Rozhen, the Nordic Optical Telescope at Roque de los Muchachos, and the MPG 2.2m telescope at La Silla. Thanks to Arunas Kucinskas, Vidas Dobrovolskas, Olya Maryeva, Ivanka Stateva, Viki, Samantha, Maren Hempel, Angela Hempel, Sam, Simon, and many others who are not mentioned here. Thanks to fellow group members at GUF for their feedback Arthur Puls, Linda Lombardo, Raphaela Melo, Annika Schichtel, and Diego Mederos Leber. Thanks to MPIA for providing access to the Nordic Optical Telescope and the Max Planck Gesellschaft (MPG) 2.2m Telescope.

This work would not have been possible without the supervision of Prof. Dr. Camilla J. Hansen, Sen. Lec. Richard J. Stancliffe, and Priv. Doz. Tanja Heftrich. Enormous thanks to mentors and colleagues at MPIA and GUF who provided advice and feedback during this project, including Dr. Hans-Walter Rix, Dr. Maria Bergemann, Dr. Nadine Neumayer, Dr. Rene Reifarth, Dr. Andrew Gallagher, Dr. Callie Clontz, Dr. Guillaume Guglion, Dr. Arvind Hughes, Dr. Eric Rohr, Dr. Siddhant Desmundkuh, Dr. Rhys Seeburger, Dr. Yash Sharma, Dr. Dhruv Muley, Dr. James Davies, Davud Sokolovic, Jan Butz, and Felix Panholzer.

We acknowledge the support of the Data Science Group at the Max Planck Institute for Astronomy (MPIA) and especially Iva Momcheva, Morgan Fouesneau, Raphael Hvedig, and James Davies for their invaluable assistance in analyzing the data and developing the software for this work. The authors acknowledge the use of large language models to assist in formatting and editing parts of this thesis.

A Appendix

A.1 Line Lists

A.2 Experimental Data

In the tables below, we list our experimental data. There are 20 Au samples, identified with a run number and a geometric name, with a 'd' or 'u' for downstream or upstream respectively. The 10 Pb samples are only identified with a run number and a geometric name. Physical data include masses, geometrical properties, and areal densities. Simulated data for each sample include the SACS_{197Au} and ϕ_{sim} values from PINO, each listed by sample in Tables A.2 and A.7. Experimental timing for each sample is shown in Tables A.3 and A.8, followed by computed decay time correction factors in Tables A.4 and A.9. In Tables A.5 and A.6 for the Au samples we list values for background scaling factors, detector efficiencies from GEANT, computed counts at 411.8 keV, the number of activated nuclei, and the computed neutron flux data. For the Pb samples, in Tables A.10a and A.10b we list the background scaling factors, detector efficiencies from GEANT, integrated β^- counts between 20 - 200 keV, the computed neutron flux, the number of activated nuclei, and neutron interaction cross sections in [cm^2].

Table A.1: Wavelengths, excitation potentials, and oscillator strengths of atomic lines used in this study, sorted by element, with NIST data quality flags. Oscillator strengths for lines that include hyper-fine splitting (hfs) are the total $\log(gf)$ from all contributing components. The ionization state is identified by the roman numerals in the parentheses, where (I) is the ground state, and (II) is the first ionized state. Adapted from Dimoff et al. (2024).

Element / λ Å	Exc. Potential eV	Osc. Str.	NIST Flag
Mg (12)			
5528.405 (I)	4.343	-0.620	B+
5711.088 (I)	4.343	-1.830	B+
Zr (40)			
4359.74 (II)	1.236	-0.510	
4496.97 (II)	0.713	-0.890	
4687.80 (I)	0.730	0.550	
4739.48 (I)	0.650	0.230	
6127.44 (I)	0.154	-1.060	
Ba (56)			
4554.033 (II)	0.000	-0.562	B (hfs)
5853.675 (II)	0.604	-1.914	B (hfs)
6141.713 (II)	0.704	-1.158	B (hfs)
6496.898 (II)	0.604	-1.111	B (hfs)
Ce (58)			
4628.161 (II)	0.516	0.140	B+
5274.229 (II)	1.044	0.130	B+
5330.556 (II)	0.869	-0.400	B
5353.524 (II)	0.879	0.090	B+
Eu (63)			
4129.70 (II)	0.000	0.109	(hfs)
4594.03 (I)	0.000	0.680	B+
5577.14 (I)	1.667	0.000	B+
6645.11 (II)	1.379	-0.517	(hfs)
Pb (82)			
4057.807 (I)	1.319	-0.170	C+

Element / λ Å	Exc. Potential eV	Osc. Str.	NIST Flag
Sr (38)			
4077.714 (II)	0.000	0.150	AA
4215.524 (II)	0.000	-0.170	AA
4607.331 (I)	0.000	0.280	AA
4722.278 (I)	1.797	-0.130	B+
4962.263 (I)	1.846	0.250	AA
5256.899 (I)	2.270	0.390	B+
Y (39)			
4374.933 (II)	0.408	0.160	A
4689.767 (I)	2.002	-0.170	A
4883.682 (II)	1.083	0.070	B
5205.722 (II)	1.032	-0.340	B+
5503.464 (I)	1.965	0.370	A
5509.894 (II)	0.992	-1.010	B+
Mo (42)			
5506.493 (I)	1.334	0.060	A+
5533.031 (I)	1.334	-0.070	A+
5570.444 (I)	1.334	-0.340	A
La (57)			
4920.98 (II)	0.126	-0.580	B+
4921.79 (II)	0.244	-0.450	B+
5114.56 (II)	0.235	-1.999	B+ (hfs)
5122.99 (II)	0.321	-2.212	B+ (hfs)
5301.98 (II)	0.403	-2.300	B+ (hfs)
5805.78 (II)	0.126	-2.940	B (hfs)
Nd (60)			
4232.378 (II)	- -	- -	B
4247.367 (II)	0.000	-0.210	B+
5212.365 (II)	0.204	-0.960	B+
5361.474 (II)	0.680	-0.370	

Table A.2: Au sample data. Mass is in [g], diameters are in [cm], cross sections are in [cm], and μ is measured in cm^{-2}.

Run	mass	d_{in}	d_{out}	μ_{areal}	σ_μ	$SACS_{197Au}$	ϕ_{sim}
1 disc d	0.0400	0.000	0.995	1.565e+20	3.152e+18	6.331e-25	2.99e+09
1 disc u	0.0399	0.000	0.988	1.583e+20	3.211e+18	6.334e-25	2.99e+09
1 ring d	0.1174	1.000	2.045	1.429e+20	2.046e+18	1.660e-24	8.62e+07
1 ring u	0.1199	0.990	2.004	1.530e+20	2.253e+18	1.688e-24	8.25e+07
2 disc d	0.0403	0.000	1.007	1.538e+20	3.060e+18	6.430e-25	3.02e+09
2 disc u	0.0383	0.000	1.009	1.456e+20	2.892e+18	6.443e-25	3.02e+09
2 ring d	0.1175	1.001	2.000	1.518e+20	2.266e+18	1.856e-24	5.82e+07
2 ring u	0.1113	1.010	1.995	1.456e+20	2.202e+18	1.893e-24	5.54e+07
3 disc d	0.0377	0.000	1.005	1.446e+20	2.884e+18	6.430e-25	3.02e+09
3 disc u	0.0358	0.000	1.016	1.341e+20	2.647e+18	6.443e-25	3.02e+09
3 ring d	0.1130	0.998	2.001	1.456e+20	2.165e+18	1.857e-24	5.82e+07
3 ring u	0.1049	0.983	1.993	1.351e+20	1.999e+18	1.893e-24	5.54e+07
4 disc d	0.0376	0.000	1.014	1.416e+20	2.799e+18	6.430e-25	3.02e+09
4 disc u	0.0398	0.000	1.027	1.460e+20	2.849e+18	6.443e-25	3.02e+09
4 ring d	0.1095	0.998	2.011	1.392e+20	2.051e+18	1.857e-24	5.82e+07
4 ring u	0.1168	0.995	2.015	1.473e+20	2.158e+18	1.893e-24	5.54e+07
5 disc d	0.0400	0.000	0.995	1.565e+20	3.152e+18	6.430e-25	3.02e+09
5 disc u	0.0399	0.000	0.988	1.583e+20	3.211e+18	6.443e-25	3.02e+09
5 ring d	0.1174	1.000	2.045	1.429e+20	2.046e+18	1.857e-24	5.82e+07
5 ring u	0.1199	0.990	2.004	1.530e+20	2.253e+18	1.893e-24	5.54e+07

Table A.3: Au experimental times. Live times are determined by the detector. Times are given in seconds.

Run	t_{live}	t_m	t_b	t_w
1 disc d	1746	1754	23870	72360
1 disc u	2302	2313	23870	69720
1 ring d	3590	3598	23870	65880
1 ring u	3980	3993	23870	61620
2 disc d	1522	1529	24310	71380
2 disc u	2207	2218	24310	80600
2 ring d	3679	3688	24310	67510
2 ring u	7169	7197	24310	73240
3 disc d	2872	2880	25030	15860
3 disc u	2662	2668	25300	16170
3 ring d	19374	19602	25297	62450
3 ring u	8129	8221	25297	82300
4 disc d	625	628	27188	69320
4 disc u	714	717	27188	70100
4 ring d	2212	2218	27188	64630
4 ring u	2182	2188	27188	67010
5 disc d	594	598	25550	72280
5 disc u	614	617	25550	73000
5 ring d	780	783	25550	70540
5 ring u	626	628	25550	71500

Table A.4: Au decay correction factors.

Run	f_{DT}	f_m	f_w	f_b	σf_b
1 disc d	0.9954	0.0052	0.8061	0.9639	1.8945e-06
1 disc u	0.9952	0.0068	0.8125	0.9639	1.8945e-06
1 ring d	0.9977	0.0106	0.8218	0.9639	1.8945e-06
1 ring u	0.9967	0.0118	0.8323	0.9639	1.8945e-06
2 disc d	0.9954	0.0045	0.8085	0.9630	1.9443e-06
2 disc u	0.9950	0.0065	0.7866	0.9630	1.9443e-06
2 ring d	0.9975	0.0109	0.8179	0.9630	1.9443e-06
2 ring u	0.9961	0.0211	0.8040	0.9630	1.9443e-06
3 disc d	0.9972	0.0085	0.6237	0.9597	2.1152e-06
3 disc u	0.9977	0.0079	0.6179	0.9597	2.1152e-06
3 ring d	0.9883	0.0566	0.8303	0.9597	2.1152e-06
3 ring u	0.9888	0.0241	0.7826	0.9597	2.1152e-06
4 disc d	0.9952	0.0018	0.8135	0.9594	2.1348e-06
4 disc u	0.9958	0.0021	0.8116	0.9594	2.1348e-06
4 ring d	0.9972	0.0065	0.8249	0.9594	2.1348e-06
4 ring u	0.9972	0.0064	0.8191	0.9594	2.1348e-06
5 disc d	0.9933	0.0017	0.8063	0.9618	2.0088e-06
5 disc u	0.9951	0.0018	0.8046	0.9618	2.0088e-06
5 ring d	0.9961	0.0023	0.8105	0.9618	2.0088e-06
5 ring u	0.9968	0.0018	0.8082	0.9618	2.0088e-06

Table A.5: Detector 1 Au scaling factors, detector efficiencies, counts, number of active nuclei, and computed neutron flux data.

Run	SF	ϵ	σ_ϵ	Counts	σ_C	N_a	σ_{N_a}	ϕ_n	σ_{ϕ_n}
1 disc d	0.00827	0.06549	2.742e-4	4.242e+04	210.6	1.608e+08	7.982e+05	1.623e+12	3.366e+10
1 disc u	0.01091	0.06549	2.742e-4	6.296e+04	255.9	1.797e+08	7.305e+05	1.792e+12	3.707e+10
1 ring d	0.01698	0.06406	2.742e-4	1.444e+04	123.0	2.676e+07	2.280e+05	1.128e+11	1.879e+09
1 ring u	0.01884	0.06406	2.742e-4	8.566e+03	94.5	1.415e+07	1.561e+05	5.479e+10	1.008e+09
2 disc d	0.00721	0.06549	2.742e-4	3.740e+04	197.8	1.622e+08	8.578e+05	1.641e+12	3.378e+10
2 disc u	0.01047	0.06549	2.742e-4	5.974e+04	249.8	1.839e+08	7.688e+05	1.906e+12	3.979e+10
2 ring d	0.01740	0.06406	2.742e-4	2.447e+04	159.7	4.451e+07	2.906e+05	1.579e+11	2.572e+09
2 ring u	0.03396	0.06406	2.742e-4	1.078e+04	106.6	1.029e+07	1.017e+05	3.732e+10	6.740e+08
3 disc d	0.01359	0.06549	2.742e-4	1.090e+04	106.8	3.266e+07	3.200e+05	3.514e+11	7.807e+09
3 disc u	0.01259	0.06549	2.742e-4	9.430e+03	99.3	3.076e+07	3.238e+05	3.559e+11	7.960e+09
3 ring d	0.09249	0.06406	2.742e-4	4.784e+03	71.3	1.673e+06	2.513e+05	6.1890+09	1.309e+08
3 ring u	0.03879	0.06406	2.742e-4	1.070e+03	32.8	9.302e+05	2.856e+05	3.636e+09	1.239e+08
4 disc d	0.00296	0.06549	2.742e-4	1.188e+04	111.5	1.251e+08	1.174e+06	1.374e+12	3.006e+10
4 disc u	0.00338	0.06549	2.742e-4	1.514e+04	125.9	1.399e+08	1.163e+06	1.487e+12	3.154e+10
4 ring d	0.01047	0.06406	2.742e-4	9.629e+03	100.3	2.893e+07	3.016e+05	1.120e+11	2.022e+09
4 ring u	0.01032	0.06406	2.742e-4	7.373e+03	87.7	2.262e+07	2.691e+05	8.109e+10	1.530e+09
5 disc d	0.00282	0.06549	2.742e-4	1.712e+04	133.7	1.909e+08	1.491e+06	1.897e+12	4.097e+10
5 disc u	0.00291	0.06549	2.742e-4	1.793e+04	136.8	1.937e+08	1.478e+06	1.899e+12	4.116e+10
5 ring d	0.00369	0.06406	2.742e-4	1.093e+04	107.0	9.436e+07	9.236e+05	3.557e+11	6.168e+09
5 ring u	0.00296	0.06406	2.742e-4	9.013e+03	97.2	9.720e+07	1.049e+06	3.356e+11	6.128e+09

Table A.6: Detector 2 Au scaling factors, detector efficiencies, counts, number of active nuclei, and computed neutron flux data.

Run	SF	ϵ	σ_ϵ	Counts	σ_C	N_a	σ_{N_a}	ϕ_n	σ_{ϕ_n}
1 disc d	0.0083	0.0687	2.769e-04	5.199e+04	232.3	1.878e+08	8.394e+05	1.895e+12	3.910e+10
1 disc u	0.0109	0.0687	2.769e-04	6.631e+04	263.3	1.804e+08	7.166e+05	1.799e+12	3.718e+10
1 ring d	0.0170	0.0678	2.769e-04	1.597e+04	128.8	2.797e+07	2.256e+05	1.179e+11	1.938e+09
1 ring u	0.0188	0.0678	2.769e-04	8.721e+03	95.3	1.361e+07	1.488e+05	5.271e+10	9.670e+08
1 disc d	0.0072	0.0687	2.769e-04	4.145e+04	207.3	1.713e+08	8.574e+05	1.733e+12	3.556e+09
1 disc u	0.0105	0.0687	2.769e-04	6.679e+04	264.2	1.959e+08	7.751e+05	2.088e+12	4.230e+10
1 ring d	0.0174	0.0678	2.769e-04	2.464e+04	159.9	4.235e+07	2.749e+05	1.502e+11	2.445e+09
1 ring u	0.0340	0.0678	2.769e-04	1.070e+04	105.6	9.653e+06	9.529e+04	3.501e+10	6.320e+08
1 disc d	0.0136	0.0687	2.769e-04	1.137e+04	108.8	3.248e+07	3.107e+05	3.493e+11	7.728e+09
1 disc u	0.0126	0.0687	2.769e-04	9.240e+03	98.0	2.872e+07	3.047e+05	3.323e+11	7.447e+09
1 ring d	0.0925	0.0678	2.769e-04	5.069e+03	73.3	1.674e+06	2.421e+04	6.196e+09	1.285e+08
1 ring u	0.0388	0.0678	2.769e-04	1.210e+03	35.0	9.938e+05	2.880e+04	3.884e+09	1.264e+08
1 disc d	0.0030	0.0687	2.769e-04	1.415e+04	121.1	1.419e+08	1.215e+06	1.559e+12	3.359e+10
1 disc u	0.0034	0.0687	2.769e-04	1.723e+04	133.8	1.516e+08	1.178e+06	1.612e+12	3.387e+10
1 ring d	0.0105	0.0678	2.769e-04	9.598e+03	100.0	2.724e+07	2.840e+05	1.054e+11	1.903e+09
1 ring u	0.0103	0.0678	2.769e-04	7.649e+03	89.2	2.216e+07	2.585e+05	7.948e+10	1.488e+09
1 disc d	0.0028	0.0687	2.769e-04	1.867e+04	139.3	1.983e+08	1.480e+06	1.971e+12	4.233e+10
1 disc u	0.0029	0.0687	2.769e-04	1.996e+04	143.9	2.056e+08	1.482e+06	2.015e+12	4.338e+10
1 ring d	0.0037	0.0678	2.769e-04	1.323e+04	117.2	1.079e+08	9.563e+05	4.067e+11	6.847e+09
1 ring u	0.0030	0.0678	2.769e-04	1.009e+04	102.3	1.028e+08	1.043e+06	3.551e+11	6.351e+09

Table A.7: Pb sample data. Mass is in [g], diameters are in [cm], cross sections are in [cm], and μ is measured in cm^{-2}.

Run	mass	d_{in}	d_{out}	μ_{areal}	σ_μ	ϕ_{sim}
1 disc	0.0811	0.000	1.015	1.52+20	3.00+18	2.99e+09
1 ring	0.2597	1.007	2.013	1.65+20	2.45+18	8.50e+07
2 disc	0.0873	0.000	1.009	1.66+20	3.29+18	3.02e+09
2 ring	0.2604	0.996	2.007	1.66+20	2.45+18	5.67e+07
3 disc	0.0871	0.000	1.016	1.63+20	3.22+18	3.02e+09
3 ring	0.2602	0.995	2.016	1.64+20	2.40+18	5.67e+07
4 disc	0.0875	0.000	1.010	1.66+20	3.29+18	3.02e+09
4 ring	0.2577	1.004	2.007	1.65+20	2.45+18	5.67e+07
5 disc	0.0811	0.000	1.015	1.52+20	3.00+18	3.02e+09
5 ring	0.2597	1.007	2.013	1.65+20	2.45+18	5.67e+07

Table A.8: Pb timing Data, part 1. Mass is in [g], diameters are in [cm], and times are in seconds.

Run	t_{live}	t_m	t_b	t_w
1 disc	36170.0	36848.0	23870.0	24289.0
1 ring	21835.0	22261.0	23870.0	500.0
2 disc	42161.0	42013.0	24311.0	25198.0
2 ring	23695.0	24058.0	24311.0	833.0
3 disc	35699.0	36359.0	25297.0	25779.0
3 ring	24339.0	24777.0	25297.0	653.0
4 disc	34183.0	34787.0	27188.0	26331.0
4 ring	24874.0	25197.0	27188.0	750.0
5 disc	40953.0	41698.0	25550.0	28645.0
5 ring	27441.0	27928.0	25550.0	535.0

Table A.9: Pb background decay correction factors.

Run	f_{DT}	f_m	f_w	f_b	σf_b
1 disc	0.9816	0.8870	0.2374	0.5222	0.0524
1 ring	0.9808	0.7322	0.9708	0.5222	0.0524
2 disc	1.0035	0.9168	0.2250	0.5112	0.0545
2 ring	0.9849	0.7592	0.9518	0.5112	0.0545
3 disc	0.9818	0.8837	0.2174	0.5020	0.0517
3 ring	0.9823	0.7692	0.9620	0.5020	0.0517
4 disc	0.9826	0.8724	0.2104	0.4889	0.0560
4 ring	0.9871	0.7749	0.9565	0.4889	0.0560
5 disc	0.9821	0.9152	0.1835	0.5089	0.0531
5 ring	0.9825	0.8085	0.9688	0.5089	0.0531

(a) Detector 1 Pb experimental data. Scaling factors, detector efficiencies, counts, neutron flux, number of active nuclei, and cross sections in [cm^2].

Run	SF	ϵ	σ_ϵ	Counts	σ_C	R	ϕ_n	σ_{ϕ_n}	N_a	σ_{N_a}	σ	σ_σ
1 disc	0.17386	9.38e-03	0.0004	4.942e+03	3.642e+02	570.98	1.70e+12	1.30e+06	4.87e+06	4.41e+05	1.87-26	1.73-27
1 ring	0.10503	9.22e-03	0.0004	2.995e+03	4.630e+02	986.43	8.38e+10	2.89e+05	8.91e+05	1.45e+05	6.41-26	1.05-26
2 disc	0.19823	9.38e-03	0.0004	6.001e+03	3.435e+02	596.14	1.80e+12	1.34e+06	6.04e+06	4.77e+05	2.01-26	1.64-27
2 ring	0.11351	9.22e-03	0.0004	4.020e+03	4.468e+02	1693.38	9.60e+10	3.09e+05	1.19e+06	1.48e+05	7.49-26	9.34-27
3 disc	0.17155	9.38e-03	0.0004	4.966e+03	3.666e+02	117.08	3.53e+11	5.94e+05	5.58e+06	5.03e+05	9.65-26	8.90-27
3 ring	0.11690	9.22e-03	0.0004	3.510e+03	4.398e+02	85.98	4.87e+09	6.98e+04	1.04e+06	1.41e+05	1.30-24	1.77-25
4 disc	0.16413	9.38e-03	0.0004	4.690e+03	3.741e+02	473.65	1.43e+12	1.19e+06	5.66e+06	5.52e+05	2.38-26	2.36-27
4 ring	0.11888	9.22e-03	0.0004	3.424e+03	4.361e+02	1693.95	9.60e+10	3.09e+05	1.03e+06	1.44e+05	6.52-26	9.13-27
5 disc	0.19674	9.38e-03	0.0004	5.683e+03	3.443e+02	628.45	1.89e+12	1.37e+06	7.21e+06	5.81e+05	2.49-26	2.06-27
5 ring	0.13177	9.22e-03	0.0004	3.891e+03	4.152e+02	6084.46	3.44e+11	5.87e+05	1.07e+06	1.28e+05	1.88-26	2.26-27

(b) Detector 2 Pb experimental data. Scaling factors, detector efficiencies, counts, neutron flux, number of active nuclei, and cross sections in [cm^2].

Run	SF	ϵ	σ_ϵ	Counts	σ_C	R	ϕ_n	σ_{ϕ_n}	N_a	σ_{N_a}	σ	σ_σ
1 disc	0.17386	9.71e-03	0.0004	4.240e+03	3.375e+02	617.89	1.84e+12	1.35e+06	4.04e+06	3.85e+05	1.43-26	1.39-27
1 ring	0.10503	9.54e-03	0.0004	2.599e+03	4.291e+02	1003.73	8.53e+10	2.92e+05	7.48e+05	1.29e+05	5.29-26	9.19-27
2 disc	0.19823	9.71e-03	0.0004	5.091e+03	3.182e+02	632.79	1.91e+12	1.38e+06	4.95e+06	4.11e+05	1.55-26	1.32-27
2 ring	0.11351	9.54e-03	0.0004	3.670e+03	4.143e+02	1606.87	9.11e+10	3.01e+05	1.05e+06	1.32e+05	6.97-26	8.80-27
3 disc	0.17155	9.71e-03	0.0004	4.223e+03	3.397e+02	112.87	3.40e+11	5.83e+05	4.59e+06	4.38e+05	8.22-26	8.03-27
3 ring	0.11690	9.54e-03	0.0004	2.960e+03	4.075e+02	88.29	5.00e+09	7.07e+04	8.49e+05	1.25e+05	1.03-24	1.52-25
4 disc	0.16413	9.71e-03	0.0004	4.015e+03	3.467e+02	525.17	1.58e+12	1.25e+06	4.68e+06	4.82e+05	1.77-26	1.86-27
4 ring	0.11888	9.54e-03	0.0004	3.445e+03	4.048e+02	1623.41	9.20e+10	3.03e+05	1.00e+06	1.31e+05	6.62-26	8.68-27
5 disc	0.19674	9.71e-03	0.0004	5.735e+03	3.204e+02	660.12	1.99e+11	1.41e+06	7.03e+06	5.42e+05	2.31-26	1.83-27
5 ring	0.13177	9.54e-03	0.0004	3.288e+03	3.847e+02	6699.45	3.79e+11	6.16e+05	8.79e+05	1.13e+05	1.39-26	1.80-27

B List of Figures

C List of Tables

D Bibliography

Exfor formats manual. Technical Report IAEA-NDS-207 Rev. 2022/06, IAEA Nuclear Data Section, Vienna, 2022.

C. Abate, O. R. Pols, R. G. Izzard, S. S. Mohamed, and S. E. de Mink. Wind Roche-lobe overflow: Application to carbon-enhanced metal-poor stars. , 552:A26, April 2013. doi: 10.1051/0004-6361/201220007.

C. Abate, O. R. Pols, R. G. Izzard, and A. I. Karakas. Carbon-enhanced metal-poor stars: a window on AGB nucleosynthesis and binary evolution. II. Statistical analysis of a sample of 67 CEMP-s stars. , 581:A22, September 2015a. doi: 10.1051/0004-6361/201525876.

C. Abate, O. R. Pols, A. I. Karakas, and R. G. Izzard. Carbon-enhanced metal-poor stars: a window on AGB nucleosynthesis and binary evolution. I. Detailed analysis of 15 binary stars with known orbital periods. , 576:A118, April 2015b. doi: 10.1051/0004-6361/201424739.

Carlo Abate, Onno R. Pols, and Richard J. Stancliffe. Understanding the orbital periods of CEMP-s stars. , 620:A63, November 2018. doi: 10.1051/0004-6361/201833780.

Monika M. Adamow. pyMOOGi - python wrapper for MOOG. In *American Astronomical Society Meeting Abstracts #230*, volume 230 of *American Astronomical Society Meeting Abstracts*, page 216.07, June 2017.

Arthur Alencastro Puls. *Investigating the Relationship Between Chemical Abundance Ratios and Ages in Red Giant Stars*. PhD thesis, The Australian National University, 2023.

A. Alksnis, A. Balklavs, U. Dzervitis, I. Eglitis, O. Paupers, and I. Pundure. General Catalog of Galactic Carbon Stars by C. B. Stephenson. Third Edition. *Baltic Astronomy*, 10:1–318, January 2001. doi: 10.1515/astro-2001-1-202.

B. J. Allen, R. L. Macklin, R. R. Winters, and C. Y. Fu. Neutron-capture cross sections of the stable lead isotopes. *Phys. Rev. C*, 8:1504–1517, Oct 1973. doi: 10.1103/PhysRevC.8.1504. URL https://link.aps.org/doi/10.1103/PhysRevC.8.1504.

D. M. Allen and B. Barbuy. Analysis of 26 barium stars. I. Abundances. , 454(3):895–915, August 2006. doi: 10.1051/0004-6361:20064912.

A. Alonso, S. Arribas, and C. Martínez-Roger. The effective temperature scale of giant stars (F0-K5). II. Empirical calibration of T_{eff} versus colours and [Fe/H]. , 140:261–277, December 1999. doi: 10.1051/aas:1999521.

A. Alves-Brito, J. Meléndez, M. Asplund, I. Ramírez, and D. Yong. Chemical similarities between Galactic bulge and local thick disk red giants: O, Na, Mg, Al, Si, Ca, and Ti. , 513:A35, April 2010. doi: 10.1051/0004-6361/200913444.

Almudena Arcones and Friedrich-Karl Thielemann. Origin of the elements. , 31(1):1, December 2023. doi: 10.1007/s00159-022-00146-x.

Martin Asplund, Nicolas Grevesse, A. Jacques Sauval, and Pat Scott. The Chemical Composition of the Sun. , 47(1):481–522, September 2009. doi: 10.1146/annurev.astro.46.060407.145222.

Z. Bao. Calculations of maxwellian-averaged cross sections and astrophysical reaction rates using evaluated nuclear data libraries. *At. Data Nucl. Data Tables*, 92:70–90, 2009. URL https://arxiv.org/abs/0905.2086.

A. Baranne, M. Mayor, and J. L. Poncet. Coravel— A new tool for radial velocity measurements. *Vistas in Astronomy*, 23(4):279–316, January 1979. doi: 10.1016/0083-6656(79)90016-3.

A. Bartkevicius. A New Version of the Catalog of CH and Related Stars (CH95 Catalog). *Baltic Astronomy*, 5:217–229, January 1996. doi: 10.1515/astro-1996-0207.

H. Beer, F. Corvi, and P. Mutti. Neutron capture of the bottleneck isotopes 138ba and 208pb, s-process studies, and the r-process abundance distribution. *The Astrophysical Journal*, 474(2):843, jan 1997. doi: 10.1086/303480. URL https://dx.doi.org/10.1086/303480.

Timothy C. Beers and Norbert Christlieb. The Discovery and Analysis of Very Metal-Poor Stars in the Galaxy. , 43(1):531–580, September 2005. doi: 10.1146/annurev.astro.42.053102.134057.

Timothy C. Beers, George W. Preston, and Stephen A. Shectman. A Search for Stars of Very Low Metal Abundance. II. , 103:1987, June 1992. doi: 10.1086/116207.

M. J. Berger. ESTAR, PSTAR, and ASTAR: Computer programs for calculating stopping-power and range tables for electrons, protons, and helium ions, December 1992.

H. A. Bethe. Energy Production in Stars. *Physical Review*, 55(5):434–456, March 1939. doi: 10.1103/PhysRev.55.434.

H. A. Bethe. Passage of energetic particles through matter. *Annual Review of Nuclear Science*, 4:1–28, 1954. doi: 10.1146/annurev.ns.04.120154.001531. URL `https://www.annualreviews.org/content/journals/10.1146/annurev.ns.04.120154.001531`.

William P. Bidelman and Philip C. Keenan. The Ba II Stars. , 114:473, November 1951. doi: 10.1086/145488.

S. Bisterzo, R. Gallino, O. Straniero, S. Cristallo, and F. Käppeler. The s-process in low-metallicity stars - II. Interpretation of high-resolution spectroscopic observations with asymptotic giant branch models. , 418(1):284–319, November 2011. doi: 10.1111/j.1365-2966.2011.19484.x.

S. Bisterzo, C. Travaglio, R. Gallino, M. Wiescher, and F. Käppeler. Galactic Chemical Evolution and Solar s-process Abundances: Dependence on the ^{13}C-pocket Structure. , 787(1):10, May 2014. doi: 10.1088/0004-637X/787/1/10.

H. M. J. Boffin and A. Jorissen. Can a barium star be produced by wind accretion in a detached binary ? , 205:155–163, October 1988.

H. E. Bond. The subgiant CH stars. , 194:95–107, November 1974. doi: 10.1086/153227.

H. Bondi and F. Hoyle. On the mechanism of accretion by stars. , 104:273, January 1944. doi: 10.1093/mnras/104.5.273.

Tanyu Bonev, Haralambi Markov, Toma Tomov, Rumen Bogdanovski, Pencho Markishki, Maya Belcheva, Wojciech Dimitrov, Krzysztof Kamiński, Ilko Milushev, Faig Musaev, Mirela Napetova, Grigor Nikolov, Plamen Nikolov, and Tihomir Tenev. ESpeRo: Echelle Spectrograph Rozhen. *Bulgarian Astronomical Journal*, 26:67, January 2017. doi: 10.48550/arXiv.1612.07226.

Rafael Brahm, Andrés Jordán, and Néstor Espinoza. CERES: A Set of Automated Routines for Echelle Spectra. , 129(973):034002, March 2017. doi: 10.1088/1538-3873/aa5455.

Alessandro Bressan, Paola Marigo, Léo. Girardi, Bernardo Salasnich, Claudia Dal Cero, Stefano Rubele, and Ambra Nanni. PARSEC: stellar tracks and isochrones with the PAdova and TRieste Stellar Evolution Code. , 427(1):127–145, November 2012. doi: 10.1111/j.1365-2966.2012.21948.x.

R Brun, R Hagelberg, M Hansroul, and J C Lassalle. *Simulation program for particle physics experiments, GEANT*. CERN, Geneva, 1978. URL `https://cds.cern.ch/record/118715`.

S. Buder, K. Lind, M. K. Ness, M. Asplund, L. Duong, J. Lin, J. Kos, L. Casagrande, A. R. Casey, J. Bland-Hawthorn, G. M. de Silva, V. D'Orazi, K. C. Freeman, S. L. Martell, K. J. Schlesinger, S. Sharma, J. D. Simpson, D. B. Zucker, T. Zwitter, K. Čotar, A. Dotter, M. R. Hayden, E. A. Hyde, P. R. Kafle, G. F. Lewis, D. M. Nataf, T. Nordlander, W. Reid, H. W. Rix, Á. Skúladóttir, D. Stello, Y. S. Ting, G. Traven, R. F. G. Wyse, and GALAH Collaboration. The GALAH survey: An abundance, age, and kinematic inventory of the solar neighbourhood made with TGAS. , 624:A19, April 2019. doi: 10.1051/0004-6361/201833218.

Sven Buder, Martin Asplund, Ly Duong, Janez Kos, Karin Lind, Melissa K. Ness, Sanjib Sharma, Joss Bland-Hawthorn, Andrew R. Casey, Gayandhi M. de Silva, Valentina D'Orazi, Ken C. Freeman, Geraint F. Lewis, Jane Lin, Sarah L. Martell, Katharine J. Schlesinger, Jeffrey D. Simpson, Daniel B. Zucker, Tomaž Zwitter, Anish M. Amarsi, Borja Anguiano, Daniela Carollo, Luca Casagrande, Klemen Čotar, Peter L. Cottrell, Gary da Costa, Xudong D. Gao, Michael R. Hayden, Jonathan Horner, Michael J. Ireland, Prajwal R. Kafle, Ulisse Munari, David M. Nataf, Thomas Nordlander, Dennis Stello, Yuan-Sen Ting, Gregor Traven, Fred Watson, Robert A. Wittenmyer, Rosemary F. G. Wyse, David Yong, Joel C. Zinn, Maruša Žerjal, and Galah Collaboration. The GALAH Survey: second data release. , 478(4):4513–4552, August 2018. doi: 10.1093/mnras/sty1281.

Sven Buder, Sanjib Sharma, Janez Kos, Anish M. Amarsi, Thomas Nordlander, Karin Lind, Sarah L. Martell, Martin Asplund, Joss Bland-Hawthorn, Andrew R. Casey, Gayandhi M. de Silva, Valentina D'Orazi, Ken C. Freeman, Michael R. Hayden, Geraint F. Lewis, Jane Lin, Katharine J. Schlesinger, Jeffrey D. Simpson, Dennis Stello,

Daniel B. Zucker, Tomaž Zwitter, Kevin L. Beeson, Tobias Buck, Luca Casagrande, Jake T. Clark, Klemen Čotar, Gary S. da Costa, Richard de Grijs, Diane Feuillet, Jonathan Horner, Prajwal R. Kafle, Shourya Khanna, Chiaki Kobayashi, Fan Liu, Benjamin T. Montet, Govind Nandakumar, David M. Nataf, Melissa K. Ness, Lorenzo Spina, Thor Tepper-García, Yuan-Sen Ting, Gregor Traven, Rok Vogrinčič, Robert A. Wittenmyer, Rosemary F. G. Wyse, Maruša Žerjal, and Galah Collaboration. The GALAH+ survey: Third data release. , 506(1):150–201, September 2021. doi: 10.1093/mnras/stab1242.

E. Margaret Burbidge, G. R. Burbidge, William A. Fowler, and F. Hoyle. Synthesis of the Elements in Stars. *Reviews of Modern Physics*, 29(4):547–650, January 1957. doi: 10.1103/RevModPhys.29.547.

M. Busso, R. Gallino, and G. J. Wasserburg. Nucleosynthesis in Asymptotic Giant Branch Stars: Relevance for Galactic Enrichment and Solar System Formation. , 37:239–309, January 1999. doi: 10.1146/annurev.astro.37.1.239.

Maurizio Busso, Roberto Gallino, David L. Lambert, Claudia Travaglio, and Verne V. Smith. Nucleosynthesis and Mixing on the Asymptotic Giant Branch. III. Predicted and Observed s-Process Abundances. , 557(2):802–821, August 2001. doi: 10.1086/322258.

M. Cabezas, M. Šlechta, P. Škoda, and B. Kubátová. OESRED, the semi-automatic reduction code for Ondřejov Echelle Spectrographs. *Zenodo*, 2023. doi: https://doi.org/10.5281/zenodo.10024183.

S. W. Campbell, B. T. MacLean, V. D'Orazi, L. Casagrande, G. M. de Silva, D. Yong, P. L. Cottrell, and J. C. Lattanzio. NGC 6752 AGB stars revisited. I. Improved AGB temperatures remove apparent overionisation of Fe I. , 605:A98, September 2017. doi: 10.1051/0004-6361/201731101.

V. M. Canuto and I. Mazzitelli. Stellar Turbulent Convection: A New Model and Applications. , 370:295, March 1991. doi: 10.1086/169815.

Bruce W. Carney, David W. Latham, Robert P. Stefanik, John B. Laird, and Jon A. Morse. Spectroscopic Binaries, Velocity Jitter, and Rotation in Field Metal-poor Red Giant and Red Horizontal-Branch Stars. , 125(1):293–321, January 2003. doi: 10.1086/345386.

F. Castelli and R. L. Kurucz. New Grids of ATLAS9 Model Atmospheres. In N. Piskunov, W. W. Weiss, and D. F. Gray, editors, *Modelling of Stellar Atmospheres*, volume 210 of *IAU Symposium*, page A20, January 2003. doi: 10.48550/arXiv.astro-ph/0405087.

M. B. Chadwick, P. G. Young, and C. Y. Fu. ENDF/B-VI data evaluation for ^{56}fe (incident neutron sublibrary, mat=2631). Endf evaluation / technical report, Los Alamos National Laboratory (LANL), September 1996. ENDF/B evaluation for ^{56}Fe; see ENDF material MAT=2631 (incident neutron sublibrary).

M. B. Chadwick, M. Herman, P. Obložinský, M. E. Dunn, Y. Danon, A. C. Kahler, D. L. Smith, B. Pritychenko, G. Arbanas, R. Arcilla, R. Brewer, D. A. Brown, R. Capote, A. D. Carlson, Y. S. Cho, H. Derrien, K. Guber, G. M. Hale, S. Hoblit, S. Holloway, T. D. Johnson, T. Kawano, B. C. Kiedrowski, H. Kim, S. Kunieda, N. M. Larson, L. Leal, J. P. Lestone, R. C. Little, E. A. McCutchan, R. E. MacFarlane, M. MacInnes, C. M. Mattoon, R. D. McKnight, S. F. Mughabghab, G. P. A. Nobre, G. Palmiotti, A. Palumbo, M. T. Pigni, V. G. Pronyaev, R. O. Sayer, A. A. Sonzogni, N. C. Summers, P. Talou, I. J. Thompson, A. Trkov, R. L. Vogt, S. C. van der Marck, A. Wallner, M. C. White, D. Wiarda, and P. G. Young. ENDF/B-VII.1 Nuclear Data for Science and Technology: Cross Sections, Covariances, Fission Product Yields and Decay Data. *Nuclear Data Sheets*, 112(12):2887–2996, December 2011. doi: 10.1016/j.nds.2011.11.002.

S. Chandrasekhar. The Maximum Mass of Ideal White Dwarfs. , 74:81, July 1931. doi: 10.1086/143324.

P. S. Chen, J. Y. Liu, and H. G. Shan. A New Infrared Photometric Study of Intrinsic and Extrinsic S-type Stars. , 158(1):22, July 2019. doi: 10.3847/1538-3881/ab2334.

Yang Chen, Léo Girardi, Alessandro Bressan, Paola Marigo, Mauro Barbieri, and Xu Kong. Improving PARSEC models for very low mass stars. , 444(3):2525–2543, November 2014. doi: 10.1093/mnras/stu1605.

Yang Chen, Alessandro Bressan, Léo Girardi, Paola Marigo, Xu Kong, and Antonio Lanza. PARSEC evolutionary tracks of massive stars up to 350 $M_\odot$ at metallicities $0.0001 \leq Z \leq 0.04$. , 452(1):1068–1080, September 2015. doi: 10.1093/mnras/stv1281.

Zhuo Chen, Adam Frank, Eric G. Blackman, Jason Nordhaus, and Jonathan Carroll-Nellenback. Mass transfer and disc formation in AGB binary systems. , 468(4):4465–4477, July 2017. doi: 10.1093/mnras/stx680.

A. Choplin, L. Siess, and S. Goriely. The intermediate neutron capture process. I. Development of the i-process in low-metallicity low-mass AGB stars. , 648:A119, April 2021. doi: 10.1051/0004-6361/202040170.

O. L. Creevey and Y. Lebreton. Masses and ages from FLAME in DR3. November 2022. URL https://dms.cosmos.esa.int/COSMOS/doc_fetch.php?id=1612899.

S. Cristallo, L. Piersanti, O. Straniero, R. Gallino, I. Domínguez, C. Abia, G. Di Rico, M. Quintini, and S. Bisterzo. Evolution, Nucleosynthesis, and Yields of Low-mass Asymptotic Giant Branch Stars at Different Metallicities. II. The FRUITY Database. , 197(2):17, December 2011. doi: 10.1088/0067-0049/197/2/17.

S. Cristallo, O. Straniero, L. Piersanti, and D. Gobrecht. Evolution, Nucleosynthesis, and Yields of AGB Stars at Different Metallicities. III. Intermediate-mass Models, Revised Low-mass Models, and the ph-FRUITY Interface. , 219(2):40, August 2015. doi: 10.1088/0067-0049/219/2/40.

S. Cristallo, D. Karinkuzhi, A. Goswami, L. Piersanti, and D. Gobrecht. Constraints of the Physics of Low-mass AGB Stars from CH and CEMP Stars. , 833(2):181, December 2016. doi: 10.3847/1538-4357/833/2/181.

B. Cseh, M. Lugaro, V. D'Orazi, D. B. de Castro, C. B. Pereira, A. I. Karakas, L. Molnár, E. Plachy, R. Szabó, M. Pignatari, and S. Cristallo. The s process in AGB stars as constrained by a large sample of barium stars. , 620:A146, December 2018. doi: 10.1051/0004-6361/201834079.

B. Cseh, B. Világos, M. P. Roriz, C. B. Pereira, V. D'Orazi, A. I. Karakas, B. Soós, N. A. Drake, S. Junqueira, and M. Lugaro. Barium stars as tracers of s-process nucleosynthesis in AGB stars. I. 28 stars with independently derived AGB mass. , 660:A128, April 2022. doi: 10.1051/0004-6361/202142468.

Xiang-Qun Cui, Yong-Heng Zhao, Yao-Quan Chu, Guo-Ping Li, Qi Li, Li-Ping Zhang, Hong-Jun Su, Zheng-Qiu Yao, Ya-Nan Wang, Xiao-Zheng Xing, Xin-Nan Li, Yong-Tian Zhu, Gang Wang, Bo-Zhong Gu, A. Li Luo, Xin-Qi Xu, Zhen-Chao Zhang, Gen-Rong Liu, Hao-Tong Zhang, De-Hua Yang, Shu-Yun Cao, Hai-Yuan Chen, Jian-Jun Chen, Kun-Xin Chen, Ying Chen, Jia-Ru Chu, Lei Feng, Xue-Fei Gong, Yong-Hui Hou, Hong-Zhuan Hu, Ning-Sheng Hu, Zhong-Wen Hu, Lei Jia, Fang-Hua Jiang, Xiang Jiang, Zi-Bo Jiang, Ge Jin, Ai-Hua Li, Yan Li, Ye-Ping Li, Guan-Qun Liu, Zhi-Gang Liu, Wen-Zhi Lu, Yin-Dun Mao, Li Men, Yong-Jun Qi, Zhao-Xiang Qi, Huo-Ming Shi, Zheng-Hong Tang, Qing-Sheng Tao, Da-Qi Wang, Dan Wang, Guo-Min Wang, Hai Wang, Jia-Ning Wang, Jian Wang, Jian-Ling Wang, Jian-Ping Wang, Lei Wang, Shu-Qing Wang, You Wang, Yue-Fei Wang, Ling-Zhe Xu, Yan Xu, Shi-Hai Yang, Yong Yu, Hui Yuan, Xiang-Yan Yuan, Chao Zhai, Jing Zhang, Yan-Xia Zhang, Yong Zhang, Ming Zhao, Fang

Zhou, Guo-Hua Zhou, Jie Zhu, and Si-Cheng Zou. The Large Sky Area Multi-Object Fiber Spectroscopic Telescope (LAMOST). *Research in Astronomy and Astrophysics*, 12(9):1197–1242, September 2012. doi: 10.1088/1674-4527/12/9/003.

D. B. de Castro, C. B. Pereira, F. Roig, E. Jilinski, N. A. Drake, C. Chavero, and J. V. Sales Silva. Chemical abundances and kinematics of barium stars. , 459(4):4299–4324, July 2016. doi: 10.1093/mnras/stw815.

E. Delgado Mena, M. Tsantaki, V. Zh. Adibekyan, S. G. Sousa, N. C. Santos, J. I. González Hernández, and G. Israelian. Chemical abundances of 1111 FGK stars from the HARPS GTO planet search program. II. Cu, Zn, Sr, Y, Zr, Ba, Ce, Nd, and Eu. , 606:A94, October 2017. doi: 10.1051/0004-6361/201730535.

E. Delgado Mena, A. Moya, V. Adibekyan, M. Tsantaki, J. I. González Hernández, G. Israelian, G. R. Davies, W. J. Chaplin, S. G. Sousa, A. C. S. Ferreira, and N. C. Santos. Abundance to age ratios in the HARPS-GTO sample with Gaia DR2. Chemical clocks for a range of [Fe/H]. , 624:A78, April 2019. doi: 10.1051/0004-6361/201834783.

J. W. den Hartogh, A. Yagüe López, B. Cseh, M. Pignatari, B. Világos, M. P. Roriz, C. B. Pereira, N. A. Drake, S. Junqueira, and M. Lugaro. Barium stars as tracers of s-process nucleosynthesis in AGB stars. II. Using machine learning techniques on 169 stars. , 672: A143, April 2023. doi: 10.1051/0004-6361/202244189.

L. Deng, A. Bressan, and C. Chiosi. Stellar evolution with turbulent diffusion. I. A new formalism of mixing. , 313:145–158, September 1996.

Pavel A. Denissenkov, Falk Herwig, Umberto Battino, Christian Ritter, Marco Pignatari, Samuel Jones, and Bill Paxton. I-process Nucleosynthesis and Mass Retention Efficiency in He-shell Flash Evolution of Rapidly Accreting White Dwarfs. , 834(2):L10, January 2017. doi: 10.3847/2041-8213/834/2/L10.

A. J. Dimoff, C. J. Hansen, R. Stancliffe, B. Kubátová, I. Stateva, A. Kučinskas, and V. Dobrovolskas. S-process nucleosynthesis in chemically peculiar binaries. , 691:A128, November 2024. doi: 10.1051/0004-6361/202450299.

A. J. Dimoff, R. J. Stancliffe, C. J. Hansen, R. M. Seeburger, and H. Taylor. Modeling the progenitors of low-mass post-accretion binaries. *arXiv e-prints*, art. arXiv:2505.22201, May 2025. doi: 10.48550/arXiv.2505.22201.

Alexander J. Dimoff and Jerome A. Orosz. Modeling Apsidal Motion in Eclipsing Binaries Using ELC. , 166(3):114, September 2023. doi: 10.3847/1538-3881/aceaf4.

I. Domínguez, S. Cristallo, O. Straniero, L. Piersanti, G. di Rico, R. Gallino, and C. Abia. The Fruity Database: Chemical Features of Low-Mass AGB Stars. In F. Kerschbaum, T. Lebzelter, and R. F. Wing, editors, *Why Galaxies Care about AGB Stars II: Shining Examples and Common Inhabitants*, volume 445 of *Astronomical Society of the Pacific Conference Series*, page 57, sep 2011.

A. S. Eddington. The internal constitution of the stars. *The Observatory*, 43:341–358, October 1920.

A. S. Eddington. *The Internal Constitution of the Stars*. 1926.

Richard Edgar. A review of Bondi-Hoyle-Lyttleton accretion. , 48(10):843–859, September 2004. doi: 10.1016/j.newar.2004.06.001.

B. Edvardsson, J. Andersen, B. Gustafsson, D. L. Lambert, P. E. Nissen, and J. Tomkin. The Chemical Evolution of the Galactic Disk - Part One - Analysis and Results. , 275: 101, August 1993.

Peter P. Eggleton. The evolution of low mass stars. , 151:351, January 1971. doi: 10.1093/mnras/151.3.351.

Peter P. Eggleton. Composition changes during stellar evolution. , 156:361, January 1972. doi: 10.1093/mnras/156.3.361.

Z. Eker, N. Filiz Ak, S. Bilir, D. Doğru, M. Tüysüz, E. Soydugan, H. Bakış, B. Uğraş, F. Soydugan, A. Erdem, and O. Demircan. A catalogue of chromospherically active binary stars (third edition). , 389(4):1722–1726, October 2008. doi: 10.1111/j.1365-2966.2008.13670.x.

Kareem El-Badry, Hans-Walter Rix, and Daniel R. Weisz. An Empirical Measurement of the Initial-Final Mass Relation with Gaia White Dwarfs. , 860(2):L17, June 2018. doi: 10.3847/2041-8213/aaca9c.

A. Escorza, H. M. J. Boffin, A. Jorissen, S. Van Eck, L. Siess, H. Van Winckel, D. Karinkuzhi, S. Shetye, and D. Pourbaix. Hertzsprung-Russell diagram and mass distribution of barium stars. , 608:A100, December 2017. doi: 10.1051/0004-6361/201731832.

A. Escorza, D. Karinkuzhi, A. Jorissen, L. Siess, H. Van Winckel, D. Pourbaix, C. Johnston, B. Miszalski, G. M. Oomen, M. Abdul-Masih, H. M. J. Boffin, P. North, R. Manick, S. Shetye, and J. Mikołajewska. Barium and related stars, and their white-dwarf companions. II. Main-sequence and subgiant starss. , 626:A128, June 2019. doi: 10.1051/0004-6361/201935390.

A. Escorza, L. Siess, H. Van Winckel, and A. Jorissen. Binary evolution along the red giant branch with BINSTAR: The barium star perspective. , 639:A24, July 2020. doi: 10.1051/0004-6361/202037487.

T. Rauscher et al. Dependence of direct neutron capture on nuclear-structure models. *Phys. Rev. C*, 57:2031–2046, 1998. doi: 10.1103/PhysRevC.57.2031. URL `https://arxiv.org/abs/nucl-th/9801005`.

Henry Eyring. The transmission coefficient in reaction rate theory. *Rev. Mod. Phys.*, 34: 616–619, Oct 1962. doi: 10.1103/RevModPhys.34.616. URL `https://link.aps.org/doi/10.1103/RevModPhys.34.616`.

C. Fabricius, E. Høg, V. V. Makarov, B. D. Mason, G. L. Wycoff, and S. E. Urban. The Tycho double star catalogue. , 384:180–189, March 2002. doi: 10.1051/0004-6361:20011822.

F. C. Fekel, K. G. Strassmeier, M. Weber, and A. Washuettl. Orbital elements and physical parameters of ten chromospherically active binary stars. , 137:369–383, June 1999. doi: 10.1051/aas:1999252.

Francis C. Fekel and Joseph J. Eitter. Chromospherically Active Stars. VII. 39 Ceti=AY Ceti, HD185151=V1764 Cygni, and Binary Synchronization. , 97:1139, April 1989. doi: 10.1086/115056.

P. François, E. Depagne, V. Hill, M. Spite, F. Spite, B. Plez, T. C. Beers, J. Andersen, G. James, B. Barbuy, R. Cayrel, P. Bonifacio, P. Molaro, B. Nordström, and F. Primas. First stars. VIII. Enrichment of the neutron-capture elements in the early Galaxy. , 476 (2):935–950, December 2007. doi: 10.1051/0004-6361:20077706.

Anna Frebel, Norbert Christlieb, John E. Norris, Timothy C. Beers, Michael S. Bessell, Jaehon Rhee, Cora Fechner, Brian Marsteller, Silvia Rossi, Christopher Thom, Lutz Wisotzki, and Dieter Reimers. Bright Metal-poor Stars from the Hamburg/ESO Survey. I. Selection and Follow-up Observations from 329 Fields. , 652(2):1585–1603, December 2006. doi: 10.1086/508506.

U. Frischknecht, R. Hirschi, and F. K. Thielemann. Non-standard s-process in low metallicity massive rotating stars. , 538:L2, February 2012. doi: 10.1051/0004-6361/201117794.

Gaia Collaboration. VizieR Online Data Catalog: Gaia DR3 Part 1. Main source (Gaia Collaboration, 2022). VizieR On-line Data Catalog: I/355. Originally published in: Astron. Astrophys., in prep. (2022), May 2022.

Gaia Collaboration, A. G. A. Brown, A. Vallenari, T. Prusti, J. H. J. de Bruijne, C. Babusiaux, M. Biermann, O. L. Creevey, D. W. Evans, L. Eyer, A. Hutton, F. Jansen, C. Jordi, S. A. Klioner, U. Lammers, L. Lindegren, X. Luri, F. Mignard, C. Panem, D. Pourbaix, S. Randich, P. Sartoretti, C. Soubiran, N. A. Walton, F. Arenou, C. A. L. Bailer-Jones, U. Bastian, M. Cropper, R. Drimmel, D. Katz, M. G. Lattanzi, F. van Leeuwen, J. Bakker, C. Cacciari, J. Castañeda, F. De Angeli, C. Ducourant, C. Fabricius, M. Fouesneau, Y. Frémat, R. Guerra, A. Guerrier, J. Guiraud, A. Jean-Antoine Piccolo, E. Masana, R. Messineo, N. Mowlavi, C. Nicolas, K. Nienartowicz, F. Pailler, P. Panuzzo, F. Riclet, W. Roux, G. M. Seabroke, R. Sordo, P. Tanga, F. Thévenin, G. Gracia-Abril, J. Portell, D. Teyssier, M. Altmann, R. Andrae, I. Bellas-Velidis, K. Benson, J. Berthier, R. Blomme, E. Brugaletta, P. W. Burgess, G. Busso, B. Carry, A. Cellino, N. Cheek, G. Clementini, Y. Damerdji, M. Davidson, L. Delchambre, A. Dell'Oro, J. Fernández-Hernández, L. Galluccio, P. García-Lario, M. Garcia-Reinaldos, J. González-Núñez, E. Gosset, R. Haigron, J. L. Halbwachs, N. C. Hambly, D. L. Harrison, D. Hatzidimitriou, U. Heiter, J. Hernández, D. Hestroffer, S. T. Hodgkin, B. Holl, K. Janßen, G. Jevardat de Fombelle, S. Jordan, A. Krone-Martins, A. C. Lanzafame, W. Löffler, A. Lorca, M. Manteiga, O. Marchal, P. M. Marrese, A. Moitinho, A. Mora, K. Muinonen, P. Osborne, E. Pancino, T. Pauwels, J. M. Petit, A. Recio-Blanco, P. J. Richards, M. Riello, L. Rimoldini, A. C. Robin, T. Roegiers, J. Rybizki, L. M. Sarro, C. Siopis, M. Smith, A. Sozzetti, A. Ulla, E. Utrilla, M. van Leeuwen, W. van Reeven, U. Abbas, A. Abreu Aramburu, S. Accart, C. Aerts, J. J. Aguado, M. Ajaj, G. Altavilla, M. A. Álvarez, J. Álvarez Cid-Fuentes, J. Alves, R. I. Anderson, E. Anglada Varela, T. Antoja, M. Audard, D. Baines, S. G. Baker, L. Balaguer-Núñez, E. Balbinot, Z. Balog, C. Barache, D. Barbato, M. Barros, M. A. Barstow, S. Bartolomé, J. L. Bassilana, N. Bauchet, A. Baudesson-Stella, U. Becciani, M. Bellazzini, M. Bernet, S. Bertone, L. Bianchi, S. Blanco-Cuaresma, T. Boch, A. Bombrun, D. Bossini, S. Bouquillon, A. Bragaglia, L. Bramante, E. Breedt, A. Bressan, N. Brouillet, B. Bucciarelli, A. Burlacu, D. Busonero, A. G. Butkevich, R. Buzzi, E. Caffau, R. Cancelliere, H. Cánovas, T. Cantat-Gaudin, R. Carballo, T. Carlucci, M. I. Carnerero, J. M. Carrasco, L. Casamiquela, M. Castellani, A. Castro-Ginard, P. Castro Sampol, L. Chaoul,

P. Charlot, L. Chemin, A. Chiavassa, M. R. L. Cioni, G. Comoretto, W. J. Cooper, T. Cornez, S. Cowell, F. Crifo, M. Crosta, C. Crowley, C. Dafonte, A. Dapergolas, M. David, and P. David. Gaia Early Data Release 3. Summary of the contents and survey properties. , 649:A1, May 2021. doi: 10.1051/0004-6361/202039657.

Gaia Collaboration, A. Vallenari, A. G. A. Brown, T. Prusti, J. H. J. de Bruijne, F. Arenou, C. Babusiaux, M. Biermann, O. L. Creevey, C. Ducourant, D. W. Evans, L. Eyer, R. Guerra, A. Hutton, C. Jordi, S. A. Klioner, U. L. Lammers, L. Lindegren, X. Luri, F. Mignard, C. Panem, D. Pourbaix, S. Randich, P. Sartoretti, C. Soubiran, P. Tanga, N. A. Walton, C. A. L. Bailer-Jones, U. Bastian, R. Drimmel, F. Jansen, D. Katz, M. G. Lattanzi, F. van Leeuwen, J. Bakker, C. Cacciari, J. Castañeda, F. De Angeli, C. Fabricius, M. Fouesneau, Y. Frémat, L. Galluccio, A. Guerrier, U. Heiter, E. Masana, R. Messineo, N. Mowlavi, C. Nicolas, K. Nienartowicz, F. Pailler, P. Panuzzo, F. Riclet, W. Roux, G. M. Seabroke, R. Sordo, F. Thévenin, G. Gracia-Abril, J. Portell, D. Teyssier, M. Altmann, R. Andrae, M. Audard, I. Bellas-Velidis, K. Benson, J. Berthier, R. Blomme, P. W. Burgess, D. Busonero, G. Busso, H. Cánovas, B. Carry, A. Cellino, N. Cheek, G. Clementini, Y. Damerdji, M. Davidson, P. de Teodoro, M. Nuñez Campos, L. Delchambre, A. Dell'Oro, P. Esquej, J. Fernández-Hernández, E. Fraile, D. Garabato, P. García-Lario, E. Gosset, R. Haigron, J. L. Halbwachs, N. C. Hambly, D. L. Harrison, J. Hernández, D. Hestroffer, S. T. Hodgkin, B. Holl, K. Janßen, G. Jevardat de Fombelle, S. Jordan, A. Krone-Martins, A. C. Lanzafame, W. Löffler, O. Marchal, P. M. Marrese, A. Moitinho, K. Muinonen, P. Osborne, E. Pancino, T. Pauwels, A. Recio-Blanco, C. Reylé, M. Riello, L. Rimoldini, T. Roegiers, J. Rybizki, L. M. Sarro, C. Siopis, M. Smith, A. Sozzetti, E. Utrilla, M. van Leeuwen, U. Abbas, P. Ábrahám, A. Abreu Aramburu, C. Aerts, J. J. Aguado, M. Ajaj, F. Aldea-Montero, G. Altavilla, M. A. Álvarez, J. Alves, F. Anders, R. I. Anderson, E. Anglada Varela, T. Antoja, D. Baines, S. G. Baker, L. Balaguer-Núñez, E. Balbinot, Z. Balog, C. Barache, D. Barbato, M. Barros, M. A. Barstow, S. Bartolomé, J. L. Bassilana, N. Bauchet, U. Becciani, M. Bellazzini, A. Berihuete, M. Bernet, S. Bertone, L. Bianchi, A. Binnenfeld, S. Blanco-Cuaresma, A. Blazere, T. Boch, A. Bombrun, D. Bossini, S. Bouquillon, A. Bragaglia, L. Bramante, E. Breedt, A. Bressan, N. Brouillet, E. Brugaletta, B. Bucciarelli, A. Burlacu, A. G. Butkevich, R. Buzzi, E. Caffau, R. Cancelliere, T. Cantat-Gaudin, R. Carballo, T. Carlucci, M. I. Carnerero, J. M. Carrasco, L. Casamiquela, M. Castellani, A. Castro-Ginard, L. Chaoul, P. Charlot, L. Chemin, V. Chiaramida, A. Chiavassa, N. Chornay, G. Comoretto, G. Contursi, W. J. Cooper, T. Cornez, S. Cowell, F. Crifo, M. Cropper, M. Crosta, C. Crowley, C. Dafonte,

A. Dapergolas, M. David, P. David, P. de Laverny, F. De Luise, R. De March, J. De Ridder, R. de Souza, A. de Torres, E. F. del Peloso, E. del Pozo, M. Delbo, A. Delgado, J. B. Delisle, C. Demouchy, T. E. Dharmawardena, P. Di Matteo, S. Diakite, C. Diener, E. Distefano, C. Dolding, B. Edvardsson, H. Enke, C. Fabre, M. Fabrizio, S. Faigler, G. Fedorets, P. Fernique, A. Fienga, F. Figueras, Y. Fournier, C. Fouron, F. Fragkoudi, M. Gai, A. Garcia-Gutierrez, M. Garcia-Reinaldos, M. García-Torres, A. Garofalo, A. Gavel, P. Gavras, E. Gerlach, R. Geyer, P. Giacobbe, G. Gilmore, S. Girona, G. Giuffrida, R. Gomel, A. Gomez, J. González-Núñez, I. González-Santamaría, J. J. González-Vidal, M. Granvik, P. Guillout, J. Guiraud, R. Gutiérrez-Sánchez, L. P. Guy, D. Hatzidimitriou, M. Hauser, M. Haywood, A. Helmer, A. Helmi, M. H. Sarmiento, S. L. Hidalgo, T. Hilger, N. Hładczuk, D. Hobbs, G. Holland, H. E. Huckle, K. Jardine, G. Jasniewicz, A. Jean-Antoine Piccolo, Ó. Jiménez-Arranz, A. Jorissen, J. Juaristi Campillo, F. Julbe, L. Karbevska, P. Kervella, S. Khanna, M. Kontizas, G. Kordopatis, A. J. Korn, Á. Kóspál, Z. Kostrzewa-Rutkowska, K. Kruszyńska, M. Kun, P. Laizeau, S. Lambert, A. F. Lanza, Y. Lasne, J. F. Le Campion, Y. Lebreton, T. Lebzelter, S. Leccia, N. Leclerc, I. Lecoeur-Taibi, S. Liao, E. L. Licata, H. E. P. Lindstrøm, T. A. Lister, E. Livanou, A. Lobel, A. Lorca, C. Loup, P. Madrero Pardo, A. Magdaleno Romeo, S. Managau, R. G. Mann, M. Manteiga, J. M. Marchant, M. Marconi, J. Marcos, M. M. S. Marcos Santos, D. Marín Pina, S. Marinoni, F. Marocco, D. J. Marshall, L. Martin Polo, J. M. Martín-Fleitas, G. Marton, N. Mary, A. Masip, D. Massari, A. Mastrobuono-Battisti, T. Mazeh, P. J. McMillan, S. Messina, D. Michalik, N. R. Millar, A. Mints, D. Molina, R. Molinaro, L. Molnár, G. Monari, M. Monguió, P. Montegriffo, A. Montero, R. Mor, A. Mora, R. Morbidelli, T. Morel, D. Morris, T. Muraveva, C. P. Murphy, I. Musella, Z. Nagy, L. Noval, F. Ocaña, A. Ogden, C. Ordenovic, J. O. Osinde, C. Pagani, I. Pagano, L. Palaversa, P. A. Palicio, L. Pallas-Quintela, A. Panahi, S. Payne-Wardenaar, X. Peñalosa Esteller, A. Penttilä, B. Pichon, A. M. Piersimoni, F. X. Pineau, E. Plachy, G. Plum, E. Poggio, A. Prša, L. Pulone, E. Racero, S. Ragaini, M. Rainer, C. M. Raiteri, N. Rambaux, P. Ramos, M. Ramos-Lerate, P. Re Fiorentin, S. Regibo, P. J. Richards, C. Rios Diaz, V. Ripepi, A. Riva, H. W. Rix, G. Rixon, N. Robichon, A. C. Robin, C. Robin, M. Roelens, H. R. O. Rogues, L. Rohrbasser, M. Romero-Gómez, N. Rowell, F. Royer, D. Ruz Mieres, K. A. Rybicki, G. Sadowski, A. Sáez Núñez, A. Sagristà Sellés, J. Sahlmann, E. Salguero, N. Samaras, V. Sanchez Gimenez, N. Sanna, R. Santoveña, M. Sarasso, M. Schultheis, E. Sciacca, M. Segol, J. C. Segovia, D. Ségransan, D. Semeux, S. Shahaf, H. I. Siddiqui, A. Siebert, L. Siltala, A. Silvelo, E. Slezak, I. Slezak, R. L. Smart, O. N. Snaith, E. Solano, F. Solitro, D. Souami, J. Souchay, A. Spagna, L. Spina, F. Spoto, I. A. Steele, H. Steidelmüller,

C. A. Stephenson, M. Süveges, J. Surdej, L. Szabados, E. Szegedi-Elek, F. Taris, M. B. Taylor, R. Teixeira, L. Tolomei, N. Tonello, F. Torra, J. Torra, G. Torralba Elipe, M. Trabucchi, A. T. Tsounis, C. Turon, A. Ulla, N. Unger, M. V. Vaillant, E. van Dillen, W. van Reeven, O. Vanel, A. Vecchiato, Y. Viala, D. Vicente, S. Voutsinas, M. Weiler, T. Wevers, Ł. Wyrzykowski, A. Yoldas, P. Yvard, H. Zhao, J. Zorec, S. Zucker, and T. Zwitter. Gaia Data Release 3. Summary of the content and survey properties. , 674: A1, June 2023. doi: 10.1051/0004-6361/202243940.

Roberto Gallino, Claudio Arlandini, Maurizio Busso, Maria Lugaro, Claudia Travaglio, Oscar Straniero, Alessandro Chieffi, and Marco Limongi. Evolution and Nucleosynthesis in Low-Mass Asymptotic Giant Branch Stars. II. Neutron Capture and the S-Process. , 497(1):388–403, April 1998. doi: 10.1086/305437.

Aruna Goswami and Wako Aoki. HD 209621: abundances of neutron-capture elements*. , 404(1):253–264, May 2010. doi: 10.1111/j.1365-2966.2010.16265.x.

Aruna Goswami, Wako Aoki, Timothy C. Beers, Norbert Christlieb, John E. Norris, Sean G. Ryan, and Stelios Tsangarides. A high-resolution spectral analysis of three carbon-enhanced metal-poor stars. , 372(1):343–356, October 2006. doi: 10.1111/j.1365-2966.2006.10877.x.

Aruna Goswami, Wako Aoki, and Drisya Karinkuzhi. Subaru/HDS study of CH stars: elemental abundances for stellar neutron-capture process studies. , 455(1):402–422, January 2016. doi: 10.1093/mnras/stv2011.

Partha Pratim Goswami, Rajeev Singh Rathour, and Aruna Goswami. Spectroscopic study of CEMP-(s & r/s) stars. Revisiting classification criteria and formation scenarios, highlighting i-process nucleosynthesis. , 649:A49, May 2021. doi: 10.1051/0004-6361/202038258.

R. F. Griffin and D. W. Beggs. Spectroscopic binaries near the North Galactic Pole paper 21 : eight short-period binaries. *Journal of Astrophysics and Astronomy*, 12:289–310, December 1991. doi: 10.1007/BF02702318.

P. Guillout, A. Klutsch, A. Frasca, R. Freire Ferrero, E. Marilli, G. Mignemi, K. Biazzo, J. Bouvier, R. Monier, C. Motch, and M. Sterzik. A spectroscopic survey of the youngest field stars in the solar neighbourhood. I. The optically bright sample. , 504(3):829–843, September 2009. doi: 10.1051/0004-6361/200811313.

Zhanwen Han, Peter P. Eggleton, Philipp Podsiadlowski, and Christopher A. Tout. The formation of barium and CH stars and related objects. , 277(4):1443–1462, December 1995. doi: 10.1093/mnras/277.4.1443.

Michael Hanke, Camilla J. Hansen, Andreas Koch, and Eva K. Grebel. ATHOS: On-the-fly stellar parameter determination of FGK stars based on flux ratios from optical spectra. , 619:A134, November 2018. doi: 10.1051/0004-6361/201833351.

C. J. Hansen, F. Primas, H. Hartman, K. L. Kratz, S. Wanajo, B. Leibundgut, K. Farouqi, O. Hallmann, N. Christlieb, and H. Nilsson. Silver and palladium help unveil the nature of a second r-process. , 545:A31, September 2012a. doi: 10.1051/0004-6361/201118643.

C. J. Hansen, A. C. Andersen, and N. Christlieb. Stellar abundances and presolar grains trace the nucleosynthetic origin of molybdenum and ruthenium. , 568:A47, August 2014. doi: 10.1051/0004-6361/201423535.

C. J. Hansen, B. Nordström, T. T. Hansen, C. R. Kennedy, V. M. Placco, T. C. Beers, J. Andersen, G. Cescutti, and C. Chiappini. Abundances of carbon-enhanced metal-poor stars as constraints on their formation. , 588:A37, April 2016a. doi: 10.1051/0004-6361/201526895.

C. J. Hansen, T. T. Hansen, A. Koch, T. C. Beers, B. Nordström, V. M. Placco, and J. Andersen. Abundances and kinematics of carbon-enhanced metal-poor stars in the Galactic halo. A new classification scheme based on Sr and Ba. , 623:A128, March 2019. doi: 10.1051/0004-6361/201834601.

Camilla J. Hansen, Maria Bergemann, Gabriele Cescutti, Patrick Francois, Almudena Arcones, Amanda I. Karakas, Karin Lind, and Cristina Chiappini. LTE or non-LTE, that is the question. *arXiv e-prints*, art. arXiv:1212.4147, December 2012b. doi: 10.48550/arXiv.1212.4147.

T. T. Hansen, J. Andersen, B. Nordström, T. C. Beers, V. M. Placco, J. Yoon, and L. A. Buchhave. The role of binaries in the enrichment of the early Galactic halo. III. Carbon-enhanced metal-poor stars - CEMP-s stars. , 588:A3, April 2016b. doi: 10.1051/0004-6361/201527409.

Tanja Heftrich, Mario Weigand, Kafa Al-Khasawleh, Benjamin Brückner, Sophia Dellmann, Ozan Can Dogan, Asmaa El Mard, Philipp Erbacher, Fabian Habermehl, Benedict Heybeck, Madeleine Margaux Gail, Kathrin Göbel, Timo Kisselbach, Deniz Kurtulgil, Markus Reich, René Reifarth, Silas Sheriff, and Meiko Volknandt. Activation

measurements of neutron capture cross sections at various temperatures. In *European Physical Journal Web of Conferences*, volume 260 of *European Physical Journal Web of Conferences*, page 11012. EDP, September 2022. doi: 10.1051/epjconf/202226011012.

U. Heiter, F. Kupka, C. van't Veer-Menneret, C. Barban, W. W. Weiss, M. J. Goupil, W. Schmidt, D. Katz, and R. Garrido. New grids of ATLAS9 atmospheres I: Influence of convection treatments on model structure and on observable quantities. , 392:619–636, September 2002. doi: 10.1051/0004-6361:20020788.

Falk Herwig. Evolution of Asymptotic Giant Branch Stars. , 43(1):435–479, September 2005. doi: 10.1146/annurev.astro.43.072103.150600.

Susanne Höfner and Hans Olofsson. Mass loss of stars on the asymptotic giant branch. Mechanisms, models and measurements. , 26(1):1, January 2018. doi: 10.1007/s00159-017-0106-5.

Julie K. Hollek, Anna Frebel, Vinicius M. Placco, Amanda I. Karakas, Matthew Shetrone, Christopher Sneden, and Norbert Christlieb. The Chemical Abundances of Stars in the Halo (CASH) Project. III. A New Classification Scheme for Carbon-enhanced Metal-poor Stars with s-process Element Enhancement. , 814(2):121, December 2015. doi: 10.1088/0004-637X/814/2/121.

F. Hoyle. The synthesis of the elements from hydrogen. , 106:343, January 1946. doi: 10.1093/mnras/106.5.343.

F. Hoyle. On Nuclear Reactions Occuring in Very Hot STARS.I. the Synthesis of Elements from Carbon to Nickel. , 1:121, September 1954. doi: 10.1086/190005.

Jarrod R. Hurley, Christopher A. Tout, and Onno R. Pols. Evolution of binary stars and the effect of tides on binary populations. , 329(4):897–928, February 2002. doi: 10.1046/j.1365-8711.2002.05038.x.

M. N. Ishigaki, W. Aoki, and M. Chiba. Chemical Abundances of the Milky Way Thick Disk and Stellar Halo. II. Sodium, Iron-peak, and Neutron-capture Elements. , 771(1):67, July 2013. doi: 10.1088/0004-637X/771/1/67.

O. Iwamoto and N. Iwamoto. Interpreted endf-6 section for ^{208}pb (mat 8237), jendl-5. IAEA EXFOR/ENDF Web Interface (SectID=14595388, req=7153), 2025. Material 82-Pb-208, JENDL-5, evaluated and interpreted as of 2015–2021.

R. G. Izzard, T. Dermine, and R. P. Church. White-dwarf kicks and implications for barium stars. , 523:A10, November 2010. doi: 10.1051/0004-6361/201015254.

E. Jofré, R. Petrucci, C. Saffe, L. Saker, E. Artur de la Villarmois, C. Chavero, M. Gómez, and P. J. D. Mauas. Stellar parameters and chemical abundances of 223 evolved stars with and without planets. , 574:A50, February 2015. doi: 10.1051/0004-6361/201424474.

Jennifer A. Johnson. Abundances of 30 Elements in 23 Metal-Poor Stars. , 139(1):219–247, March 2002. doi: 10.1086/338117.

Henrik Jönsson, Jon A. Holtzman, Carlos Allende Prieto, Katia Cunha, D. A. García-Hernández, Sten Hasselquist, Thomas Masseron, Yeisson Osorio, Matthew Shetrone, Verne Smith, Guy S. Stringfellow, Dmitry Bizyaev, Bengt Edvardsson, Steven R. Majewski, Szabolcs Mészáros, Diogo Souto, Olga Zamora, Rachael L. Beaton, Jo Bovy, John Donor, Marc H. Pinsonneault, Vijith Jacob Poovelil, and Jennifer Sobeck. APOGEE Data and Spectral Analysis from SDSS Data Release 16: Seven Years of Observations Including First Results from APOGEE-South. , 160(3):120, September 2020. doi: 10.3847/1538-3881/aba592.

A. Jorissen and M. Mayor. Radial velocity monitoring of a sample of barium and S stars using CORAVEL : towards an evolutionary link between barium and S stars ? , 198: 187–199, June 1988.

A. Jorissen, S. Van Eck, M. Mayor, and S. Udry. Insights into the formation of barium and Tc-poor S stars from an extended sample of orbital elements. , 332:877–903, April 1998. doi: 10.48550/arXiv.astro-ph/9801272.

A. Jorissen, S. Van Eck, H. Van Winckel, T. Merle, H. M. J. Boffin, J. Andersen, B. Nordström, S. Udry, T. Masseron, L. Lenaerts, and C. Waelkens. Binary properties of CH and carbon-enhanced metal-poor stars. , 586:A158, February 2016. doi: 10.1051/0004-6361/201526992.

A. Jorissen, H. M. J. Boffin, D. Karinkuzhi, S. Van Eck, A. Escorza, S. Shetye, and H. Van Winckel. Barium and related stars, and their white-dwarf companions. I. Giant stars. , 626:A127, June 2019. doi: 10.1051/0004-6361/201834630.

Finia P. Jost, Marta Molero, Gerard Navó, Almudena Arcones, Martin Obergaulinger, and Francesca Matteucci. Neutrino-driven Core-collapse Supernova Yields in Galactic

Chemical Evolution. *arXiv e-prints*, art. arXiv:2407.14319, July 2024. doi: 10.48550/arXiv.2407.14319.

Colby Jurgenson, Debra Fischer, Tyler McCracken, David Sawyer, Matt Giguere, Andrew Szymkowiak, Fernando Santoro, and Gary Muller. Design and Construction of VUES: The Vilnius University Echelle Spectrograph. *Journal of Astronomical Instrumentation*, 5(2):1650003-239, June 2016. doi: 10.1142/S2251171716500033.

Colby A. Jurgenson, Debra A. Fischer, Tyler M. McCracken, Rebecca A. Stoll, Andrew E. Szymkowiak, Matt J. Giguere, Fernando G. Santoro, and Gary Muller. Design of a radial velocity spectrograph for the Moletai Astronomical Observatory. In Suzanne K. Ramsay, Ian S. McLean, and Hideki Takami, editors, *Ground-based and Airborne Instrumentation for Astronomy V*, volume 9147 of *Society of Photo-Optical Instrumentation Engineers (SPIE) Conference Series*, page 91477F, July 2014. doi: 10.1117/12.2056491.

P. Kabáth, M. Skarka, S. Sabotta, E. Guenther, D. Jones, T. Klocová, J. Šubjak, Jiří Žák, M. Špoková, M. Blažek, J. Dvořáková, D. Dupkala, J. Fuchs, A. Hatzes, E. Kortusová, R. Novotný, E. Plávalová, L. Řezba, J. Sloup, P. Škoda, and M. Šlechta. Ondřejov Echelle Spectrograph, Ground Based Support Facility for Exoplanet Missions. , 132 (1009):035002, March 2020. doi: 10.1088/1538-3873/ab6752.

F. Käppeler, R. Gallino, S. Bisterzo, and Wako Aoki. The s process: Nuclear physics, stellar models, and observations. *Reviews of Modern Physics*, 83(1):157–194, January 2011. doi: 10.1103/RevModPhys.83.157.

Amanda I. Karakas and John C. Lattanzio. The Dawes Review 2: Nucleosynthesis and Stellar Yields of Low- and Intermediate-Mass Single Stars. , 31:e030, July 2014. doi: 10.1017/pasa.2014.21.

Amanda I. Karakas, Christopher A. Tout, and John C. Lattanzio. The eccentricities of the barium stars. , 316(3):689–698, August 2000. doi: 10.1046/j.1365-8711.2000.03561.x.

D. Karinkuzhi, S. Van Eck, A. Jorissen, S. Goriely, L. Siess, T. Merle, A. Escorza, M. Van der Swaelmen, H. M. J. Boffin, T. Masseron, S. Shetye, and B. Plez. When binaries keep track of recent nucleosynthesis. The Zr-Nb pair in extrinsic stars as an s-process diagnostic. , 618:A32, October 2018. doi: 10.1051/0004-6361/201833084.

D. Karinkuzhi, S. Van Eck, S. Goriely, L. Siess, A. Jorissen, T. Merle, A. Escorza, and T. Masseron. Low-mass low-metallicity AGB stars as an efficient i-process site explaining CEMP-rs stars. , 645:A61, January 2021a. doi: 10.1051/0004-6361/202038891.

D. Karinkuzhi, S. Van Eck, A. Jorissen, A. Escorza, S. Shetye, T. Merle, L. Siess, S. Goriely, and H. Van Winckel. Sr and Ba abundances: Comparing machine-learning with star-by-star analyses. High-resolution re-analysis of suspected LAMOST barium stars. , 654:A140, October 2021b. doi: 10.1051/0004-6361/202141629.

Drisya Karinkuzhi and Aruna Goswami. Chemical analysis of CH stars - I. Atmospheric parameters and elemental abundances. , 440(2):1095–1113, May 2014. doi: 10.1093/mnras/stu148.

Drisya Karinkuzhi and Aruna Goswami. Chemical analysis of CH stars - II. Atmospheric parameters and elemental abundances. , 446(3):2348–2362, January 2015. doi: 10.1093/mnras/stu2079.

Noriyuki Katoh, Yoichi Itoh, Eri Toyota, and Bun'ei Sato. Determination of Orbital Elements of Spectroscopic Binaries Using High-dispersion Spectroscopy. , 145(2):41, February 2013. doi: 10.1088/0004-6256/145/2/41.

A. Kaufer, O. Stahl, S. Tubbesing, P. Nørregaard, G. Avila, P. Francois, L. Pasquini, and A. Pizzella. Commissioning FEROS, the new high-resolution spectrograph at La-Silla. *The Messenger*, 95:8–12, March 1999.

Andreas Kaufer and Luca Pasquini. FEROS: the new fiber-linked echelle spectrograph for the ESO 1.52-m telescope. In Sandro D'Odorico, editor, *Optical Astronomical Instrumentation*, volume 3355 of *Society of Photo-Optical Instrumentation Engineers (SPIE) Conference Series*, pages 844–854, July 1998. doi: 10.1117/12.316798.

Philip C. Keenan. The Spectra of CH Stars. , 96:101, July 1942. doi: 10.1086/144435.

Rudolf Kippenhahn, Alfred Weigert, and Achim Weiss. *Stellar Structure and Evolution*. 2013. doi: 10.1007/978-3-642-30304-3.

Glenn F Knoll. *Radiation detection and measurement*. John Wiley & Sons, 2010.

Chiaki Kobayashi, Amanda I. Karakas, and Maria Lugaro. The Origin of Elements from Carbon to Uranium. , 900(2):179, September 2020. doi: 10.3847/1538-4357/abae65.

Andreas Koch, Andrew McWilliam, George W. Preston, and Ian B. Thompson. Metal-poor stars towards the Galactic bulge: A population potpourri. , 587:A124, March 2016. doi: 10.1051/0004-6361/201527413.

P. Koubský, P. Mayer, J. Čáp, F. Ždárský, J. Zeman, L. Pína, and Z. Melich. Ondřejov Echelle Spectrograph - OES. *Publications of the Astronomical Institute of the Czechoslovak Academy of Sciences*, 92:37–43, January 2004.

H. Krieger. *Strahlenphysik, Dosimetrie und Strahlenschutz. Band 1 Grundlagen.* B.G. Teubner Stuttgart, 1989.

Pavel Kroupa, Carsten Weidner, Jan Pflamm-Altenburg, Ingo Thies, Jörg Dabringhausen, Michael Marks, and Thomas Maschberger. The Stellar and Sub-Stellar Initial Mass Function of Simple and Composite Populations. In Terry D. Oswalt and Gerard Gilmore, editors, *Planets, Stars and Stellar Systems. Volume 5: Galactic Structure and Stellar Populations*, volume 5, page 115. 2013. doi: 10.1007/978-94-007-5612-0_4.

P. Krynski, L. Siess, A. Jorissen, and P. J. Davis. Formation of Ba stars: Impact of wind Roche lobe overflow and circumbinary disk in shaping the orbital parameters. , 697: A179, May 2025. doi: 10.1051/0004-6361/202453503.

Guilherme Limberg, Silvia Rossi, Timothy C. Beers, Hélio D. Perottoni, Angeles Pérez-Villegas, Rafael M. Santucci, Yuri Abuchaim, Vinicius M. Placco, Young Sun Lee, Norbert Christlieb, John E. Norris, Michael S. Bessell, Sean G. Ryan, Ronald Wilhelm, Jaehyon Rhee, and Anna Frebel. Dynamically Tagged Groups of Very Metal-poor Halo Stars from the HK and Hamburg/ESO Surveys. , 907(1):10, January 2021. doi: 10.3847/1538-4357/abcb87.

Zheng-Wei Liu, Richard J. Stancliffe, Carlo Abate, and Elvijs Matrozis. Three-dimensional Hydrodynamical Simulations of Mass Transfer in Binary Systems by a Free Wind. , 846 (2):117, September 2017. doi: 10.3847/1538-4357/aa8622.

Katharina Lodders. Solar System Abundances and Condensation Temperatures of the Elements. , 591(2):1220–1247, July 2003. doi: 10.1086/375492.

L. Lombardo, C. J. Hansen, F. Rizzuti, G. Cescutti, L. I. Mashonkina, P. François, P. Bonifacio, E. Caffau, A. Alencastro Puls, R. Fernandes de Melo, A. J. Gallagher, Á. Skúladóttir, A. J. Koch-Hansen, and L. Sbordone. Chemical Evolution of R-process Elements in Stars (CERES): III. Chemical abundances of neutron capture elements from Ba to Eu. , 693:A293, January 2025. doi: 10.1051/0004-6361/202452283.

P. K. Lu, D. W. Dawson, A. R. Upgren, and E. W. Weis. A catalog of spectral classification and photometry of Barium stars. , 52:169–181, June 1983. doi: 10.1086/190863.

Phillip K. Lu. Taxonomy of Barium Stars. , 101:2229, June 1991. doi: 10.1086/115845.

Sara Lucatello, Stelios Tsangarides, Timothy C. Beers, Eugenio Carretta, Raffaele G. Gratton, and Sean G. Ryan. The Binary Frequency Among Carbon-enhanced, s-Process-rich, Metal-poor Stars. , 625(2):825–832, June 2005. doi: 10.1086/428104.

R. Earle Luck. Abundances in the Local Region. III. Southern F, G, and K Dwarfs. , 155 (3):111, March 2018. doi: 10.3847/1538-3881/aaa9b5.

Maria Lugaro, Borbála Cseh, Blanka Világos, Amanda I. Karakas, Paolo Ventura, Flavia Dell'Agli, Reto Trappitsch, Melanie Hampel, Valentina D'Orazi, Claudio B. Pereira, Giuseppe Tagliente, Gyula M. Szabó, Marco Pignatari, Umberto Battino, Ashley Tattersall, Mattias Ek, Maria Schönbächler, Josef Hron, and Larry R. Nittler. Origin of Large Meteoritic SiC Stardust Grains in Metal-rich AGB Stars. , 898(2):96, August 2020. doi: 10.3847/1538-4357/ab9e74.

Maria Lugaro, Marco Pignatari, René Reifarth, and Michael Wiescher. The s Process and Beyond. *Annual Review of Nuclear and Particle Science*, 73:315–340, September 2023. doi: 10.1146/annurev-nucl-102422-080857.

R. L. Macklin and J. H. Gibbons. Capture-cross-section studies for 30—220-kev neutrons using a new technique. *Phys. Rev.*, 159:1007–1012, Jul 1967. doi: 10.1103/PhysRev.159.1007. URL `https://link.aps.org/doi/10.1103/PhysRev.159.1007`.

R. L. Macklin, J. Halperin, and R. R. Winters. Neutron Capture by 208Pb at Stellar Temperatures. , 217:222–226, October 1977. doi: 10.1086/155572.

Z. Magic, A. Weiss, and M. Asplund. The Stagger-grid: A grid of 3D stellar atmosphere models. III. The relation to mixing length convection theory. , 573:A89, January 2015. doi: 10.1051/0004-6361/201423760.

Steven R. Majewski, Ricardo P. Schiavon, Peter M. Frinchaboy, Carlos Allende Prieto, Robert Barkhouser, Dmitry Bizyaev, Basil Blank, Sophia Brunner, Adam Burton, Ricardo Carrera, S. Drew Chojnowski, Kátia Cunha, Courtney Epstein, Greg Fitzgerald, Ana E. García Pérez, Fred R. Hearty, Chuck Henderson, Jon A. Holtzman, Jennifer A. Johnson, Charles R. Lam, James E. Lawler, Paul Maseman, Szabolcs Mészáros, Matthew Nelson, Duy Coung Nguyen, David L. Nidever, Marc Pinsonneault, Matthew Shetrone, Stephen Smee, Verne V. Smith, Todd Stolberg, Michael F. Skrutskie, Eric Walker, John C. Wilson, Gail Zasowski, Friedrich Anders, Sarbani Basu,

Stephane Beland, Michael R. Blanton, Jo Bovy, Joel R. Brownstein, Joleen Carlberg, William Chaplin, Cristina Chiappini, Daniel J. Eisenstein, Yvonne Elsworth, Diane Feuillet, Scott W. Fleming, Jessica Galbraith-Frew, Rafael A. García, D. Aníbal García-Hernández, Bruce A. Gillespie, Léo Girardi, James E. Gunn, Sten Hasselquist, Michael R. Hayden, Saskia Hekker, Inese Ivans, Karen Kinemuchi, Mark Klaene, Suvrath Mahadevan, Savita Mathur, Benoît Mosser, Demitri Muna, Jeffrey A. Munn, Robert C. Nichol, Robert W. O'Connell, John K. Parejko, A. C. Robin, Helio Rocha-Pinto, Matthias Schultheis, Aldo M. Serenelli, Neville Shane, Victor Silva Aguirre, Jennifer S. Sobeck, Benjamin Thompson, Nicholas W. Troup, David H. Weinberg, and Olga Zamora. The Apache Point Observatory Galactic Evolution Experiment (APOGEE). , 154(3):94, September 2017. doi: 10.3847/1538-3881/aa784d.

Geoffrey W. Marcy and R. P. Butler. Precision Radial Velocities with an Iodine Absorption cell. , 104:270, April 1992. doi: 10.1086/132989.

Paola Marigo, Léo Girardi, Alessandro Bressan, Philip Rosenfield, Bernhard Aringer, Yang Chen, Marco Dussin, Ambra Nanni, Giada Pastorelli, Thaíse S. Rodrigues, Michele Trabucchi, Sara Bladh, Julianne Dalcanton, Martin A. T. Groenewegen, Josefina Montalbán, and Peter R. Wood. A New Generation of PARSEC-COLIBRI Stellar Isochrones Including the TP-AGB Phase. , 835(1):77, January 2017. doi: 10.3847/1538-4357/835/1/77.

L. Mashonkina, P. Jablonka, Yu. Pakhomov, T. Sitnova, and P. North. The formation of the Milky Way halo and its dwarf satellites; a NLTE-1D abundance analysis. I. Homogeneous set of atmospheric parameters. , 604:A129, August 2017. doi: 10.1051/0004-6361/201730779.

T. Masseron, J. A. Johnson, B. Plez, S. van Eck, F. Primas, S. Goriely, and A. Jorissen. A holistic approach to carbon-enhanced metal-poor stars. , 509:A93, January 2010. doi: 10.1051/0004-6361/200911744.

E. Matrozis and R. J. Stancliffe. Radiative levitation in carbon-enhanced metal-poor stars with s-process enrichment. , 592:A29, July 2016. doi: 10.1051/0004-6361/201628540.

E. Matrozis, C. Abate, and R. J. Stancliffe. How much mass and angular momentum can the progenitors of carbon-enriched stars accrete? , 606:A137, October 2017. doi: 10.1051/0004-6361/201730746.

Michel Mayor and Didier Queloz. A Jupiter-mass companion to a solar-type star. , 378 (6555):355–359, November 1995. doi: 10.1038/378355a0.

R. D. McClure. The binary nature of the CH stars. , 280:L31–L34, May 1984. doi: 10.1086/184263.

R. D. McClure, J. M. Fletcher, and J. M. Nemec. The binary nature of the barium stars. , 238:L35–L38, May 1980. doi: 10.1086/183252.

Robert D. McClure and A. W. Woodsworth. The Binary Nature of the Barium and CH Stars. III. Orbital Parameters. , 352:709, April 1990. doi: 10.1086/168573.

Andrew McWilliam, George W. Preston, Christopher Sneden, and Leonard Searle. Spectroscopic Analysis of 33 of the Most Metal Poor Stars. II. , 109:2757, June 1995. doi: 10.1086/117486.

J. Meléndez and B. Barbuy. Both accurate and precise gf-values for Fe II lines. , 497(2): 611–617, April 2009. doi: 10.1051/0004-6361/200811508.

Paul W. Merrill. Spectroscopic Observations of Stars of Class S. , 116:21, July 1952. doi: 10.1086/145589.

S. Mohamed and Ph. Podsiadlowski. Wind Roche-Lobe Overflow: a New Mass-Transfer Mode for Wide Binaries. In R. Napiwotzki and M. R. Burleigh, editors, *15th European Workshop on White Dwarfs*, volume 372 of *Astronomical Society of the Pacific Conference Series*, page 397, September 2007.

S. Mohamed and Ph. Podsiadlowski. Mass Transfer in Mira-type Binaries. *Baltic Astronomy*, 21:88–96, January 2012. doi: 10.1515/astro-2017-0362.

P. Neyskens, S. van Eck, A. Jorissen, S. Goriely, L. Siess, and B. Plez. The temperature and chronology of heavy-element synthesis in low-mass stars. , 517(7533):174–176, January 2015. doi: 10.1038/nature14050.

P. E. Nissen, E. Hoeg, and W. J. Schuster. Surface Gravities of Metal-Poor Stars Derived from HIPPARCOS Parallaxes. In R. M. Bonnet, E. Høg, P. L. Bernacca, L. Emiliani, A. Blaauw, C. Turon, J. Kovalevsky, L. Lindegren, H. Hassan, M. Bouffard, B. Strim, D. Heger, M. A. C. Perryman, and L. Woltjer, editors, *Hipparcos - Venice 1997*, volume 402 of *ESA Special Publication*, pages 225–230, August 1997.

Ken'ichi Nomoto, Chiaki Kobayashi, and Nozomu Tominaga. Nucleosynthesis in Stars and the Chemical Enrichment of Galaxies. , 51(1):457–509, August 2013. doi: 10.1146/annurev-astro-082812-140956.

John E. Norris, Sean G. Ryan, and Timothy C. Beers. Extremely Metal-poor Stars. IV. The Carbon-rich Objects. , 488(1):350–363, October 1997. doi: 10.1086/304695.

J. A. Orosz and P. H. Hauschildt. The use of the NextGen model atmospheres for cool giants in a light curve synthesis code. , 364:265–281, December 2000.

Jerome A. Orosz, William F. Welsh, Nader Haghighipour, Billy Quarles, Donald R. Short, Sean M. Mills, Suman Satyal, Guillermo Torres, Eric Agol, Daniel C. Fabrycky, Daniel Jontof-Hutter, Gur Windmiller, Tobias W. A. Müller, Tobias C. Hinse, William D. Cochran, Michael Endl, Eric B. Ford, Tsevi Mazeh, and Jack J. Lissauer. Discovery of a Third Transiting Planet in the Kepler-47 Circumbinary System. , 157(5):174, May 2019. doi: 10.3847/1538-3881/ab0ca0.

P.B. Pal, V.P. Varshney, and D.K. Gupta. Approximate expressions for continuous slowing down approximation ranges of high energy electrons and positrons. *Nuclear Instruments and Methods in Physics Research Section B: Beam Interactions with Materials and Atoms*, 21(1):14–19, 1987. ISSN 0168-583X. doi: https://doi.org/10.1016/0168-583X(87)90133-9. URL `https://www.sciencedirect.com/science/article/pii/0168583X87901339`.

Bill Paxton, Lars Bildsten, Aaron Dotter, Falk Herwig, Pierre Lesaffre, and Frank Timmes. Modules for Experiments in Stellar Astrophysics (MESA). , 192(1):3, January 2011. doi: 10.1088/0067-0049/192/1/3.

C. B. Pereira and S. Junqueira. Spectroscopic analysis of two CH subgiant stars: HD 50264 and HD 87080. , 402:1061–1071, May 2003. doi: 10.1051/0004-6361:20030209.

C. B. Pereira, J. V. Sales Silva, C. Chavero, F. Roig, and E. Jilinski. Chemical abundances and kinematics of a sample of metal-rich barium stars. , 533:A51, September 2011. doi: 10.1051/0004-6361/201117070.

C. B. Pereira, E. Jilinski, N. A. Drake, D. B. de Castro, V. G. Ortega, C. Chavero, and F. Roig. CD-62°1346: an extreme halo or hypervelocity CH star? , 543:A58, July 2012. doi: 10.1051/0004-6361/201219122.

M. Pignatari, R. Hirschi, M. Wiescher, R. Gallino, M. Bennett, M. Beard, C. Fryer, F. Herwig, G. Rockefeller, and F. X. Timmes. The ^{12}C + ^{12}C Reaction and the Impact on Nucleosynthesis in Massive Stars. , 762(1):31, January 2013. doi: 10.1088/0004-637X/762/1/31.

Vinicius M. Placco, Anna Frebel, Timothy C. Beers, Norbert Christlieb, Young Sun Lee, Catherine R. Kennedy, Silvia Rossi, and Rafael M. Santucci. Metal-poor Stars Observed with the Magellan Telescope. II. Discovery of Four Stars with [Fe/H] ¡= -3.5. , 781(1): 40, January 2014a. doi: 10.1088/0004-637X/781/1/40.

Vinicius M. Placco, Anna Frebel, Timothy C. Beers, and Richard J. Stancliffe. Carbon-enhanced Metal-poor Star Frequencies in the Galaxy: Corrections for the Effect of Evolutionary Status on Carbon Abundances. , 797(1):21, December 2014b. doi: 10.1088/0004-637X/797/1/21.

I. Platais, D. Pourbaix, A. Jorissen, V. V. Makarov, L. N. Berdnikov, N. N. Samus, T. Lloyd Evans, T. Lebzelter, and J. Sperauskas. Hipparcos red stars in the H_pV_{T2} and VI_C systems. , 397:997–1010, January 2003. doi: 10.1051/0004-6361:20021589.

A. Plompen, G. Zerovnik, et al. Interpreted endf section for 82-pb-208 (mat 8237), jeff-3.3. EXFOR/ENDF interface, IAEA Nuclear Data Section, 2025. Accessed via IAEA EXFOR web interface, SectID 9134974, req 7153.

Onno R. Pols, Christopher A. Tout, Peter P. Eggleton, and Zhanwen Han. Approximate input physics for stellar modelling. , 274(3):964–974, June 1995. doi: 10.1093/mnras/274.3.964.

D. Pourbaix, A. A. Tokovinin, A. H. Batten, F. C. Fekel, W. I. Hartkopf, H. Levato, N. I. Morrell, G. Torres, and S. Udry. $S_B{}^9$: $The ninth catalogue of spectroscopic binary orbits.$, 424 : $727 - -732, September 2004. doi$: .

L. Prandtl. 7. Bericht über Untersuchungen zur ausgebildeten Turbulenz. *Zeitschrift Angewandte Mathematik und Mechanik*, 5(2):136–139, January 1925. 10.1002/zamm.19250050212.

N. Prantzos, C. Abia, M. Limongi, A. Chieffi, and S. Cristallo. Chemical evolution with rotating massive star yields - I. The solar neighbourhood and the s-process elements. , 476(3):3432–3459, May 2018. 10.1093/mnras/sty316.

B. Pritychenko, S.F. Mughaghab, and A.A. Sonzogni. Calculations of maxwellian-averaged cross sections and astrophysical reaction rates using the endf/b-vii.0, jeff-3.1, jendl-3.3, and

endf/b-vi.8 evaluated nuclear reaction data libraries. *Atomic Data and Nuclear Data Tables*, 96(6):645–748, November 2010. ISSN 0092-640X. 10.1016/j.adt.2010.05.002. URL http://dx.doi.org/10.1016/j.adt.2010.05.002.

Meenakshi Purandardas, Aruna Goswami, Partha Pratim Goswami, J. Shejeelammal, and Thomas Masseron. Chemical analysis of CH stars - III. Atmospheric parameters and elemental abundances. , 486(3):3266–3289, July 2019. 10.1093/mnras/stz759.

W. Ratynski and F. Käppeler. Neutron capture cross section of ^{197}Au: A standard for stellar nucleosynthesis. *Phys. Rev. C*, 37:595–604, Feb 1988. 10.1103/PhysRevC.37.595. URL https://link.aps.org/doi/10.1103/PhysRevC.37.595.

U. Ratzel, C. Arlandini, F. Käppeler, A. Couture, M. Wiescher, R. Reifarth, R. Gallino, A. Mengoni, and C. Travaglio. Nucleosynthesis at the termination point of the s process. , 70(6):065803, December 2004. 10.1103/PhysRevC.70.065803.

R. Reifarth, M. Heil, F. Käppeler, and R. Plag. Pino—a tool for simulating neutron spectra resulting from the 7li(p,n) reaction. *Nuclear Instruments and Methods in Physics Research Section A: Accelerators, Spectrometers, Detectors and Associated Equipment*, 608 (1):139–143, 2009. ISSN 0168-9002. https://doi.org/10.1016/j.nima.2009.06.046. URL https://www.sciencedirect.com/science/article/pii/S0168900209013011.

R. Reifarth, C. Lederer, and F. Käppeler. Neutron reactions in astrophysics. *Journal of Physics G: Nuclear and Particle Physics*, 41(5):053101, 2014. URL https://exp-astro.de/docs/reifarth_14_neutron_review.pdf.

A. Reiners and G. Basri. On the magnetic topology of partially and fully convective stars. , 496(3):787–790, March 2009. 10.1051/0004-6361:200811450.

Ian U. Roederer, John J. Cowan, Amanda I. Karakas, Karl-Ludwig Kratz, Maria Lugaro, Jennifer Simmerer, Khalil Farouqi, and Christopher Sneden. The Ubiquity of the Rapid Neutron-capture Process. , 724(2):975–993, December 2010. 10.1088/0004-637X/724/2/975.

D. Romano, A. I. Karakas, M. Tosi, and F. Matteucci. Quantifying the uncertainties of chemical evolution studies. II. Stellar yields. , 522:A32, November 2010. 10.1051/0004-6361/201014483.

M. P. Roriz, M. Lugaro, C. B. Pereira, N. A. Drake, S. Junqueira, and C. Sneden. Rubidium in Barium stars. , 501(4):5834–5844, March 2021a. 10.1093/mnras/staa3888.

M. P. Roriz, M. Lugaro, C. B. Pereira, C. Sneden, S. Junqueira, A. I. Karakas, and N. A. Drake. Heavy elements in barium stars. , 507(2):1956–1971, October 2021b.

10.1093/mnras/stab2014.

M. P. Roriz, N. Holanda, L. V. da Conceição, S. Junqueira, N. A. Drake, A. Sonally, and C. B. Pereira. High-resolution Spectroscopic Analysis of Four Unevolved Barium Stars. , 167(4):184, April 2024. 10.3847/1538-3881/ad29f2.

Sean G. Ryan, John E. Norris, and Timothy C. Beers. Extremely Metal-poor Stars. II. Elemental Abundances and the Early Chemical Enrichment of the Galaxy. , 471:254, November 1996. 10.1086/177967.

Edward F. Schlafly and Douglas P. Finkbeiner. Measuring Reddening with Sloan Digital Sky Survey Stellar Spectra and Recalibrating SFD. , 737(2):103, August 2011. 10.1088/0004-637X/737/2/103.

K. Schreckenbach. *High Precision (n,e) Spectroscopy*, pages 125–143. Springer US, Boston, MA, 1979. ISBN 978-1-4613-2940-4. 10.1007/978-1-4613-2940-4$_7$.URL.

Klaus-Peter Schroder, Onno R. Pols, and Peter P. Eggleton. A critical test of stellar evolution and convective core 'overshooting' by means of zeta Aurigae systems. , 285(4): 696–710, March 1997. 10.1093/mnras/285.4.696.

M. Schwarzschild. Stellar Structure and Evolution. *Smithsonian Contributions to Astrophysics*, 1:177, January 1956.

S. Shetye, S. Van Eck, A. Jorissen, H. Van Winckel, L. Siess, S. Goriely, A. Escorza, D. Karinkuzhi, and B. Plez. S stars and s-process in the Gaia era. I. Stellar parameters and chemical abundances in a sub-sample of S stars with new MARCS model atmospheres. , 620:A148, December 2018. 10.1051/0004-6361/201833298.

S. Shetye, S. Goriely, L. Siess, S. Van Eck, A. Jorissen, and H. Van Winckel. Observational evidence of third dredge-up occurrence in S-type stars with initial masses around 1 $M_\odot$. , 625:L1, May 2019. 10.1051/0004-6361/201935296.

S. Shetye, S. Van Eck, S. Goriely, L. Siess, A. Jorissen, A. Escorza, and H. Van Winckel. Discovery of technetium- and niobium-rich S stars: The case for bitrinsic stars. , 635:L6, March 2020. 10.1051/0004-6361/202037481.

Shreeya Shetye, Sophie Van Eck, Alain Jorissen, Stephane Goriely, Lionel Siess, Hans Van Winckel, Bertrand Plez, Michel Godefroid, and George Wallerstein. S stars and s-process in the Gaia era. II. Constraining the luminosity of the third dredge-up with Tc-rich S stars. , 650:A118, June 2021. 10.1051/0004-6361/202040207.

Jennifer Simmerer, Christopher Sneden, John J. Cowan, Jason Collier, Vincent M. Woolf, and James E. Lawler. The Rise of the s-Process in the Galaxy. , 617(2):1091–1114, December 2004. 10.1086/424504.

M. F. Skrutskie, R. M. Cutri, R. Stiening, M. D. Weinberg, S. Schneider, J. M. Carpenter, C. Beichman, R. Capps, T. Chester, J. Elias, J. Huchra, J. Liebert, C. Lonsdale, D. G. Monet, S. Price, P. Seitzer, T. Jarrett, J. D. Kirkpatrick, J. E. Gizis, E. Howard, T. Evans, J. Fowler, L. Fullmer, R. Hurt, R. Light, E. L. Kopan, K. A. Marsh, H. L. McCallon, R. Tam, S. Van Dyk, and S. Wheelock. The Two Micron All Sky Survey (2MASS). , 131 (2):1163–1183, February 2006. 10.1086/498708.

Chris Sneden. MOOG: a Half Century of Joys and Concerns. In *American Astronomical Society Meeting Abstracts*, volume 55 of *American Astronomical Society Meeting Abstracts*, page 227.04, September 2023.

Chris Sneden, Jacob Bean, Inese Ivans, Sara Lucatello, and Jennifer Sobeck. MOOG: LTE line analysis and spectrum synthesis. Astrophysics Source Code Library, record ascl:1202.009, February 2012.

M. G. Soto and J. S. Jenkins. Spectroscopic Parameters and atmosphEric ChemIstriEs of Stars (SPECIES). I. Code description and dwarf stars catalogue. , 615:A76, July 2018. 10.1051/0004-6361/201731533.

C. Soubiran, N. Brouillet, and L. Casamiquela. Assessment of [Fe/H] determinations for FGK stars in spectroscopic surveys. , 663:A4, July 2022. 10.1051/0004-6361/202142409.

S. G. Sousa, N. C. Santos, V. Adibekyan, E. Delgado-Mena, and G. Israelian. ARES v2: new features and improved performance. , 577:A67, May 2015. 10.1051/0004-6361/201425463.

J. Sperauskas, L. Začs, W. J. Schuster, and V. Deveikis. The Binary Nature of CH-Like Stars. , 826(1):85, July 2016. 10.3847/0004-637X/826/1/85.

R. J. Stancliffe. Thermohaline Mixing and Isotopic Ratios in AGB Stars. In F. Kerschbaum, R. F. Wing, and J. Hron, editors, *Why Galaxies Care about AGB Stars III: A Closer Look in Space and Time*, volume 497 of *Astronomical Society of the Pacific Conference Series*, page 253, August 2015.

R. J. Stancliffe, E. Glebbeek, R. G. Izzard, and O. R. Pols. Carbon-enhanced metal-poor stars and thermohaline mixing. , 464(3):L57–L60, March 2007. 10.1051/0004-6361:20066891.

R. J. Stancliffe, L. Fossati, J. C. Passy, and F. R. N. Schneider. Confronting uncertainties in stellar physics: calibrating convective overshooting with eclipsing binaries. , 575:A117, March 2015. 10.1051/0004-6361/201425126.

Richard J. Stancliffe. The formation of barium giants via mass accretion in binary systems. , 505(4):5554–5566, August 2021. 10.1093/mnras/stab1734.

Richard J. Stancliffe and John J. Eldridge. Modelling the binary progenitor of Supernova 1993J. , 396(3):1699–1708, July 2009. 10.1111/j.1365-2966.2009.14849.x.

Richard J. Stancliffe and Evert Glebbeek. Thermohaline mixing and gravitational settling in carbon-enhanced metal-poor stars. , 389(4):1828–1838, October 2008. 10.1111/j.1365-2966.2008.13700.x.

Richard James Stancliffe. *The Evolution and Nucleosynthesis of Thermally Pulsing Asymptotic Giant Branch Stars*. PhD thesis, University of Cambridge, UK, October 2005.

Else Starkenburg, Matthew D. Shetrone, Alan W. McConnachie, and Kim A. Venn. Binarity in carbon-enhanced metal-poor stars. , 441(2):1217–1229, June 2014. 10.1093/mnras/stu623.

M. Steinmetz, T. Zwitter, A. Siebert, F. G. Watson, K. C. Freeman, U. Munari, R. Campbell, M. Williams, G. M. Seabroke, R. F. G. Wyse, Q. A. Parker, O. Bienaymé, S. Roeser, B. K. Gibson, G. Gilmore, E. K. Grebel, A. Helmi, J. F. Navarro, D. Burton, C. J. P. Cass, J. A. Dawe, K. Fiegert, M. Hartley, K. S. Russell, W. Saunders, H. Enke, J. Bailin, J. Binney, J. Bland-Hawthorn, C. Boeche, W. Dehnen, D. J. Eisenstein, N. W. Evans, M. Fiorucci, J. P. Fulbright, O. Gerhard, U. Jauregi, A. Kelz, L. Mijović, I. Minchev, G. Parmentier, J. Peñarrubia, A. C. Quillen, M. A. Read, G. Ruchti, R. D. Scholz, A. Siviero, M. C. Smith, R. Sordo, L. Veltz, S. Vidrih, R. von Berlepsch, B. J. Boyle, and E. Schilbach. The Radial Velocity Experiment (RAVE): First Data Release. , 132 (4):1645–1668, October 2006. 10.1086/506564.

Matthias Steinmetz, Guillaume Guiglion, Paul J. McMillan, Gal Matijevič, Harry Enke, Georges Kordopatis, Tomaž Zwitter, Marica Valentini, Cristina Chiappini, Luca Casagrande, Jennifer Wojno, Borja Anguiano, Olivier Bienaymé, Albert Bijaoui, James Binney, Donna Burton, Paul Cass, Patrick de Laverny, Kristin Fiegert, Kenneth Freeman, Jon P. Fulbright, Brad K. Gibson, Gerard Gilmore, Eva K. Grebel, Amina Helmi, Andrea Kunder, Ulisse Munari, Julio F. Navarro, Quentin Parker, Gregory R. Ruchti, Alejandra Recio-Blanco, Warren Reid, George M. Seabroke, Alessandro Siviero, Arnaud Siebert, Milorad Stupar, Fred Watson, Mary E. K. Williams, Rosemary F. G. Wyse, Friedrich Anders,

Teresa Antoja, Danijela Birko, Joss Bland-Hawthorn, Diego Bossini, Rafael A. García, Ismael Carrillo, William J. Chaplin, Yvonne Elsworth, Benoit Famaey, Ortwin Gerhard, Paula Jofre, Andreas Just, Savita Mathur, Andrea Miglio, Ivan Minchev, Giacomo Monari, Benoit Mosser, Andreas Ritter, Thaise S. Rodrigues, Ralf-Dieter Scholz, Sanjib Sharma, Kseniia Sysoliatina, and RAVE Collaboration. The Sixth Data Release of the Radial Velocity Experiment (RAVE). II. Stellar Atmospheric Parameters, Chemical Abundances, and Distances. , 160(2):83, August 2020a. 10.3847/1538-3881/ab9ab8.

Matthias Steinmetz, Gal Matijevič, Harry Enke, Tomaž Zwitter, Guillaume Guiglion, Paul J. McMillan, Georges Kordopatis, Marica Valentini, Cristina Chiappini, Luca Casagrande, Jennifer Wojno, Borja Anguiano, Olivier Bienaymé, Albert Bijaoui, James Binney, Donna Burton, Paul Cass, Patrick de Laverny, Kristin Fiegert, Kenneth Freeman, Jon P. Fulbright, Brad K. Gibson, Gerard Gilmore, Eva K. Grebel, Amina Helmi, Andrea Kunder, Ulisse Munari, Julio F. Navarro, Quentin Parker, Gregory R. Ruchti, Alejandra Recio-Blanco, Warren Reid, George M. Seabroke, Alessandro Siviero, Arnaud Siebert, Milorad Stupar, Fred Watson, Mary E. K. Williams, Rosemary F. G. Wyse, Friedrich Anders, Teresa Antoja, Danijela Birko, Joss Bland-Hawthorn, Diego Bossini, Rafael A. García, Ismael Carrillo, William J. Chaplin, Yvonne Elsworth, Benoit Famaey, Ortwin Gerhard, Paula Jofre, Andreas Just, Savita Mathur, Andrea Miglio, Ivan Minchev, Giacomo Monari, Benoit Mosser, Andreas Ritter, Thaise S. Rodrigues, Ralf-Dieter Scholz, Sanjib Sharma, Kseniia Sysoliatina, and RAVE Collaboration. The Sixth Data Release of the Radial Velocity Experiment (RAVE). I. Survey Description, Spectra, and Radial Velocities. , 160 (2):82, August 2020b. 10.3847/1538-3881/ab9ab9.

C. B. Stephenson. A general catalogue of S stars. *Publications of the Warner & Swasey Observatory*, January 1984.

Oscar Straniero, Roberto Gallino, and Sergio Cristallo. s process in low-mass asymptotic giant branch stars. , 777:311–339, October 2006. 10.1016/j.nuclphysa.2005.01.011.

Takuma Suda, Shimako Yamada, Yutaka Katsuta, Yutaka Komiya, Chikako Ishizuka, Wako Aoki, and Masayuki Y. Fujimoto. The Stellar Abundances for Galactic Archaeology (SAGA) data base - II. Implications for mixing and nucleosynthesis in extremely metal-poor stars and chemical enrichment of the Galaxy. , 412(2):843–874, April 2011. 10.1111/j.1365-2966.2011.17943.x.

Jing Tang, Alessandro Bressan, Philip Rosenfield, Alessandra Slemer, Paola Marigo, Léo Girardi, and Luciana Bianchi. New PARSEC evolutionary tracks of massive stars at low metallicity: testing canonical stellar evolution in nearby star-forming dwarf galaxies. , 445(4):4287–4305, December 2014. 10.1093/mnras/stu2029.

J. H. Telting, G. Avila, L. Buchhave, S. Frandsen, D. Gandolfi, B. Lindberg, H. C. Stempels, S. Prins, and NOT staff. FIES: The high-resolution Fiber-fed Echelle Spectrograph at the Nordic Optical Telescope. *Astronomische Nachrichten*, 335(1):41, January 2014. 10.1002/asna.201312007.

Cajo J. F. Ter Braak. A Markov Chain Monte Carlo version of the genetic algorithm Differential Evolution: easy Bayesian computing for real parameter spaces. *Statistics and Computing*, 16(3):239–249, September 2006. 10.1007/s11222-006-8769-1.

Tom Theuns, Henri M. J. Boffin, and Alain Jorissen. Wind accretion in binary stars - II. Accretion rates. , 280(4):1264–1276, June 1996. 10.1093/mnras/280.4.1264.

Yuan-Sen Ting, Charlie Conroy, Hans-Walter Rix, and Phillip Cargile. The Payne: Self-consistent ab initio Fitting of Stellar Spectra. , 879(2):69, July 2019. 10.3847/1538-4357/ab2331.

J. Tonry and M. Davis. A survey of galaxy redshifts. I. Data reduction techniques. , 84: 1511–1525, October 1979. 10.1086/112569.

Luke Martin Graham Tyas. *The SALT HRS Spectrograph*. PhD thesis, Durham University, UK, May 2012.

S. Udry, A. Jorissen, M. Mayor, and S. Van Eck. A CORAVEL radial-velocity monitoring of giant BA and S stars: Spectroscopic orbits and intrinsic variations. I. , 131:25–41, July 1998. 10.1051/aas:1998249.

M. Van der Swaelmen, H. M. J. Boffin, A. Jorissen, and S. Van Eck. The mass-ratio and eccentricity distributions of barium and S stars, and red giants in open clusters. , 597: A68, January 2017. 10.1051/0004-6361/201628867.

Sophie Van Eck, Pieter Neyskens, Alain Jorissen, Bertrand Plez, Bengt Edvardsson, Kjell Eriksson, Bengt Gustafsson, Uffe Gråe Jørgensen, and Åke Nordlund. A grid of MARCS model atmospheres for late-type stars. II. S stars and their properties. , 601:A10, May 2017. 10.1051/0004-6361/201525886.

J. Th. van Loon, M. R. L. Cioni, A. A. Zijlstra, and C. Loup. An empirical formula for the mass-loss rates of dust-enshrouded red supergiants and oxygen-rich Asymptotic Giant Branch stars. , 438(1):273–289, July 2005. 10.1051/0004-6361:20042555.

Klemen Čotar, Tomaž Zwitter, Janez Kos, Ulisse Munari, Sarah L. Martell, Martin Asplund, Joss Bland-Hawthorn, Sven Buder, Gayandhi M. de Silva, Kenneth C. Freeman, Sanjib Sharma, Borja Anguiano, Daniela Carollo, Jonathan Horner, Geraint F. Lewis, David M. Nataf, Thomas Nordlander, Denis Stello, Yuan-Sen Ting, Chris Tinney, Gregor

Traven, Rob A. Wittenmyer, and Galah Collaboration. The GALAH survey: a catalogue of carbon-enhanced stars and CEMP candidates. , 483(3):3196–3212, March 2019. 10.1093/mnras/sty3155.

Petr Škoda, Brankica Šurlan, and Sanja Tomić. Investigation of residual blaze functions in slit-based echelle spectrograph. In Ian S. McLean and Mark M. Casali, editors, *Ground-based and Airborne Instrumentation for Astronomy II*, volume 7014 of *Society of Photo-Optical Instrumentation Engineers (SPIE) Conference Series*, page 70145X, July 2008. 10.1117/12.789284.

A. Wachter, K. P. Schröder, J. M. Winters, T. U. Arndt, and E. Sedlmayr. An improved mass-loss description for dust-driven superwinds and tip-AGB evolution models. , 384: 452–459, March 2002. 10.1051/0004-6361:20020022.

B. Warner. The barium stars. , 129:263, January 1965. 10.1093/mnras/129.3.263.

Jinmi Yoon, Timothy C. Beers, Vinicius M. Placco, Kaitlin C. Rasmussen, Daniela Carollo, Siyu He, Terese T. Hansen, Ian U. Roederer, and Jeff Zeanah. Observational Constraints on First-star Nucleosynthesis. I. Evidence for Multiple Progenitors of CEMP-No Stars. , 833(1):20, December 2016. 10.3847/0004-637X/833/1/20.

O. Zamora, C. Abia, B. Plez, I. Domínguez, and S. Cristallo. The chemical composition of carbon stars. The R-type stars. , 508(2):909–922, December 2009. 10.1051/0004-6361/200912843.

Xiangyu Zhang, Gregory M. Green, and Hans-Walter Rix. Parameters of 220 million stars from Gaia BP/RP spectra. , 524(2):1855–1884, September 2023. 10.1093/mnras/stad1941.